

INTERFACE FORMATION AND THIN FILM DEPOSITION FOR
MOLECULAR AND ORGANIC ELECTRONICS

A Dissertation

Presented to the Faculty of the Graduate School
of Cornell University

In Partial Fulfillment of the Requirements for the Degree of
Doctor of Philosophy

by

Aravind Srinivasa Killampalli

January 2006

© 2006 Aravind Srinivasa Killampalli

INTERFACE FORMATION AND THIN FILM DEPOSITION FOR MOLECULAR AND ORGANIC ELECTRONICS

Aravind Srinivasa Killampalli, Ph. D.

Cornell University 2006

Organic materials are playing an increasing role in modern microelectronic devices-beyond their traditional role as photoresists. Emerging applications such as low- κ dielectrics, semiconductors and components in molecular electronics demand excellent control of the interface between organic and inorganic materials. To date, almost all work concerning the formation of inorganic-on-organic structures on pre-existing organic layers has involved elemental evaporation of metal thin films. An alternative approach has been examined via the reaction of an organo-transition metal complex, tetrakis(dimethylamido)titanium, $\text{Ti}[\text{N}(\text{CH}_3)_2]_4$, with self-assembled monolayers (SAMs) terminated by -OH, -NH₂ and -CH₃ groups, using x-ray photoelectron spectroscopy (XPS). This is the first detailed study which clearly correlates the reactivity of $\text{Ti}[\text{N}(\text{CH}_3)_2]_4$ with the functionality and density of molecules in a self-assembled monolayer. Extent of reaction, stoichiometry at the interface, ligand loss and decomposition have also been investigated in this study.

A second area of research has involved the formation of organic-on-inorganic structures. Supersonic molecular beams have been employed as sources for deposition of thin films of pentacene, an organic semiconductor, on bare SiO₂ and SiO₂ modified with hexamethyldisilazane (HMDS). Organic materials are often bound by rather weak dispersion (van der Waals) forces and crystallize in different phases, separated in total energy by a few k_BT. Consequently, considerable promise exists in the use of these energy tunable molecular beams for the deposition of organic thin films. Experiments have provided significant insight into fundamental phenomena involved in nucleation in the monolayer regime, and both the kinetics of thin film deposition and the microstructure in the multilayer regime, evidenced by results from ellipsometry and atomic force microscopy (AFM). Promising performance characteristics have been obtained for organic thin film transistors (OTFTs) fabricated from these pentacene films which can be correlated to film microstructure. Finally, modification of the dielectric surface with hexamethyldisilazane (HMDS) has been found to strongly influence nucleation and greatly enhance OTFT performance, possibly due to reduced charge trapping at the semiconductor-dielectric interface.

BIOGRAPHICAL SKETCH

Aravind Srinivasa Killampalli was born in Madras, India on February 13, 1979 and attended St. Michael's Academy where he graduated at the top of his high school class in 1996. He was always fascinated by computers as a kid and wondered how they were made. He moved to the Birla Institute of Technology and Science (BITS), Pilani, India to pursue a Bachelors degree in Chemical Engineering. Four years later he graduated from BITS, Pilani with distinction and again at the top of his class. During his tenure at BITS, Pilani he participated in two internship programs at the Central Leather Research Institute (CLRI) and the Southern Petrochemical Industries Corporation (SPIC), both in Madras, India. During these internships, he developed computer algorithms to model industrial reactors and researched materials for electrodes in polymer electrolyte membrane fuel cells (PEMFCs). During his final year at BITS, Pilani he undertook a study oriented project on reactors for chemical vapor deposition and followed his interests in this area to join the Ph. D program at Cornell University. At Cornell, primary support for his research came from the Cornell Center for Materials Research (CCMR). He received the Edna O. and William C. Hooey Award for Excellence in Graduate Research in December 2004 and was a finalist for the Nottingham Prize at the Physical Electronics Conference in Madison, WI in June 2005. Aravind was awarded the Ph.D in Chemical Engineering in January 2006 and he moved on to work with Intel Corp. in Portland, OR in their division primarily responsible for research and development of CVD processes.

*To my parents, brother, paternal aunts and grandmother
for their perennial affection, understanding and support*

Gnanam Paramam Balam

ACKNOWLEDGMENTS

I am indebted to Prof. James R. Engstrom for being an excellent advisor throughout my stay at Cornell University. He is a very thorough and careful surface scientist in pursuit of the truth behind any experimental result and has helped me inculcate these values. I am grateful to my committee members, Prof. Paulette Clancy and Prof. Joel Brock and to Prof. George G. Malliaras for fruitful discussions concerning organic electronics. I would also like to express my gratitude to Brian Ford and Glenn Swan for prompt help on numerous occasions with ongoing efforts in the laboratories or when new parts needed to be fabricated.

I had the opportunity to work with two senior graduate students, Dr. Paul F. Ma who taught me the ropes with vacuum technology and Dr. Todd W. Schroeder who allowed me to participate in the design and construction of our new supersonic molecular beam system for use at Cornell High Energy Synchrotron Source (CHESS) and I am grateful to both of them. I would also like to thank fellow ERG member Abhishek Dube who has been my comrade in arms in the lab and a good friend outside and younger members Manish Sharma and Jared Mack for their assistance. Malliaras group members Alexios Papadimitratos and Yuanjia Zhang have been excellent collaborators and it has been a pleasure working with them.

My stay in Ithaca has been made enjoyable by several friends, Venkat, Vishal, Dhananjay and Sourav and I am thankful to them for their company. Special thanks to my friends from childhood: Kalyan, Sudhanva and Manthram. We have had the best of times together going back to high school.

Last but not the least, I am eternally thankful to my dad and mom, both professors, for inculcating the importance of science and mathematics at a young age and for always being there for me. Also, my aunts and grandmother for all the love and affection they have showered on me. My little brother has always looked up to me for inspiration and guidance and I hope that I have done well so far and look to do better in the future.

This work was supported by the Cornell Center for Materials Research (CCMR), a Materials Research Science and Engineering Center of the National Science Foundation (DMR-0079992). Additional support was also provided by a Nanoscale Interdisciplinary Research Team on Inorganic-Organic Interfaces (NSF-ECS-0210693) and the Semiconductor Research Corporation via the Center for Advanced Interconnect Systems Technologies (SRC task 995.011).

TABLE OF CONTENTS

1. Introduction.....	1
1.1 Transistors and Integrated Circuits: Current technology.....	1
1.2 Future Directions and Emerging Technologies.....	6
1.2.1 Molecular Electronics.....	7
1.2.1.1 Self-assembled monolayers.....	8
1.2.1.2 Conjugated oligomeric systems.....	10
1.2.1.3 Polyphenylene and polyphenylene based molecules.....	11
1.2.2 Barrier layers.....	11
1.2.3 Organic electronics.....	13
1.3 Thin film deposition.....	17
1.3.1 Physical deposition processes.....	17
1.3.2 Chemical deposition processes.....	19
1.3.3 Nucleation and morphology of thin films.....	24
1.3.4 Atomistic nucleation model.....	28
1.4 Molecular beam techniques.....	30
1.4.1 Characterization of molecular beams.....	31
1.4.1.1 Effusive beams.....	32
1.4.1.2 Supersonic molecular beams.....	34
1.4.2 Supersonic molecular beam scattering.....	41
1.4.2.1 Non-reactive molecular beam scattering.....	42
1.4.2.1.1 Elastic scattering.....	42
1.4.2.1.2 Inelastic scattering.....	42
1.4.2.1.3 Trapping and desorption.....	43

1.4.2.1.4	Molecular chemisorption.....	46
1.4.2.2	Reactive scattering.....	46
1.4.2.2.1	Direct collisional activation.....	47
1.4.2.2.2	Precursor-mediated dissociation.....	48
1.4.2.2.3	Collision induced dissociation.....	49
1.4.3	Thin film deposition using supersonic molecular beams.....	50
1.5	References.....	52
2.	Experimental Procedures.....	56
2.1	Formation of inorganic-organic interfaces.....	56
2.1.1	Description of molecular beam system.....	56
2.1.2	Description and characterization of vapor delivery source.....	61
2.1.3	Sample preparation.....	64
2.1.3.1	Materials.....	64
2.1.3.2	Substrate preparation.....	64
2.1.3.3	Formation of self-assembled monolayers (SAMs).....	65
2.1.3.4	Formation of terminal groups.....	66
2.1.3.5	Characterization of self-assembled monolayers.....	67
2.1.3.5.1	Contact angle measurements.....	67
2.1.3.5.2	Ellipsometry.....	67
2.1.3.5.3	Atomic force microscopy (AFM).....	68
2.1.3.5.4	X-ray photoelectron spectroscopy (XPS).....	68

2.1.4	Interface formation experiments.....	69
2.1.4.1	Estimation of the flux of $\text{Ti}[\text{N}(\text{CH}_2)_2]_4$	69
2.1.4.2	Experimental procedures.....	70
2.1.4.3	X-ray photoelectron spectroscopy (XPS).....	71
2.2	Deposition of organic thin films.....	72
2.2.1	Description of thin film deposition system.....	72
2.2.2	Optimization of supersonic molecular beams of pentacene.....	80
2.2.3	Sample preparation and handling.....	92
2.2.3.1	Thermal oxide clean.....	92
2.2.3.2	Hexamethyldisilazane (HMDS) coating.....	93
2.2.4	Thin film deposition procedures.....	93
2.2.5	Ex-situ analysis techniques.....	96
2.2.5.1	Ellipsometry.....	96
2.2.5.2	Atomic force microscopy (AFM).....	96
2.2.6	Organic thin film transistors (OTFTs).....	98
2.2.7	Variable substrate temperature experiments.....	99
2.2.7.1	Thin film deposition system (G-Line system).....	99
2.2.7.2	Beam characterization and optimization.....	106
2.2.7.3	Thin film deposition procedures.....	107
2.3	References.....	108
3.	The reaction of tetrakis(dimethylamido)titanium with self-assembled monolayers possessing –OH, –NH₂ and –CH₃ terminal groups.....	110
3.1	Overview.....	110

3.2	Introduction.....	111
3.3	Results and discussion.....	114
3.3.1	Characterization of the self-assembled monolayers – the reactive surface.....	114
3.3.2	Reaction of $\text{Ti}[\text{N}(\text{CH}_2)_2]_4$ with SAMs – adsorption kinetics.....	122
3.3.3	Reaction of $\text{Ti}[\text{N}(\text{CH}_2)_2]_4$ with SAMs – microstructure of the adlayer.....	130
3.4	Conclusions.....	148
3.5	References.....	150
4.	Nucleation of pentacene on silicon dioxide at hyperthermal energies.....	156
4.1	Overview.....	156
4.2	Introduction.....	156
4.3	Experimental Methods.....	158
4.4	Results and discussion.....	160
4.5	Conclusions.....	170
4.6	References.....	171
5.	Nucleation of pentacene thin films on silicon dioxide modified with hexamethyldisilazane.....	173
5.1	Overview.....	173
5.2	Introduction.....	173
5.3	Experimental Methods.....	175
5.4	Results and discussion.....	177
5.5	Conclusions.....	185
5.6	References.....	187

6. Supersonic gas source deposition of pentacene thin films.....	189
6.1 Overview.....	189
6.2 Introduction.....	190
6.3 Experimental procedures.....	193
6.4 Results and discussion.....	195
6.4.1 Multilayers on SiO ₂	195
6.4.2 Effect of substrate temperature.....	220
6.4.3 Multilayers on SiO ₂ modified with HMDS.....	226
6.5 Conclusions.....	233
6.6 References.....	234
7. Organic thin film transistors of pentacene films deposited	
using supersonic molecular beams.....	238
7.1 Overview.....	238
7.2 Introduction.....	238
7.3 Experimental methods.....	241
7.4 Results and discussion.....	243
7.5 Conclusions.....	258
7.6 References.....	259
8. Summary.....	262
9. Appendices.....	268
9.1 Temperature calibration.....	268
9.2 Heatable skimmer mounting plate.....	272

LIST OF FIGURES

Figure 1-1	Schematic diagram of a metal oxide semiconductor field effect transistor (MOSFET).....	3
Figure 1-2	Scanning electron microscopy (SEM) images of typical interconnect structures.....	5
Figure 1-3	Schematic representation of a self-assembled monolayer (SAM).....	9
Figure 1-4	Schematic representation of the atomic layer deposition (ALD) process.....	21
Figure 1-5	(a) Atomistic processes in film nucleation and (b) growth modes as a function of film coverage.....	23
Figure 1-6	Schematic illustration of atomistic processes involved in film formation.....	25
Figure 1-7	Schematic representation of (a) effusive and (b) supersonic molecular beam systems.....	33
Figure 1-8	Energy distribution of pentacene molecules for effusive and supersonic beams using H ₂ and He as the seeding gas.....	36
Figure 1-9	Illustration of the structures formed during a supersonic expansion.....	39
Figure 1-10	One dimensional potential energy diagrams for gas-surface interactions.....	44
Figure 1-11	Illustration of the three different reactive scattering mechanisms.....	45
Figure 2-1	Schematic drawing of molecular beam scattering chamber.....	57
Figure 2-2	Schematic drawing of delivery system for Ti[N(CH ₃) ₂] ₄	60

Figure 2-3	Waveforms for the exposure of a substrate to $\text{Ti}[\text{N}(\text{CH}_3)_2]_4$	62
Figure 2-4	AUTOCAD 3-dimensional rendering of thin film deposition system.....	73
Figure 2-5	Schematic side and top views of thin film deposition system.....	74
Figure 2-6	Schematic representation of supersonic beam source for low vapor pressure materials.....	78
Figure 2-7	Beam intensity for CO_2 seeded in helium carrier gas as a function of carrier gas flow rate (conical skimmer in forward position).....	82
Figure 2-8	Beam intensity for CO_2 seeded in helium carrier gas as a function of carrier gas flow rate (conical skimmer in rear position).....	83
Figure 2-9	Beam to background ratio for CO_2 seeded in helium carrier gas as a function of carrier gas flow rate (conical skimmer in rear position).....	84
Figure 2-10	Beam intensity for pentacene seeded in helium carrier gas as a function of carrier gas flow rate (conical skimmer in forward position).....	85
Figure 2-11	Beam intensity for pentacene seeded in helium carrier gas as a function of carrier gas flow rate (conical skimmer in rear position).....	86
Figure 2-12	Beam to background ratio for pentacene seeded in helium carrier gas as a function of carrier gas flow rate (conical skimmer in forward position).....	87
Figure 2-13	Beam Intensity for pentacene seeded in helium carrier gas as a function of carrier gas flow (trumpet shaped	

	skimmer in rear position).....	89
Figure 2-14	Beam to background ratio for pentacene seeded in helium carrier gas as a function of carrier gas flow rate (trumpet-shaped skimmer in rear position).....	90
Figure 2-15	Schematic representation of the multiple exposure technique employed during thin film nucleation and growth.....	94
Figure 2-16	Side view schematic drawing of the gas source deposition system.....	100
Figure 2-17	Top view schematic drawing of the gas source deposition system.....	101
Figure 2-18	Beam Intensity for pentacene seeded in helium carrier gas as a function of carrier gas flow rate (G-Line system with 1mm conical skimmer in forward position).....	104
Figure 2-19	Intensity for pentacene seeded in helium carrier gas as a function of carrier gas flow rate (G-Line system with conical 1.5 mm skimmer in forward position).....	105
Figure 3-1	Atomic force micrographs of -OH, -NH ₂ and -CH ₃ terminated SAMs.....	117
Figure 3-2	XP spectrum for Si(2p) feature of chemical oxide.....	119
Figure 3-3	XP spectra for N(1s) and C(1s) features for SAMs.....	121
Figure 3-4	XP spectra of the Ti (2p) feature for a chemical oxide surface exposed to Ti[N(CH ₃) ₂] ₄ at T _s = 30°C.....	123
Figure 3-5	Coverage-exposure relationship for Ti[N(CH ₃) ₂] ₄ on all four substrates at T _s = -50 °C.....	125
Figure 3-6	Coverage-exposure relationship for Ti[N(CH ₃) ₂] ₄ on all four substrates at T _s = 30 °C.....	126

Figure 3-7	Coverage-exposure relationship for $\text{Ti}[\text{N}(\text{CH}_3)_2]_4$ on all four substrates at $T_s = 110\text{ }^\circ\text{C}$	127
Figure 3-8	Initial probability of adsorption for $\text{Ti}[\text{N}(\text{CH}_3)_2]_4$ on all four substrates as a function of T_s	129
Figure 3-9	Ti saturation concentration for adsorption for $\text{Ti}[\text{N}(\text{CH}_3)_2]_4$ on all four substrates as a function of T_s	131
Figure 3-10	Peak areas of the O(1s) and C(1s) regions derived from XP spectra of a $-\text{CH}_3$ terminated SAM ($\equiv\text{Si}-(\text{CH}_2)_{17}-\text{CH}_3$) as a function of take-off angle.....	133
Figure 3-11	Ti(2p) peak area for $\text{Ti}[\text{N}(\text{CH}_3)_2]_4$ adsorbed on all four substrates as a function of take-off angle.....	134
Figure 3-12	Relationship Ti concentration in the saturated adlayers and SAM concentration.....	138
Figure 3-13	Ratio of N to Ti in the saturated adlayer (from XPS) for $\text{Ti}[\text{N}(\text{CH}_3)_2]_4$ adsorbed on all four substrates as a function of T_s	141
Figure 3-14	Binding energy of the Ti(2p _{3/2}) peak in the saturated adlayer for $\text{Ti}[\text{N}(\text{CH}_3)_2]_4$ adsorbed on chemical oxide and the $-\text{NH}_2$ terminated SAM as a function of attenuation corrected Ti density.....	144
Figure 4-1	Atomic force micrographs of pentacene on SiO_2 as a function of exposure ($E_i = 6.7\text{ eV}$, $\theta_i = 0^\circ$).....	161
Figure 4-2	Coverage-exposure relationships (from AFM) for adsorption of pentacene on SiO_2 at four E_i and normal incidence.....	162
Figure 4-3	The initial probability of adsorption of pentacene on SiO_2 as a function of θ_i for four E_i	164

Figure 4-4	Initial (normalized) probability of adsorption of pentacene on SiO ₂ as a function of scaled incident kinetic energy.....	166
Figure 4-5	Maximum island densities for pentacene on SiO ₂ as a function of θ_i , for four E_i	167
Figure 4-6	Maximum island densities for pentacene on SiO ₂ vs. the sub-monolayer growth rate for all E_i and θ_i	168
Figure 5-1	Atomic force micrographs of pentacene on SiO ₂ surfaces modified with HMDS as a function of exposure ($E_i = 6.7$ eV, $\theta_i = 0^\circ$).....	178
Figure 5-2	Occupancy of the first and second monolayers of pentacene as a function of total amount of material deposited on clean SiO ₂ and SiO ₂ modified with HMDS.....	180
Figure 5-3	The probability of adsorption of pentacene on clean SiO ₂ and SiO ₂ modified with HMDS as a function of E_i	183
Figure 5-4	Maximum island densities for pentacene on clean SiO ₂ and SiO ₂ modified with HMDS as a function of the growth rate in the sub-monolayer regime.....	184
Figure 6-1	Atomic force micrographs of multilayer films of pentacene on SiO ₂ as a function of exposure ($E_i = 6.7$ eV, $\theta_i = 0^\circ$).....	196
Figure 6-2	Thickness-exposure relationships, deduced from ellipsometry for the adsorption of pentacene on a pentacene multilayer for four E_i and three θ_i	198
Figure 6-3	Probability of adsorption of pentacene on a thin film as a function of E_i and θ_i	202
Figure 6-4	Initial (normalized) probability of adsorption of pentacene on a multilayer on SiO ₂ as a function of scaled incident	

	kinetic energy.....	203
Figure 6-5	Ratio of multilayer and submonolayer deposition rates as a function of E_i and θ_i	205
Figure 6-6	The ratio of multilayer to submonolayer deposition rates as a function of scaled incident kinetic energy.....	206
Figure 6-7	Atomic force micrographs of pentacene thin films on SiO_2 as a function of E_i , deposition time of 40 min., $\theta_i = 0^\circ$	208
Figure 6-8	Evolution of the 1-dimensional power spectral density (PSD) as a function of spatial frequency for four E_i , $\theta_i = 0^\circ$	210
Figure 6-9	Roughness exponent α as a function of incident energy for two angles of incidence, 0° and 75°	212
Figure 6-10	Root mean square (RMS) roughness as a function of film thickness for pentacene films deposited with four E_i , $\theta_i = 0^\circ$	213
Figure 6-11	Growth exponent β as a function of incident energy for three θ_i - 0° , 45° and 75°	218
Figure 6-12	Growth exponent β as a function of film growth rates ($\text{\AA}\cdot\text{s}^{-1}$).....	219
Figure 6-13	Pentacene film thickness as a function of T_s for four E_i and two sets of fluxes.....	221
Figure 6-14	Root mean square (RMS) roughness as a function of film thickness for pentacene films deposited at the three T_s	222
Figure 6-15	Atomic force micrographs of pentacene films deposited on SiO_2 for two E_i and three T_s	224
Figure 6-16	Atomic force micrographs of pentacene on SiO_2 modified with HMDS ($E_i = 6.7 \text{ eV}$, $\theta_i = 0^\circ$).....	227

Figure 6-17	(a) Thickness-exposure relationships, for the adsorption of pentacene on a multilayer at the four E_i for $\theta_i = 0$. The substrate was SiO_2 modified with HMDS. (b) The initial probability of adsorption of pentacene on a multilayer deposited on SiO_2 modified with HMDS and bare SiO_2 as a function of E_i , $\theta_i = 0$	228
Figure 6-18	Roughness exponent α and growth exponent β as a function of E_i for pentacene films deposited on SiO_2 modified with HMDS.....	231
Figure 7-1	Top and bottom contact configurations for OTFTs.....	242
Figure 7-2	Correlation length obtained from 1DPSD analysis of AFM images plotted as a function of thickness for pentacene thin films deposited on SiO_2 for four E_i and $\theta_i = 0$	244
Figure 7-3	Thickness-averaged correlation length plotted as a function of E_i for pentacene thin films deposited on SiO_2 and SiO_2 modified with HMDS.....	246
Figure 7-4	Mobility of organic thin film transistors plotted as a function of thickness-averaged correlation length for pentacene films deposited on (a) SiO_2 and (b) SiO_2 modified with HMDS.....	247
Figure 7-5	Drain-to-source current plotted as a function of drain-to-source voltage for pentacene thin film transistors fabricated on (a) SiO_2 and (b) SiO_2 modified with HMDS.....	253
Figure 9-1	Temperature calibration curve for sample surface (beam scattering system).....	269

Figure 9-2	Temperature calibration curve for sample surface (thin film deposition system – G-Line).....	271
Figure 9.3	AUTOCAD drawing of skimmer mounting plate (designed for the thin film deposition system – G-Line).....	263

LIST OF TABLES

Table 1-1	Nucleation parameters p and E for the atomistic nucleation model summarizing nucleation behavior.....	27
Table 3-1	Properties of self-assembled monolayers.....	115
Table 6-1	Rapid roughening of thin films.....	216
Table 7-1	Performance characteristics of organic thin film transistors.....	252

LIST OF ABBREVIATIONS

a-Si:H	amorphous silicon
AFM	atomic force microscopy
ALD	atomic layer deposition
BEOL	back end of the line
CMOS	complementary metal-oxide-semiconductor
CVD	chemical vapor deposition
eV	electron volt
FET	field effect transistor
FEOL	front end of the line
GIXD	grazing incidence x-ray diffraction
GR	growth rate
HMDS	hexamethyldisilazane
IC	integrated circuit
KPZ	Karder-Parisi-Zhang class of materials
LEED	low energy electron diffraction
LCVD	laser induced chemical vapor deposition
LN ₂	liquid nitrogen
MBE	molecular beam epitaxy
MOSFET	Metal oxide semiconductor field effect transistor
OTFT	organic thin film transistor
OTS	octadecyltrichlorosilane
PHCVD	photo enhanced chemical vapor deposition
PSD	power spectral density
PVD	physical vapor deposition

QMS	quadrupole mass spectrometry
RD	random deposition
SAM	self-assembled monolayer
SEM	scanning electron microscopy
TOF	time of flight
UHV	ultra-high vacuum
XPS	x-ray photoelectron spectroscopy

LIST OF SYMBOLS

α	roughness exponent
	function or parameter characterizing the velocity distribution of a molecular beam
A	perpendicular energy coefficient
β	growth exponent
B	parallel energy coefficient
c	stream velocity of a molecular beam
$\langle C_p \rangle$	mole fraction mean heat capacity of a mixture of gases
C_p	specific heat capacity at constant pressure
C_p	specific heat capacity at constant volume
d	nozzle orifice diameter
d_{pen}	height of monolayer film of pentacene
E_D	activation energy for desorption
E_{i^*}	critical cluster dissociation energy
E_i	incident kinetic energy
E_S	activation energy for surface diffusion
F	incident flux of molecules in a supersonic beam
γ	interfacial energy
	ratio of C_p to C_v
ΔG	Gibbs free energy
I_{on}	saturation current when transistor is turned on
I_{off}	current flowing through transistor when $V_{\text{GS}} = 0$
I_{DS}	drain-to-source current
i^*	critical cluster size (number of molecules)

λ	mean free path of a molecule
Kn	Knudsen number
μ	electronic mobility
$\langle m \rangle$	mole fraction mean mass of a mixture of gases
m	molecular weight
m_{cg}	carrier gas flow rate
ML	monolayer
N_{max}	maximum island density
P_0	stagnation pressure
P_n	nozzle pressure or stagnation pressure
S	inverse subthreshold slope
S_A	probability of adsorption
S_I	probability of incorporation
θ_i	angle of incidence (from surface normal)
T_e, T_b	temperature of evaporator for low vapor pressure materials
T_n, T_{noz}	nozzle temperature
T_s	substrate temperature
v	velocity
V_{th}	threshold voltage
V_{DS}	drain to source voltage
V_{GS}	gate-to-source voltage
w	root mean square roughness
ξ	thickness-averaged correlation length

1. Introduction

The invention of the transistor at Bell Labs in 1947 by Walter Brattain, John Bardeen and William Shockley sparked the astonishing advances made in microelectronics over the last 50 years. In 1959, Jack Kilby and Robert Noyce independently developed the integrated circuit (IC) where not just the transistor, but an entire electronic circuit could be fabricated out of a single crystal of silicon and thereby miniaturized to the size of a pencil point. Since these path-breaking discoveries, over the years, transistors and their integrated circuits have become integral parts of our day-to-day lives. Almost every electronic gadget that is used today incorporates integrated circuits; computers, portable electronics including mobile phones, personal digital assistants, audio and video players and radios; household appliances like ovens, washing machines, drying machines, dishwashers and microwave ovens and entertainment choices like the television, gaming systems, music and video players. Automobiles with computers for engine control, safety and emissions systems; satellites, space exploration programs, advances in weapons and security systems and health care have all been possible owing to widespread use of transistors and ICs in the modern world.

1.1 Transistors and Integrated Circuits: Current technology

Gordon Moore, in 1965 [1], predicted that the number of transistors per given area would double every year but revised the timeline to 18 months in 1975. This paradigm, called Moore's Law also predicted an associated

decrease in overall cost of production per transistor owing to miniaturization, and has fueled the development of electronic technology in leaps and bounds. Almost four decades later, Moore's law continues to hold due to advances in lithography and deposition techniques. While a detailed description of the advances made in transistor technology over the years is beyond the scope of this work, it is useful to look at the structure of a metal oxide field effect transistor (MOSFET), to understand the basic structure and operation of a typical transistor, and perceive the challenges faced in the near future. Shown in Fig. 1-1 is the schematic structure for a MOSFET. These transistors consist of a series of layers: a semiconductor layer (usually a slice, or wafer, from a single crystal of silicon), a layer of silicon dioxide (the oxide) and a layer of metal. These layers are patterned in a manner which permits transistors to be formed in the semiconductor material (the "substrate"). Silicon dioxide is a very good insulator, so a very thin layer can be used (currently 0.8 nm). Polycrystalline silicon (poly) has been widely used for the gate electrode. Polysilicon gate FET's have replaced virtually all of the older devices using metal gates in large scale integrated circuits. Both metal and polysilicon FET's are sometimes referred to as IGFET's (insulated gate field effect transistors) since the silicon dioxide under the gate is an insulator. Electrical charge, or current, can flow from the source to the drain. This flow is controlled by the voltage applied to the gate. The semiconductor material in the source and drain regions is "doped" with a different type of material than in the region under the gate, so an NPN or PNP type structure exists between the source and drain region of a MOSFET. The source is the terminal, or node, which acts as the source of charge carriers. These charge carriers leave the source and travel to

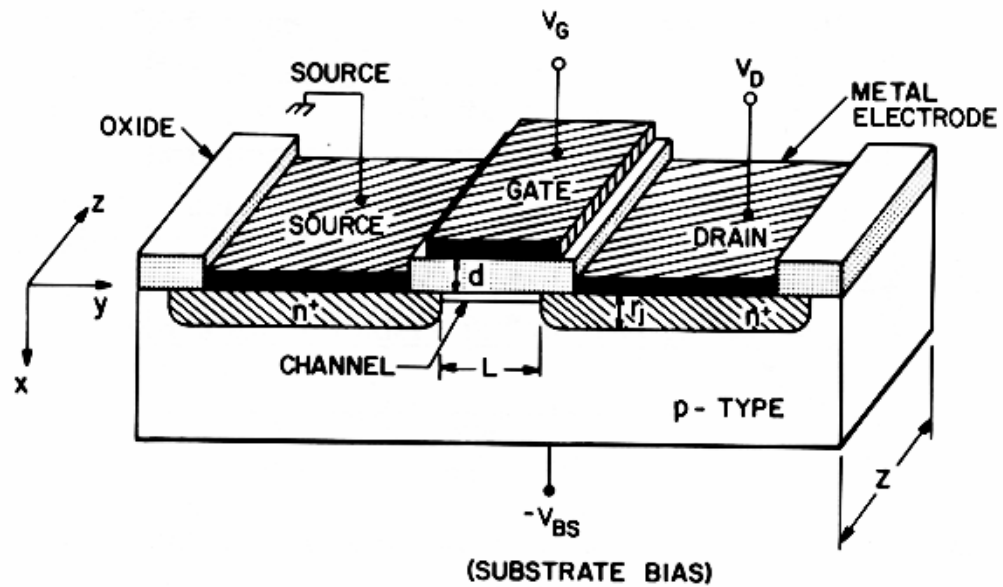


Figure 1–1 The structure of a metal oxide semiconductor field effect transistor (MOSFET). The substrate is usually single crystal silicon, source, drain and source regions are heavily doped and the gate electrode is a metal. The gate oxide is currently silicon dioxide. The structure is built through a sequence of processes including lithography, ion implantation, deposition, oxidation, annealing and etching. From Reference [2].

the drain. The area under the gate oxide is called the “channel”. The MOSFET can operate as an efficient switch for current flowing between the source and drain region of the device.

Creation of transistors on a silicon die is commonly referred to as the Front End of the Line (FEOL) in the semiconductor industry. Continuing to deliver innovation to make the predictions of Moore’s law a reality has required the integration of a wide variety of materials, engineering of optimized transistor structures and the shrinking of the nominal size of individual components in these integrated circuits. State of the art requires building insulating layers of silicon dioxide that are as thin as 0.8 nm and placing transistors close enough to each other to allow for a channel length (L , c.f. Fig. 1–1) of 65 nm for the current “technology node”. There are several issues that come into play at these extremely small dimensions including the mechanical integrity, capacitance and uniformity of the insulating film, the ability to dope the silicon in very well confined regions and to well controlled depths by ion implantation and the ability to pattern source, drain and gate electrodes accurately, all the while taking into account the fact that these processes are integrated and affect one another. This decrease in size to accommodate advances in the density and speed of transistors fabricated on a silicon die could also lead to non–statistical and unpredictable behavior of individual components, increased fabrication costs and power consumption associated with increasing leakage currents and heat dissipation. An important, exploratory research area trying to address some of these issues deals with a different approach where devices can be constructed bottom–up from the molecular level, a field popularly known as Molecular Electronics.

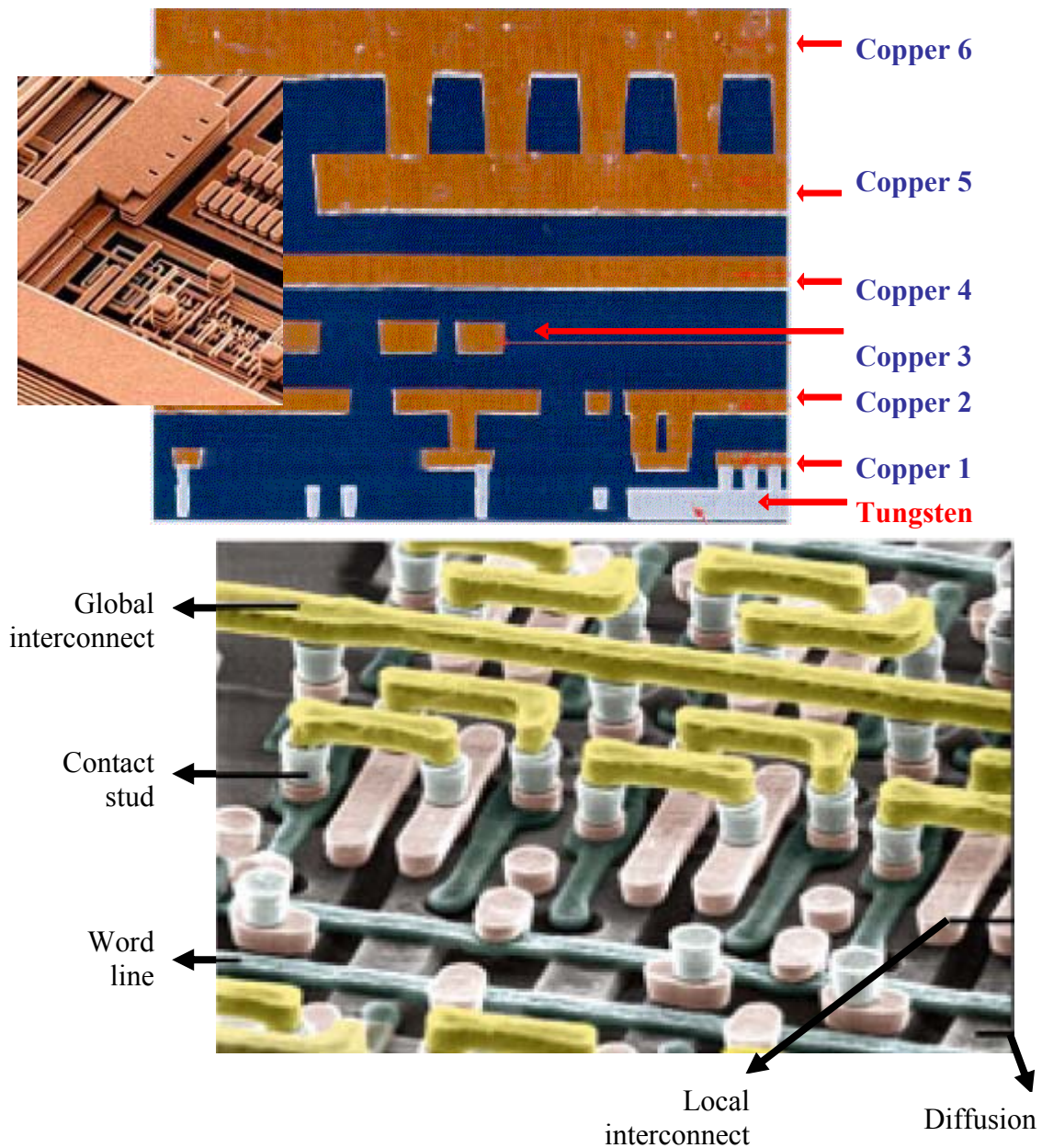


Figure 1–2 Scanning electron microscopy (SEM) images of typical interconnect structures. The top left (inset) and bottom images show the individual metals layers with the interlayer dielectric removed. The top right image shows the cross-sectional view of multilayers of metal wires connected to transistors on the silicon die (not shown). Reprinted from IBM promotional materials.

With an increase in the density of transistors on a silicon die, additional difficulties arise with respect to wiring these transistors to the outside world, referred to as the Back End of the Line (BEOL). Fig. 1–2 shows scanning electron micrograph (SEM) images of typical interconnect structures. Challenges include building several layers of metallic wires (copper in the current generation of technology) separated from each other and from adjacent layers by a dielectric material with a low dielectric constant (κ), referred to as the interlayer dielectric (ILD). The objective is minimization of signal delay, cross talk and power dissipation in interconnect structures in order to obtain optimum performance. These goals become increasingly challenging as the wires are brought closer to each other by miniaturization. With these shrinking dimensions, silicon dioxide, the dielectric material of choice, has to be replaced by newer materials which are porous to decrease the dielectric constant. Pores should be fully closed and of uniformly small size, achieving pore volume low enough to provide adequate mechanical properties. Finally, metal wires in interconnects are fabricated in horizontal and vertical structures, the latter being dual damascene structures including a trench and a via. Diffusion of metal into the dielectric or silicon is a significant problem and current techniques to minimize this problem deal with deposition of conformal barrier layers of refractory materials like titanium or tantalum metals or their nitrides.

1.2 Future directions and emerging technologies

Very soon, the dimensions of these individual transistors will approach the physical limits of atomic structure posing significant processing challenges in areas such as choice and integration of materials, patterning, conformal

deposition and selective etching of high aspect ratio structures. Simultaneously, improvements in switching efficiency and minimization of power consumption have to be achieved.

1.2.1 Molecular Electronics

This drive to further miniaturization of silicon based electronics has led to the development of a whole new field with a bottom–up approach where individual devices would be molecular scale components giving rise to the nanoelectronics of the future. The first discussion of this field was within the United States Defense Department as a theoretical area of promise in the late 1950s. It was presaged by Richard Feynman in his famous speech at the annual meeting of the American Physical Society in 1959: “There is plenty of room at the bottom”. The subject was then given some concrete direction by a theoretical proposal by Aviram and Ratner in 1974 [3] of an electrical rectification or diode behavior, by a single molecule with suitable electronic asymmetry. In the last decade, several advances have been made in this field, thanks to a burst of new direct measurements of the electronic behavior either of single molecules or “self–assembled monolayers” – single molecule ordered films – either by scanning tunneling microscopy (STM) or conducting atomic force microscopy (AFM). Current research is using molecules in such electronic applications as interconnects, switches, rectifiers, transistors, nonlinear components, dielectrics, photovoltaics and memories. For electronics applications, molecular structures have four distinct advantages [4]:

1. Size. The size scale of molecules is between 1 and 100 nm, a scale that permits functional nanostructures with accompanying advantages in cost, efficiency and power dissipation.
2. Assembly and recognition. One can exploit specific intermolecular interactions to form structures by nanoscale self-assembly. Molecular recognition can be used to modify electronic behavior, providing both switching and sensing capabilities on the single-molecule scale.
3. Dynamical stereochemistry. Many molecules have multiple distinct stable geometric structures or isomers and these have distinct optical and electronic properties.
4. Synthetic tailorability. By choice of composition and geometry, one can extensively vary a molecule's transport, binding, optical and structural properties. The tools of molecular synthesis are fairly well developed.

Molecules have their disadvantages, such as instability at high temperatures and mechanical fragility to further processing steps. In addition, molecular devices could be quite challenging as the number of molecules, their configuration, purity and numerous other important variables are not easily known and not amenable to known characterization tools. There have been three types of molecular structures that have been widely studied in the last decade.

1.2.1.1 Self-assembled monolayers

A significant step forward in the fabrication of molecular electronic devices was the advent of self-assembly methodologies [5–8] to prepare stable

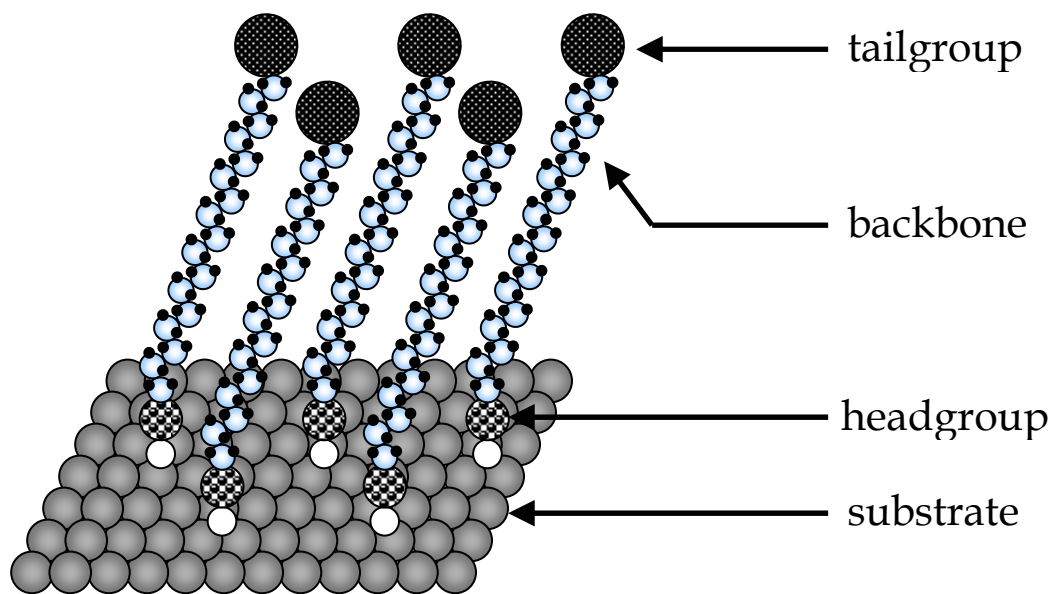


Figure 1–3 Schematic representation of a self-assembled monolayer (SAM) showing the three individual components of each molecule namely headgroup, backbone and tailgroup.

adherent molecular films on suitable substrates with ordered geometries and a wide range of terminal functionalities. Each molecule in a self-assembled monolayer (SAM) film consists of three components: an active headgroup which binds to a suitable substrate, a functional tailgroup which provides for a wide variety of surface terminations and the backbone which permits the ordering of a layer by van der Waals interactions with neighboring molecules. Fig. 1–3 shows the structure of a typical SAM film. A self-assembled system attempts to reach a thermodynamically stable state driven by the global minimization of free energy and tends to eliminate growing foreign or faulty structures of molecules during the assembly process. This intrinsic error-correction advantage makes SAMs inherently manufacturable and thus technologically attractive and cost effective.

In addition, SAM films can be designed and engineered to provide extremely high functional density. For example, one can realize a switch or a memory out of a single monolayer. On the other hand, in order to perform highly complex functions such as those of current integrated circuits, a self-assembly strategy that enables easy formation of complex patterns to “program” the structures and electrical properties of materials at nanometer levels needs to be developed.

1.2.1.2 Conjugated Oligomeric Systems

Another approach to harnessing molecules as individual electronic components, involves the use of conjugated oligomers. The term “conjugated” means an alternation of multiple and single bonds linking a sequence of bonded atoms, such that there is an extended series of overlapping orbitals (for example

in benzene, all C–C–C bond angles are 120° , all six carbons are sp^2 hybridized, each carbon has a p orbital perpendicular to the plane of the ring which overlaps with two neighboring orbitals leading to a picture of benzene in which six π electrons are completely delocalized around the ring). Oligomers are generated by joining one molecular unit to itself a few times. This repeated unit is the equivalent of the unit cell in the solid state; referred to as a monomer. Thus, in conjugated oligomers, in addition to a framework of σ bonds that establishes molecular structure, delocalized π electrons allow for electronic transport.

1.2.1.3 Polyphenylene and Polyphenylene-based Molecules

The delocalization in benzene can be extended to other adjacent atoms. Binding benzene rings forms a chain-like structure called polyphenylene. Borrowing the idea of di-block copolymers from bulk organic materials, one can also insert other types of molecular groups into a polyphenylene chain (e.g., singly bonded aliphatic groups ($-\text{CH}_2-\text{CH}_2-$), doubly bonded ethenyl groups ($-\text{CH}=\text{CH}-$), and triply bonded ethynyl groups ($-\text{C}\equiv\text{C}-$)) to obtain polyphenylene-based molecules. In these molecules, delocalized π orbitals extend across and merge with the neighboring aromatic ring and multiple bonded groups, maintaining delocalization throughout the length of the molecule.

1.2.2 Barrier Layers

Current technology employs copper-based interconnects and low dielectric constant (κ) metallization schemes to minimize the resistance times

capacitance (RC) time delay limiting signal transmission in emerging chip and system architectures. However, Cu has been shown to diffuse rapidly into Si and SiO₂. Cu can homogeneously distribute in the bulk of the wafer during high temperature anneals with defects or impurities acting as gettering sites. Interstitial point defects, complexes, precipitates or surface segregation could occur to different extents when the wafer is cooled.

Consequently a barrier layer or liner is required to prevent Cu diffusion [9]. The main requirements for the barrier layer material are:

1. The ability to prevent the diffusion of Cu into the surrounding dielectric,
2. A relatively low electrical resistivity since the effective resistivity of a metal line is a combination of the resistivity of the metal plus the barrier layer material,
3. Interactions with Cu which permits good adhesion and nucleation properties.

To this end, transition metals and their nitrides have emerged as the most promising materials for this application, namely, Ti/TiN and Ta/TaN. Furthermore, the nitrides have been found to be better diffusion barriers at the same thickness compared to the pure metals. In previous studies, TiN has been found to prevent Cu diffusion for up to 2 hours at a temperature of 575 °C [10] whereas TaN films have been shown to retain barrier properties for a five minute rapid thermal anneal at 750 °C [11]. As a result, TiN and TaN deposition has also received much attention. The traditional method of deposition has been reactive plasma sputtering in a N₂ atmosphere. More recently, CVD of TiN using TiCl₄ and NH₃ as reactants has shown promise for depositing conformal films in high aspect ratio trenches [12]. However the

high temperatures required ($> 500\text{ }^{\circ}\text{C}$) for this deposition are not compatible with other processing steps involved in IC fabrication.

Organometallic precursors of Ti and Ta have recently been shown to be good candidates for use in low temperature conformal deposition of TiN and TaN when used alternately with a nitrogen-containing precursor (e.g. NH_3 or $\text{N}(\text{CH}_3)_2$) by a technique called Atomic Layer Deposition (ALD, c.f. section 1.3.2). Efforts directed towards obtaining fundamental insight into the interactions of tetrakis(dimethylamido)titanium, TDMAT (an organometallic precursor for TiN), with various functionalized self-assembled monolayers (studied as model low- κ surfaces), employing a molecular beam, are described in chapter 3. Issues addressed include:

1. formation of a conformal organic film by self-assembly techniques with a variety of functional terminations,
2. study of the first half reaction for the formation of titanium nitride using TDMAT, on this functionalized organic film.

1.2.3 Organic Electronics

In 1977, Alan Heeger, Hideki Shirakawa, Alan McDiarmid and their co-workers at the University of Pennsylvania accidentally discovered that they could vary the electrical conductivity of the conjugated polymer, polyacetylene, over 11 orders of magnitude – from an insulator to a semiconductor to a metal – by adding trace amounts of a donor or acceptor to the material [13]. This remarkable observation immediately opened a range of applications for conducting polymers, including organic electronics. The first organic thin film transistor (OTFT) with usefully large current modulation used polythiophene as

the organic semiconductor, heavily doped silicon substrate as gate and a thermally grown silicon dioxide layer as gate dielectric. A carrier field effect mobility of $10^{-5} \text{ cm}^{-2}\text{-V}^{-1}\text{-s}^{-1}$ was obtained. Most of the early OTFTs were fabricated using polymers as the active semiconductor. The first small-molecule OTFT showing useful current modulation was demonstrated in 1988 by Clarisse and co-workers, based on thermally evaporated scandium diphthalocyanine (ScPc₂) and nickel phthalocyanine (NiPc) with an on/off current ratio of 10^3 and a carrier mobility of $10^{-3} \text{ cm}^{-2}\text{-V}^{-1}\text{-s}^{-1}$. This result was an order of magnitude larger than the best mobility reported for polymer thin film transistors at the time.

Since these early demonstrations, the incorporation of organic materials in electronic circuits has increased exponentially over the last decade with potential applications being light-emitting displays and printable electronic circuits. Like their traditional inorganic counterparts, organic semiconductors can function either as p-type or n-type. While in p-type semiconductors, the majority carriers are holes, in n-type semiconductors the majority carriers are electrons. Several small molecules, self-assembled monolayers, fused aromatics, oligomers or other conjugated polymers have been studied with applications to organic electronics. Among the small molecule films, most organic semiconductors are p-type including pentacene, α -sexithiophene and phthalocyanine. A small number of n-type materials have been identified as well, including C₆₀, halogenated phthalocyanines and naphthalene derivatives.

OTFTs fabricated from these materials cannot rival the performance of field-effect transistors based on single crystal inorganic semiconductors such as Si, Ge and GaAs, which have charge carrier mobilities larger by three to four orders of magnitude. Consequently, OTFTs are not useful in applications

involving very high switching speeds. However, these devices can be competitive candidates for existing or novel thin film transistor applications owing to the following advantages:

1. low cost,
2. low processing temperatures close to room temperature,
3. choice of a variety of substrates including cheap flexible ones,
4. large area coverage,
5. compatibility with a wide variety of other materials.

Such applications include switching devices for active matrix flat panel displays (AMFPDs) based on liquid crystal pixels (i.e. active matrix liquid crystal displays or AMLCDs), active matrix organic light emitting diodes (AMOLEDs) [14], or “electronic paper” displays [15] based on pixels comprising either electrophoretic ink-containing microcapsules[16] or twisting balls. Additionally, sensors [17], low-end smart cards, and radio-frequency identification tags (RFIDs) [18] consisting of organic integrated circuits have been proposed and prototype all-polymer integrated circuits have been demonstrated.

The application of organic materials to electronic circuits will vary based on required performance standards. For example, in AMLCDs, the active backplane consists of TFTs made from hydrogenated amorphous silicon (a-Si:H) with entrenched technology for large area applications. OTFTs can enable applications that are not achievable with this technology involving plastic substrates. However, for OTFTs to compete directly with a-Si:H thin film transistors, they should exhibit device performance similar to the latter, i.e. field effect mobility $\mu = 1 \text{ cm}^2\text{-V}^{-1}\text{-s}^{-1}$, current modulation (on/off ratio, $I_{\text{on/off}}$) of 10^6 or higher and a reasonable operating threshold voltage of 15 V or less.

Additionally, these transistors should be stable after prolonged exposure to ambient conditions and should not exhibit large threshold voltage shifts.

A very promising candidate for applications to organic transistors is pentacene, a five ring molecular system of the monomer benzene. A small molecule p-type organic semiconductor, it has been widely studied owing to its superior field effect mobility and environmental stability. However, there are several questions that remain unanswered concerning the performance of OTFTs made from polycrystalline films of pentacene. First, nucleation of pentacene on suitable substrates and the morphology at the interface is not well understood. In addition, fundamental insight into growth mechanisms is yet to be gleaned. This knowledge would be crucial to correlating submonolayer and thin film morphology with the performance of OTFTs. A supersonic source of pentacene permits control of incident kinetic energy and flux. The effect of these parameters together with angle of incidence and the nature of the substrate on film nucleation, deposition and morphology are examined in chapters 4–6. More specifically, in chapters 4–5, the nucleation of pentacene films on thermal silicon dioxide and SiO_2 substrates modified with hexamethyldisilazane (HMDS) using a supersonic molecular beam source is detailed. In chapter 6, deposition of thin films of pentacene and the evolution of thin film structure and morphology are described. The effect of substrate temperature on film morphology is also examined. Finally, in chapter 7, efforts directed at fabrication of organic thin film transistors of pentacene deposited using a supersonic beam source on bare thermal SiO_2 and thermal SiO_2 substrates modified with HMDS are delineated. An understanding of performance characteristics in relation to properties of pentacene thin films is obtained.

1.3 Thin film deposition

Thin film deposition techniques are essential to the development of material structures forming the core of semiconductor devices such as microprocessors and memory units. Requirements for thin solid films of a wide variety of materials deposited from the gas, liquid or solid phase with improved quality, purity and versatile applicability as well as improved understanding of the physics and chemistry of films, interfaces, surfaces and microstructures has fueled the rapid evolution of technology in this field.

1.3.1 Physical Deposition Processes

Deposition of thin films is primarily classified into two types of processes: physical deposition and chemical deposition. As the names suggest, in physical vapor deposition (PVD) the process is purely physical in that molecules that are transported from a source travel in straight lines and deposit on the substrate without undergoing intermediate chemical reactions. Physical deposition processes include molecular beam epitaxy (MBE), evaporation, sputter deposition, glow discharge and plasma-assisted processes. Most precursors in PVD processes are individual atoms or clusters of atoms. This type of deposition process is typically “line of sight” in that molecules only deposit on surfaces that are directly in their path. There are several types of PVD processes. In molecular beam epitaxy (MBE) the reactant is heated to suitable temperatures in a crucible or Knudsen cell, slowly evaporating the elemental or molecular constituents of the film onto a substrate held at a temperature suitable for epitaxy and re-evaporation of excess reactants.

Shutters provide control of exposure to multiple sources and crucible temperature determines the flux. Sputtering involves the ejection of surface atoms from an electrode surface by momentum transfer from bombarding ions to surface atoms. This technique could be used as an etching process for surface cleaning and pattern delineation. There are several methods of producing the bombarding species resulting in different sub-classes including diode, reactive, bias, magnetron and ion-beam sputtering. In plasma-assisted processing, the material to be deposited is made the cathode of a glow discharge and simultaneously heated by radiation or radio frequency induction. The resulting energetic reactive ions are used to decompose or break down reactant gases, either yielding the desired product film or enhancing a given deposition process. Plasma deposition processes are used to produce films at lower substrate temperatures and in a more energy efficient fashion than other techniques. One application of this technique is the deposition of secondary passivation films of silicon nitride on semiconductor devices. Other physical deposition techniques include anodization for producing thin oxide films of metals such as aluminum, microwave electron cyclotron resonance (ECR) deposition and cathodic arc deposition.

In general, PVD processes yield high deposition rates with adsorption coefficients close to unity. However, there are several disadvantages including the inability to determine the nature of intermediate species involved, poor step coverages, difficulties in controlling the composition of alloy materials and the non-selective nature of the deposition process.

1.3.2 Chemical Deposition Processes

These processes typically involve chemical reactions and intermediate species leading to the formation of suitable thin films. Films can be deposited chemically from both the vapor phase and the liquid phase. Solution based deposition of inorganic thin films is facilitated by electrochemical processes (e.g. electroplating) and chemical deposition processes (e.g. reduction plating and electroless plating) used to deposit metallic films for semiconductor applications. In contrast, in chemical vapor deposition (CVD), the reactants undergo a chemical reaction in the vapor phase at or near the substrate leading to the deposition of a thin film. This technique enables the deposition of thin films and coatings of a wide variety of materials essential to advanced technological applications where strict tolerances concerning purity and composition must be met. Both chemical composition and physical structure of deposited films can be tailored by controlling the reaction chemistry and deposition conditions like temperature, pressure, reactant concentrations, flow rates and reactor geometry. There can be multiple precursors which could be either simple or complex inorganic, organic or even organometallic molecules. Most CVD processes are chosen to be heterogenous reactions to prevent powdery deposits and particulate contamination from gas phase reactions. These processes provide uniform coverage over high aspect ratio structures as the reactant molecules can diffuse on the substrate or undergo multiple collisions before reaction/deposition occurs – a significant advantage over physical vapor deposition. Thin CVD films find applications as dielectrics, elemental and compound semiconductors, insulators as well as conductors in the semiconductor industry. Other applications include hard and wear resistant

coatings in tool technology, corrosion resistant coatings in metallurgical applications and bulk coatings of refractory materials. Several types of CVD processes have emerged over the years. In thermal processing, the substrate provides the source for the inorganic constituent of an oxide overlayer. Although more limited and involving much higher substrate temperatures than conventional CVD processing, this technique is critical to producing silicon dioxide and silicon nitride films of high purity for incorporation into integrated circuits. Photo enhanced CVD (PHCVD) is based on activation of reactants in the vapor phase by electromagnetic radiation, usually short wave ultraviolet radiation. Laser-induced CVD (LCVD) utilizes a laser beam for highly localized heating of the substrate and then film deposition is initiated by surface reactions. Atmospheric pressure CVD, hot filament CVD, electron-enhanced CVD and plasma-enhanced CVD processes also find unique applications. Plasma-assisted CVD processes facilitates lower processing temperatures. However, the nature of intermediate species is not well understood.

Atomic layer deposition (ALD) is a relatively new and very useful CVD technique to produce thin conformal coatings on high aspect ratio structures. ALD utilizes two sequential self-limiting reactions that occur between two separate gas phase precursors and a suitable solid substrate (Fig. 1-4). In the first half reaction, one precursor (A) is introduced in the vacuum system and saturates the surface after which it is purged from the system using species (C) to eliminate any gas phase reaction with the second precursor. Then the second precursor (B) is introduced and reacts with the first precursor at the surface producing the requisite product which is a metal oxide or nitride in most cases, Finally, any remaining reactant is purged by the purge species (C). By

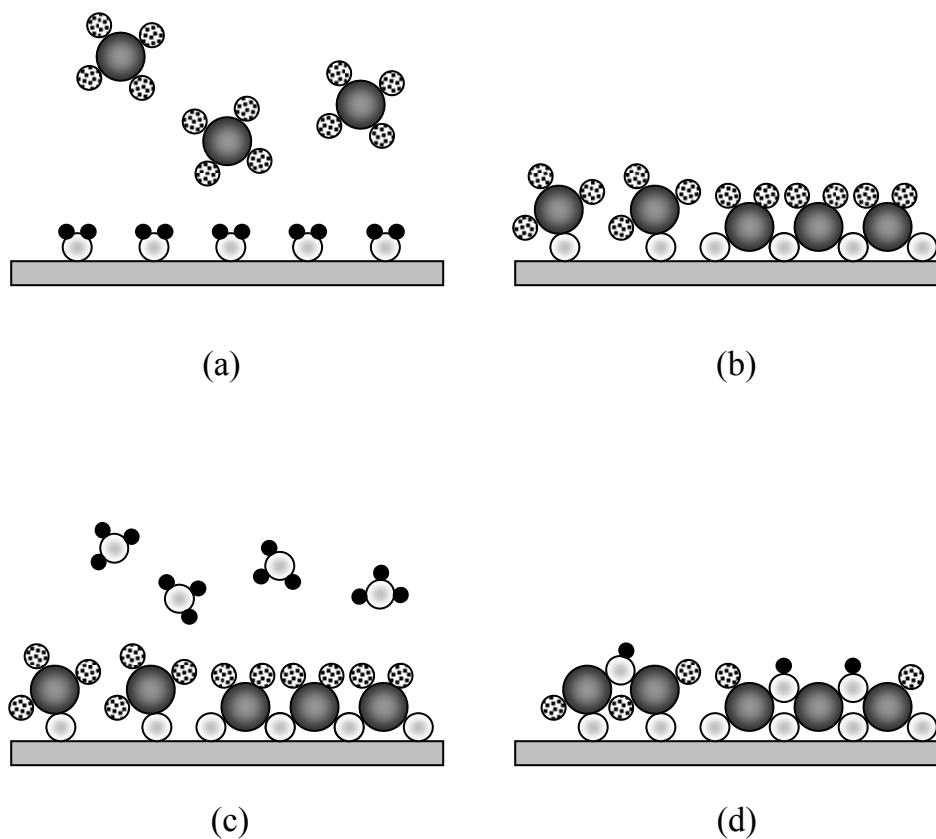


Figure 1–4 Schematic representation of the Atomic Layer Deposition (ALD) process. The first step (a) involves the exposure of a functionalized surface to the precursor A. After surface reaction of this precursor (b), a purge gas C eliminates excess reactant. Then the second precursor B is introduced (c) which reacts with the first precursor to form the desired product (d). Potential routes for carbon contamination are also illustrated. This sequence of ACBCACBC... is executed to deposit a thin film.

repeating this binary sequence, called a cycle, (ACBCACBC...) of surface reactions, a thin film can be deposited. Advantages of ALD include:

1. atomic layer control of film thickness,
2. linear correlation between film thickness and number of cycles,
3. conformal coating over high aspect ratio structures,
4. lower thermal budget than conventional CVD processes,
5. wide variety of starting materials to produce required oxide and nitride films.

The only disadvantage with ALD is lower deposition rates compared to PVD and traditional CVD processes. Surface saturation at each reaction stage followed by a purge cycle contributes to the lower deposition rate. However, with continued shrinking of device dimensions, film thicknesses are also decreasing and ALD is becoming a more viable technique for depositing ultra thin films.

Although films have been deposited using ALD, there is very little fundamental insight into the surface reactions and intermediates involved in this process. The reaction of tetrakis(dimethylamido)titanium with self-assembled alkyltrichlorosilane monolayers terminated by $-OH$, $-NH_2$ and $-CH_3$ groups is described in Chapter 3. The kinetics of adsorption of TDMAT with these self-assembled monolayers is examined explicitly as a function of substrate temperature. In addition, the stoichiometry of the interface formed by the reaction of TDMAT with these functionalized monolayers is described in detail. This is the first quantitative study of the first half reaction in the ALD of titanium nitride from the TDMAT precursor on functionalized self-assembled monolayers.

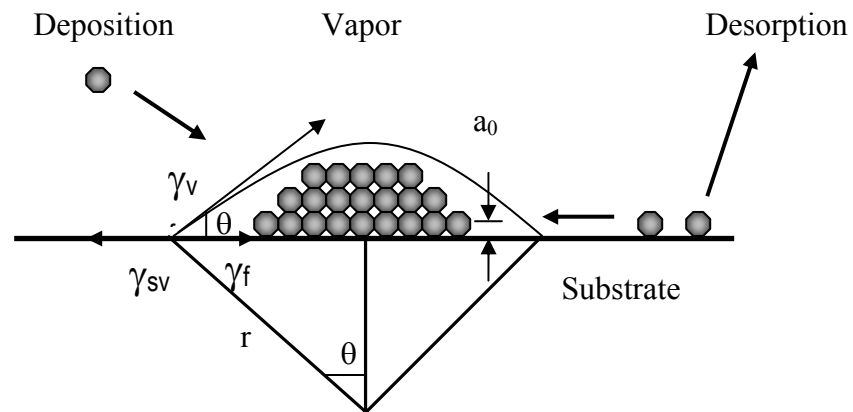


Figure 1–5(a) Atomistic processes involved in the nucleation of a thin film from the vapor phase onto a substrate.

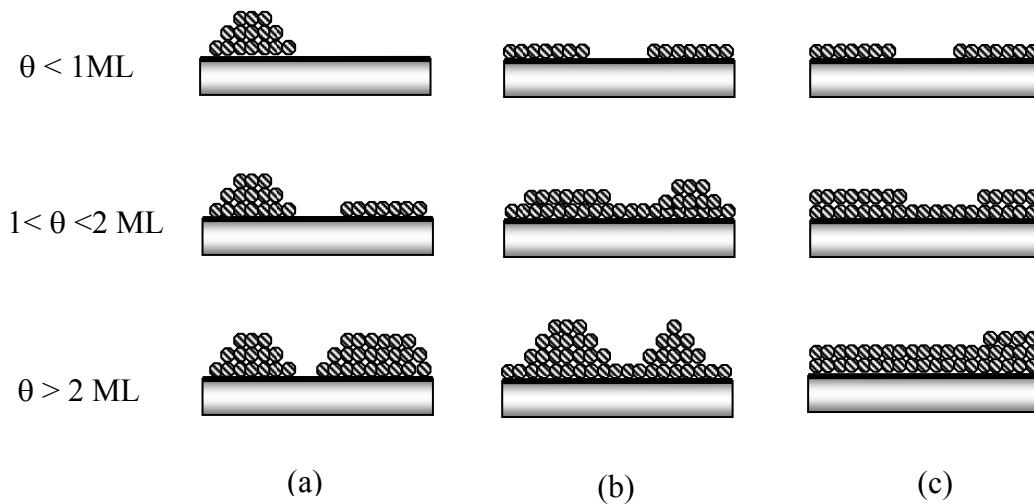


Figure 1–5(b) Three growth modes shown schematically as a function of film coverage θ : (a) three–dimensional or Volmer–Weber growth, (b) two dimensional growth becoming three–dimensional or Stranski–Krastanov growth and (c) layer by layer or Frank–van der Merwe growth.

Chemical processes for thin film deposition are crucial steps in the fabrication of today's semiconductor devices. An excellent understanding of atomistic processes involved in the nucleation and deposition of these films is therefore critical to understanding these processes in order to scale films to smaller dimensions for the next generation of integrated circuits.

1.3.3 Nucleation and morphology of thin films

A conceptually simple model for nucleation of thin films is Capillarity theory [19]. Atoms or molecules from the vapor phase impinge on the substrate and can undergo several processes including non-reactive scattering, physisorption or chemisorption depending on the material system resulting in incorporation of these atoms into existing islands, surface diffusion or desorption from the substrate. A schematic of these basic processes on a substrate surface is provided in Fig. 1–5.

The free energy change accompanying the formation of an aggregate of mean dimension r is given by:

$$\Delta G = a_3 r^3 \Delta G_v + a_1 r^2 \gamma_{vf} + a_2 r^2 \gamma_{fs} - a_2 r^2 \gamma_{sv} \quad (1-1)$$

The free-energy change per unit volume is ΔG_v and is negative in order for gas phase supersaturation to yield nucleation. γ is the interfacial energy at the different interfaces designated by vf for vapor and film, fs for film and substrate and sv for substrate and vapor and the prefactors represent the curved surface area, the projected circular area on the substrate and the volume of the cap

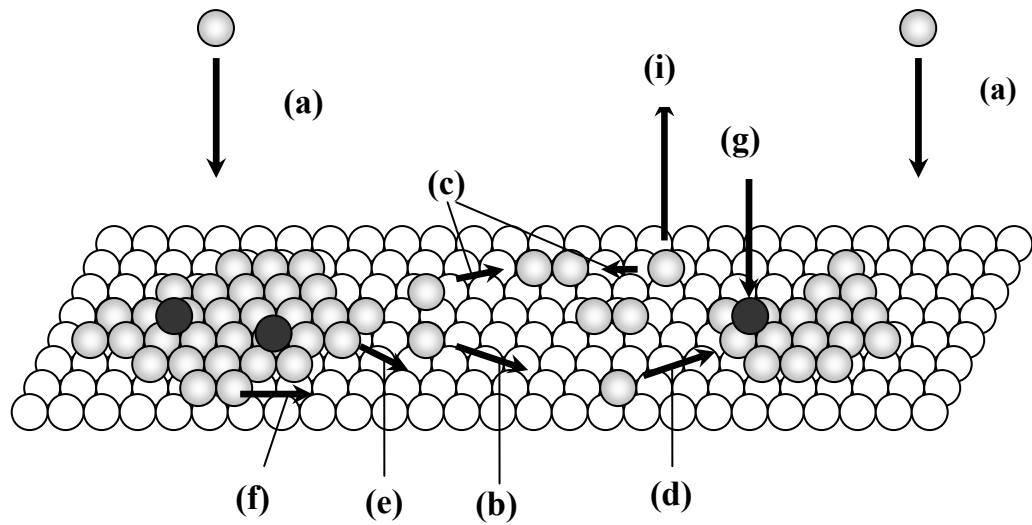


Figure 1–6 Schematic illustration of atomistic processes involved in film formation. An atom approaching the surface (a) can adsorb on the surface, becoming an adatom and undergo surface diffusion (b). Adatoms can meet to form dimers (c), incorporate into existing islands (d), detach from them (e) or even diffuse along the island edge (f). Deposition of adatoms on top of islands and corresponding processes (g) are to be considered as well.

shaped nucleus (c.f. Fig. 1–5). Mechanical equilibrium among interfacial forces yields:

$$\gamma_{sv} = \gamma_{fs} + \gamma_{vf} \cos \theta \quad (1-2)$$

where θ is the contact angle (Fig. 1–5) which depends on the surface properties of the materials involved.

Three different growth modes can be identified based on the interfacial forces between film, substrate and vapor respectively. If $\gamma_{sv} < \gamma_{fs} + \gamma_{vf}$ then it is island growth since $\theta > 0$. If $\gamma_{sv} = \gamma_{fs} + \gamma_{vf}$ then the growth mode is layer-by-layer since $\theta = 0$ and the film wets the surface. For Stranski–Krastanov growth, $\gamma_{sv} > \gamma_{fs} + \gamma_{vf}$, and island formation on the layers is permitted due to the strain energy per unit area of the film being large with respect to γ_{vf} .

By differentiating Eqn. 1–1, the critical nucleus size can be obtained:

$$r^* = \frac{-2(a_1\gamma_{vf} + a_2\gamma_{fs} - a_2\gamma_{sv})}{3a_3\Delta G_v} \quad (1-3)$$

and by substituting r^* back into Eqn. 1–1 along with the geometric constants, it can be shown that the energy barrier for nucleation ΔG^* is:

$$\Delta G^* = \left(\frac{16\pi\gamma_{vf}^3}{3\Delta G_v^2} \right) \left(\frac{2 - 3\cos\theta + \cos^3\theta}{4} \right) \quad (1-4)$$

The critical nucleus size r^* defines the size of stable nuclei. Nuclei above the size of r^* tend to grow in size while nuclei smaller than r^* will disappear by shrinking in size. The first factor in Eqn. 1–4 is the energy barrier for homogeneous nucleation and is the upper limit for the case of heterogeneous nucleation. A relationship for the rate of nucleation can be derived using the

Table 1–1 Nucleation parameters p and E for the atomistic nucleation model summarizing nucleation behavior by Venables et al. [20]

Regime	3D Islands	2D Islands
Extreme incomplete	$p = (2/3)i^*$	i^*
	$E = (2/3) [E_{i^*} + (i^* + 1)E_D - E_S]$	$E_{i^*} + (i^* + 1)E_D - E_S$
Initially incomplete	$p = 2i^*/5$	$i^*/2$
	$E = (2/5) (E_{i^*} + i^*E_D)$	$(1/2) (E_{i^*} + i^*E_D)$
Complete	$p = i^*/(i^* + 2.5)$	$i^*/(i^* + 2)$
	$E = (E_{i^*} + i^*E_S)/(i^* + 2.5)$	$(E_{i^*} + i^*E_S)/(i^* + 2)$

critical nucleus size r^* , energy barrier for nucleation ΔG^* , an estimate of the overall impingement flux, surface diffusion and desorption rates.

1.3.4 Atomistic nucleation model

Although capillarity theory provides a conceptually simple and qualitative model of film nucleation; it does not incorporate phenomena at the atomistic scale which renders this theory inaccurate when it comes to quantitative predictions. Atomistic theories of nucleation [19] describe the role of individual atoms and associations of small numbers of atoms during the earliest stages of film formation. An atom approaching a substrate can undergo several processes once adsorbed to form an adatom (Fig. 1–6). These include surface diffusion, attachment to other adatoms to form dimers, incorporation into existing islands, detaching from an island or even diffusing around the edge of an island. In addition, the deposition of adatoms on top of existing islands and corresponding processes need to be considered as well.

Approaches to account for atomistic phenomena include the Walter – Rhodin theory [21] and more recent kinetic approaches. The Walton–Rhodin theory expresses the nucleation rate of small clusters N_{i^*} as a function of measurable parameters rather than macroscopic quantities like ΔG^* , γ , or θ that are not known with certainty and are difficult to estimate. These parameters include the flux R , critical island size i^* , critical dissociation energy E_{i^*} (defined as the energy required to disintegrate a *critical* cluster containing i atoms into i separate adatoms), monomer concentration per unit area n_0 , activation energies of desorption E_D and surface diffusion E_S and substrate temperature T . The expression for nucleation rate is:

$$N_{i^*} = Ra_0^2 n_0 \left(\frac{R}{vn_0} \right)^{i^*} \exp \left(\frac{(i^* + 1)E_D - E_S + E_{i^*}}{kT} \right) \quad (1-5)$$

One of the important applications of this theory is to epitaxial growth of thin films, where the crystallographic geometry of stable clusters has been related to different conditions of supersaturation and substrate temperature. Kinetic approaches involving rate equations similar to those describing the kinetics of chemical reactions are used to express the time rate of change of cluster densities in terms of the processes that occur at the surface of the substrate namely adatom arrival at the substrate (flux term), migration and capture or incorporation into islands and desorption. Coalescence of islands is neglected in this model. Because these theories and models are complex mathematically and physically, this discussion will stress important results without resorting to extensive development of derivations. Venables et al. [20] have neatly summarized nucleation behavior for cases where the critical cluster size i^* assumes any integer value. The general expression for stable cluster density N_S is given by:

$$N_S = An_0 \left| \frac{R}{n_0 v} \right|^p \exp \frac{E}{kT} \quad (1-6)$$

where A is a calculable dimensionless constant dependent on substrate coverage, parameters p and E depend on the condensation regime and are summarized in Table 1-1. Three regimes of condensation and two types of island nuclei are considered. At high substrate temperatures and/or low deposition rates, the re-evaporation rate from the surface will control adatom density and exceed the rate of diffusive capture of growing nuclei. This is the

incomplete condensation regime where adsorption–desorption equilibrium is rapidly established. At low substrate temperatures and/or high deposition rates, re–evaporation is not important as E_D is large, and this regime is *complete condensation*. Intermediate condensation regimes can occur depending on deposition conditions and corresponding parameters are listed in the table. These generalized equations permit estimation of activation energies as well as the critical cluster size. It can also be shown that the Walter–Rhodin theory is a special case of more general rate theory.

1.4 Molecular Beam Techniques

For over three decades, experiments utilizing molecular beams in conjunction with techniques from surface science have been instrumental in elucidating fundamental phenomena occurring during thin film deposition. Prior to using these molecular beams, most experiments did not allow the explicit examination of the state of the precursor molecule on gas–surface dynamics as well as thin film growth. In addition, experiments associated with thin film deposition involved several chemical reaction pathways and mechanisms occurring in parallel, which could not be isolated and studied individually. Reactions in the gas phase further added to the complexity of the system studied. Molecular beam techniques have played a crucial role in understanding the interactions of a precursor molecule in the gas phase with a substrate and elucidating chemical reaction pathways associated with thin film growth.

1.4.1 Characterization of molecular beams

A molecular beam is a stream of electrically neutral molecules produced by expanding a gas through an orifice into a region of low pressure and collimating the flow by several apertures along the beam line. Based on the type of source, molecular beams can be classified into two broad categories: effusive and supersonic beams. The primary difference between these two types of beams is denoted by the Knudsen number Kn , defined as the ratio of the molecular mean free path (λ) of the gas to a characteristic length scale of the source; in this case, the diameter of the source orifice (d):

$$Kn = \frac{\lambda}{d} \quad (1-7)$$

Kn determines the extent of inter-molecular interactions in a gas expanding through said orifice. There are two limiting cases for the Knudsen number. If $Kn \gg 1$, molecules travel long distances without undergoing collisions with each other, molecule-wall collisions are much more frequent and transport is ballistic or molecular. This is typical for an effusive beam. If $Kn \ll 1$, the molecules undergo several collisions with each other and transport is continuum as in the case of a supersonic expansion. These two types of beams are described in further detail in the next two sections.

1.4.1.1 Effusive beams

An effusive beam has low source pressure which ensures free molecular flow through the source orifice. Owing to the small number of interactions between molecules expanding in an effusive beam, they are characterized by a Maxwell–Boltzmann velocity distribution which is a function of the source temperature (T_n). The flux–weighted velocity distribution, $I(v)$, is given by:

$$I(v) = \left(\frac{2}{\alpha^4}\right)v^3 \exp\left(-\frac{v^2}{\alpha^2}\right) \quad (1-8)$$

where $\alpha^2 = 2k_B T_n/m$, k_B is the Boltzmann constant, and m is the molecular weight. From this expression the average translational energy, $\langle E_i \rangle$ can be calculated by the integration of the individual molecular kinetic energies over the flux–weighted velocity distribution. This results in $\langle E_i \rangle = 2k_B T_n$, which demonstrates the low–energy nature of effusive beams. For example, for a nozzle temperature of 500 °C, $\langle E_i \rangle$ is 133 meV.

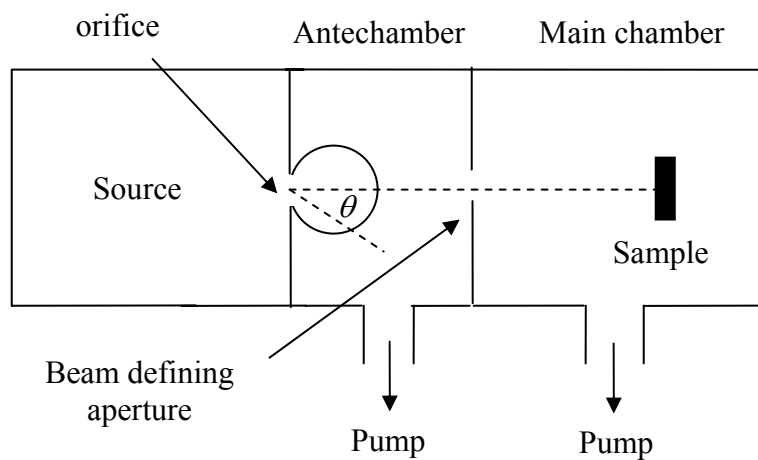
The flux distribution of the effusive beam can be expressed using Boltzmann statistics, or the cosine angular distribution:

$$F_i = \frac{P_n}{\sqrt{2\pi m k_B T_n}} \frac{\pi d_n^2/4}{\pi x^2} \cos \theta \quad (1-9)$$

where P_n and d_n are the source pressure and nozzle diameter respectively and x is the distance between the source and substrate. Multichannel glass capillary arrays can be used to produce higher fluxes for effusive molecular beams.

Effusive beams hold a distinct advantage over supersonic beams in ease of production and characterization. However, they also have several drawbacks

a) Effusive beam



b) Supersonic beam

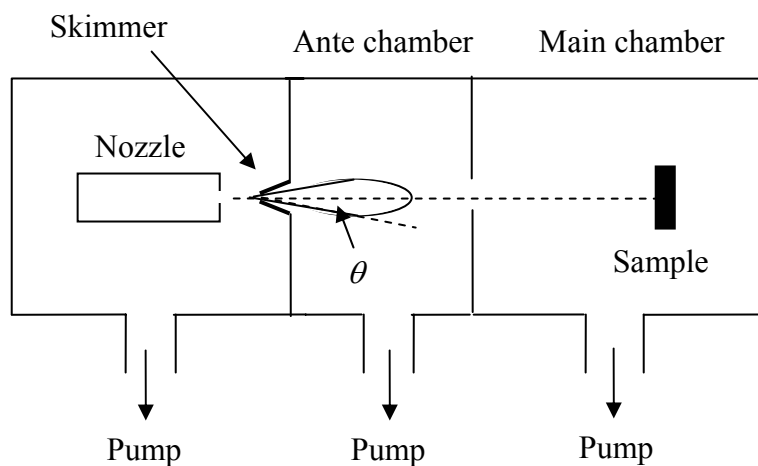


Figure 1–7 Schematic representation of: a) effusive and b) supersonic molecular beam systems. The closed curves downstream of the orifice and the skimmer represent the relative intensity distribution (reproduced from [22]).

including a low and limited range of incident kinetic energies, wide energy and angular distributions, lower fluxes and lower beam to background intensity. As a result, effusive beams have been used widely for uniform film deposition over large area substrates. Many of these limitations are overcome with the use of supersonic molecular beams.

1.4.1.2 Supersonic molecular beams

Supersonic beams are formed via an adiabatic (isentropic) expansion of a gas from a nozzle at high pressure into a vacuum chamber called the source chamber. During this process, random thermal molecular motion is converted into directed translational motion, owing to the continuum nature of the source, producing a nearly monoenergetic beam. A schematic view of the generation of effusive and supersonic beams is provided in Fig. 1–7.

Supersonic molecular beams offer several unique advantages. These include:

1. independent control over the translational, electronic, vibrational and rotational states of a molecule before and after a gas–surface interface encounter,
2. seeding techniques (where an inert, fast–moving and light gas such as H₂ or He accelerates slow moving heavier gas molecules) allow for a wide range of translational energies,
3. excellent control of the flux of a beam of these molecules,
4. peaked angular distribution of molecules in the beam,
5. narrow tunable velocity distribution of molecules in the beam,

6. excellent control of spatial reaction of these molecules on a substrate with the ability to deposit spatially confined and uniform thin films,
7. minimization of reactions between species in the gas phase,
8. utilization of ultrahigh vacuum systems to maintain ultraclean environments critical to thin film deposition with applications in the semiconductor industry,
9. the availability of a wide range of *in-situ* and *real-time* diagnostic tools, employed in ultrahigh vacuum, used to characterize the molecular beam and gather information pertinent to gas-surface reactivity, the structure and composition of deposited films.

With these distinctive advantages, several applications have emerged for supersonic molecular beams. Scattering of these beams, with well defined internal state distributions, is an excellent technique to probe interactions between these gas molecules and a variety of substrates. Scattering could be elastic, inelastic or reactive. In addition, these beams can be employed to deposit thin films. New techniques in film deposition have been recently developed [23] owing to the ability to accurately characterize and precisely collimate these beams.

The flux-weighted velocity distribution, $I(v)$, of a supersonic molecular beam is given by:

$$I(v) = N(c, \alpha) v^3 \exp\left(-\frac{(v-c)^2}{\alpha^2}\right) \quad (1-10)$$

where $N(c, \alpha)$ is a normalization constant, and c is the most probable velocity, defined as:

$$c = \left[\frac{2\gamma k_B T_n}{(\gamma - 1)m} \right]^{0.5} \quad (1-11)$$

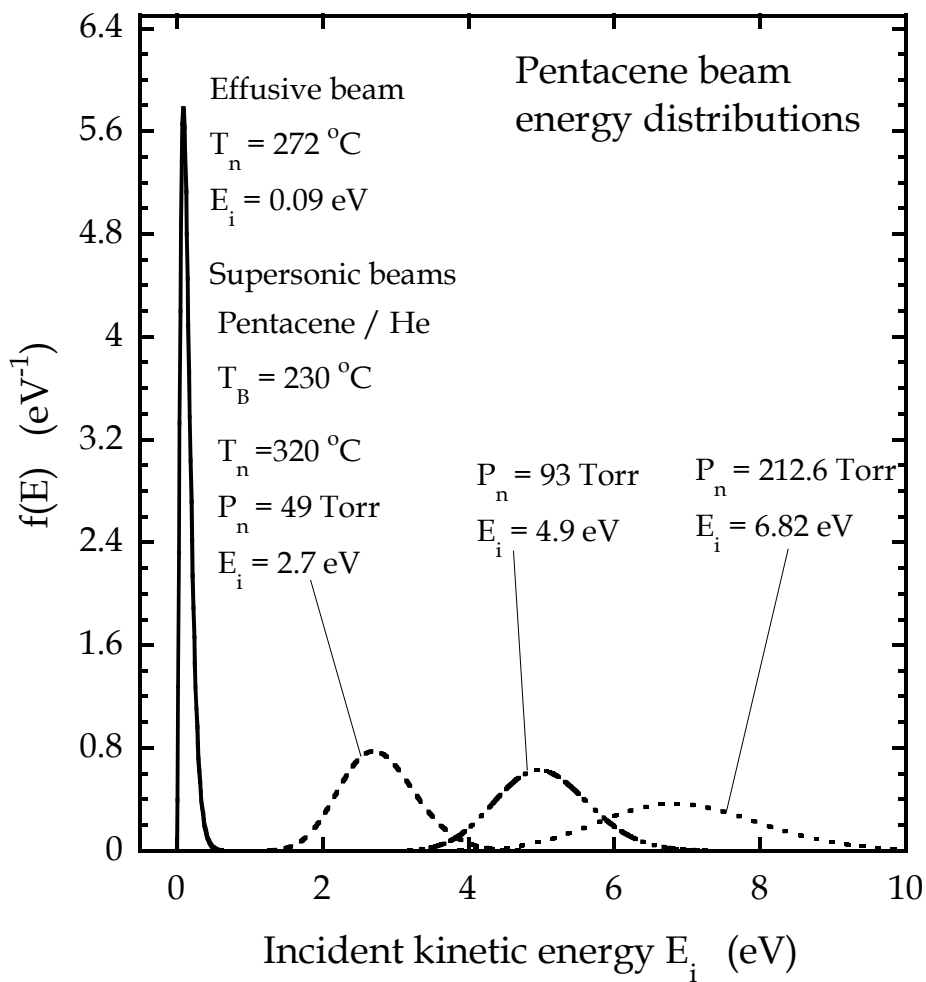


Figure 1–8 Energy distribution of pentacene molecules for effusive and supersonic beams using H_2 and He as the seeding gas. Beam conditions are indicated.

where $\gamma = C_p/C_v$ is the ratio of heat capacities, T_n is the nozzle temperature, α is a measure of spread in the velocities of the gas parallel to the flow direction with $\alpha^2 = 2k_B T_{B||}/m$ where $T_{B||}$ is the axial translational temperature and m is the mass of the reactant gas. Equation 1–10 reduces to a Maxwellian distribution when $c = 0$ and $\alpha^2 = 2k_B T_n/m$. The resultant beam has a centerline flux an order of magnitude higher than an effusive beam and the angular distribution is proportional to $\cos^4\theta$ for a pure gas under ideal conditions. Shown in Fig. 1–8 is the resultant energy distribution for pentacene gas mixtures at different nozzle conditions. Also plotted for comparison is the distribution of an effusive beam under ideal expansion conditions.

Molecules start with thermal velocities in the high pressure region upstream of the flow-limiting orifice (the nozzle) called the stagnation state (pressure P_0 , temperature T_0). The pressure difference imposed by vacuum downstream of the nozzle (background pressure P) accelerates these molecules to sonic speeds, given by $s = (\gamma k_B T_n/m)^{0.5}$, provided P_0 / P_b exceeds a critical value:

$$\frac{P_0}{P_b} \geq \left[\frac{(\gamma + 1)}{2} \right]^{\gamma/(\gamma-1)} \quad (1-12)$$

which is less than 2.1 for all gases. A figure of merit for the expansion is the Mach number M , defined as the ratio of the gas velocity to the speed of sound, v/s . Therefore, in order for the expansion to be supersonic, the pressure ratio must be higher than the critical value to make $M > 1$. If the pressure ratio is less than the critical value, molecules will exit the nozzle subsonically with exit pressure P_b and without further expansion. In that case, the terminal velocity, v_∞ , may be derived to be:

$$v_{\infty} = \sqrt{\frac{2k_B}{m} \left(\frac{\gamma}{\gamma-1} \right) T_n} \quad (1-13)$$

In a seeded supersonic beam, all molecules in the mixture are accelerated to the same velocity rather than energy. This is the basis for the ability to enhance the kinetic energy of a heavy molecule in a dilute mixture with light molecules. In such a mixture, assuming ideal molar heat capacities, the maximum possible translational energy of a reactant is given by:

$$\langle E_i \rangle = \frac{m_i}{\langle m \rangle} \langle C_p \rangle T_n \quad (1-14)$$

where m_i is the mass of the reactant gas, $\langle m \rangle$ is the mole fraction mean mass of the gas mixture, $\langle C_p \rangle$ is the mole fraction mean heat capacity of the mixture, and T_n is the nozzle temperature. In most cases, the expansion is not ideal and both velocity and temperature of the precursor molecule deviate from ideal values. The non-ideality from these cases are termed velocity and temperature slip respectively. For both cases, it results in a lower than expected energy from Eqn. 1-14. Thus Eqn. 1-14 should only be used as an upper bound for the average beam energy.

As illustrated in Fig. 1-7, in practice the extraction of a supersonic beam requires a skimmer placed a short distance downstream of the nozzle in the isentropic region of the expansion known as the zone of silence (shown in Fig. 1-9). The molecules traveling beyond the nozzle in a supersonic beam are traveling in excess of the speed of sound and cannot “sense” downstream boundary conditions because information in fluids propagates at the speed of

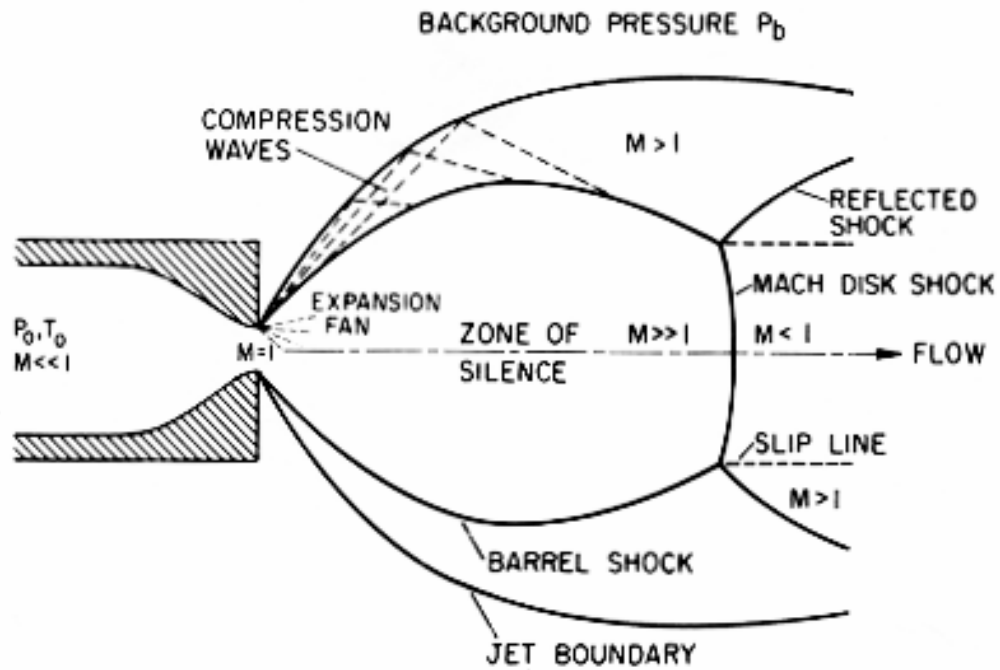


Figure 1–9 Illustration of the structures formed during a supersonic expansion. The figure shows what is commonly known as a “Free Jet” expansion which is produced without any downstream structures affecting the boundary conditions of the expansion (reproduced from [25]).

sound. As a result, very thin nonisentropic regions of large density, pressure, temperature and velocity gradients develop. Called shock waves, these structures are to be avoided in a supersonic beam.

The skimmer is conical or trumpet-like in shape with a small aperture at the apex used to extract molecules from the zone of silence. Its shape minimizes the backscattering of molecules into the free jet stream out of the nozzle. The advantage of extracting the beam near the continuum region of the flow within the isentropic zone of silence is the smaller scale of the apparatus. Disadvantages include problems with skimmer interference, requirement for an additional stage to pump on the beam and potential spreading of the beam downstream of the skimmer. After extraction, the molecules in the beam travel into a separate chamber, usually called the ante-chamber, where further pumping minimizes the beam to background ratio. In addition, modulation of the beam can be carried out in the antechamber either with a fast rotating blade chopper or a slow linear translator. Finally the beam passes into the main chamber through an aperture which spatially defines the beam on the substrate. Translation of the sample relative to the beam results in a unique experimental technique for thin film deposition detailed in section 2.2.4.

Besides the velocity and temperature slip problems mentioned previously, other factors such as mass focusing in a seeded beam can affect the flux distribution of the supersonic beam. Even for expansions of pure gases, a theoretical estimate of the flux is complicated by the number of variables that can affect the expansion i.e. T_n , P_n , d_n , experimental configuration and pumping conditions in each separate chamber. Although empirical models have been developed to estimate the effects of velocity and temperature slip [24] and mass focusing [25], it is difficult to extend these models to more complex molecules.

Currently, the only exact method of determining the energy of reactant molecules in a supersonic beam is to measure them using time of flight techniques. The flux can also be estimated experimentally by using an effusive beam as a calibration standard.

1.4.2 Supersonic molecular beam scattering

Supersonic molecular beams have been used extensively to study the dynamics of film deposition processes where the interaction of the gaseous molecule with the substrate can be broadly classified into two categories, namely, non-reactive or reactive scattering. This classification is dependent on whether the scattered or absorbed species has changed chemically from the incident molecule. The outcome of this interaction between gas molecule and substrate is dependent on the incident kinetic energy and state of the molecule, the chemical nature and temperature of atoms/molecules in the substrate. Supersonic beams allow excellent control of kinetic energy, composition and flux of incident molecules. The nature of the substrate as well as its temperature determines the inter-molecular potential energy between the incident molecule and the surface. The intra-molecular potential energy is determined by the electronic structure of the molecules. The following are descriptions of the different types of scattering events during molecular beam impingement on a surface.

1.4.2.1 Non-reactive molecular beam scattering

Non-reactive scattering can generally be categorized into four types: 1) elastic scattering; 2) inelastic scattering; 3) molecular trapping and desorption; and 4) molecular chemisorption.

1.4.2.1.1 Elastic scattering

Elastic scattering occurs when the translational and internal energy of the molecule remains unchanged after its scattering from the surface. During this process, the incident molecules scatter from the substrate with an extremely narrow angular distribution peaked at the specular angle. Since this is a single collision process in most situations, surface residence times are typically less than 10^{-12} sec [27]. These events are characteristic of beams with light atoms such as H_2 and He. The simple physical nature of the process permits direct correlation of the angular distribution of the scattered beam to surface topology.

1.4.2.1.2 Inelastic scattering

In inelastic scattering, molecules lose translational energy after single (direct inelastic scattering) or multiple (indirect inelastic scattering) collisions with the surface of the substrate. Incident translational energy is either converted to internal energy or dissipated by the generation of surface phonons. Scattered molecules still retain memory of their incident trajectories. As a result, they have a wider energy and angular distribution compared to elastic scattering. Surface residence times are determined by the number of collisions

undergone by incident molecules with the surface. As opposed to elastic scattering, this mechanism is typical for cases where the incident molecule has a similar mass compared to the surface atoms. For the case of multiple phonon excitations, the characterization of the angular distribution can yield information regarding the mechanisms of gas–surface energy exchange.

1.4.2.1.3 Trapping and desorption

In this process, incident gas molecules adsorb and equilibrate on the substrate before desorbing. Interactions between the adsorbate and substrate are weak van der Waals type forces with a long–range attractive component. These forces arise from dispersion (temporary and fluctuating dipole moments) or permanent dipole moments between the adsorbate and substrate leading to equilibration. Also called “physisorption”, binding energies are on the order of 50 – 500 meV per atom and these energies are comparable to the sublimation energy of rare gas solids. Equilibration results in desorbing molecules exhibiting Maxwell–Boltzmann velocity distributions characterized by the temperature of the substrate. In addition, their angular distribution is symmetric and peaked about the surface normal and usually displays a sine or near cosine distribution as opposed to direct scattering. Surface residence times for trapped molecules are longer than a vibrational period for the species adsorbed in the gas–surface potential well. Typical systems are rare gases or small molecules on layered compounds or metals, with the experiments performed below room temperature [28]. Weak adsorption energies result in physisorbed atoms or molecules desorbing readily at elevated substrate temperatures. The fraction of incident molecules remaining on the substrate yields the trapping probability.

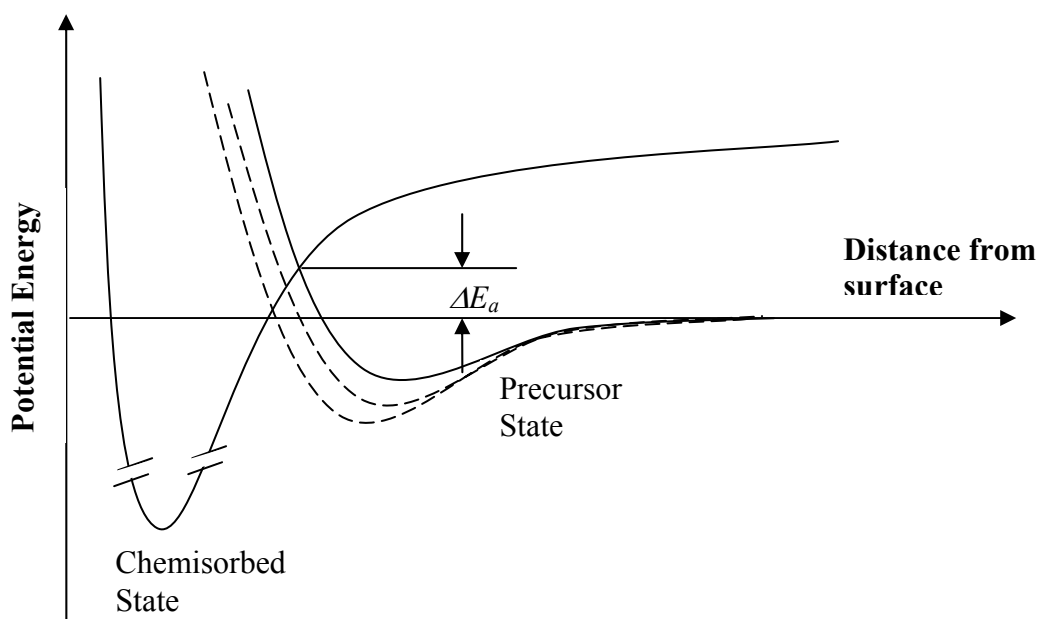


Figure 1–10 One-dimensional potential energy diagram for gas–surface interactions. The chemisorbed state exhibits a much deeper potential well than the physisorbed state. The activation energy to go from a physisorbed to a chemisorbed state is indicated as ΔE_a in the diagram. The dashed lines illustrate the dependence of the potential on variables such as adsorption sites, orientations, and impact parameters.

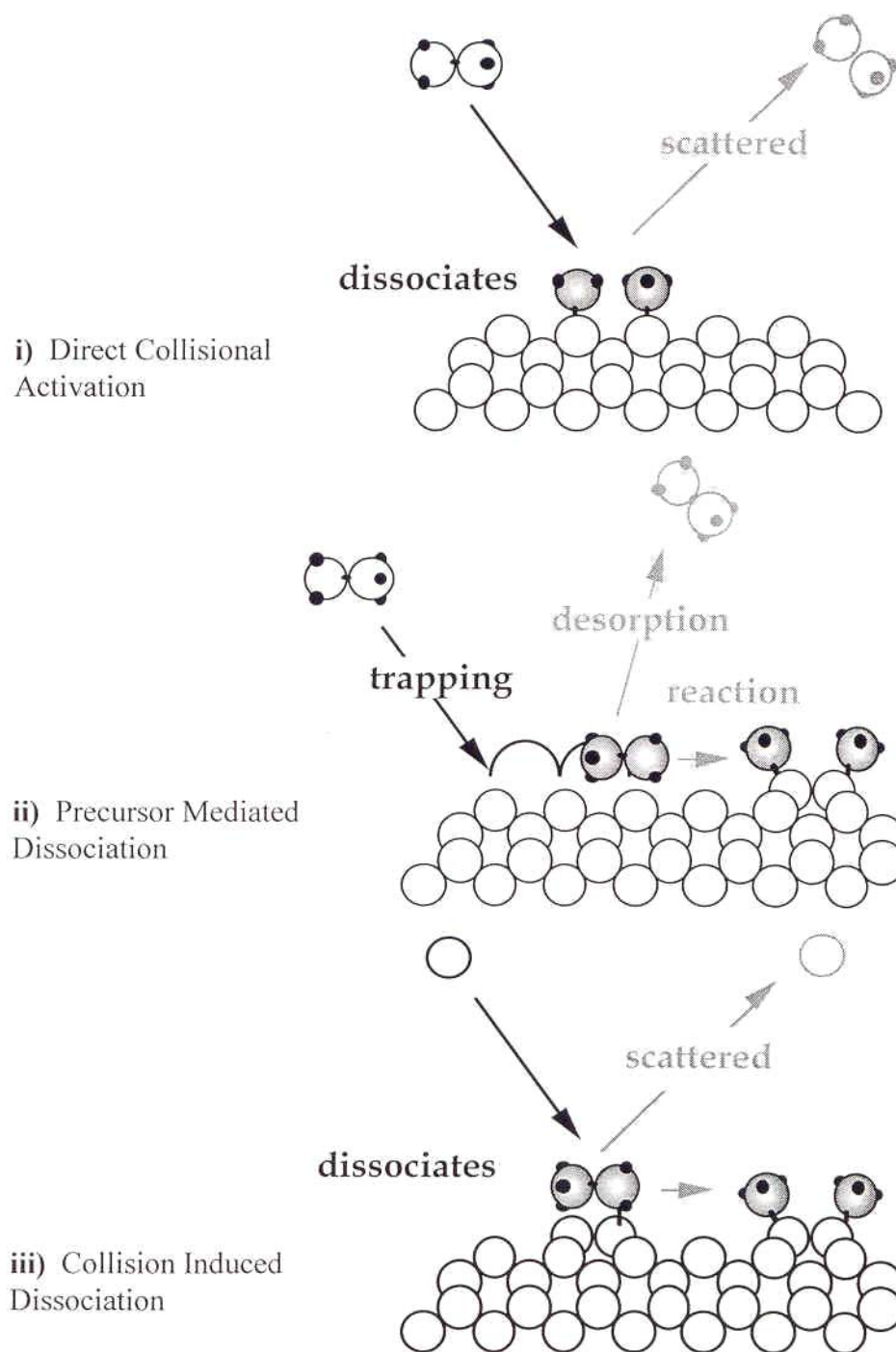


Figure 1–11 Illustration of the three different reactive scattering mechanisms: (i) direct collisional activation, (ii) precursor–mediated dissociation, and (iii) collision–induced dissociation.

1.4.2.1.4 Molecular chemisorption

Molecular chemisorption occurs when a molecule binds to the substrate through a chemical bond and retains its chemical identity. Adsorbed species are strongly bound (bond strengths are of the order of 1–10 eV/atom) and stable upto room temperature. Molecules desorbing from a chemisorbed state have a cosine angular distribution and a Maxwellian velocity distribution. Chemisorption can occur either directly (sometimes via activation due to the incident kinetic energy of the molecule) or through trapping followed by chemisorption. The one dimensional potential energy diagram characterizing both physisorption and chemisorption wells for a typical gas–substrate interaction, as a function of the distance between the molecule and the substrate is given in Fig. 1–10.

1.4.2.2 Reactive scattering

In reactive scattering, bonds within the incident gas molecules are broken and new chemical bonds are formed between the atoms of the molecule and the atoms/molecules on the substrate. The incident molecules are typically required to overcome a sizable activation barrier in order to dissociatively adsorb on the surface. Hence the dissociative adsorption step is usually the rate–limiting step in a thin film growth process. Reactive scattering can be categorized into three different mechanisms: direct collisional activation, trapping or precursor–mediated dissociation, and collision–induced dissociation. Shown in Fig. 1–11 is an illustration of these three different mechanisms.

1.4.2.2.1 Direct collisional activation

In the case of direct collisional activation, the incident molecules which possess enough translational energy along the reaction coordinate to overcome the activation barrier dissociate upon first impact while other molecules simply reflect off the substrate. The most important parameters affecting the reaction probability, S_R , are the incident kinetic energy and angle of the molecule. For the incident kinetic energy, the average reaction probability does not increase linearly with increasing translational energy due to the multiple distributions of energy states in the molecule. Rather, the incident translational energy has an exponential effect on S_R . The effect of the incident angle, θ_i , is often coupled with the translational energy using so-called energy scaling arguments. For example, in the simplest case of a one-dimensional barrier to dissociation on a flat surface, the effective energy in promoting the reaction is the normal component of the incident kinetic energy, given by $E_n = E_i \cos^2 \theta_i$. This is called normal energy scaling and has been observed for several systems, e.g. reactions on W(110) [29] and Ni(111)[30]. Energy transfer is more efficient at smaller angles of incidence, hence S_R usually decreases with increasing θ_i . For more complicated surface topologies, a quantity known as the scaled energy ($\langle E_{\perp} \rangle = E_i \cos^n \theta_i$) has been used effectively to describe the effect of incident angle. In these cases, both normal and parallel energy contribute to reactions at the substrate. In certain systems, n has been observed to be 0 (e.g. N_2 on W(110) [31]). This is referred to as total energy scaling; i.e. S_R is only dependent on the total incident kinetic energy of the molecule and not on the magnitude of individual components.

For the case of direct dissociation, the surface temperature does not have a profound effect on S_R as the molecules are not thermalized on the surface through an adsorption step. Surface temperature only affects the surface thermal vibration, characterized by a thermal energy, $k_B T_s$, which is typically much smaller than the incident kinetic energy. However, the effect of surface temperature will be more dramatic if a large number of surface vibrational modes participate in the reaction. Concerning the effect of internal energies of the incident molecules, rotational motion does not couple efficiently with motion over the dissociation barrier. For an attractive surface, where the activation barrier would be located at the entrance channel, translational energy will be more efficient in promoting the reaction, whereas vibrational energy would be more efficient on a repulsive surface characterized by a late barrier.

1.4.2.2.2 Precursor-mediated dissociation

In precursor-mediated adsorption, the incident molecule is first accommodated on the surface through a trapping or physisorption process before dissociating or diffusing to a more favorable site for dissociation. This intermediate stage before dissociation is usually termed a “precursor” state. In contrast to direct dissociation, the barrier may be significantly lower for precursor-mediated dissociation although lower incident kinetic energies are required for trapping to occur. Since this is a two step process, the reaction probability S_R is also composed of two parts: the trapping probability ζ and the probability of dissociation. S_R can be represented as:

$$S_R = \zeta \frac{k_r}{k_r + k_d} \quad (1-15)$$

where k_r is the rate constant in going from the precursor state to the chemisorbed state, and k_d is the rate constant for desorption from the precursor state.

In the first step of this mechanism, the incident kinetic energy and angle of the molecules will strongly influence the trapping probability while the substrate temperature will only have a minor effect. It is anticipated that trapping probability decreases with incident kinetic energy as the molecule has to accommodate with the substrate. Further, increasing the angle of incidence decreases incident momentum normal to the substrate, thereby making it easier for the molecule to dissipate its energy through interactions with the substrate. In the second step of this process, the molecules can either desorb or dissociate on the surface. Both these processes are fully controlled by substrate temperature T_s and the activation energies for dissociation, E_{dis} , and desorption, E_{des} , will be crucial. If $(E_{dis} - E_{des}) > 0$, dissociation will increase with increasing T_s . If this quantity is < 0 , desorption will be more important at higher substrate temperatures. Therefore, the effect of substrate temperature on reaction probability can provide insight into the activation energies for dissociation and desorption.

1.4.2.2.3 Collision-induced dissociation

As illustrated in Fig. 1-11 (iii), collision-induced dissociation requires collisions of high energy molecules with a substrate already covered by adsorbates, in order for dissociation of these adsorbates to occur. Since pre-adsorbed molecules dissociate utilizing the energy of incident molecules, it is desirable for the impacting molecules to have a small collision cross section and

high kinetic energy in order to increase the probability of dissociation per collision. This process can be modeled by hard sphere collision theory and has useful implications for catalysis where the adsorbate-covered catalyst is continually bombarded by a large flux of high-energy molecules.

1.4.3 Thin film deposition using supersonic molecular beams

Until recently, supersonic molecular beams have been used almost exclusively as a gas source for molecular beam scattering experiments. These beams provide much higher fluxes than typical vapor deposition processes. In addition, excellent control over the energetic state and flux of incident molecules can be obtained. As a result, chemical deposition techniques can be developed which may be activated or strongly influenced even at low substrate temperatures. Some techniques have already been outlined in the previous discussions and include plasma-enhanced CVD which activates process chemistries through the ionization of process gases and atomic layer deposition (ALD) which employs self-limiting dissociative chemistries activated at low process temperatures. As demonstrated in numerous molecular beam scattering experiments, many process chemistries exist for reactions at the surface of the substrate may be optimized through the use of enhanced translational energies. Owing to their several unique advantages, supersonic molecular beams could be employed as an independent technique or in conjunction with plasma-enhanced processes or ALD, to carry out nucleation and deposition of thin films with superior attributes compared to other techniques. Several investigators have examined the use of supersonic free jet sources for the deposition of inorganic materials such as Ge on GaAs(100) [32,33], GaAs epitaxy using tri-methyl

gallium ($\text{Ga}(\text{CH}_3)_3$) [34], GaN [35,36] and organic materials like pentacene on SiO_2 [37–39]. In the case of organic thin films, the ability to tune properties of an incident molecule can strongly affect nucleation in the submonolayer regime as well as morphology of these films in the multilayer regime. As a result, correlations can be established between resultant film microstructure and performance characteristics of organic thin film transistors (OTFTs). Efforts towards this goal are outlined in Chapters 4–7. The ability to precisely characterize and collimate supersonic beams has led to novel techniques in film deposition studies [23,40] employed in these experiments.

1.5 References

1. G. E. Moore, *Electronics* **38** (1965).
2. S. M. Sze, *Physics of Semiconductor Devices, Second Edition* (John Wiley and Sons, NY, 1981).
3. A. Aviram and M. A. Ratner, *Chem. Phys. Lett.* **29**, 277 (1974).
4. J. R. Heath and M. A. Ratner, *Physics Today*, 43 (2003).
5. R. Maoz and J. Sagiv, *Langmuir* **3**, 1034 (1987).
6. R. G. Nuzzo and D. L. Allara, *J. Am. Chem. Soc.* **105**, 4481 (1983).
7. Y. Xia, J. A. Rogers, K. E. Paul and G. M. Whitesides, *Chem. Rev.* **99**, 1823 (1999).
8. G. E. Poirier, *Chem. Rev.* **97**, 1117 (1997).
9. A. E. Kaloyeros and E. Eisenbraun, *Annu. Rev. Mater. Sci.* **30**, 363 (2000)
10. S. -K. Rha, W. -J. Lee, S. -Y. Lee, Y. -S. Hwang, Y. -J. Lee, D. -I. Kim, D. -W. Kim, S. -S. Chun and C. -O. Park, *Thin Solid Films* **320**, 134 (1998).
11. G. S. Chen and S. T. Chen, *J. Appl. Phys.* **87**, 8473 (2000)
12. *Interconnect and Contact Metallization for ULSI*, edited by G. S. Mathad, H. S., Rathore, Y. Arita (The Electrochemical Society Proceedings Series, Pennington, NJ, 2000), 46–55.
13. C. K. Chiang, C. R. Fincher, Jr., Y. W. Park, A. J. Heeger, H. Shirakawa, E. J. Louis, S. C. Gau and A. G. MacDiarmid, *Phys. Rev. Lett.* **39**, 1098 (1977).
14. (a) R. Friend, J. Burroughes and T. Shimoda, *Phys. World* **12**, 35 (1999);
(b) W. Riess, H. Riel, T. Beierlein, W. Brütting, P. Müller and P. F. Seidler, *IBM J. Res. & Dev.* **45**, 77 (2001).

15. (a) J. A. Rogers, Z. Bao, K. Baldwin, A. Dodabalapur, B. Crone, V. R. Raju, V. Kuck, H. Katz, K. Amundson, J. Ewing and P. Drzaic, *Proc. Nat. Aca. Sci.* **98**, 4835 (2001); (b) C. D. Sheraw, L. Zhou, J. R. Huang, D. J. Gundlach, T. N. Jackson, M. G. Kane, I. G. Hill, M. S. Hammond, J. Campi, B. K. Greening, J. Francl and J. West, *Appl. Phys. Lett.* **80**, 1088 (2002); (c) G. H. Gelinck et al., *Nat. Mat.* **3**, 106 (2004).
16. B. Comiskey, J. D. Albert, H. Yoshizawa and J. Jacobson, *Nature* **394**, 253 (1998).
17. (a) Z. -T. Zhu, J. T. Mason, R. Dieckmann and G. G. Malliaras, *Appl. Phys. Lett.* **81**, 4643 (2002); (b) B. K. Crone, A. Dodabalapur, R. Sarpeshkar, A. Gelperin, H. E. Katz and Z. Bao, *J. Appl. Phys.* **91**, 10140 (2002).
18. (a) D. Voss, *Nature* **407**, 442 (2000); (b) P. F. Baude, D. A. Ender, M. A. Haase, T. W. Kelley, D. V. Muyres and S. D. Theiss, *Appl. Phys. Lett.* **82**, 3964 (2003).
19. M. Ohring, *The Materials Science of Thin Films* (Academic Press, London, UK, 1992).
20. J. A. Venables, *Introduction to Surface and Thin Film Processes* (Cambridge University Press, Cambridge, UK, 2000).
21. D. Walton, T. N. Rhodin and R. W. Rollins, *J. Chem. Phys.* **38**, 2698 (1963).
22. J. B. Anderson, *Molecular Beams and Low Density Gas Dynamics*, edited by P. P. Wegener (Marcel Dekker, New York, USA, 1974).
23. S. E. Roadman, N. Maity, J. N. Carter and J. R. Engstrom, *J. Vac. Sci. Technol. A* **16**, 3423 (1998).

24. L. -Q. Xia, M. E. Jones, N. Maity and J. R. Engstrom, *J. Vac. Sci. Technol. A* **13**, 2651 (1995).
25. J. Fernandez de la Mora and J. Rosell-Llompart, *J. Chem. Phys.* **91**, 2603 (1989).
26. *Atomic and Molecular Beam Methods Vol. 1*, edited by G. Scoles (Oxford University Press, NY, 1988).
27. *Dynamics of Gas-Surface Interactions*, edited by C. T. Rettner and M. N. R. Ashfold (The Royal Society of Chemistry, Cambridge, UK, 1991).
28. A. C. Luntz, M. D. Williams and D. S. Bethune, *J. Chem. Phys.* **89**, 4381 (1988).
29. C. T. Rettner, H. E. Pfnür and D. J. Auerbach, *Phys. Rev. Lett.* **54**, 2716 (1985).
30. M. B. Lee, Q. Y. Yang, S. L. Tang and S. T. Ceyer, *J. Chem. Phys.* **85**, 1693 (1986).
31. D. J. Auerbach, H. E. Pfnür, C. T. Rettner, J. E. Schlaegel, J. Lee and R. J. Madix, *J. Chem. Phys.* **81**, 2515 (1984).
32. D. Eres, D. H. Lowndes and J. Z. Tischler, *Appl. Phys. Lett.* **55**, 1008 (1989).
33. D. Eres, D. H. Lowndes, J. Z. Tischler, J. W. Sharp, T. E. Haynes and M. F. Chisholm, *J. Appl. Phys.* **67**, 1361 (1990).
34. S. Zhang, J. Cui, A. Tanaka and Y. Aoyagi, *Appl. Phys. Lett.* **64**, 1105 (1994).
35. B. A. Ferguson, A. Sellidj, B. B. Doris and C. B. Mullins, *J. Vac. Sci. Technol. A* **14**, 825 (1996).
36. A. Sellidj, B. A. Ferguson, T. J. Mattord, B. G. Streetman and C. B. Mullins, *Appl. Phys. Lett.* **68**, 3314 (1996).

37. L. Casalis, M. F. Danisman, B. Nickel, G. Bracco, T. Toccoli, S. Iannotta and G. Scoles, *Phys. Rev. Lett.* **90**, 206101–1 (2003).
38. S. Iannotta and T. Toccoli, *J. Polymer Sc. B* **41**, 2501 (2003).
39. F. De Angelis, T. Toccoli, A. Pallaoro, N. Coppedè, L. Mariucci, G. Fortunato and S. Iannotta, *Synth. Met.* **146**, 291 (2004).
40. S. E. Roadman, S. W. Levine, Y. –J. Zheng, P. Clancy and J. R. Engstrom, *Appl. Phys. Lett.* **74**, 25 (1999).

2. Experimental Methods

2.1 Formation of inorganic–organic interfaces

2.1.1 Description of molecular beam system

The formation of an interface between organometallic precursor tetrakis(dimethylamido)titanium ($\text{Ti}[\text{N}(\text{CH}_3)_2]_4$, (TDMAT)) and self-assembled monolayers possessing a variety of terminal functional groups was studied in a custom designed ultrahigh vacuum (UHV) molecular beam system [1]. A schematic view of the experimental apparatus is provided in Fig. 2–1. This system was initially designed for experiments employing a supersonic molecular beam. However, a vapor delivery source with a microcapillary array doser was constructed to produce a collimated effusive beam and employed for these experiments (c.f. section 2.1.4).

The main chamber (volume ~ 40 L) is pumped by a 400 L/s turbomolecular pump equipped with magnetic bearings (Leybold Vacuum, 340M) and a titanium sublimation pump equipped with a cryoshroud is flashed after every bakeout. A base pressure of 2×10^{-9} Torr is routinely achieved after a 24 hour bakeout at 150 °C. Substrates are mounted on a sample manipulator (Thermionics Vacuum Products) capable of 5 degrees of freedom (x, y, z translations, polar rotation and tilt), which allows the sample to be transported between two foci within the system. Both foci lie on the axis of the supersonic molecular beam. The first focal point positions the sample at the intersection of

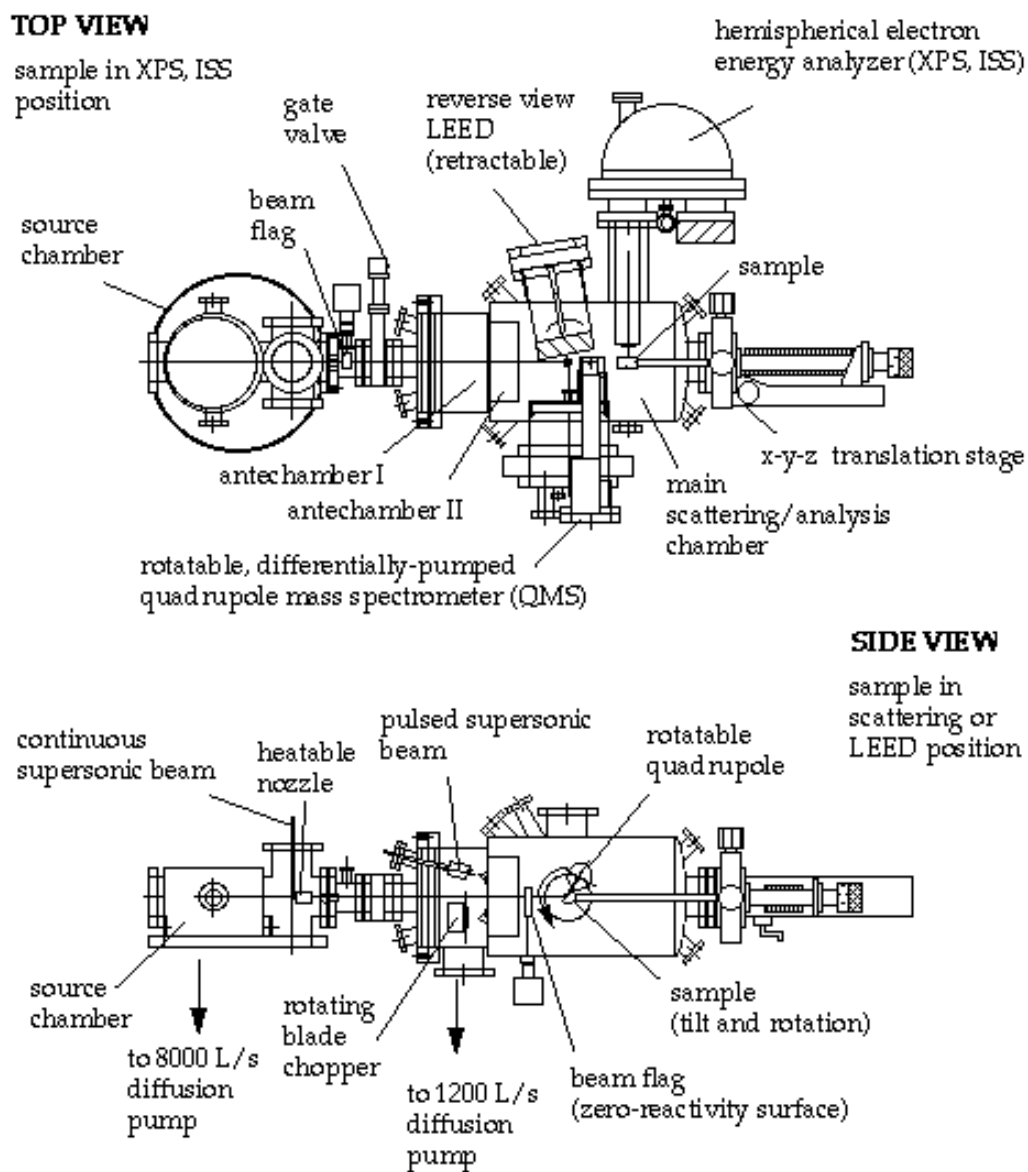


Figure 2-1 Schematic drawing of molecular beam scattering chamber.

the foci of a hemispherical energy analyzer and a twin anode (Mg/Al) x-ray source (VSW), a doubly-differentially pumped ion gun, the supersonic beam and the effusive beam. The second focal point positions the sample at the intersection of the axis of rotation of a quadrupole mass spectrometer (QMS, Extrel, EX-800), whose ionization source is located 5.7 cm from the sample, the focal point of a set of retractable rear-view low-energy electron diffraction (LEED) optics, the supersonic beam and a 2-3/4" port to which the effusive source can be moved. The quadrupole mass spectrometer is mounted off-axis on a 10" rotatable platform at 90° to the line of flight of the molecular beam. The platform is equipped with differentially-pumped spring-loaded teflon seals (Thermionics) pumped by a 10 L/s ion pump. The mass spectrometer is housed in a separate chamber pumped by a 60 L/s turbomolecular pump. This chamber is isolated from the main chamber by an additional spring-loaded teflon seal such that the turbomolecular pump can be mounted in a permanently fixed position. The flange that isolates the main and mass spectrometer chambers is equipped with a cylindrical reservoir, cooled with liquid nitrogen that surrounds the ionization region of the quadrupole. An oxygen-free high-conductivity (OHFC) cap mounted at the end of the reservoir, fitted with an orifice, defines the acceptance solid angle of the QMS detector, which is $\pm 2^\circ$. This configuration allows measurement of time-of-flight (TOF) of molecules in the beam, with the sample retracted to the first focal point, as well as angular distribution of molecules scattered from the surface of the sample.

Above the second focal point is the load-lock pumped by a $240 \text{ L}\cdot\text{s}^{-1}$ corrosive turbo pump (Pfeiffer Vacuum, TPU 240H). Samples are transferred into the load-lock which is pumped down to below 1×10^{-6} Torr after which they are introduced through a gate valve onto the manipulator in the main

chamber. The load–lock mechanism consists of a sample transfer arm and fork employing a STLC (Thermionics) type transfer system which mates to the sample manipulator. Solid back or “picture frame” type Mo platens can be used. The picture frame assembly utilizes a retaining ring to minimize thermal stresses incurred and to provide temperature uniformity during experiments studying the effect of substrate temperature. Its open back design allows for direct radiant heating using a tungsten ribbon mounted behind the sample, while indirect cooling to approximately 170 K is provided by contact, through copper braids to a liquid nitrogen cooled reservoir. The solid back platen is useful for samples of smaller size and/or custom shapes. The temperature at the surface of the substrate is calibrated using a chromel–alumel (type K) thermocouple wedged between the retaining ring and the substrate; the reference is another thermocouple attached to the back of the manipulator.

A supersonic molecular beam can be generated using a stainless steel nozzle in the source chamber. This beam passes through antechamber I which is pumped by a baffled (water–cooled) 1200 L/s diffusion pump charged with Santovac 5 polyphenyl ether fluid. Antechamber II is pumped by a titanium sublimation pump, a 270° sector cylindrical reservoir cooled with liquid nitrogen, and the 240 L/s corrosive turbomolecular pump which also pumps on the load–lock – switching is accomplished through pneumatically operated solenoid valves. The source chamber and antechamber I are separated by a pneumatically operated gate valve. This valve was closed permanently for the experiments described here and the diffusion pump in antechamber II was used to evacuate that chamber and minimize any leaks from the source chamber which was not under vacuum.

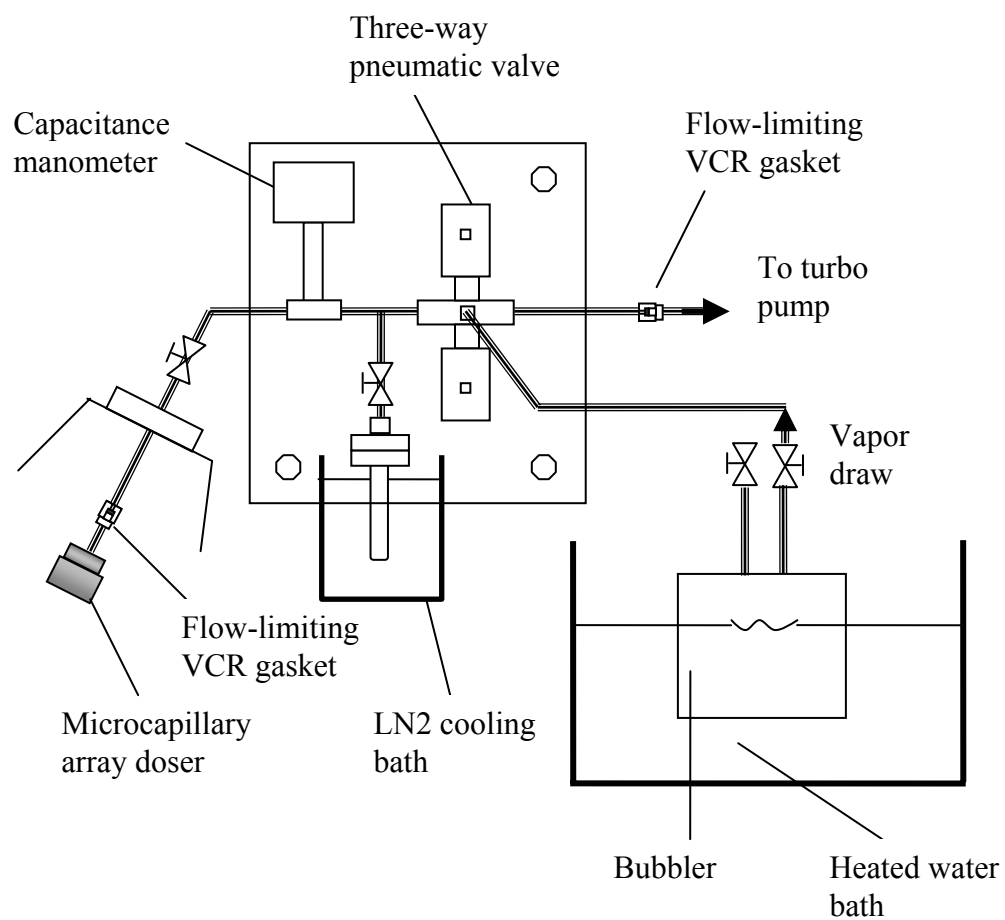


Figure 2–2 Schematic drawing of delivery system for organometallic precursor tetrakis(dimethylamido)titanium $\text{Ti}[\text{N}(\text{CH}_3)_2]_4$ (TDMAT) through a microcapillary array doser.

2.1.2 Description and characterization of vapor delivery source

A vapor delivery source was designed and constructed to produce an effusive beam of $\text{Ti}[\text{N}(\text{CH}_3)_2]_4$ and is shown schematically in Fig. 2-2. A microcapillary array doser (Burle Technologies) made of lead silicate glass, (0.3 mm thick, 18 mm diameter of capillary area, 5 μm pore size, 6 μm center to center spacing with solid border) was used to deliver a uniform flux of $\text{Ti}[\text{N}(\text{CH}_3)_2]_4$ to the surface of the sample, without producing a significant rise in the background partial pressure. The doser was mounted on a 2-3/4" flange with a 4" translation stage. As a result, it was translated to be 25.4 mm from the center of the sample during exposures and retracted when analysis was conducted by x-ray photoelectron spectroscopy (XPS). A 1/4" silver plated 316 SS VCR gasket with an aperture 178.8 μm in diameter and 125 ± 25 μm long was placed upstream of the doser. For most experiments, the flow of $\text{Ti}[\text{N}(\text{CH}_3)_2]_4$ through the doser was metered by controlling the temperature of the bubbler (set at 0 °C for all experiments), and using the gasket as a flow-limiting orifice. $\text{Ti}[\text{N}(\text{CH}_3)_2]_4$ in the bubbler was initially stored under nitrogen which was pumped out through the main chamber. Vapor in the bubbler was drawn to the doser in the main chamber, through 1/4" stainless steel tubing (ID: 0.18") via a three-way pneumatically operated bellows valve. Switching the valve resulted in either transporting $\text{Ti}[\text{N}(\text{CH}_3)_2]_4$ to the main chamber or to the 240 L/s corrosive turbomolecular pump. In order to equalize the resistance to flow through both paths, a second 150 μm flow-limiting VCR orifice was also used in the exhaust line to the turbo pump and placed at approximately the same distance from the three-way valve as compared to its counterpart in the line to

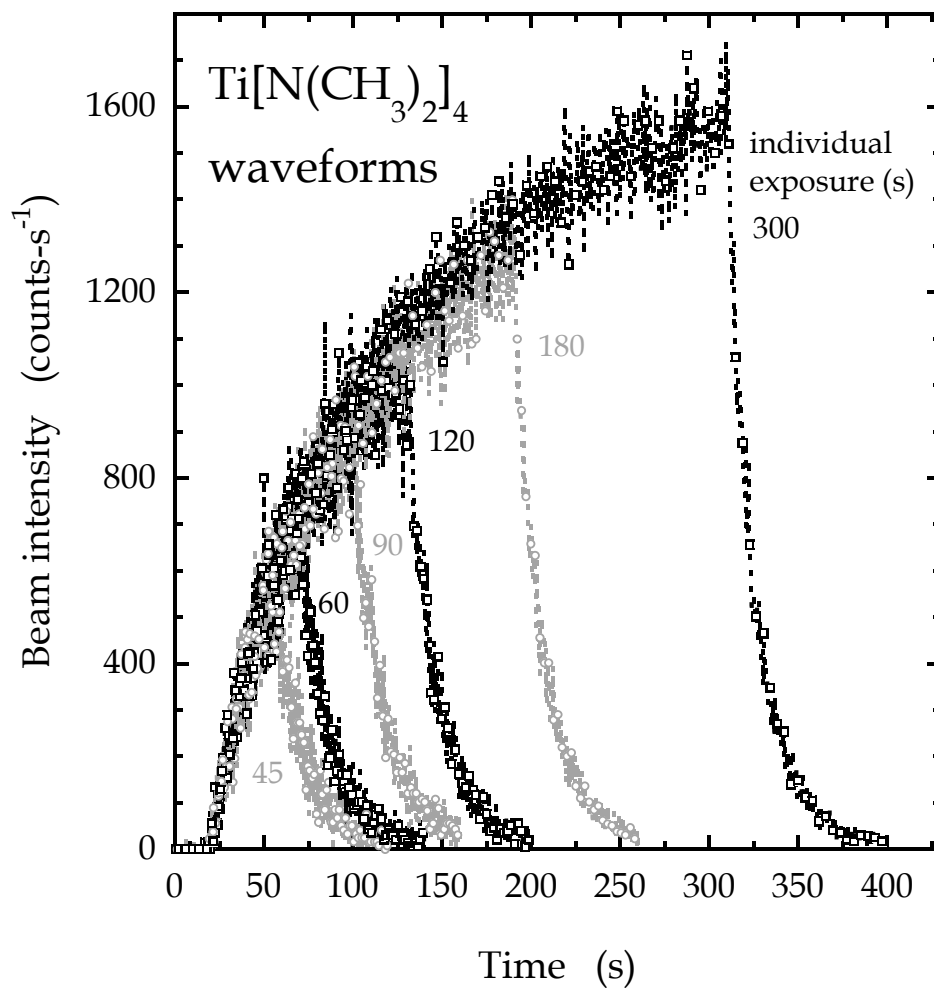


Figure 2–3 Waveforms for exposure of a substrate to Ti[N(CH₃)₂]₄. Numbers listed indicate individual times for each exposure in seconds.

the doser. The objective here was to minimize transients associated with the switching of the bellows valve. The vapor pressure of $\text{Ti}[\text{N}(\text{CH}_3)_2]_4$ in equilibrium with liquid was measured using a capacitance manometer (MKS) located downstream of the three-way valve. Beyond this manometer, a bakeable bellows valve was used primarily to isolate the $\text{Ti}[\text{N}(\text{CH}_3)_2]_4$ source from the main chamber during bakeouts. In order to minimize transients associated with the end of an exposure, a liquid nitrogen cooled glass tube was located downstream of the three-way valve, acted as a cryopump and was used to shunt exposures through a manually operated valve.

Passivation of all stainless steel lines with $\text{Ti}[\text{N}(\text{CH}_3)_2]_4$ was crucial for these experiments. Following a bakeout of the main chamber with the bakeable valve closed, all stainless lines transporting $\text{Ti}[\text{N}(\text{CH}_3)_2]_4$ were baked out ($> 100\text{ }^\circ\text{C}$) separately for at least two hours. Next, $\text{Ti}[\text{N}(\text{CH}_3)_2]_4$ was run through the exhaust line for 30 min., trapped between the three-way valve and bakeable valve for 10 min. and then run through the doser for 30 min. Further, prior to every experiment, the three-way valve was switched two times and the pressure readings of the ion gauge in the main chamber and the manometer were observed to make sure that transients due to passivation were eliminated. Waveforms of exposures, thus optimized, are illustrated in Fig. 2–3. These were obtained using the QMS ionizer at 90° and line of sight to the doser. The size of the aperture on the QMS cap was 10 mm in diameter. The initial rise is exponential and can be attributed to the dependence on chamber pumping speed. As can be seen, the liquid nitrogen reservoir contributes significantly to a sharp decrease in intensity when the three-way valve is switched. An estimate for the absolute flux of $\text{Ti}[\text{N}(\text{CH}_3)_2]_4$ reaching the sample surface was made and will be detailed in section 2.1.4.1.

2.1.3 Sample preparation

2.1.3.1 Materials

The following chemicals (Sigma–Aldrich) were purchased and used as received: hexadecane, chloroform, and carbon tetrachloride, all anhydrous and > 99%; tetrahydrofuran (THF), > 99%, A.C.S. reagent; 1.0 M borane–tetrahydrofuran (BH₃–THF) complex; 37% hydrochloric acid, A.C.S. reagent; 30% hydrogen peroxide, A.C.S. reagent; and sodium hydroxide pellets, reagent grade. The solvents, 99% dicyclohexyl and THF (Fisher Scientific) were used after being dried using 8 mesh Drierite (W. A. Hammond Drierite). The following trichlorosilane precursors (Gelest) were used as received: 11–cyanoundecyltrichlorosilane, 10–undecenyltrichlorosilane, and *n*–octadecyltrichlorosilane. Tetrakis(dimethylamido)titanium (TDMAT) Ti[N(CH₃)₂]₄, ≥ 99.999% purity based on metals analyzed, and ≥ 99% purity based on an assay by NMR, was obtained from Schumacher. Chloroform, 99.8% HPLC grade with 50 ppm pentene (Fisher Scientific) was used to sonicate freshly cleaved silicon wafers. The following chemicals (Mallinckrodt Baker Inc.) were also used as received: CMOSTM grade acetone, CMOSTM grade 2–propanol, and buffered oxide etch (BOE) (6:1 CMOSTM grade NH₄F–HF aqueous solution). Nanostrip (Cyantek) was also used as received.

2.1.3.2 Substrate Preparation

The starting substrates were 100 mm single side polished, 500–550 μm thick Si (100) wafers, doped with B to a resistivity of 38–63 Ω–cm. The

substrates were scribed with a Florod LASER 1 MEL 40 laser system and subsequently cleaved into 16 samples, each of size 16.75 mm × 16.75 mm. After cleaving, these samples were sonicated in chloroform, washed with deionized (DI) water, dried with N₂, and then dipped in BOE for 1 min. A thin layer of silicon dioxide (so-called “chemical oxide”) was grown by placing the samples in Nanostrip solution (a stabilized formulation of sulphuric acid and hydrogen peroxide) for 15 min. at 75 °C. The samples were then subject to a BOE and Nanostrip treatment for a second time. This procedure consistently produces a chemical oxide on the surface with a thickness of 20–25 Å, which is fully wet by water with an advancing contact angle of < 15° and a receding contact angle of < 10° [2]. This oxide has been reported to possess ~ 5 × 10¹⁴ SiOH groups–cm⁻² [3, 4]. Without further processing, this surface is the “chemical oxide” referred to below.

2.1.3.3 Formation of self-assembled monolayers (SAMs)

All SAMs were formed by liquid phase deposition on chemical oxide. Deposition was carried out in a glove box (Unilab, M. Braun Inc.) equipped with a refrigeration unit (temperatures to –35 °C) and a nitrogen atmosphere with < 1 ppm O₂. All glassware was rinsed repeatedly with acetone, isopropanol and DI water followed by baking at 150 °C overnight before use. The solvents used were 4:1 hexadecane:chloroform for octadecyltrichlorosilane (Cl₃–Si–(CH₂)₁₇–CH₃), and bicyclohexyl for 10–undecenyltrichlorosilane (Cl₃–Si–(CH₂)₉–CH=CH₂) and 11–cyanoundecyltrichlorosilane (Cl₃–Si–(CH₂)₁₁–CN). The solvents were chosen such that their freezing point was below the transition temperature (10 °C for 11–carbon chains and 28 °C for

18-carbon chains) which was not to be exceeded for the formation of well-ordered SAMs [5,6]. All solutions were ~ 2.5 mM concentration of the SAM precursor molecule in the solvent. Substrates were dipped in the SAM solution for 1 hour for the $-\text{CH}=\text{CH}_2$ and $-\text{CH}_3$ terminated SAMs and 3 min. for the $-\text{CN}$ terminated SAM. Upon withdrawal from the solution, samples were sonicated in anhydrous chloroform for 10–25 min. to remove any polymerized residue, not bonded to the substrate. Finally, the substrates were washed in DI water, dried with N_2 and stored in precleaned fluoroware containers in a dessicator.

2.1.3.4 Formation of terminal groups

The vinyl-terminated SAM ($\equiv\text{Si}-(\text{CH}_2)_9-\text{CH}=\text{CH}_2$) was converted to a $-\text{OH}$ terminated SAM ($\equiv\text{Si}-(\text{CH}_2)_9-\text{CH}_2-\text{CH}_2\text{OH}$) by a 2 hour dip in 1.0 M BH_3 -THF solution followed by a dry THF rinse, and a 2 min. dip in a 30% H_2O_2 :0.1N NaOH solution. Samples were then washed with DI water, dried with N_2 and stored in precleaned fluoroware containers. This treatment has been found to convert $\sim 97\%$ of the vinyl groups to $-\text{OH}$ groups for a 16 carbon SAM [3]. The $-\text{CN}$ terminated SAM ($\equiv\text{Si}-(\text{CH}_2)_{11}-\text{CN}$) was converted into an $-\text{NH}_2$ terminated SAM ($\equiv\text{Si}-(\text{CH}_2)_{11}-\text{CH}_2-\text{NH}_2$) by a 4 hour dip in 1.0 M BH_3 -THF solution, followed by a 1 hour dip in methanol, and finally a 15 min. dip in 10% HCl to deprotonate the amine group. Wafers were washed with DI water, dried with N_2 and stored in precleaned fluoroware containers. This treatment has been found to reduce the $-\text{CN}$ group completely [7].

2.1.3.5 Characterization of self-assembled monolayers

2.1.3.5.1 Contact Angle Measurements

Contact angle measurements were carried out with a NRL CA Goniometer (Rame-Hart Inc.). Measurements were performed with an advancing droplet volume of at least 3 μL and a receding droplet volume of about 2 μL . Contact angles were measured on each side of the droplet and in five different areas on each sample, and the average of these values is reported. Typical values for the standard deviation were 2–3°.

2.1.3.5.2 Ellipsometry

Measurements of the thickness of the SAMs were performed with a Gaertner L-120A ellipsometer, which employs a He-Ne (632.8nm) laser light source, incident at 70° with respect to the surface normal. For the refractive indices, a value of 1.46 has been reported for the chemical oxide [8], whereas values of 1.42–1.44 have been reported for the SAMs examined here. The latter is valid for liquid and solid straight-chain saturated hydrocarbons [3]. Sensitivity of the calculated thickness to the value assumed for the refractive index was small—a change of 0.05 resulted in less than a 1 Å change in the estimated thickness of the monolayer. This fact allowed us to simplify the analysis. Specifically, the thickness of the chemical oxide was first measured, and subsequently the thickness of the combined chemical oxide/SAM layer was measured, assuming a refractive index of 1.46 for the composite layer. The

difference between these values gives the thickness of the SAM. Measurements of this type were made in 3–5 different areas on each sample and repeated on different samples. The estimated error in these measurements is $\pm 1 \text{ \AA}$.

2.1.3.5.3 Atomic Force Microscopy (AFM)

Images were acquired with a Dimension 3100 scanning probe microscope (Veeco Instruments) in tapping mode using Tap 300 SPM probes (Nanodevices Inc.).

2.1.3.5.4 X-ray photoelectron spectroscopy (XPS)

XPS was carried out using a twin anode x-ray source (Mg/Al) and a CLASS 100 concentric hemispherical energy analyzer (VSW Worldwide). Mg K α x-rays (1253.6 eV) were used throughout this study. Survey scans (e.g. 0–1300 eV kinetic energy) were carried out in the fixed retardation ratio mode, whereas detailed scans (range of ~ 20 eV over a single feature) were carried out in the fixed analyzer transmission mode. The emission current for the source was 20 mA and the electron voltage was 12 kV. Short scans (0.5 eV/s, 10 cycles) were used for C (1s), O (1s) and Si (2p) peaks. As a consequence, damage to the SAMs due to exposure to the x-rays was not manifest in the experiments reported here [9]. The take-off angle for photoelectrons was 38.5° with respect to the surface normal for experiments examining the kinetics of adsorption. A background subtraction method first proposed by Shirley [10] was used in all analyses of the peaks. Peak areas and peak positions were

obtained by fitting the spectra to a product Gaussian–Lorentzian (G–L) function of the form:

$$f(x) = \frac{h}{[1 + M(x - x_0)^2 / \beta^2] \exp[(1 - M)[(\ln 2)(x - x_0)^2] / \beta^2]} \quad (2-1)$$

where h is peak height, M is the mixing ratio relating to the fractional contribution of the Gaussian and Lorentzian components, x_0 is the peak center and β is a parameter that is nearly 0.5 (FWHM). A value of 0.9 was used for M for all peaks. These product G–L functions have been widely used to provide good quality fits substituting for Voigt functions [11], which involve a convolution of a Gaussian with a Lorentzian function. Product functions also produce smaller residuals compared to sum G–L functions [12].

2.1.4 Interface formation experiments

2.1.4.1 Estimation of flux of $\text{Ti}[\text{N}(\text{CH}_3)_2]_4$

An estimate for the absolute flux of $\text{Ti}[\text{N}(\text{CH}_3)_2]_4$ reaching the sample surface was made using the following procedure. First, the resistance to flow was calculated for the section of (4.57 mm i.d.) tubing between the capacitance manometer (MKS) (placed between the bubbler and the flow–limiting orifice); the flow–limiting aperture, and the capillary array. For typical conditions (measured partial pressure of $\text{Ti}[\text{N}(\text{CH}_3)_2]_4$ at the bubbler < 0.05 Torr), the flow–limiting orifice provided ~ 90% of the resistance to flow. Coupled with the measured partial pressure, this gave a total throughput of 4.171×10^{14} molecules– s^{-1} of $\text{Ti}[\text{N}(\text{CH}_3)_2]_4$ entering the chamber. Second,

using established correlations for the angular distribution produced by capillary array dosers [13], the fraction of the flux that was intercepted by the sample was computed. Accounting for the sample area and the angle of incidence gives the incident flux of $\text{Ti}[\text{N}(\text{CH}_3)_2]_4$ (2.798×10^{13} molecules $\text{-cm}^{-2}\text{-s}^{-1}$). The variation of the (relative) flux over the area sampled by XPS was estimated to be no greater than $\pm 1.5\%$. A check of the calculated conductance was made using a flow of pure He, using a calibrated mass flow controller and the capacitance manometer. A check of the angular distribution produced by the capillary array doser was also made, using the (rotatable) mass spectrometer placed in a line-of-sight position and, as a reference, a nozzle consisting of a single aperture that produced an effusive flux. The accuracy of the absolute flux was estimated to be at best $\pm 30\%$.

2.1.4.2 Experimental procedures

All self-assembled monolayer films were deposited in the liquid phase and on chemical oxide, as described above. A polycrystalline Au sample (1000 Å of Au, deposited at 2 Å-s^{-1} , on 100 Å of Cr, deposited at 4 Å-s^{-1} , both on a Si (100) wafer with a native oxide layer at the surface) was used as reference standard for XPS. The Au and Cr thin films were deposited in a CVC SC4500 system (Cornell Nanoscale Facility) by e-beam evaporation. After XPS analysis of the Au reference standard sample [scanning the Au (4f) peak], the substrate of interest possessing a self-assembled monolayer was transferred into the ultrahigh vacuum chamber via a fast-entry load-lock. Once a base pressure of *ca.* 2×10^{-9} Torr was achieved, experiments involving $\text{Ti}[\text{N}(\text{CH}_3)_2]_4$ were initiated. First, the sample was brought to temperature (here, either

–50°C, 30°C or 110°C). In all cases, the sample was cooled to –50 °C first and then heated to the desired temperature. Calibration data are provided in the Appendix (section. 9–1). It should be noted in passing that, for a 11–carbon undecenyltrichlorosilane SAM, annealing to above 125°C for 2 hours in a 10^{-2} – 10^{-3} Torr ambient was found to result in disordering as evidenced by water and hexadecane contact angle measurements. In addition, the 11–carbon SAM and 18–carbon SAM on SiO₂ have been reported to undergo disordering with a drastic increase in surface roughness from 0.4 nm to 1.5 nm and 2.0 nm respectively (from AFM) on annealing to above 140°C in a 10^{-2} – 10^{-3} Torr ambient [14] for time periods of about 5 hours. Second, XP spectra were obtained (*vide supra*) to verify SAM identity, and to quantify the coverage. Next, the SAM surface was exposed to Ti[N(CH₃)₂]₄ through the doser, where exposures ranged from 45 to 390 s. After each exposure, the Ti (2p) peak was scanned (*vide infra*) in order to quantify Ti[N(CH₃)₂]₄ adsorption on the SAM surface. Exposures and the acquisition of XP spectra were repeated until saturation of the adlayer was apparent. After saturation was attained, detailed scans of C(1s), O(1s), N(1s) and Si(2p) peaks were obtained.

2.1.4.3 X–ray photoelectron spectroscopy

In most cases the Ti(2p) and N(1s) peaks were scanned at a rate of $0.5 \text{ eV}\cdot\text{s}^{-1}$, and 20 consecutive spectra were acquired in the fixed analyzer transmission mode. For studies of the adsorption kinetics the take–off angle of the photoelectrons was fixed at 38.5°, and a 5mm diameter circular spot on the sample was analyzed. For the experiments involving a variable (0°–65°) take–off angle, a $1 \times 10 \text{ mm}^2$ rectangular slit was used to maintain maximum field of

focus. All experiments involving angle resolved XPS (ARXPS) were conducted at $T_s = 110$ °C. Peak positions for the Ti(2p) feature were obtained in manner essentially identical to that described above. Peak areas for the Ti(2p) feature were obtained by numerical integration following a Shirley background subtraction.

2.2 Deposition of organic thin films

2.2.1 Description of thin film deposition system

Deposition of pentacene thin films was carried out in another custom designed ultrahigh vacuum chamber (AUTOCAD rendering in Fig. 2–4 and schematic drawings in Fig. 2–5) [15]. The system is separated into four main compartments plus a load–lock system: the source, ante, main and analysis chambers. Gate valves are located between the analysis and main chamber and also the source and antechamber. These valves allow isolation of individual chambers to facilitate maintenance and modifications without having to vent the entire system.

Supersonic molecular beams are generated in the source chamber. The antechamber is located in–between the source chamber and the main chamber. The main purpose of an antechamber is to allow differential pumping and to allow further collimation of the beam before it enters the main chamber. Furthermore, in most supersonic molecular beam systems, modulation of the beam is done in the antechamber(s) in order to perform experiments such as time–of flight measurements and real–time measurements of probabilities of

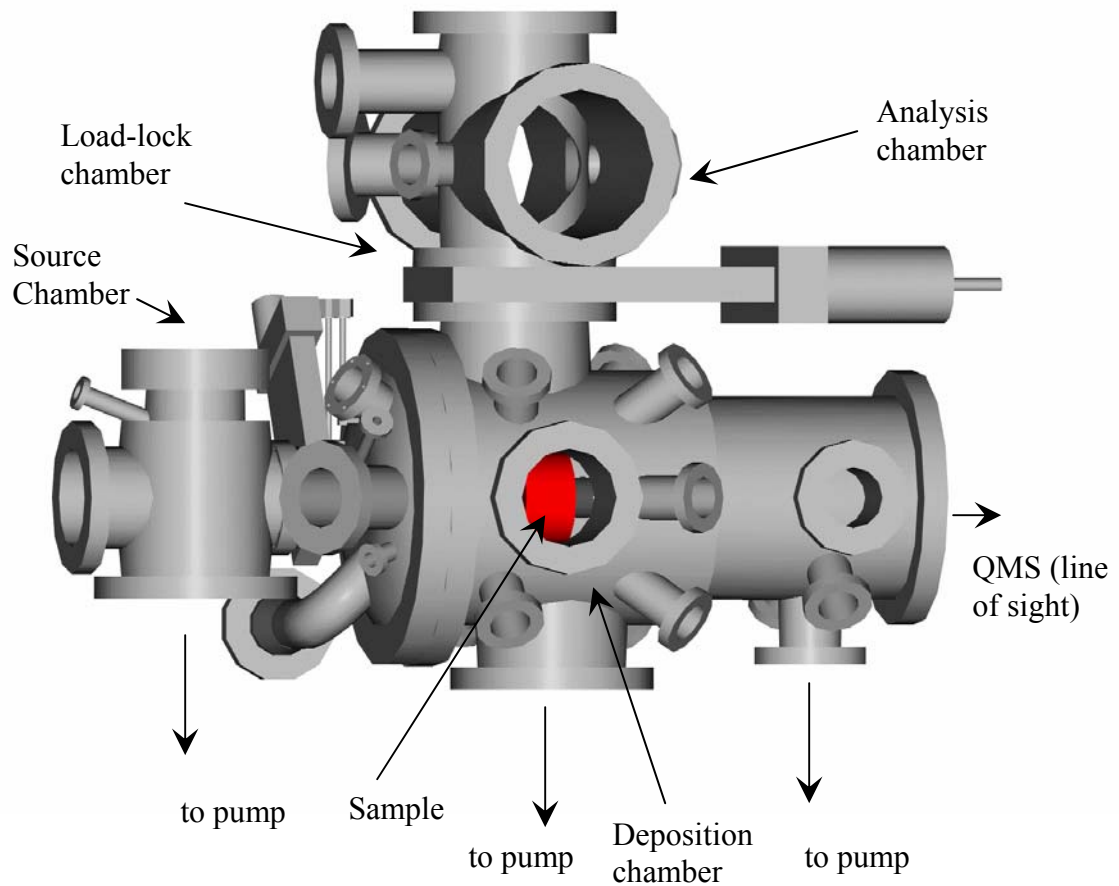


Figure 2-4 AUTOCAD three-dimensional rendering of thin film deposition system.

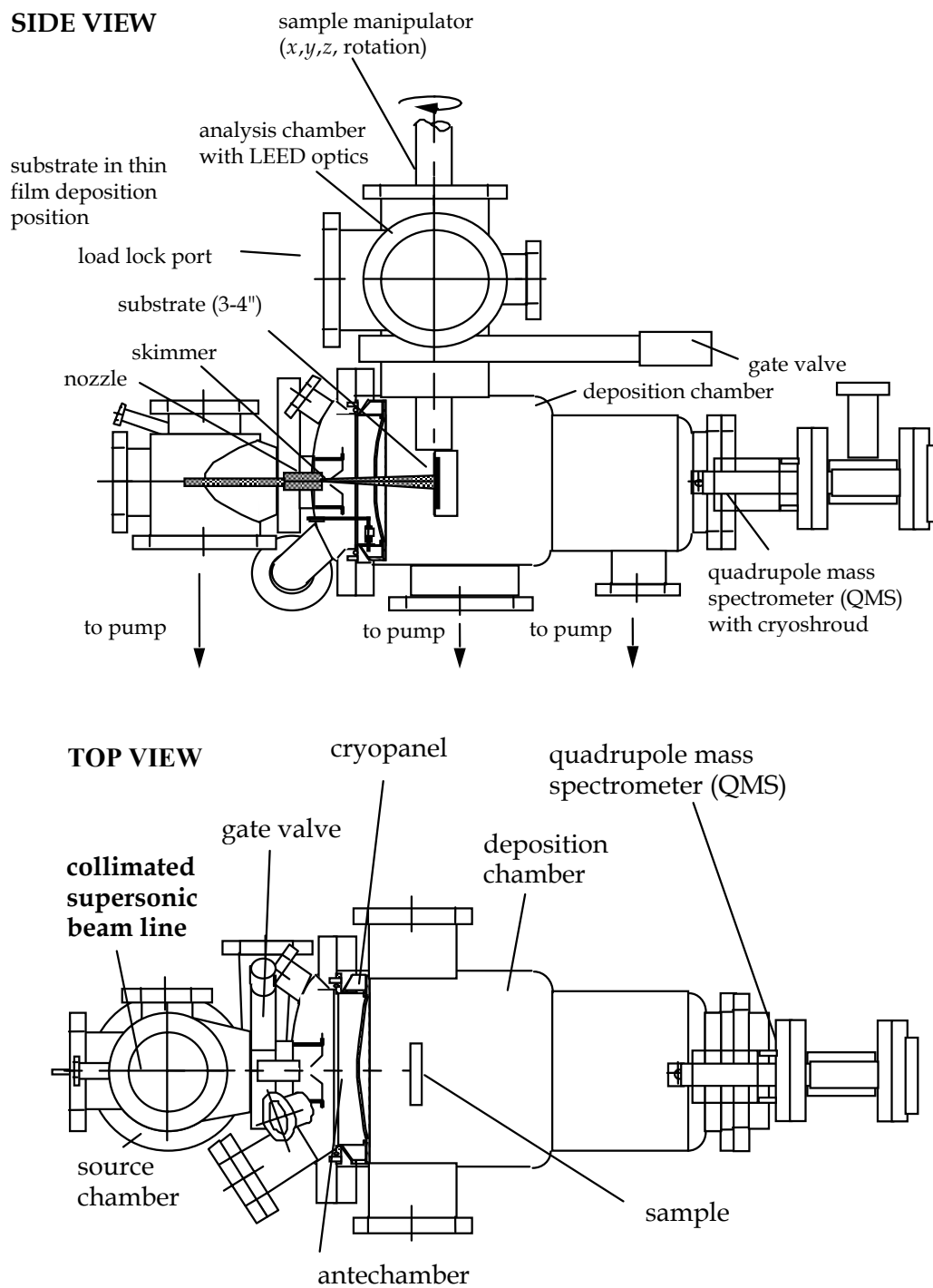


Figure 2-5 Schematic side and top views of the thin film deposition system.

adsorption. In this system, the antechamber is pumped by a high throughput turbomolecular pump (Balzers TPU 62H). Pumping of condensable gases such as water is further aided by an annulus shaped liquid nitrogen shroud. When cooled with liquid nitrogen, this shroud helps to maximize beam to background ratios. Located immediately adjacent to the antechamber is the main chamber where thin films are deposited on suitable substrates. The main chamber is pumped by a $400 \text{ L}\cdot\text{s}^{-1}$ magnetically levitated turbomolecular pump (Osaka TG 403M). After bakeout at $120 \text{ }^\circ\text{C}$ for 24 – 48 hours, the main chamber can routinely reach a base pressure of 5×10^{-10} Torr or below. Located in the main chamber is an Extrel QMS (Extrel EX-800). The QMS is mounted in a direct line-of-sight position at the end of the chamber. A liquid nitrogen shroud surrounds the ionizing region of the mass spectrometer. This shroud has been designed to accept several mass spectrometers including an Extrel EX800, a Hiden 3F/300 Epic and a VG SX 200. The surface of the shroud within the deposition chamber is cooled using liquid nitrogen to minimize background contribution from carrier gas and condensable species. The shroud is also capable of accepting a stainless steel tube or “skirt”, which connects to the base flange thereby allowing non-condensable gases to be differentially pumped through the shroud via a $2 \frac{3}{4}$ ” CF flange teed off of the main housing. The substrates were mounted in platens made out of Mo, which were held in place on a sample manipulator (Thermionics). The manipulator is capable of movements in the x, y, z directions as well as rotational motion in the azimuthal (along the beam axis) and polar (normal to the beam axis) directions. All motions are controlled by stepper motors (except for the y-direction) which allows for precise and programmable movements controlled by software. The manipulator is capable of moving between the analysis and main chambers

using the z translation which has an approximate travel of 16". The x and y directions have approximately 1 inch travel while the rotational degrees of freedom are capable of complete 360° rotations inside the main chamber.

There are two focal points associated with the design of this system. The first focal point is located in the main chamber and positions the sample at the intersection of the supersonic molecular beam as well as several other ports for gas sources (such as atomic hydrogen or ammonia) or infrared temperature measurement devices. At this focal point, the sample is 2.68" from the final beam defining aperture along the beam axis. Due to the close proximity of the sample to the aperture plate, most gas sources must come through the antechamber in order to avoid very low angles of incidence to the sample. The second focal point is located in the analysis chamber where the sample can be positioned for sample transfer through a fast entry load-lock or analysis using a reverse view low energy electron diffraction (LEED) system (Omicron).

The load-lock is pumped by a 300 L-s⁻¹ magnetically levitated turbo pump (Seiko, STPH 300C), and reaches a base pressure of 5×10^{-7} Torr within a couple of hours of loading a fresh sample. The load-lock and the analysis chambers are separated by a gate valve and the sample is transferred between the chambers using a magnetically coupled linear-rotary feedthrough with a STLC (Thermionics) type transfer system. The platen can be alternatively locked and unlocked onto either the manipulator or transfer arm through sets of pins. Mo Platens capable of holding 3 and 4 inch wafers as well as samples of dimensions 1 cm x 1 cm and 1.7 cm x 1.7 cm can be used. Samples sit in recessed wells in these platens and are held in place by a retaining ring. The platens expose the back of the sample to facilitate radiative heating and retaining rings help minimize thermal stresses incurred during heating.

The substrates can be heated radiatively by a 3", 3 kW graphite heater which is encapsulated in pyrolytic BN for chemical resistance. This heater is capable of heating 3" and 4" wafers to temperatures exceeding 850 °C and to as high as 950 °C for short periods of time during annealing processes. Sample surface temperatures can be measured using a pyrometer for temperatures greater than 350 °C. A chromel–alumel (type–K) thermocouple is also mounted on the back of the manipulator and is calibrated to temperature measurements at the surface of the sample (obtained using either a pyrometer or thermocouple). The manipulator also has the ability to provide active cooling for faster response to temperature control. The cooling fluid is usually water: either reverse osmosis (RO) water from the building water supply or deionized water from a recirculating chiller.

Owing to the very low vapor pressure of most organic species, an *in vacuo* container (the evaporator) has been designed and employed to generate supersonic molecular beams in the source chamber [16]. This evaporator is directly connected to the gas delivery line and a heatable nozzle using 1/8" tubing and 1–1/3" CF flanges. Carrier gases of hydrogen, helium or nitrogen are used to produce supersonic expansions of organic molecules such as pentacene. Carrier gases are fed to the system using general service mass flow controllers (MKS) and stagnation pressures are measured using capacitance manometers upstream of the chamber. Stagnation pressures are generally between 35 and 300 Torr depending on the gas mixture and nozzle temperature. The nozzle consists of a 150 – 250 μm aperture in a 125 μm stainless steel plate that is welded to the end of an electropolished 1/4" stainless steel tube. Both the nozzle and the evaporator can be heated using tungsten ribbon heaters,

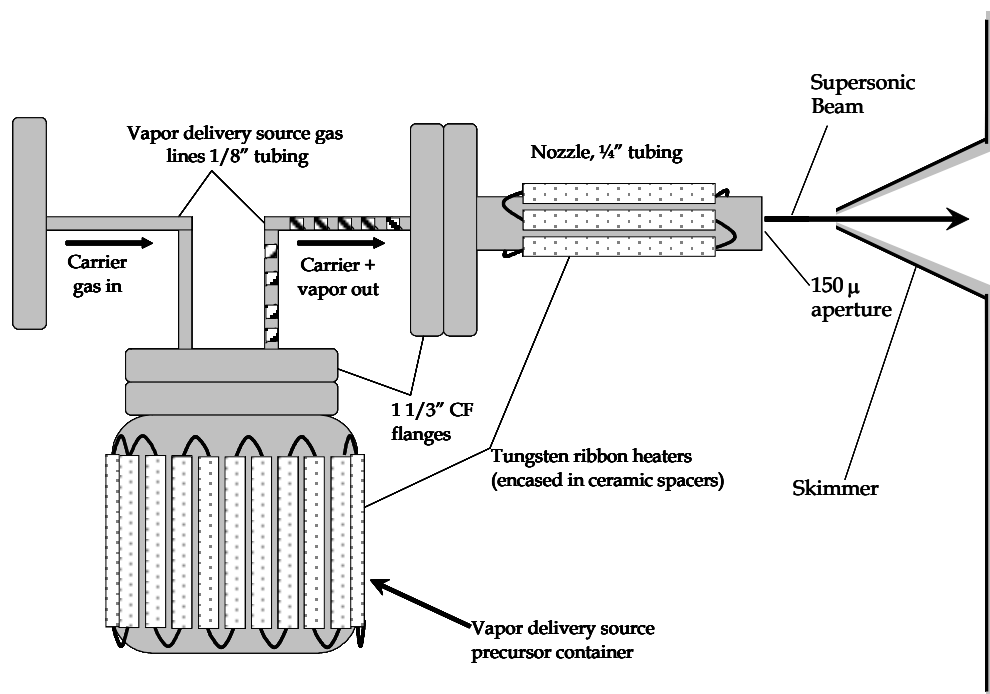


Figure 2–6 Schematic representation of supersonic beam source for low vapor pressure materials.

which are encased in 1/8" (ID) ceramic tubing and affixed using tantalum wire. Carrier gases fed to the evaporator are mixed with vapors of the organic species using a baffle within the evaporator, before the carrier-vapor mixture exits through a 1/8" tube and enters the nozzle. Coating of this 1/8" tubing resulted in non-uniform intensities of supersonic molecular beams. To fix this problem, tungsten ribbon encased in flexible ceramic sleeves has been used to heat this section of 1/8" tubing between the stainless steel nozzle and the evaporator. The entire nozzle/evaporator assembly is mounted on a precision x-y-z manipulator and the temperatures of the nozzle (T_n), evaporator (T_e) and 1/8" tube section (T_t) can be monitored independently using chromel-alumel type (K-type) thermocouples spot welded to their surfaces. The gas mixtures are expanded into a source chamber which is pumped using a 520 L-s^{-1} corrosion resistant turbomolecular pump (Pfeiffer TMU 520C). The expanded gas passes through a trumpet-shaped Ni skimmer (1.5 mm in diameter) mounted on a stainless steel plate and into the antechamber. The vapor delivery source, nozzle and skimmer assembly are shown schematically in Fig. 2-6.

The skimmer can be mounted in two positions along the beamline, placing the nozzle at approximately 14 and 24 cm from the sample surface when in the so called "forward" and "rear" positions respectively. This flexibility in design provides control over reactant flux to the sample surface or quadrupole mass spectrometer (QMS) as dictated by the requirements of a specific experiment. The beam passes through the skimmer into the antechamber where a reciprocating beam flag is used, to define precise exposures of the sample to the molecular beam. The beam is finally collimated by a beam defining aperture before entering the main chamber.

2.2.2 Optimization of supersonic molecular beams of pentacene

The supersonic expansion from the nozzle is aligned with the aperture at the apex of the skimmer and with the beamline of the chamber by adjusting the x and y micrometers of the nozzle manipulator. Intensity of the supersonic beam entering the main chamber is monitored using a quadrupole mass spectrometer (QMS) that is placed on the beam axis. This intensity can be optimized for different beam energies by dealing with the following parameters:

1. the diameter of the nozzle
2. the nozzle skimmer distance
3. diameter of the aperture at the apex of the skimmer
4. the location of the skimmer
5. the geometry of the skimmer

The nozzle and skimmer diameters directly control the volume of the carrier gas – vapor mixture entering the source and antechamber respectively. If these dimensions are too large, beam to background is adversely affected and if too small, intensity is reduced. 150 μm nozzle apertures and 1.5 mm diameter skimmers have been utilized in this study in order to obtain the most intense beams while maintaining excellent beam to background ratios. The nozzle skimmer distance, the location and geometry of the skimmer all influence the interference between the supersonic expansion and the skimmer in the source chamber. This interference can arise in two ways:

1. Beam molecules can be scattered by molecules reflected from the exterior surface of the skimmer.

2. Beam molecules can also be scattered by collisions with the gas that builds up inside the skimmer through collisions with the interior surface of the skimmer.

In order to characterize the supersonic expansion, intensity and beam to background ratios of beams of CO₂ (a molecule with smaller cross-section) and pentacene, seeded in helium, were obtained for different carrier gas flow rates. Two types of skimmers, i.e. conical and trumpet shaped, and two skimmer positions, i.e. the forward and rear positions, were also used. Data are plotted in Figs. 2-7 to 2-14. From these plots, several important observations can be made. As expected, the intensity is always higher with the skimmer in the forward position compared to the rear position as the source is closer to the mass spectrometer in this case.

For a beam of CO₂ seeded in helium (Figs. 2-7 and 2-8), the intensity does not pass through a pronounced maximum when the skimmer is in the forward position. However, for the rear position, a maximum is observed with respect to flow for a nozzle-skimmer distance of 0.11-0.21". This is indicative of attenuation of the beam at higher flows by background gas either in the nozzle-skimmer region or in the antechamber. The maxima in the beam intensity vs. flow data shift to lower flows as the nozzle-skimmer distance is decreased. This indicates that attenuation is perhaps more significant in the antechamber than the nozzle-skimmer region. For both skimmer positions the optimal nozzle skimmer distance is ~ 0.3". Beam to background ratios are also close to maximum for 0.3" of separation (Fig. 2-9) and decrease with decreasing nozzle-skimmer distances. For this case, intensity increases with carrier gas flow and enters a plateau region. The onset of this plateau is

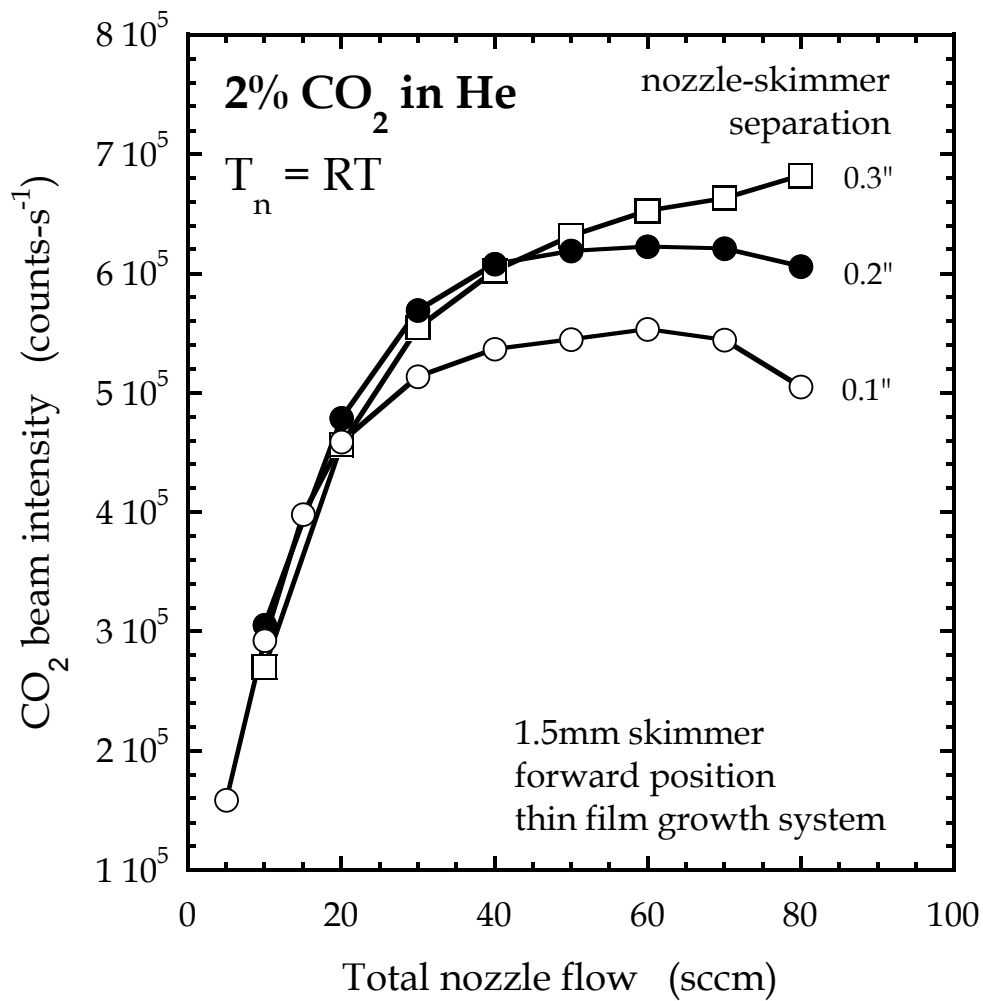


Figure 2-7 Beam intensity for CO₂ seeded in helium carrier gas as a function of carrier gas flow for the thin film deposition system. Conical skimmer is in the forward position.

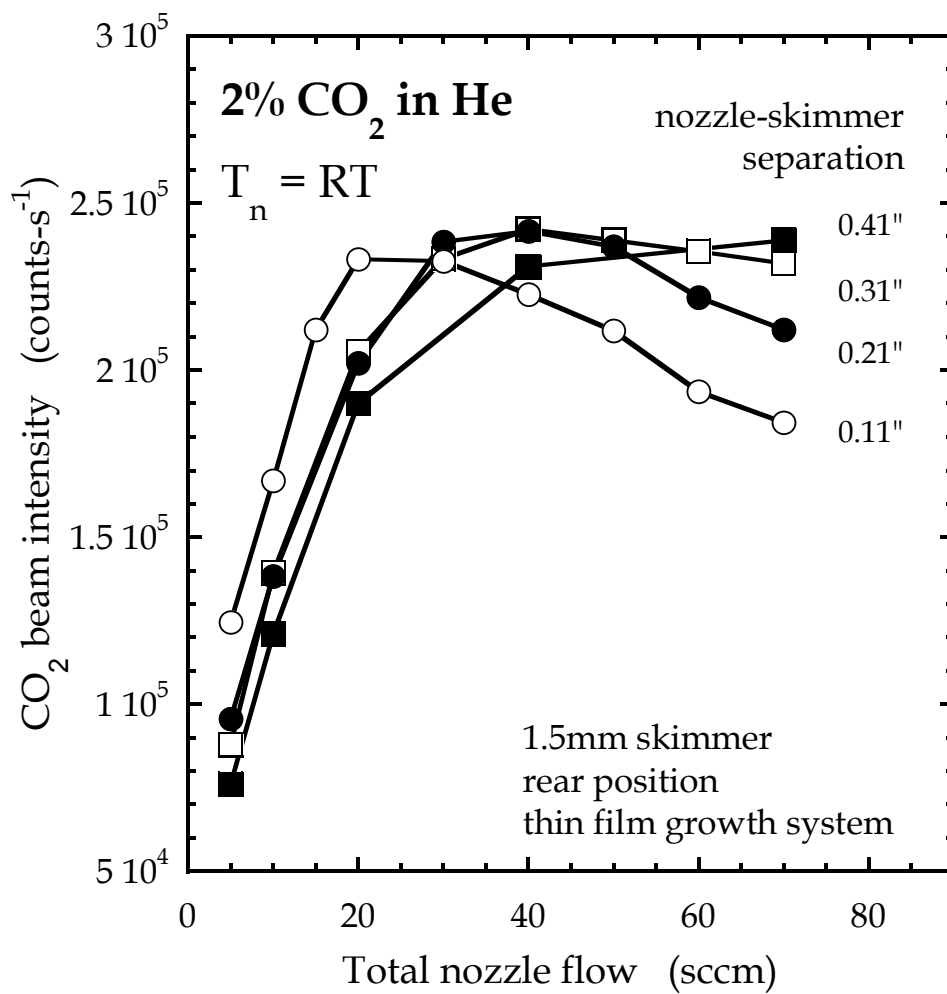


Figure 2-8 Beam intensity for CO₂ seeded in helium carrier gas as a function of carrier gas flow for the thin film deposition system. Conical skimmer is in the rear position.

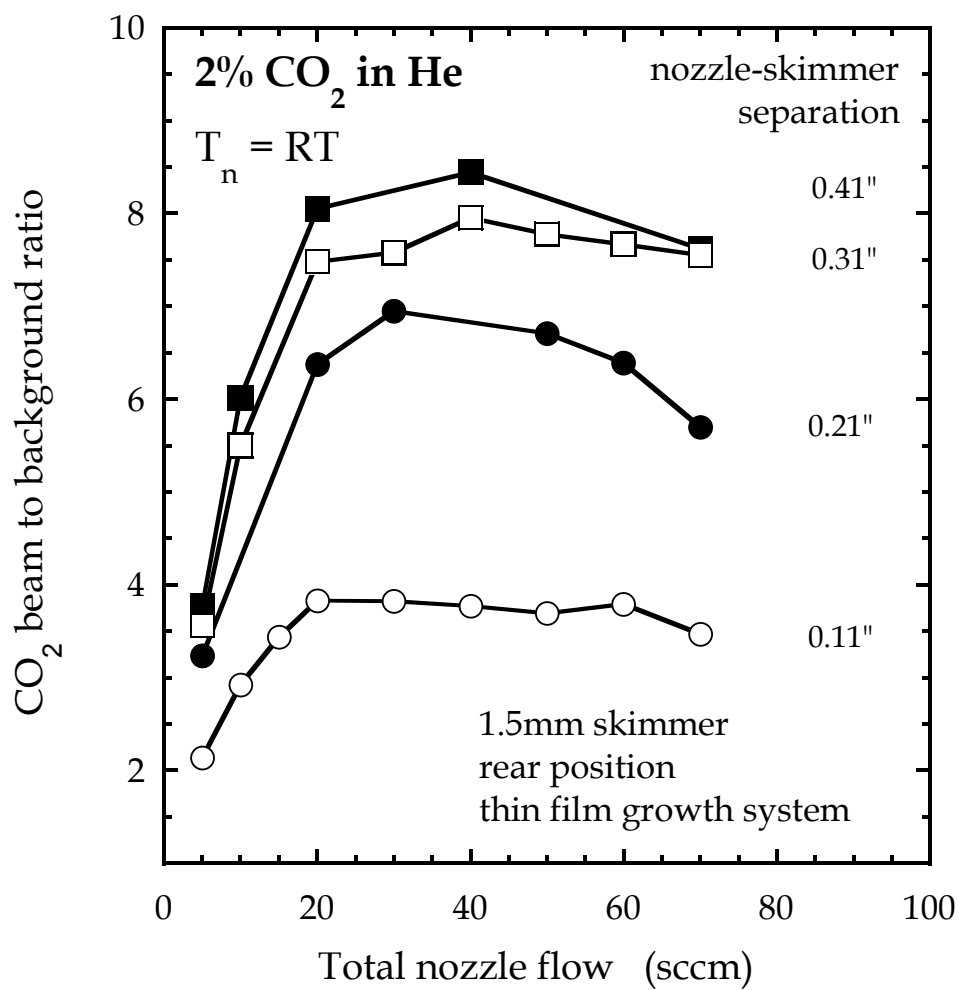


Figure 2-9 Beam to background ratio for CO₂ seeded in helium carrier gas as a function of carrier gas flow for the thin film deposition system. Conical skimmer is in the rear position.

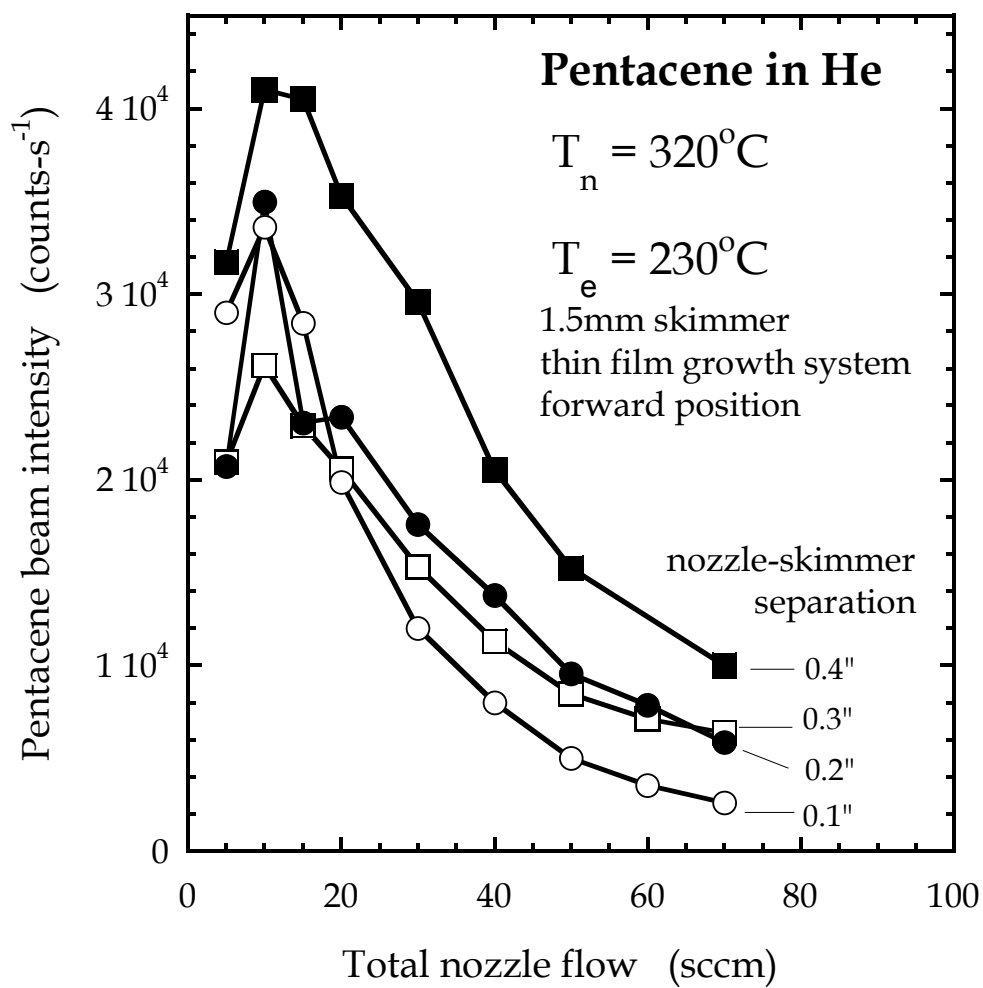


Figure 2-10 Beam intensity for pentacene seeded in helium carrier gas as a function of carrier gas flow for the thin film deposition system. Conical skimmer is in the forward position.

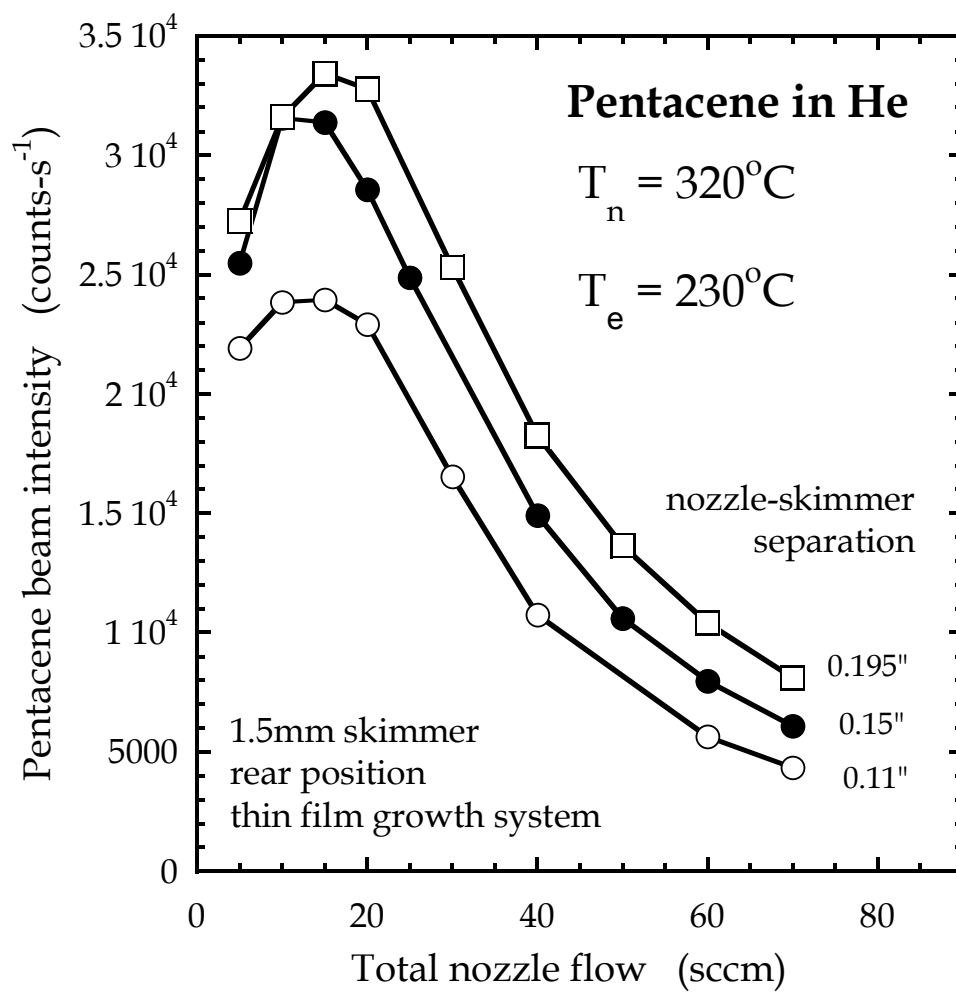


Figure 2–11 Beam intensity for pentacene seeded in helium carrier gas as a function of carrier gas flow for the thin film deposition system. Conical skimmer is in the rear position.

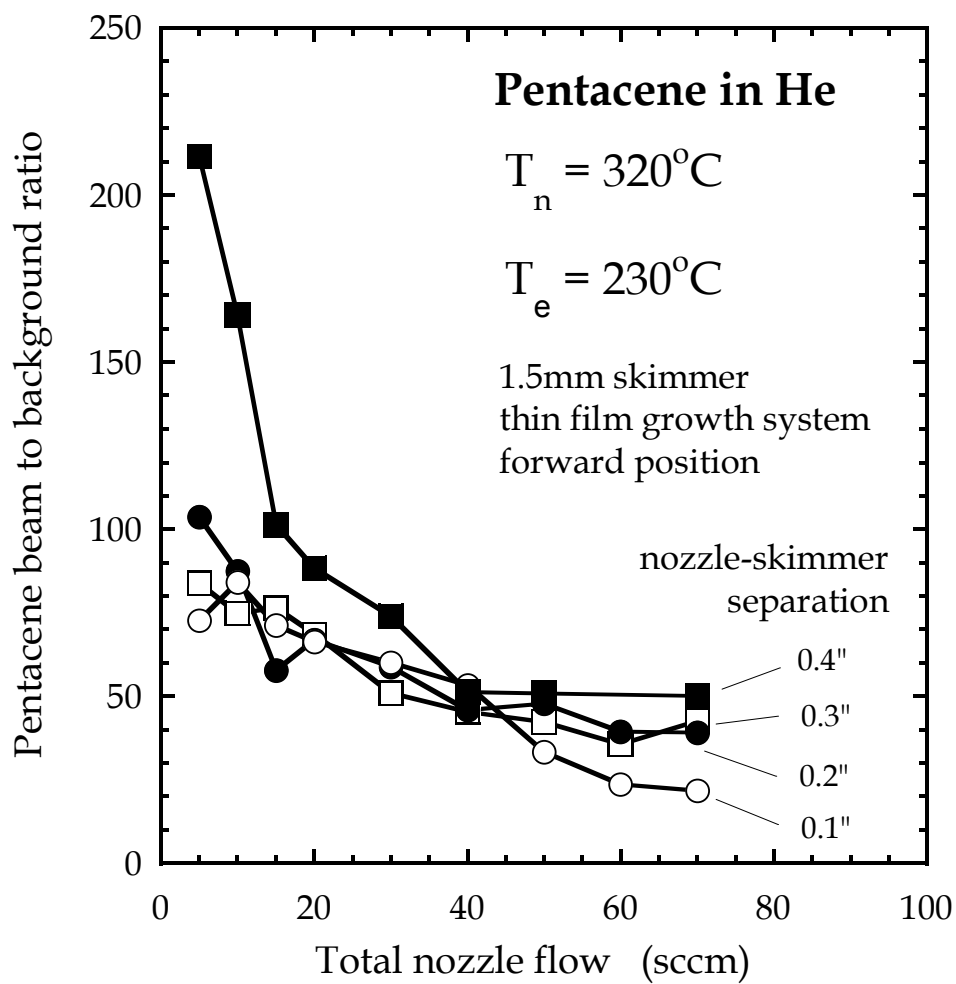


Figure 2–12 Beam to background ratio for pentacene seeded in helium carrier gas as a function of carrier gas flow for the thin film deposition system. Conical skimmer is in the forward position.

dependent on the position of the skimmer. When in the forward position, this plateau occurs at ~ 40 sccm of total flow. When in the rear position, however, this plateau shifts to lower flows and occurs at 30 sccm. Therefore, in the rear position, with a nozzle–skimmer distance of 0.3", intensity is constant for a larger range of carrier gas flows.

For the case of a pentacene beam seeded in helium (Figs. 2–10, 2–11, 2–12) beam intensity decreases when the nozzle–skimmer distance is reduced, for all flow rates and for both forward and rear skimmer positions, indicating attenuation of the beam either in the nozzle–skimmer region or in the antechamber. In addition, beam intensity passes through a far more pronounced maximum for both positions of the skimmer and for all nozzle–skimmer distances. These maxima do not shift appreciably when the nozzle–skimmer distance is reduced. With the skimmer in the forward position, the intensity reaches a maximum at ~ 10 sccm of total flow, and falls off rapidly with increasing flow. However, in the rear position, intensity stays close to the maximum value for a larger range of flows (10 – 25 sccm). Further, the drop off in intensity from the maximum is lower for the rear position compared to the forward position. This could be due to better pumping of the region between the nozzle and the skimmer as it is located directly above the turbomolecular pump in the source chamber. Therefore, the *rear position* would be the better choice for these experiments. An added advantage is that as the skimmer is located beyond the gate valve on the source chamber side, it could be closed to isolate this chamber. This proved to be very useful when the skimmer got coated with pentacene and had to be cleaned occasionally.

The next improvement to the intensity of the beam was made with

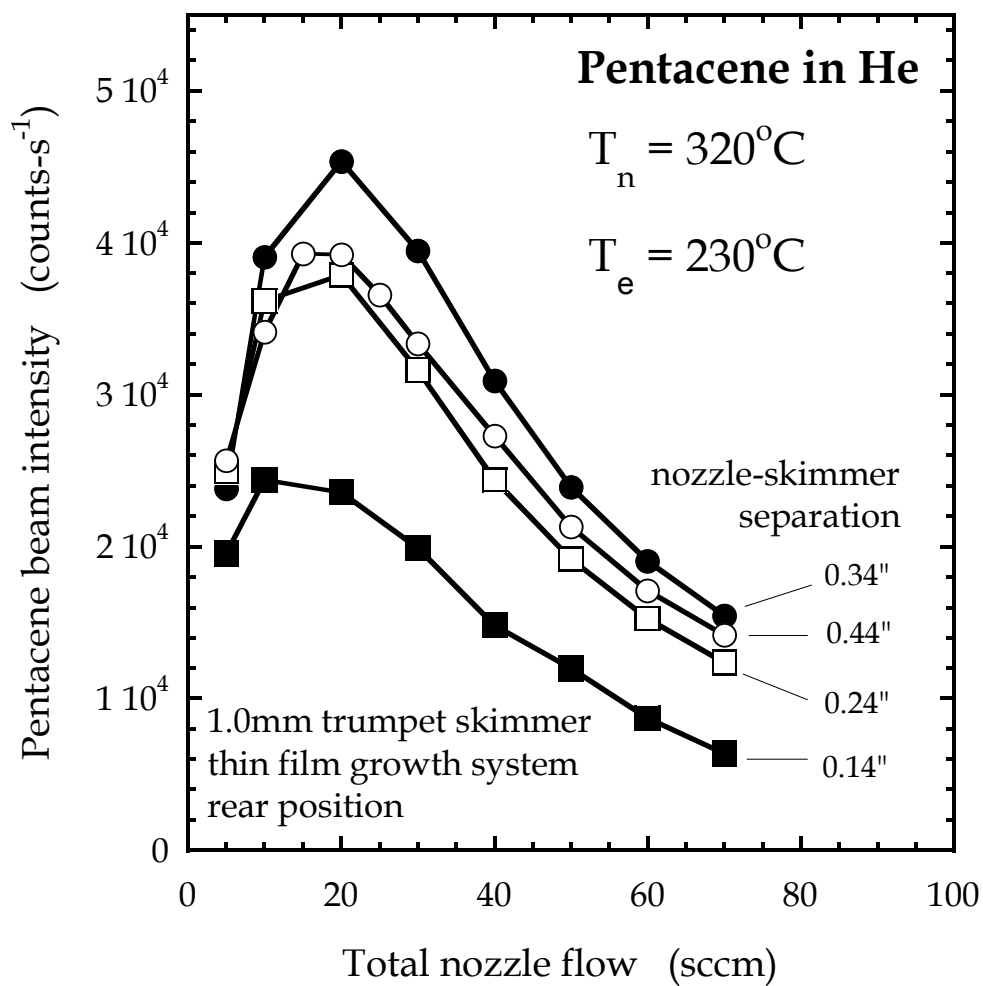


Figure 2–13 Beam intensity for pentacene seeded in helium carrier gas as a function of carrier gas flow for the thin film deposition system. Trumpet-shaped skimmer is in the rear position.

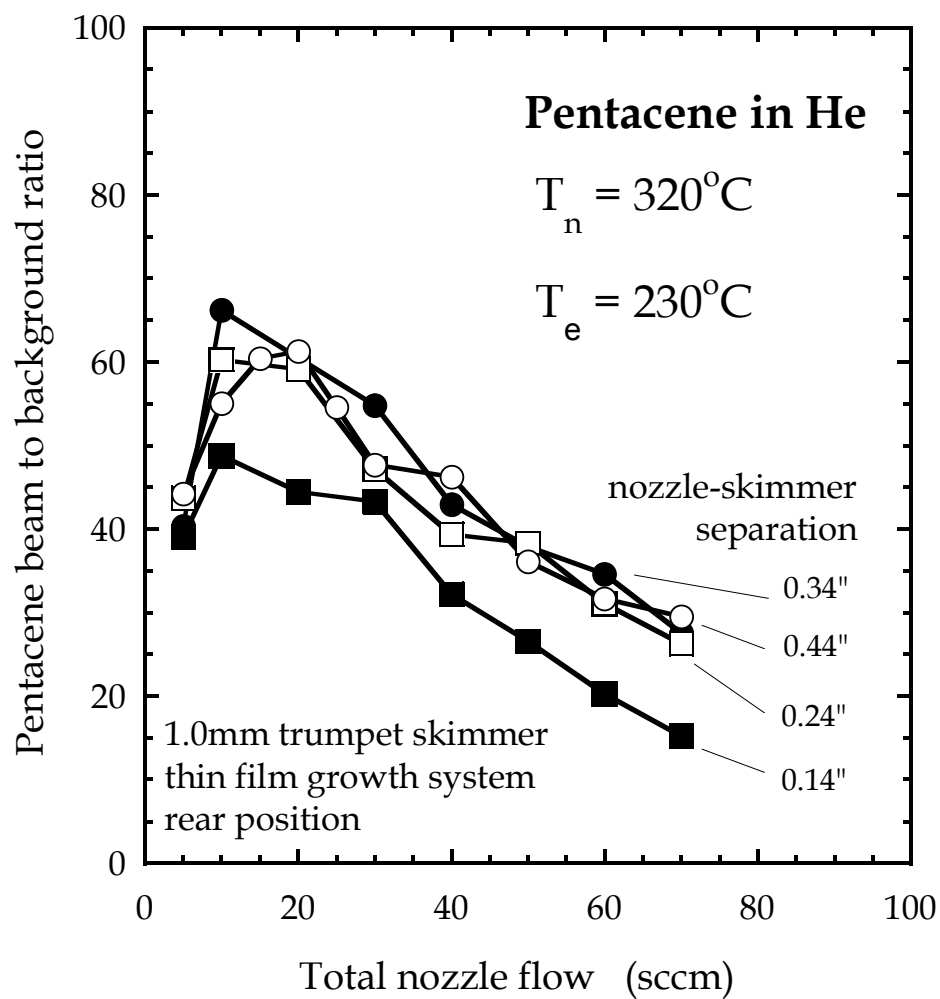


Figure 2-14 Beam to background ratio for pentacene seeded in helium carrier gas as a function of carrier gas flow for the thin film deposition system. Trumpet-shaped skimmer is in the rear position.

respect to the geometry of the skimmer. By utilizing a skimmer that is trumpet-shaped rather than conical, the small skimmer angle at the orifice can reduce interference from reflected molecules, while the flared shape having a larger angle at the base can also minimize excess gas buildup inside the skimmer. Shown in Figs. 2-13 and 2-14 are intensity and beam to background ratio for a pentacene beam seeded in helium as a function of carrier gas flow rate. A 1.0 mm *trumpet shaped skimmer* was used for these experiments. From Fig. 2-13, it is apparent that beam intensity increases for all flow rates when nozzle-skimmer distance decreases from 0.44" to 0.34". At lower nozzle-skimmer distances, beam intensity decreases for all flow rates and this is suggestive of interference between the nozzle and the skimmer or attenuation in the antechamber. For the range 0.14-0.34" of nozzle-skimmer distance, intensity goes through a reasonable maximum with increasing flow rate and again this maximum does not shift appreciably when the nozzle is moved closer to the skimmer. However, the drop off in intensity from the peak value is lower by $\sim 30\%$ compared to a 1.5 mm conical skimmer and is also more gradual. For nozzle-skimmer distances between 0.14-0.34", beam to background ratios (Fig. 2-14) are comparable to pentacene beams seeded in helium with the 1.5 mm conical skimmer in the forward position (Fig. 2-12). In other words, this ratio is not affected by the choice of skimmer.

From all the above experiments, the primary conclusions are that a nozzle-skimmer distance of ~ 0.34 ", a trumpet shaped skimmer and the rear position yield the best results for a supersonic molecular beam of pentacene. Hence, this was the chosen configuration for all thin film deposition experiments. The skimmer size used was 1.5 mm. This size did not provide any significant improvements over the 1.0 mm skimmer.

2.2.3 Sample preparation and handling

Substrates were Si (100) wafers (Wacker–Siltronic, p–type, 4" dia., 500–550 μm thick, 38–63 $\Omega\text{-cm}$) subject to a RCA–1 clean, 15 s. HF dip and a RCA–2 clean immediately before growth of SiO_2 . The approximately 300 nm thick SiO_2 films were grown by wet thermal oxidation at 1100 $^\circ\text{C}$ – growth time was 19 min. The thermal oxide furnace was used at the Cornell Nanoscale Science and Technology Facility (CNF). Whole 4" wafers were used for experiments studying thin film nucleation and deposition. Highly doped n or p–type wafers were subjected to the above processing steps and cut into squares of size 16.75 mm \times 16.75 mm for use as substrates for depositing films used to make thin film transistors.

2.2.3.1 Thermal oxide clean

Immediately prior to placement into the load–lock of the vacuum chamber, these wafers were placed in anhydrous CHCl_3 solution (99%+) and wiped clean with a swab. The objective was to remove macroscopic particles and organic matter. Next, the wafers were sonicated in CHCl_3 solution for 15 min. They were allowed to air dry and then sonicated in H_2O for another 15 min. Next, they were washed with copious amounts of deionized water and dried with nitrogen. Finally, they were subject to a ultraviolet light–ozone clean (UV–Ozone) for 10 min. to remove any remaining organic residues. Within 15 min. of the UV–Ozone clean, samples were placed in the load–lock of the thin film deposition chamber.

2.2.3.2 Hexamethyldisilazane (HMDS) coating

After the UV–Ozone clean, samples were placed in the YES LP–III vapor priming oven at the CNF. HMDS was deposited from the vapor phase after several successive evacuation and purge cycles used to dehydrate the substrate held at 150 °C. Deposition time was 5 min. and the vapor pressure was 6 torr. The entire process lasted 25 min. Samples removed from the oven were placed in the load–lock of the thin film deposition system within 15 min.

2.2.4 Thin film deposition procedures

Pentacene (99.8%, Sigma–Aldrich Corp.) was heated to temperatures between 240 and 300 °C in the custom designed *in situ* evaporator to obtain the desired vapor pressure and entrained in carrier gases of He and N₂ (99.999% pure from Air Gas Inc.). Flow of carrier gases, F_{cg} , was controlled using an MKS flowmeter upstream of the inlet to the in–vacuum bubbler. The nozzle, downstream of the bubbler, consisted of 0.25" dia. stainless steel tubing, and a 125 μm thick end plate with a 150 μm orifice and was heated to $T_n = 450$ °C during these experiments to prevent condensation of pentacene in the lines downstream of the bubbler. Evaporator temperature, T_e , was varied to maintain a constant flux of pentacene in doubly differentially pumped beams of different energies – energies obtained were 1.5 eV (determined from time of flight measurements [16]) by seeding pentacene in 10 sccm N₂, and 2.7 eV, 4.5 eV and 6.7 eV by seeding in 10, 25 and 70 sccm of He respectively. Pentacene molecular beams were skimmed using a trumpet shaped skimmer (1.5 mm

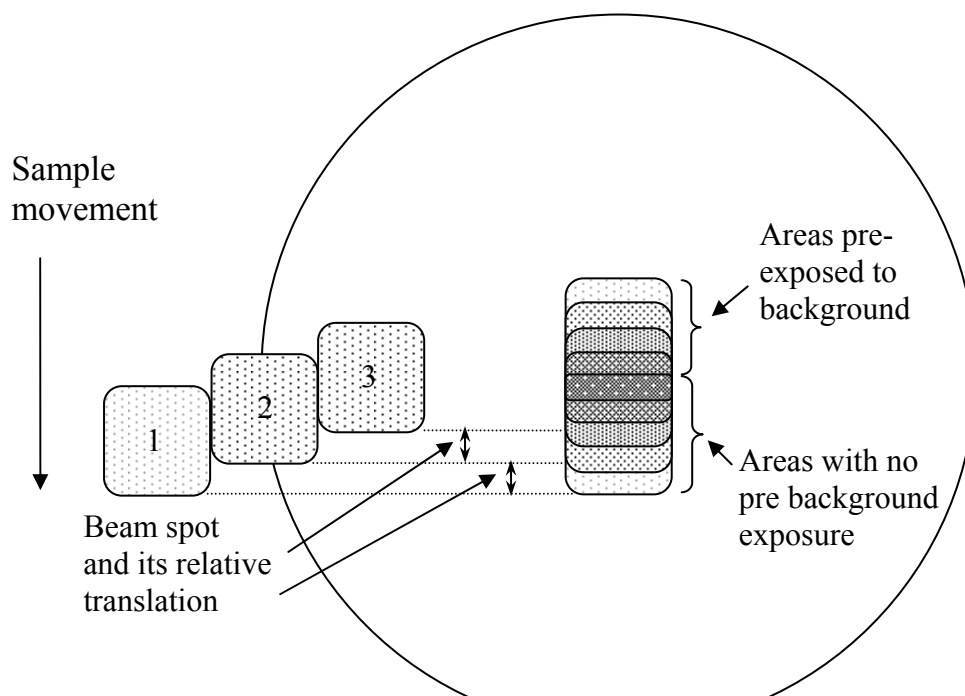


Figure 2–15 Schematic representation of the multiple exposure technique employed during thin film nucleation and growth. The figure shows a 2–step, three–spot experiment which produces 5 distinct exposures to precursor gases in the molecular beam.

aperture), could be shuttered and then passed through a beam defining aperture producing a well collimated 0.45" square beam spot on the substrate at normal incidence. During a typical experiment, the nozzle and bubbler were heated maintaining a temperature difference of $\sim 150 - 200$ °C with a low carrier gas flow rate of 10 sccm. The 1/8" tube between the evaporator and nozzle was heated to within 50 – 100 °C of nozzle temperature. The sample was cleaned and transferred to the precision sample manipulator, located in the analysis chamber, prior to liquid nitrogen cooling of the ante-chamber and the cryoshroud on the quadrupole mass spectrometer (QMS) located downstream and line of sight along the beam axis. Once the bubbler reached the desired temperature, the beam was monitored with the mass spectrometer to ensure that the desired flux was obtained and was stable. The sample was then translated into the beam after opening a gate valve to the analysis chamber and maintained at room temperature $T_s = 21 \pm 3^\circ$.

A technique that exploits the well collimated nature of the molecular beam has been employed for thin film deposition. During exposure to pentacene, the sample is translated perpendicular to the beam axis. This translation is a fraction of the dimension of the beam spot on the sample (usually the total dimension divided by the number of time intervals). As a result, a number of different spots on the substrate called "terraces" are produced, representing different exposure times while still maintaining the same deposition conditions (T_n, T_e, T_s, F_{cg}). Shown in Fig. 2–15 is a schematic representation of this deposition technique where overall exposure time of the sample to the beam is minimized. At most, two deposition runs were carried out on a given 4" wafer to produce different sets of terraces – the background contribution to the deposited films was negligible (evidenced from atomic force

microscopy (AFM) images of unexposed regions of the substrate). For the smaller square samples, two films were deposited on adjacent samples to provide sufficient statistics for thin film transistor devices fabricated from these films with different channel lengths. The effect of incident kinetic energy and angle of incidence on film nucleation and growth was studied. It is important to note that the mass spectrometer is a density detector and the flux determined was velocity corrected and maintained constant for all energies and angles of incidence.

2.2.5 *Ex situ* analysis techniques

2.2.5.1 Ellipsometry

The thickness of underlying thermal silicon dioxide was determined using a Rudolph AutoEL – IV ellipsometer at the CNF. The refractive index was fixed at 1.462 for these films. Next, the thickness of the pentacene film was determined using a two layer model. Inputs to this model included the thickness of underlying oxide, a refractive index of 1.46 for that film and a refractive index of 1.43 for the pentacene film [17]. The estimated error in these measurements is $\pm 1 \text{ \AA}$.

2.2.5.2 Atomic Force Microscopy (AFM)

Following thin film deposition and removal of the substrate from the chamber, the samples were examined *ex situ* using a Digital Instruments Dimension 3100 scanning probe microscope (Veeco Instruments) in tapping

mode. Typical images obtained were of size $20 \times 20 \mu\text{m}^2$ and subjected to a second order plane fit using Nanoscope software (v 5.0).

Spatial resolution of the roughness and correlations between roughness and specific surface features is provided by power spectral density (PSD) analysis. This is accomplished by calculating the square magnitude of the coefficients of the Fourier transform of a digitized surface profile. When carried out in one dimension, the transformed data are referred to as one dimensional PSD spectra (1DPSD). For a surface profile line scan, the 1DPSD at a given frequency (f) is given by:

$$PSD(f) = \frac{1}{L} \left| \int_0^L dx h(x) e^{i2\pi fx} \right|^2 \quad (2-2)$$

in units of nanometers cubed, where L is the scan length and $h(x)$ is the line profile in the fast scan direction x .

1DPSD analysis can be used to characterize the roughness and surface structure and also to obtain scaling exponents [18–20]. Since, a 1DPSD spectrum provides the variation of PSD power (magnitude) as a function of spatial frequency (or inversely, lateral length scale), the analysis provides the correlation between roughness and the length and spacing of specific surface features. For example, a flat 1DPSD region (zero slope) indicates a range of frequency independent roughness, whereas a region of finite constant slope indicates self-affine roughness scaling. Such a structure exhibits a power-law decay $PSD(f) = K_0 f^{-\gamma}$ over a finite range of frequencies. The roughness scaling exponent α is related to γ in this case by $\alpha = (\gamma-d)/2$ where the line scan dimension d equals 1 in this case. All AFM images obtained were of size $20 \mu\text{m} \times 20 \mu\text{m}$ and subjected to a second order plane fit using Nanoscope

software (v.5.0). One dimensional PSDs were calculated using the same software along the fast scan direction and single line PSDs were averaged. For each scan length L , spatial frequencies range between $1/L$ and the Nyquist frequency $256/L$. The growth exponent β was determined by plotting film root mean square (RMS) roughness R obtained from AFM images using Nanoscope software (v 5.0), as a function of thickness t . Data were fit to a power law yielding this exponent.

2.2.6 Organic thin film transistors

Samples were heavily doped p-type and n-type silicon wafers of size $16.75 \text{ mm} \times 16.75 \text{ mm}$. 3100 \AA of silicon dioxide was grown by wet thermal oxidation at $1100 \text{ }^\circ\text{C}$. Samples were then subject to cleaning procedures described above involving sonication in chloroform and water followed by UV-Ozone treatment immediately prior to deposition of 400 \AA thick pentacene films. These films were deposited at four different incident kinetic energies: 1.5, 2.7, 4.5 and 6.7 eV. Top drain and source gold contacts 250 \AA thick were thermally sublimed at a rate of 4 \AA-s^{-1} using a shadow mask to define between 9 to 12 transistors in each sample, 3 per row having a channel length of 31.25, 75 and $125 \text{ }\mu\text{m}$ respectively. Electrical characterization was carried out in a four-point probe station under vacuum (10^{-6} torr) at room temperature. The field-effect mobility, μ_{FE} was extracted from the saturation regime [21] according to

$$I_{D,sat} = \frac{W}{L} \frac{\epsilon_i}{d_{ox}} \mu_{FE} V_{DS} (V_G - V_t)^2 \quad (2-3)$$

where I_{DS} is the drain-to-source current; W/L is the channel width to length ratio; d_{ox} is the thickness of the gate dielectric with dielectric constant ϵ_i ; V_{DS} is the drain-to-source voltage; V_G is the gate voltage; V_t is the threshold voltage and $I_{D,sat}$ is the drain-to-source current in the saturation regime.

2.2.7 Variable substrate temperature experiments

2.2.7.1 Thin film deposition system (G-Line system)

Thin film deposition experiments at a variety of substrate temperatures were also carried out in the newest system designed for experiments at G-Line, at the Cornell High Energy Synchrotron Source (CHESS) (c.f. Figs. 2-16 and 2-17). This system has been described in detail elsewhere [16]. The deposition chamber (volume ≈ 18 L) is pumped by a 500 L-s^{-1} compound turbomolecular-drag pump (Pfeiffer TMU 521P) and routinely achieves base pressures below 5×10^{-10} Torr after a 24 hour bakeout at 140°C . A sample manipulator accommodates samples up to approximately $1" \times 1"$ in size and is positioned vertically (from the bottom of the chamber) such that the surface of the sample is precisely at the main focal point of the chamber. Opposed to the sample are two rectangular Be windows. The first is positioned horizontally to allow synchrotron x-rays to enter the chamber from varying angles with respect to the surface of the sample. After scattering from the sample, the x-rays pass through the second vertically positioned Be window before being detected by a scintillating type x-ray detector mounted on a Huber stage. A third Be window may be mounted on a $3\text{-}3/8"$ CF flange in the horizontal plane defined by the

Side View

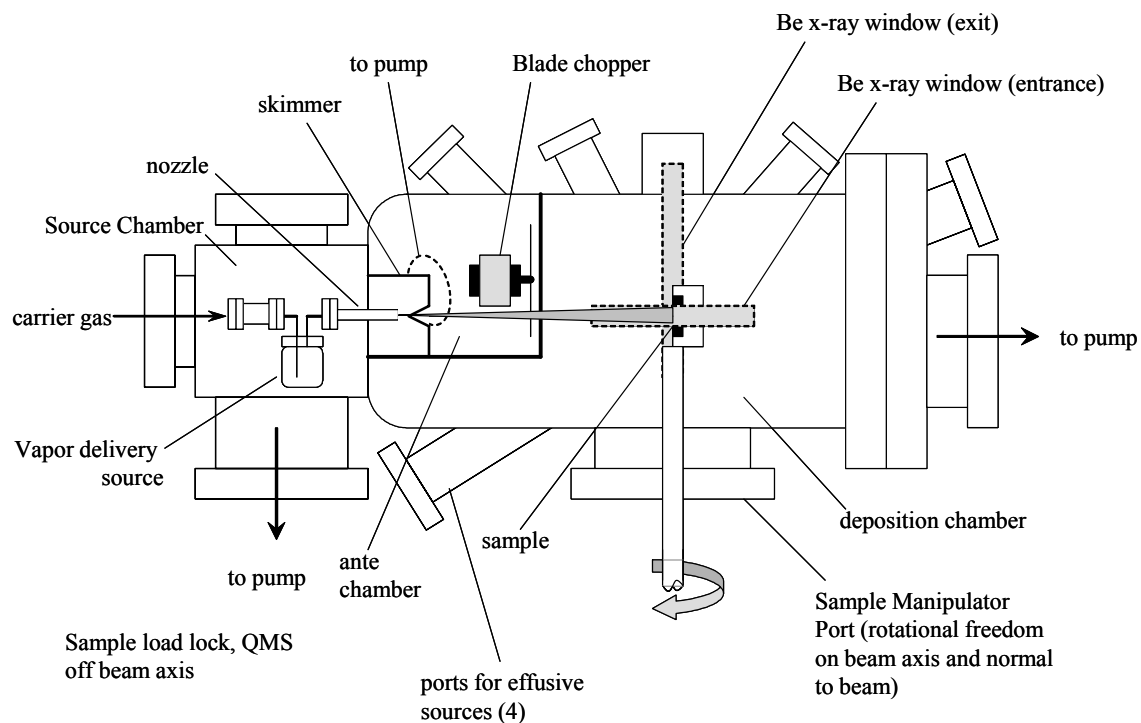


Figure 2–16 Side view schematic drawing of the gas source deposition system (G-Line system).

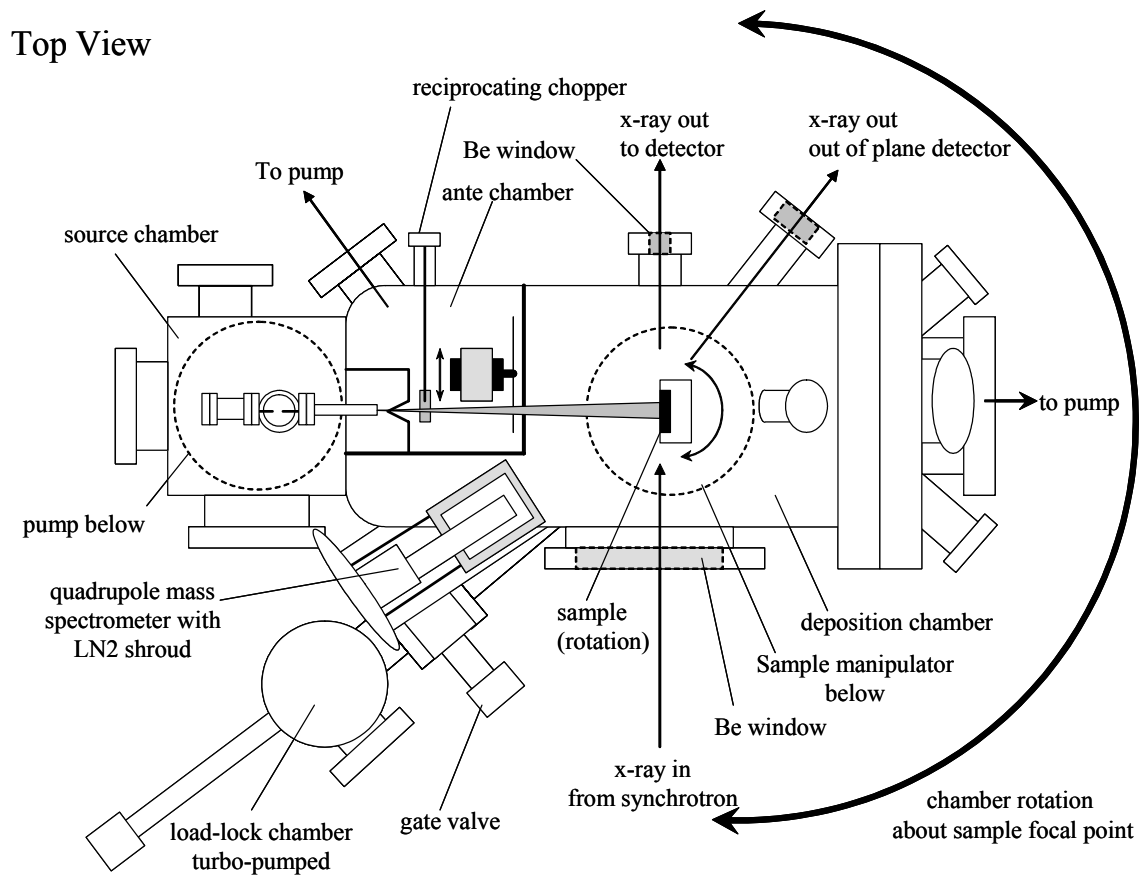


Figure 2–17 Top view schematic drawing of the gas source deposition system (G–Line system).

entering x-rays as shown in Fig. 2-17. The system is mounted on an optical table allowing for the precise manipulation (x, y, z rotation) of the UHV chamber with respect to the entering x-rays. Further rotational manipulation of the sample in the plane defined by the entering x-rays, as well as about the surface normal, allows a number of x-ray scans and real-time experiments to be performed. Monitoring the intensity of scattered x-rays during film growth from a position of grazing incidence while at the so-called anti-Bragg position allows a determination of thin film growth modes and film quality. Following the deposition of thin films, in plane x-ray diffraction scans (using the vertically opposed Be window) allow for the determination of crystal texture, while out of plane scans (using the third Be window) allows for further determination of crystal structure and quality.

A quadrupole mass spectrometer (Extrel EX-800) with cryoshroud (described in section 2.2.1) may be mounted within the deposition chamber in a number of positions. During experiments where the molecular beam is scattered from the sample surface and a direct measurement is desired, the QMS is mounted facing the sample at an angle of 55° from the supersonic molecular beam which is described below. During the characterization of molecular beams using time of flight (TOF) methods, the sample manipulator is removed from the system and the QMS is mounted on a linear translation stage in a so called direct beam position, such that the molecular beam is in-line with the axis of the mass spectrometer. The QMS may also be mounted on flanges that allow the ionizer to be placed in a cross-molecular-beam position (manipulator removed) or a non-line-of-sight position to allow for indirect scattering experiments such as measurements of probabilities of adsorption. The sample manipulator (custom, Thermionics NW Inc.) is capable of two

rotational degrees of freedom (Θ , azimuthal), as outlined above, and employs an ion pumped (2 L-s^{-1}) differentially sealed rotary platform. The sample dock is fitted with a radiant graphite heater, which is encapsulated in pyrolytic BN, and is capable of continuously heating Si samples to temperatures in excess of $1000 \text{ }^\circ\text{C}$. Further, indirect cooling to approximately 170 K is provided by contact, through copper braids to a liquid nitrogen cooled reservoir. Samples are mounted on a Mo platen with a thin backing plate to maximize heat transfer from the radiant heater. A transferable thermocouple is attached to the platen and enables direct measurement of sample temperature. A second thermocouple is located at the back of the manipulator and is used as the reference standard for temperature calibration. Samples can be transferred to and from a load-lock chamber using an STLC (Thermionics) transfer system. The load-lock chamber is pumped by a 60 L-s^{-1} turbomolecular-drag pump (Pfeiffer TMU 071 P) and achieves pressures below 5×10^{-8} Torr after a few hours of pumping.

Supersonic molecular beams of organic materials can be generated in the source chamber using the evaporator/nozzle assembly described in section 2.2.1. A heatable skimmer mounted on a macor base plate has been designed and constructed and is described in detail in the Appendix (section 9.2). The molecular beam then passes into an antechamber which is pumped by a 70 L-s^{-1} turbomolecular drag pump (Pfeiffer, TMU 071 P) and a liquid nitrogen reservoir. A reciprocating beam flag is used to define exposures of a sample to the molecular beam, in order to begin and end thin film depositions precisely. A rotating blade chopper can also be employed to produce fast molecular beam waveforms (timescales $< 1\text{ms}$), which are used for example, in coordination

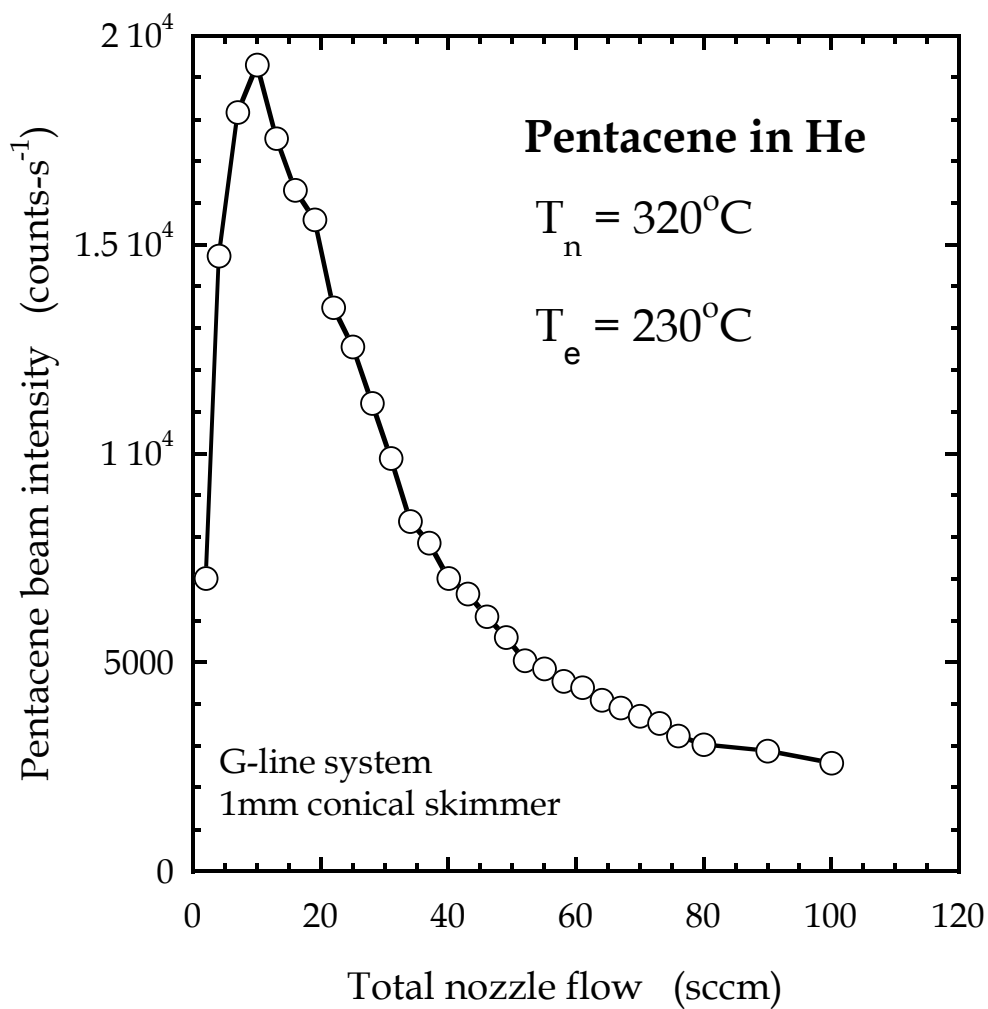


Figure 2–18 Intensity for pentacene seeded in helium carrier gas as a function of carrier gas flow for the G–Line system. Conical 1 mm skimmer was used in the forward position.

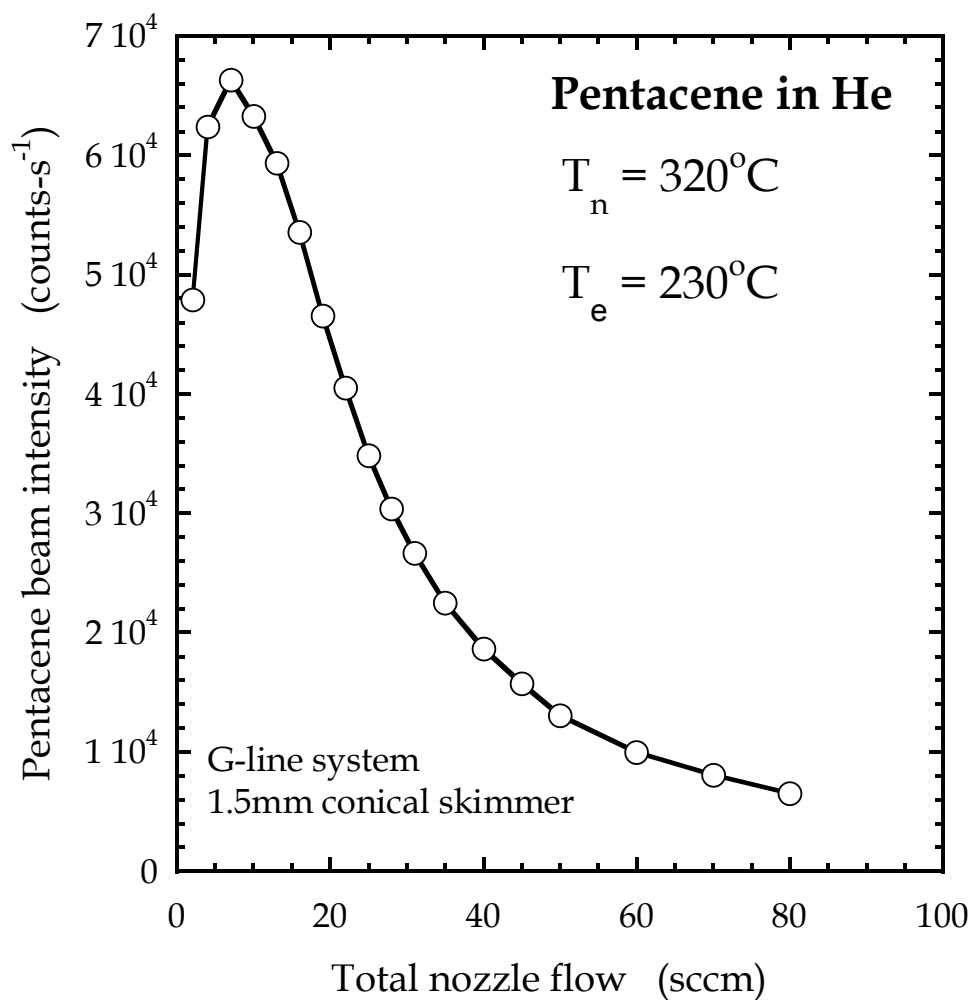


Figure 2–19 Intensity for pentacene seeded in helium carrier gas as a function of carrier gas flow for the G–Line system. Conical 1.5 mm skimmer was used in the forward position.

with a quadrupole mass spectrometer and a multi-channel scalar data acquisition card (ORTEC MCS-pci) during the characterization of molecular beams using time of flight (TOF) measurements or in modulated molecular beam reactive scattering experiments (MMBRS). The blade chopper is mounted on a linear translation stage such that it can be translated out of the beam flight path in order to allow for both slow and fast experiments to be performed without altering the apparatus. The total distance from the nozzle to the substrate is approximately 20.5 cm with the distance traveled by molecules within the antechamber being 8.9 cm. The blade of the fast chopper is 9.3 cm from the surface of the sample.

2.2.7.2 Beam characterization and optimization

Supersonic beams of pentacene were generated using the evaporator/nozzle assembly described in section 2.2.1. Intensity of pentacene beams as a function of carrier gas flow rate, for two skimmer sizes (1 mm and 1.5 mm), is plotted in Figs. 2-18 and 2-19. Intensity peaks at a flow rate of 10 sccm for the 1mm skimmer and 6 sccm for the 1.5 mm skimmer. This seems to indicate that beam intensity might be somewhat affected in the antechamber in spite of using a liquid nitrogen cooled reservoir. Further, there is significant attenuation of beam intensity with increasing flow rate. The approach chosen for these experiments was to increase the temperature of the evaporator to overcome a decrease in beam flux for higher carrier gas flow rates. As the skimmer is in the forward position and the nozzle is much closer to the sample in comparison to the thin film deposition system, evaporator

temperatures were still lower than experiments carried out on that system (195 – 220 °C).

2.2.7.3 Thin film deposition procedures

Thin films of pentacene were deposited using experimental procedures similar to those detailed in section 2.2.4. The sample was cooled with liquid nitrogen to a temperature of -70 °C, and then was heated to the desired temperature. Calibration data for control of the temperature of the sample are provided in the Appendix (Fig. 9–2).

2.3 References

1. L. -Q. Xia, M. E. Jones, N. Maity and J. R. Engstrom, *J. Vac. Sci. Technol. A* **13**, 2651 (1995).
2. A. Liebmann-Vinson, L. M. Lander, M. D. Foster, W. J. Brittain, E. A. Vogler, C. F. Majkrzak, and S. Satija, *Langmuir* **12**, 2256 (1996).
3. S. R. Wasserman, Y. -T. Tao, and G. M. Whitesides, *Langmuir* **5**, 1074 (1989).
4. M. M. Sung, G. J. Kluth and R. Maboudian, *J. Vac. Sci. Technol. A* **17**, 540 (1999).
5. J. B. Brzoska, I. B. Azouz and F. Rondelez, *Langmuir* **10**, 4367 (1994).
6. G. J. Kluth, M. M. Sung and R. Maboudian, *Langmuir* **13**, 3775 (1997).
7. N. Balachander and C. N. Sukenik, *Langmuir* **6**, 1621(1990).
8. *Handbook of Optical Constants of Solids*; edited by E. D. Palik (Academic Press: New York, 1985).
9. E. Frydman, H. Cohen, R. Maoz and J. Sagiv, *Langmuir* **13**, 5089 (1997).
10. D. A. Shirley, *Phys. Rev. B* **5**, 4709 (1972).
11. *Practical Surface Analysis: Volume I, Auger and X-ray Photoelectron Spectroscopy, 2nd ed.*, edited by M. P. Seah and D. Briggs (John Wiley and Sons, Chichester, England, 1990).
12. J. M. Conny and C. J. Powell, *Surf. Interface Anal.* **29**, 856 (2000).
13. C. T. Campbell and S. M. Valone, *J. Vac. Sci. Technol. A* **3**, 408 (1985).
14. M. Calistri-Yeh, E. J. Kramer, R. Sharma, W. Zhao, M. H. Rafailovich, J. Sokolov, and J. D. Brock, *Langmuir* **12**, 2747 (1996).
15. S. E. Roadman, N. Maity, J. N. Carter and J. R. Engstrom, *J. Vac. Sci. Technol. A* **16**, 3423 (1998).

16. T. W. Schroeder, Ph.D thesis, Cornell University, 2004.
17. S. P. Park, S. S. Kim, J. H. Kim, C. N. Whang and S. Im, *Appl. Phys. Lett.* **80**, 2872 (2002).
18. P. Dumas, B. Bouffakhreddine, C. Amra, O. Vatel, E. Andre, R. Galindo and F. Salvan, *Europhys. Lett.* **22**, 717 (1993).
19. G. W. Collins, S A. Letts, E. M. Fearon, R. L. McEachern and T. P. Bernat, *Phys. Rev. Lett.* **73**, 708 (1994).
20. C. Douketis, Z. Wang, T. L. Haslett and M. Moskovits, *Phys. Rev. B* **51**, 11022 (1995).
21. R. Ruiz, A. Papadimitratos, A. C. Mayer and G. G. Malliaras, *Adv. Mater.* **17**, 1795 (2005).

3. The reaction of Tetrakis(dimethylamido)titanium with self-assembled alkyl-trichlorosilane monolayers possessing –OH, –NH₂ and –CH₃ terminal groups*

3.1 Overview

The reactions of tetrakis(dimethylamido)titanium, $\text{Ti}[\text{N}(\text{CH}_3)_2]_4$, with alkyltrichlorosilane self-assembled monolayers (SAMs) terminated by –OH, –NH₂ and –CH₃ groups have been investigated with X-ray photoelectron spectroscopy (XPS). For comparison, a chemically oxidized Si surface, which serves as the starting point for formation of the SAMs, has also been investigated. In this work the kinetics of adsorption, the spatial extent and stoichiometry of the reaction were examined. Chemically oxidized Si has been found to be the most reactive surface examined here, followed by the –OH, –NH₂ and –CH₃ terminated SAMs, in that order. On all surfaces the reaction of $\text{Ti}[\text{N}(\text{CH}_3)_2]_4$ was relatively facile, as evidenced by a rather weak dependence of the initial reaction probability on substrate temperature ($T_s = -50$ to 110 °C), and adsorption could be described by first-order Langmuirian kinetics. The use of angle-resolved XPS demonstrated clearly that the anomalous reactivity of the –CH₃ terminated SAM could be attributed to reaction of $\text{Ti}[\text{N}(\text{CH}_3)_2]_4$ at the SAM/SiO₂ interface. Reaction on the –NH₂ terminated SAM proved to be the “cleanest,” where essentially all of the reactivity could be associated with the terminal amine group. In this case, approximately one $\text{Ti}[\text{N}(\text{CH}_3)_2]_4$ was

* *J. Am. Chem. Soc.* **127**, 6300 (2005)

adsorbed per two SAM molecules. On all surfaces there was significant loss of the N(CH₃)₂ ligand, particularly at high substrate temperatures, T_s = 110 °C. These results show for the first time that it is possible to attach a transition metal coordination complex from the vapor phase to a surface with an appropriately functionalized self-assembled monolayer.

3.2 Introduction

Inorganic–organic interfaces, owing to their unique chemical and electronic properties, are playing an increasingly important role in several technologies including organic light emitting diodes (OLEDs) [1,2] molecular electronics [3–6] and microelectronic interconnect technology: e.g., interfaces between carbon–based low- κ dielectrics and metallic/inorganic diffusion barriers [7–9]. Despite their importance, formation of these interfaces is not fully understood. Self-assembly is a popular method for making highly ordered (over nm length scales) organic monolayer films on metallic and semiconductor substrates [10–12]. These self-assembled “organic–on–inorganic” monolayers (SAMs) have been widely studied as model surfaces owing to their ease of formation, self-limiting growth characteristics and the specificity of their reaction enabling the tailoring of surface properties by varying the functional end group. “Inorganic–on–organic” interfaces are also important in applications such as barrier layers (e.g., encapsulation of the aforementioned metallic interconnects), reflective coatings, and electrical contacts for both OLEDs and molecular electronics. Formation of these interfaces, however, is much less mature in comparison to “organic–on–inorganic” interfaces

constructed using SAMs. To date, the inorganic component of the interface has been a metal or an oxide formed by (elemental) evaporation in vacuum, or by deposition in the liquid phase using a metal complex.

Formation of thin films on SAMs by liquid phase deposition has attracted recent interest. The reactions of TiCl_4 [13,15,17], $\text{Ti}(\text{OCH}(\text{CH}_3)_2)_4$ [14], aqueous titanium peroxide solutions [16], $\text{Ti}(\text{OC}_2\text{H}_5)_2\text{Cl}_2$ [17] and $\text{Ti}(\text{OC}_2\text{H}_5)_4$ [17] with alkyltrichlorosilane SAMs bearing sulfonate [13,15,16], hydroxyl [14,16] amine [16] and methyl [17] groups, phenyltrichlorosilane [17] and aminopropyltriethoxysilane [17] SAMs have been investigated. X-ray photoelectron spectroscopy (XPS) has been used to probe elemental composition [14,15,16,17] and film morphology [13] has been studied. Vapor phase evaporative deposition of elemental metals on functionalized SAMs has also been studied. Jung and Czanderna [18–20] examined the evaporation of elemental metals onto SAMs with different organic functional end groups (OFGs) and categorized metal/OFG interactions to be “strong” (e.g., Cr/COOH or Cu/COOH where metals react primarily with the OFG) or “weak” (e.g., Cu/OH, Cu/CN, Ag/CH₃ or Ag/COOH where metals penetrate the SAM). Using *in situ* XPS analysis, Allara and co-workers [21] found elemental titanium to be highly reactive with the –OH, –CN, and –COOCH₃ terminated alkanethiol SAMs, forming TiO_x and TiN_x species at low coverages and TiC_x species at high coverages, possibly due to reaction with the SAM backbone. Allara and co-workers [22,24] also studied the reaction of elemental aluminum with –CH₃, –COOCH₃ and –COOH [23] terminated alkanethiol self-assembled monolayers on polycrystalline gold. While significant penetration of Al to the SAM/Au interface was observed for the –CH₃ terminated SAM, reaction of Al

with the $-\text{COOCH}_3$ and $-\text{COOH}$ terminated SAMs was confined to the SAM/vacuum interface. The deposition of thin inorganic films on SAMs using organometallic precursors has received relatively less attention despite the fact that such a process might provide superior control over interface formation. Of the few studies that have been conducted, spatial selectivity and thin film morphology were examined during the formation of Au and Pd films on thiol SAMs [25]. For Al deposition from trimethylaminealane on $-\text{OH}$, $-\text{COOH}$ and $-\text{CH}_3$ terminated thiol SAMs [26,27], interfacial chemistry was examined using XPS, but an explicit examination of the kinetics of adsorption was not attempted. Among these studies, Woell et al. [26] carried out the sole study of interface formation in ultrahigh vacuum (UHV).

Results are presented concerning the adsorption and reaction of a titanium coordination compound, tetrakis(dimethylamido)titanium ($\text{Ti}[\text{N}(\text{CH}_3)_2]_4$), with alkyltrichlorosilane SAMs terminated by $-\text{OH}$, $-\text{NH}_2$ and $-\text{CH}_3$ groups. The adsorption of $\text{Ti}[\text{N}(\text{CH}_3)_2]_4$ on functionalized SAMs was chosen as a model for the first key reaction to inorganic thin film deposition of titanium nitride (TiN) on organic surfaces. Bradley and coworkers [28,29] carried out early studies of the reactions of $\text{Ti}[\text{N}(\text{CH}_3)_2]_4$ with NH_3 to form titanium nitride films in solution and reported facile transamination reactions leading to multiple metal–nitrogen bonds. More recently, TiN films have been employed as diffusion barriers in microelectronic circuits owing to their excellent chemical and thermal stability, low bulk resistivity and excellent adhesion [30–34]. Although TiCl_4 has been used as a precursor for TiN films, the temperatures involved are too high for microelectronic processing and Cl contamination is a significant problem [35–36]. Consequently, other precursors

have been explored and $\text{Ti}[\text{N}(\text{CH}_3)_2]_4$, in particular, has been studied extensively as a precursor for the formation of TiN thin films via chemical vapor (CVD) [37–51] and atomic layer deposition (ALD) [52–55] techniques. In this study x-ray photoelectron spectroscopy is employed to quantify the kinetics of adsorption of the titanium precursor, $\text{Ti}[\text{N}(\text{CH}_3)_2]_4$, and as a tool to probe the spatial extent of reaction, e.g., surface vs. sub-surface adsorption. As such, this represents the first in-depth study, carried out in UHV, of the reaction of a transition metal complex with a set of SAMs possessing different functional endgroups.

The experimental apparatus, sample preparation, experimental procedures as well as analytical techniques employed are described in detail in Chapter 2.1. In brief, all experiments involved three sequential stages. First, trichlorosilane SAMs were formed on SiO_2 surfaces. In some cases, following SAM formation, the substrates were subjected to additional chemical conversion steps to form the desired organic functional endgroup. Second, and prior to insertion into vacuum, the substrates were characterized using contact angle measurements, ellipsometry and atomic force microscopy (AFM). Third, the substrates were transferred into a custom-designed UHV chamber [56] for additional analysis using XPS, and eventual exposure to the titanium coordination complex. Once in the UHV chamber, XPS was used to determine the coverage–exposure relationship for $\text{Ti}[\text{N}(\text{CH}_3)_2]_4$ on the different SAMs, and, in selected cases, angle resolved XPS (ARXPS) was used to probe the spatial extent of reaction of the precursor.

Table 3-1 Properties of self-assembled monolayers*

Surface	Contact angle			Thickness (ellipsometry)	Density (cm ⁻² , XPS)	Roughness (AFM)
	advancing	receding	hysteresis			
chemical oxide	< 15°	< 10°	-	20 – 25 Å	-	3.02 Å
≡Si-(CH ₂) ₁₇ -CH ₃	112° ± 0.6°	109.7° ± 4.7°	2.3°	27 Å	3.09 × 10 ¹⁴	4.19 Å
					3.99 × 10 ¹⁴	
	110-112° [10]			27.5 Å [57]		
≡Si-(CH ₂) ₁₀ -CH ₂ OH	54.9° ± 1.7°	50.4° ± 2.2°	4.5°	17 Å	2.96 × 10 ¹⁴	4.04 Å
	50-60° [57]			16 Å [57]		
≡Si-(CH ₂) ₁₂ -NH ₂	59.4° ± 3.9°	47.0° ± 3.4°	12.4°		4.38 × 10 ¹⁴	4.44 Å
	63° ± 2.0° [58]	42.0 ± 4.0 [58]	21.0° [58]			

*this work unless otherwise indicated

3.3 Results and discussion

3.3.1 Characterization of self-assembled monolayers: the reactive surface

The chemical oxide and the three SAM surfaces were characterized by measurements of the contact angle, ellipsometry and AFM (*c.f.* Table 3–1). For the –OH, –NH₂ and –CH₃ terminated SAMs, the contact angles measured were within the ranges reported previously [10,56,57,58]. For the –CH₃ SAM, ellipsometric film thickness was 27 Å. In previous work on –CH₃ terminated alkyl SAMs, the film thickness, L , was found to be given by $L(\text{Å}) = 1.26n + 4.78$, where n is the number of carbon atoms in the backbone [57]. Using this formula for $n = 18$, predicts $L = 27.46$ Å, essentially identical to that measured here. For the –OH terminated SAM, the thickness was consistent with the reported value of 16 Å [57].

In Fig. 3–1 micrographs obtained using AFM are presented for the –OH, –NH₂ and –CH₃ terminated SAMs. All images represent 250×250 nm² scans, and were acquired in tapping mode. As may be seen, in all cases the images indicate a very uniform monolayer, with no evidence of large (several nm²) defects in the adlayer. It should be noted, however, that AFM will not be effective in detecting defects such as grain boundaries, and isolated defects occupying only a few nm². Root mean square (RMS) surface roughness is ~ 4 Å for all the three SAMs examined here (*cf.* Table 3–1). The roughness of underlying chemical silicon dioxide measured by AFM is 3.02 Å, thus, the SAMs appear to uniformly cover the underlying substrate.

XP spectra were acquired for all four reactive surfaces examined here.

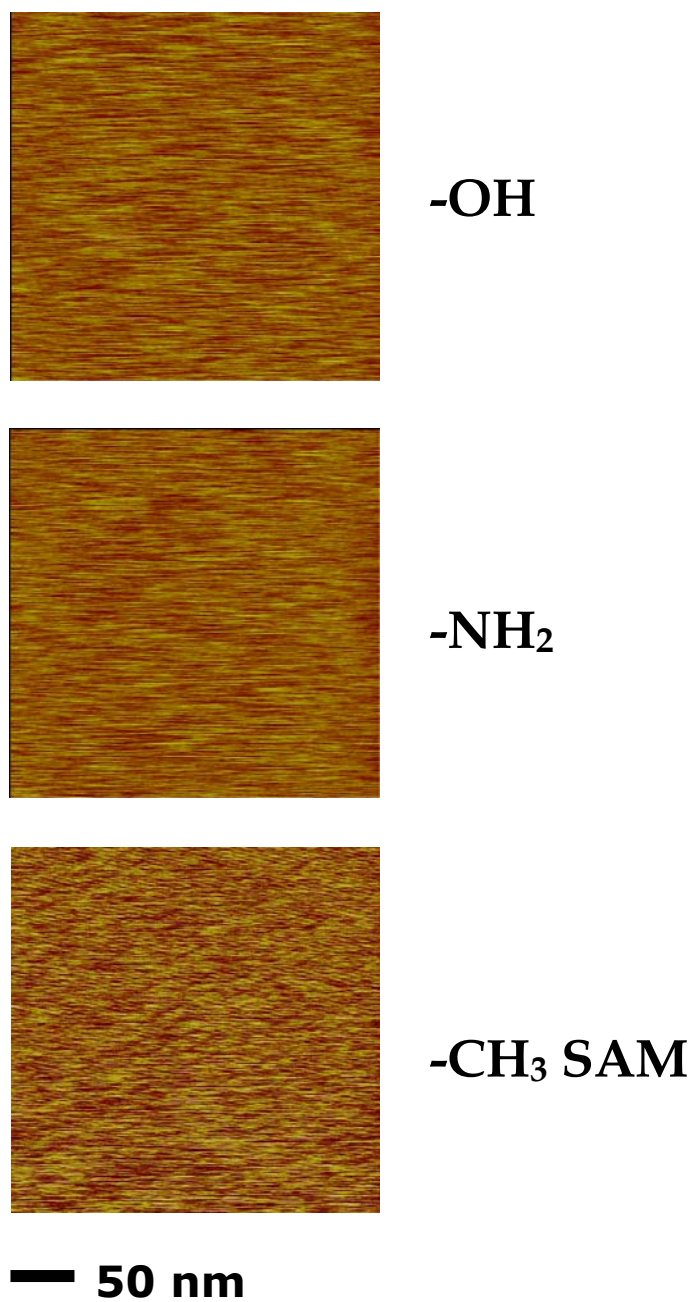


Figure 3–1 Atomic force micrographs of the three SAM surfaces examined here: -OH , -NH_2 and -CH_3 terminated. RMS roughness was $\sim 4\text{\AA}$ for all surfaces (cf. Table 3–1).

The survey spectrum for chemical oxide showed three elements: silicon (2s, 153 eV; 2p, 99.7 eV) [59], O (1s, 532 eV) [60] and C (1s, 285 eV) [57]. In Fig. 3–2 the Si (2p) spectrum for the chemical oxide is presented. As may be seen, there is a shoulder on the high binding energy side of the Si(2p) peak that is from the SiO₂ thin film. Analysis of this spectrum, fitting the Si(2p) feature to two peaks of equal FWHM gives a chemical shift of 3.46 eV for the peak associated with SiO₂, which can be compared to a value of 3.5 eV that has been previously reported [61] for chemical oxide grown using an RCA clean. In addition, the Si (2p) peak for chemical oxide is at 103.2 eV (cf. 103.5 eV [62]). An estimate for the thickness of the chemical oxide can be made from this Si (2p) feature [63] by using known values for the inelastic mean free path of the Si(2p) photoelectrons in SiO₂ ($\lambda_{\text{Si}(2p),\text{SiO}_2} = 31.4 \text{ \AA}$ [63]) and Si ($\lambda_{\text{Si}(2p),\text{Si}} = 26.3 \text{ \AA}$ [63]). This procedure yields a value of 8 Å, which is less than that obtained from ellipsometry.

Survey XP spectra for all three SAMs gave peaks only for the following components: C(1s), 285 eV; Si(2s), 153 eV; Si(2p), 99.7 eV; O(1s), 532 eV; and N(1s), 400.6–401.2 eV (only for the –NH₂ SAM) [58]. No Cl was detected by XPS. Chemical conversion from vinyl to –OH termination was verified in two ways. First, the area of the O(1s) peak increased by 14% for the –OH SAM as compared to that observed for the underlying substrate (chemical oxide). The second observation involves the C(1s) peak (*vide infra*). Chemical conversion of the –CN group to –NH₂ was verified by examining the N(1s) peak. In Fig. 3–3 spectra for the N(1s) peak for both a –NH₂ terminated SAM and a –CN terminated SAM are plotted, the latter not subjected to the chemical conversion described above in section 2.1.3.4. Each spectrum was fit to a

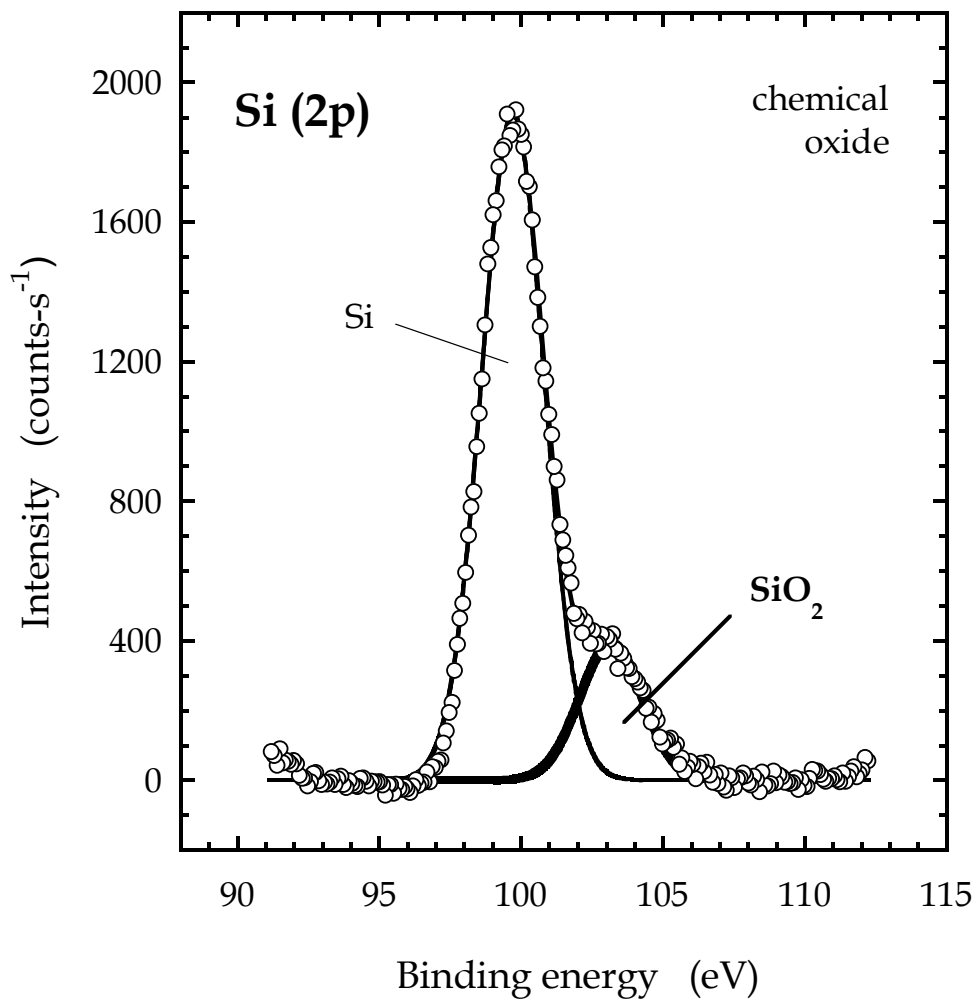


Figure 3–2 XPS spectrum of the Si (2p) feature for silicon dioxide (“chemical oxide”) on silicon. The spectrum has been fitted to two peaks (at 99.7 and 103.16 eV) as described in the text, and these are indicated by the smooth curves.

single Gaussian–Lorentzian product function. As may be seen, the N(1s) peak is shifted by 1.25 eV for the –NH₂ terminated SAM with respect to the –CN terminated SAM, which can be compared to a shift of 0.7–1.3 eV reported previously [58], confirming the effectiveness of the chemical conversion.

Also presented in Fig. 3–3 are C(1s) spectra obtained from the –OH, –NH₂ and –CH₃ terminated SAMs which were fit to one (–CH₃ terminated SAM) or two (–NH₂ and –OH terminated SAMs) Gaussian–Lorentzian product functions. These spectra provide additional evidence as to the effectiveness of the chemical conversion, and can be used to estimate the coverage of the SAMs. As may be seen, the peak for the 18–carbon chain SAM is the largest, which is expected if the 2–d packing densities are similar for the three SAMs. The spectra are best described by fits to one peak for the –CH₃ terminated SAM, and to two peaks for the –OH and –NH₂ terminated SAMs. The high energy shoulders are of course associated with the terminal –CH₂– groups bound to the –OH and –NH₂ endgroups. The fits give chemical shifts of 3.44 eV (cf. 1.6 eV [57]) for the –OH SAM, and 2.84 eV for the –NH₂ SAM. In these fits, the ratios of the peak height of the chemically shifted component to that of the –CH₂– backbone were not free parameters but were fixed to be 0.146 for the –OH SAM, and 0.137 for the –NH₂ SAM (calculated using $\lambda_{\text{SAM,C(1s)}} = 24.5 \text{ \AA}$ [64]).

As indicated above, the C(1s) feature can be used to estimate the absolute coverage of the SAMs. To accomplish this, one needs to account for the photoelectron cross–sections, σ , for the C(1s) and the Au(4f_{7/2}) peaks, the analyzer transmission, T(E), which is inversely proportional to the kinetic energy for the spectra acquired in Fig. 3–3 (E = 968.6 and 1169.6 eV,

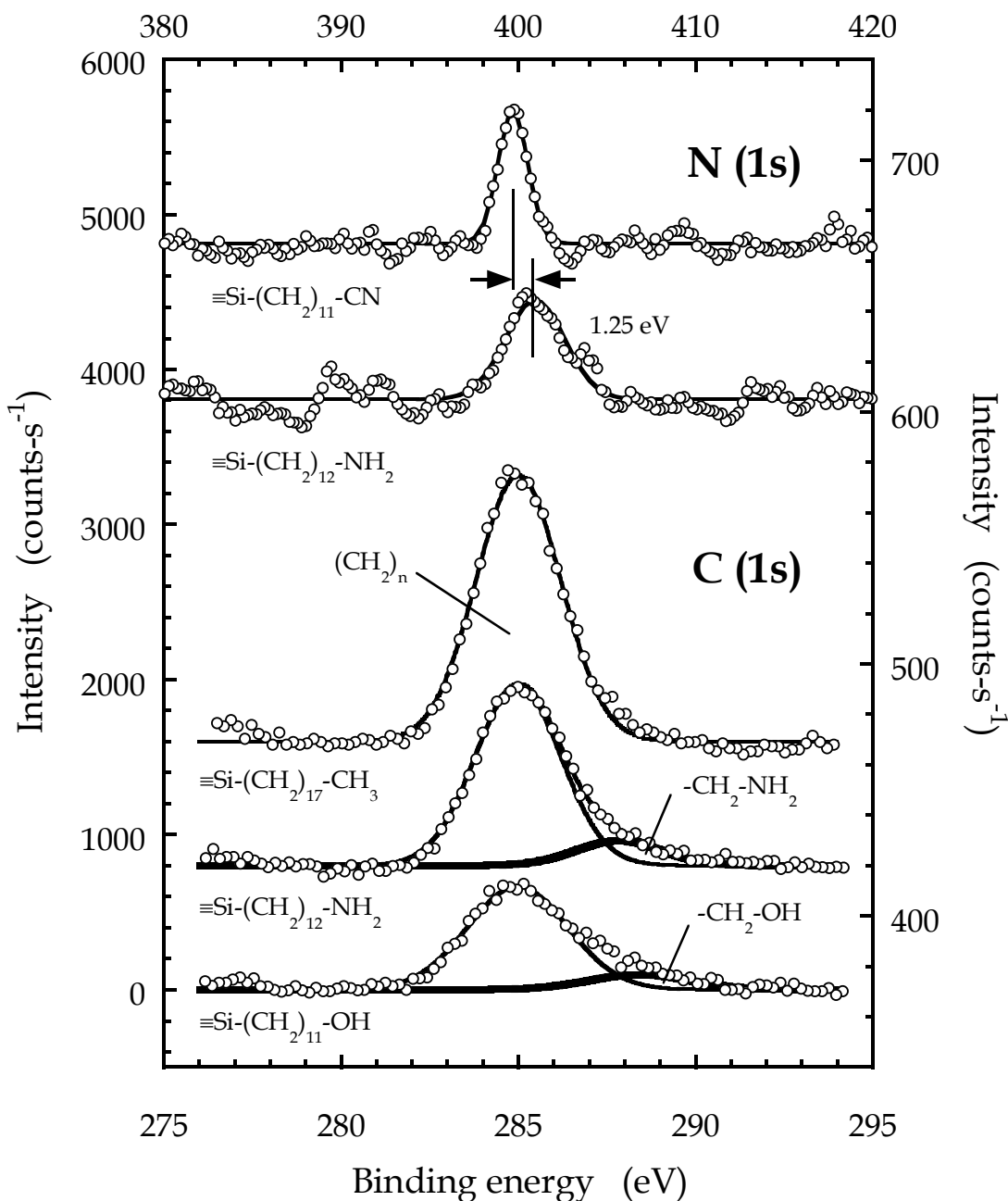


Figure 3-3 XP spectra of the N(1s) (upper) and C(1s) (lower) features for the SAMs considered here. The N(1s) spectra, demonstrate the chemical conversion from a -CN to a -NH₂ terminated SAM. The C(1s) spectra indicate the presence of a reactive functional group for the latter two spectra. These C(1s) spectra are also used to compute the coverage of the SAMs.

respectively), the atomic density of the two elements, N , and the inelastic mean free path, λ , for the photoelectrons. Concerning these, $\sigma_{\text{Au}}/\sigma_{\text{C}} = 9.8$ [59], $N_{\text{Au}} = 5.88 \times 10^{22}$ atoms -cm^{-3} [65], and $\lambda_{\text{Au}} = 15.5$ Å [66]. The atomic density of C in the SAM depends on the coverage or density of the SAM, n_{SAM} (molecules -cm^{-2}), and mean spacing between C in the backbone, d_{C} . Integrated intensity is proportional to $\sigma_{\text{C}} (n_{\text{SAM}}/d_{\text{C}}) \lambda_{\text{C}} T(E_{\text{C}}) [1 - \exp(-n d_{\text{C}}/\lambda_{\text{C}} \cos \theta)]$, where n is the number of C in the backbone of the SAM and θ is the take-off angle. For the inelastic mean free path of the C(1s) photoelectrons $\lambda_{\text{C}} = 24.5$ Å [64] is used. Making use of these expressions and the spectra shown in Fig. 3–3 the density of the SAMs, n_{SAM} has been computed (Table 3–1). Given the assumptions made here to calculate these values, their absolute accuracy is approximately $\pm 30\%$, whereas the relative accuracy should be much better, i.e. $\pm 10\%$. The densities range from 2.96 to 4.38 to $3.09\text{--}3.99 \times 10^{14}$ molecules -cm^{-2} for the -OH , -NH_2 and -CH_3 SAM respectively. These values can be compared to previous work where values of $4\text{--}5$, $3.7\text{--}4.2$ and 5.7×10^{14} molecules -cm^{-2} have been reported for $\equiv\text{Si}\text{-(CH}_2\text{)}_{17}\text{-CH}_3$ and $\equiv\text{Si}\text{-(CH}_2\text{)}_{11}\text{-CH}_3$ SAMs on native oxide [67], $\text{=Si(CH}_3\text{)-(CH}_2\text{)}_3\text{-NH}_2$ on native oxide [68] and $\equiv\text{Si}\text{-(CH}_2\text{)}_3\text{-NH}_2$ on Davisil silica [69], respectively.

3.3.2 Reaction of $\text{Ti[N(CH}_3\text{)}_2\text{]}_4$ with SAMs: adsorption kinetics

The adsorption of $\text{Ti[N(CH}_3\text{)}_2\text{]}_4$ on chemical oxide and the three SAMs possessing different endgroups described above has been examined at three substrate temperatures, $T_{\text{s}} = -50$ °C, 30 °C and 110 °C. In Fig. 3–4 Ti(2p)

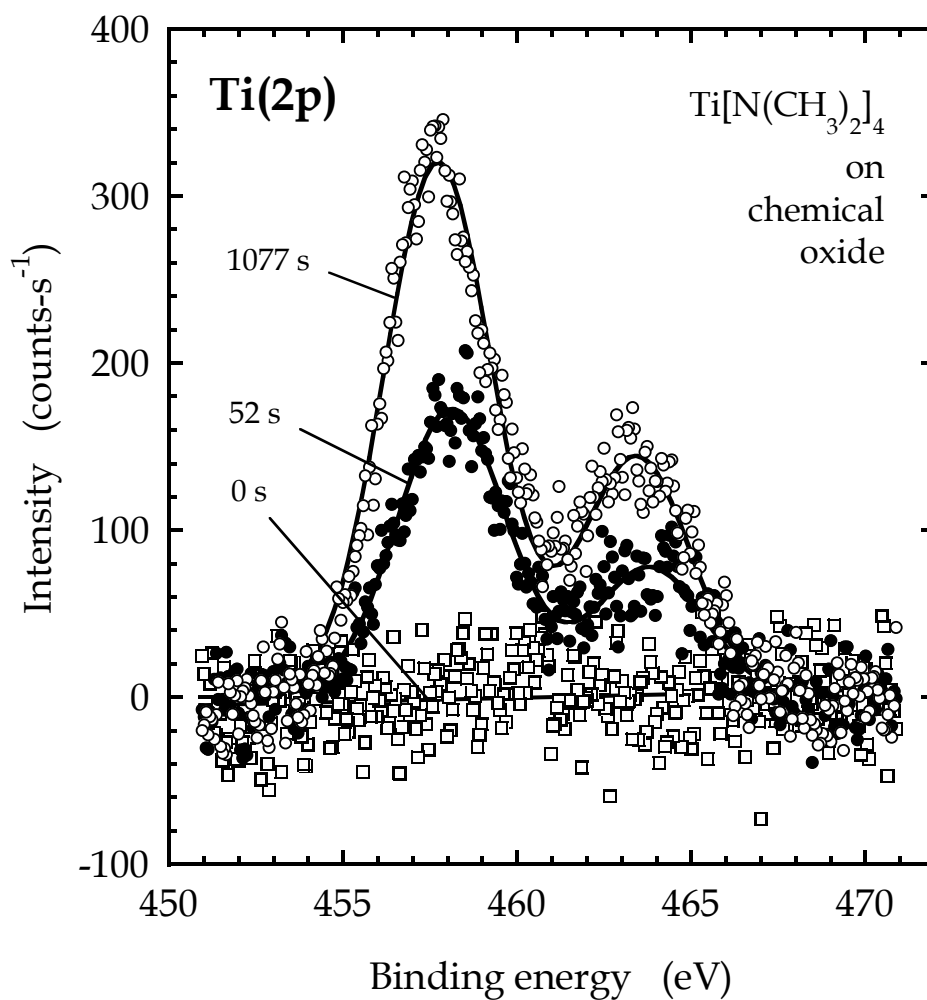


Figure 3–4 XPS spectra of the Ti (2p) feature for a chemical oxide surface exposed to $\text{Ti}[\text{N}(\text{CH}_3)_2]_4$ at 30°C . Spectra have been fitted to two peaks using Gaussian–Lorentzian product functions. Exposure times of the surface to TDMAT are as indicated.

spectra are plotted for $\text{Ti}[\text{N}(\text{CH}_3)_2]_4$ adsorption on chemical oxide at $T_s = 30\text{ }^\circ\text{C}$. The smooth curves represent a fit of the spectra to a mixed Gaussian–Lorentzian function where a ratio of 0.45:1 is assumed for the area of the $2p_{1/2}$ and $2p_{3/2}$ peaks [70]. As may be seen, the peak areas increase with increasing exposure. There also is a slight shift in the peak position with increasing exposure, the $\text{Ti}(2p_{3/2})$ peak shifts from 458.1 (52 s) to 457.7 eV (1077 s). This shift of 0.4 eV could represent more Ti–O bonds present at low coverages, e.g., $[(\text{CH}_3)_2\text{N}]_2\text{Ti}(-\text{O}-\text{Si})_2$ vs. $[(\text{CH}_3)_2\text{N}]_3\text{Ti}(-\text{O}-\text{Si})$ species at high coverage.

Plotted in Figs. 3–5 to 3–7 are the coverage–exposure relationships for $\text{Ti}[\text{N}(\text{CH}_3)_2]_4$ adsorption on chemical oxide, the –OH SAM, the –NH₂ SAM and the –CH₃ SAM, all at $T_s = -50\text{ }^\circ\text{C}$, $30\text{ }^\circ\text{C}$ and $110\text{ }^\circ\text{C}$. To quantify the Ti density on the surface, spectra from bulk single crystal TiO_2 (Commercial Crystal Laboratories Inc., Naples, FL) were collected, where the integrated intensity is proportional to $\sigma_{\text{Ti}} N_{\text{Ti}} \lambda_{\text{Ti}} T(E_{\text{Ti}})$ ($\lambda_{\text{Ti}} = 20.67\text{ \AA}$ [71] and $N_{\text{Ti}} = 3.2 \times 10^{22}\text{ atoms-cm}^{-3}$). The titanium atoms in the $\text{Ti}[\text{N}(\text{CH}_3)_2]_4$ adlayer were modeled as a thin film of thickness d_{Ti} and titanium atomic density N'_{Ti} , whose integrated intensity is proportional to $\sigma_{\text{Ti}} N'_{\text{Ti}} d_{\text{Ti}} T(E_{\text{Ti}})/\cos\theta$, assuming $d_{\text{Ti}} \ll \lambda_{\text{Ti}}$. The quantity plotted in Fig. 3–5 is $N'_{\text{Ti}} d_{\text{Ti}}$ (atoms-cm^{-2}), and the greatest uncertainty in these absolute values is associated with the assumed value for λ_{Ti} (probably at least $\pm 30\%$). In all cases a number of models were fit to the data, including a first–order Langmuir model, and models assuming that an extrinsic mobile precursor exists for adsorption (e.g., the Kisliuk model [72]). The data were sufficiently well described by first–order Langmuirian kinetics, *viz*:

$$\frac{d\theta}{dt} = \left(\frac{S_{R,0}F}{n_s} \right) (1 - \theta) \quad (3-1)$$

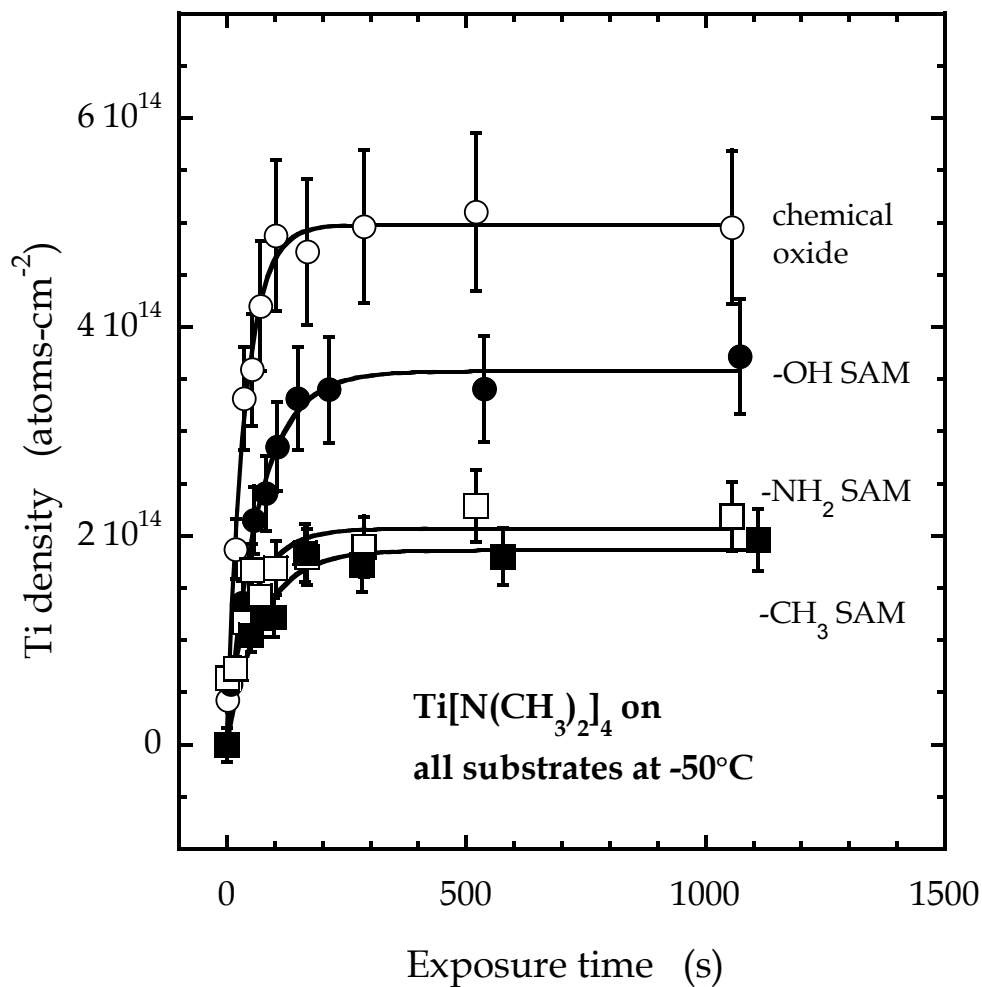


Figure 3-5 Coverage-exposure relationship, deduced from XPS, for the adsorption of $\text{Ti}[\text{N}(\text{CH}_3)_2]_4$ on chemical oxide, $-\text{OH}$ terminated SAM, $-\text{NH}_2$ terminated SAM and $-\text{CH}_3$ terminated SAM at a substrate temperature of -50°C . The fits to the data, shown as smooth curves, are for a first-order Langmuirian model of adsorption.

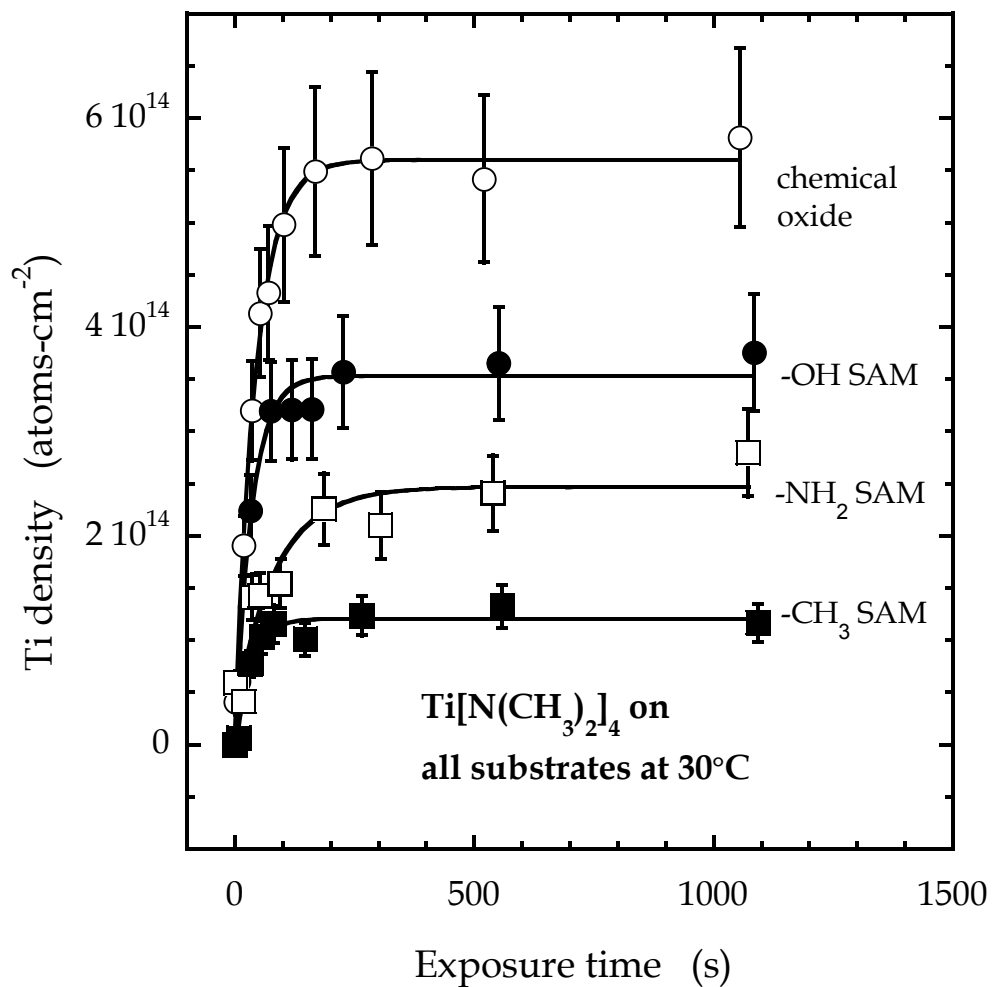


Figure 3-6 Coverage-exposure relationship, deduced from XPS, for the adsorption of $\text{Ti}[\text{N}(\text{CH}_3)_2]_4$ on chemical oxide, -OH terminated SAM, -NH₂ terminated SAM and -CH₃ terminated SAM at a substrate temperature of 30 °C. The fits to the data, shown as smooth curves, are for a first-order Langmuirian model of adsorption.

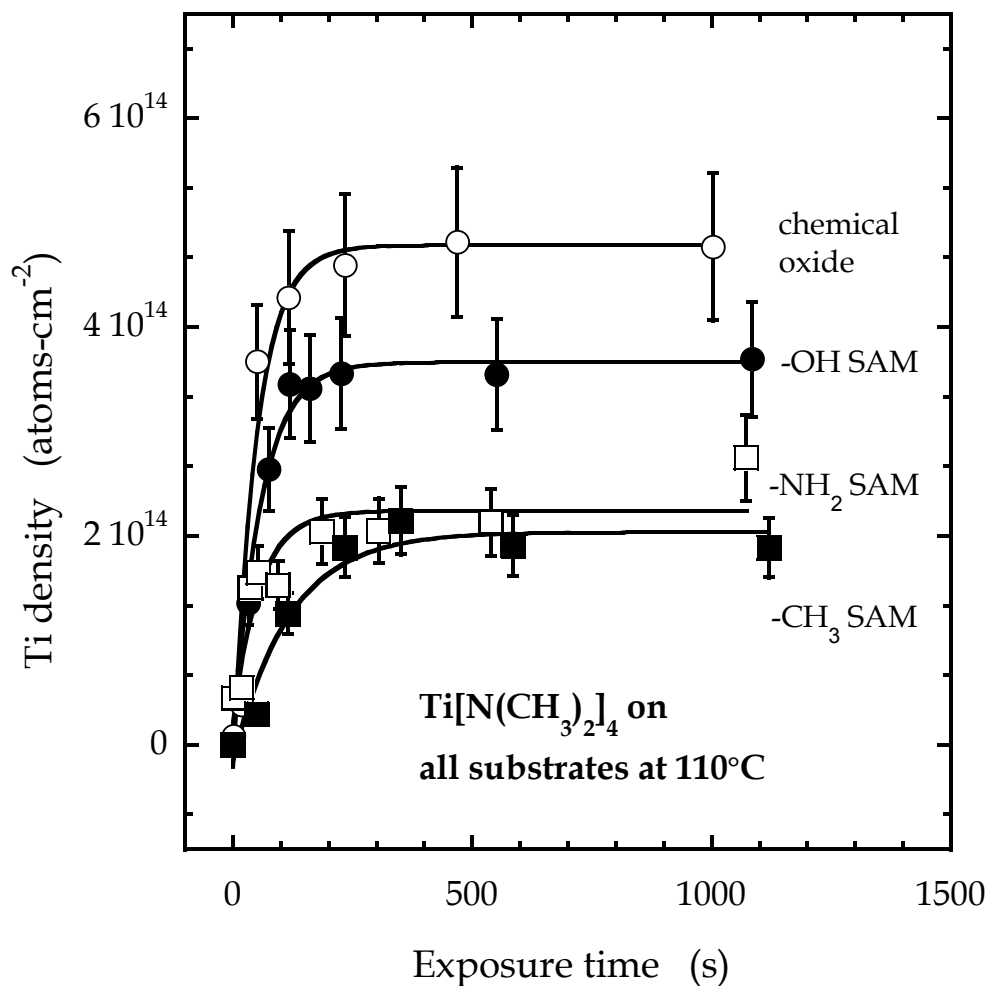


Figure 3-7 Coverage-exposure relationship, deduced from XPS, for the adsorption of $\text{Ti}[\text{N}(\text{CH}_3)_2]_4$ on chemical oxide, $-\text{OH}$ terminated SAM, $-\text{NH}_2$ terminated SAM and $-\text{CH}_3$ terminated SAM at a substrate temperature of 110°C . The fits to the data, shown as smooth curves, are for a first-order Langmuirian model of adsorption.

where θ is the coverage of adsorbed $\text{Ti}[\text{N}(\text{CH}_3)_2]_4$, $S_{\text{R},0}$ is the initial probability of adsorption, F is the incident flux of $\text{Ti}[\text{N}(\text{CH}_3)_2]_4$ ($\text{molecules}\cdot\text{cm}^{-2}\cdot\text{s}^{-1}$), and n_s is the saturation coverage ($\text{molecules}\cdot\text{cm}^{-2}$).

From the fits to the data displayed in Figs. 3–5 to 3–7, coupled with an estimate of the incident flux of $\text{Ti}[\text{N}(\text{CH}_3)_2]_4$, both the initial reaction probability, $S_{\text{R},0}$, and the saturation coverage, n_s can be evaluated. In Fig. 3–8 the initial reaction probability is plotted as a function of temperature for the four surfaces examined here, where the data have been normalized to the value for $S_{\text{R},0}$ measured on chemical oxide at $T_s = -50$ °C. As may be seen the initial reaction probability is highest on the chemical oxide, and $S_{\text{R},0}$ decreases slightly with increasing substrate temperature. Making use of an estimate for the absolute flux of $\text{Ti}[\text{N}(\text{CH}_3)_2]_4$ yields $S_{\text{R},0} \sim 0.48$ on chemical oxide at $T_s = -50$ °C, exhibiting an average value of ~ 0.43 for the reaction conditions examined here. Given the uncertainty in the values for estimates of the absolute flux and coverage, these absolute values for $S_{\text{R},0}$ possess uncertainties of $\sim 50\%$. Next in reactivity is the $-\text{OH}$ terminated SAM, with an average value that is $\sim 62\%$ of that observed on chemical oxide. Reactivity of the $-\text{NH}_2$ and $-\text{CH}_3$ terminated SAMs are comparable (30% and 23% of that on chemical oxide), and no significant trend with substrate temperature is observed. For these reaction conditions, the observation of finite reactivity with the $-\text{CH}_3$ terminated SAM is unexpected, and this is considered in further detail below.

In Fig. 3–9 the Ti saturation coverage is plotted for the four surfaces examined here as a function of substrate temperature. This quantity exhibits only a weak dependence on substrate temperature for all four surfaces examined. In comparing the surfaces, the ranking essentially follows that

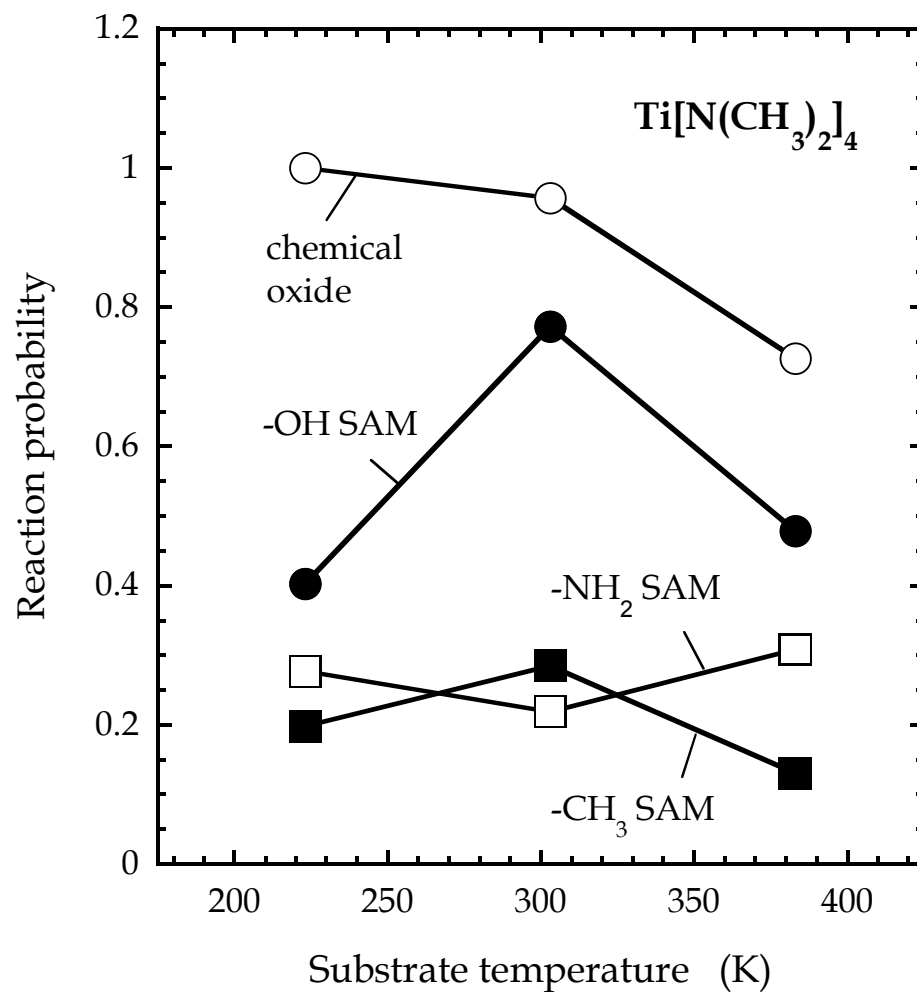


Figure 3–8 Initial probability of adsorption for $\text{Ti}[\text{N}(\text{CH}_3)_2]_4$ on chemical oxide and $-\text{OH}$, $-\text{NH}_2$ and $-\text{CH}_3$ terminated SAMs, as a function of substrate temperature. The data have been normalized to that observed for $\text{Ti}[\text{N}(\text{CH}_3)_2]_4$ on chemical oxide at $T_s = -50\text{ }^\circ\text{C}$. Error bars are plotted and are typically smaller than the size of the data points displayed.

observed for the initial reaction probability. The average saturation density on the chemical oxide is $\sim 5.12 \times 10^{14}$ atoms -cm^{-2} , for the SAMs it is 3.59, 2.26 and 1.70×10^{14} atoms -cm^{-2} , for the -OH , -NH_2 and -CH_3 terminations. These values, certainly the latter, should be compared to the number density of functional groups present on the surface. In addition, these values assume there is no attenuation of the Ti(2p) photoelectrons in the adlayer.

3.3.3 Reaction of $\text{Ti}[\text{N}(\text{CH}_3)_2]_4$ with SAMs: microstructure of the adlayer

The results presented above, particularly those related to the chemisorption of TDMAT in Figs. 4–9, demand a more in-depth analysis of the chemisorbed layer. In particular, the starting surface to the formation of the SAMs, i.e. the chemical oxide, is the most reactive surface examined here. Thus, the possibility exists that the buried SAM/ SiO_2 interface may retain substantial reactivity that must be accounted for in the analysis of these results. ARXPS is a very useful technique to probe the spatial extent of reaction of $\text{Ti}[\text{N}(\text{CH}_3)_2]_4$ with the SAMs. By varying the take-off angle of emitted photoelectrons, those emitted by Ti atoms reacting at the SAM/ SiO_2 interface are attenuated as compared to those from the Ti atoms reacting at the top of the SAM. Consequently, the Ti peak area may decrease with increasing take-off angle if all Ti atoms were at the SAM/ SiO_2 interface, while the Ti peak area may actually increase with increasing take-off angle, if Ti atoms react with the terminal group of the SAM, owing to geometric effects.

First, ARXPS of the unreacted -CH_3 terminated SAM is considered, namely the integrated areas for the O(1s) and C(1s) peaks as a function of

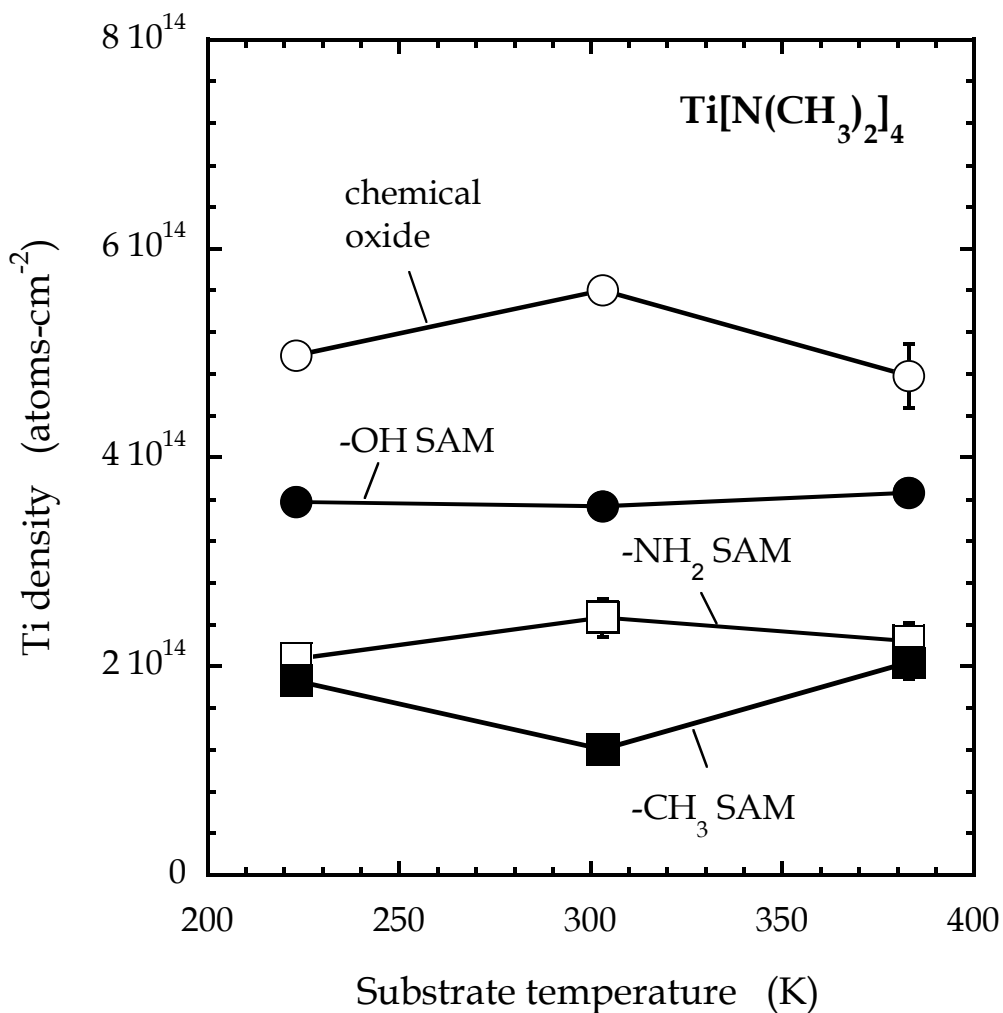


Figure 3–9 Concentration of titanium at saturation from the adsorption of $\text{Ti}[\text{N}(\text{CH}_3)_2]_4$ on chemical oxide and $-\text{OH}$, $-\text{NH}_2$ and $-\text{CH}_3$ terminated SAMs, as a function of substrate temperature. Densities in all cases were deduced from XPS and assumed no attenuation of the $\text{Ti}(2p)$ photoelectrons emanating from Ti in the adlayer. Error bars are plotted and are typically smaller than the size of the data points displayed.

take-off angle. Photoemission from the SAM will be analyzed with a model that assumes that the underlying chemical oxide of thickness d_{ox} , is covered uniformly by the SAM, of thickness d_{SAM} . The corresponding inelastic mean free paths of the photoelectrons in the two layers are given by λ_{ox} and λ_{SAM} . For emission from the C in the SAM, the intensity is given by:

$$I_{C(1s)}(\theta) = I_{0,SAM,C(1s)} \left(1 - \exp\left(-\frac{d_{SAM}}{\lambda_{SAM,C(1s)} \cos\theta} \right) \right) \quad (3-2)$$

whereas that for emission from the O in the chemical oxide is given by:

$$I_{O(1s)}(\theta) = I_{0,ox,O(1s)} \exp\left(-\frac{d_{SAM}}{\lambda_{SAM,O(1s)} \cos\theta} \right) \left(1 - \exp\left(-\frac{d_{ox}}{\lambda_{ox,O(1s)} \cos\theta} \right) \right) \quad (3-3)$$

where I_0 represents the emission from a semi-infinite thin film of either the SAM [for C(1s)] or the chemical oxide [for O(1s)]. Data displayed in Fig. 3–10 have been fitted simultaneously to the two above expressions minimizing the sum of the squares for both the O (1s) and C (1s) curves. In a fit to the data, up to five parameters could be included: the intensities corresponding to the semi-infinite thin films ($I_{0,i}$) and the three attenuation factors $(d/\lambda)_{SAM,C(1s)}$, $(d/\lambda)_{SAM,O(1s)}$, and $(d/\lambda)_{ox,O(1s)}$. To reduce the number of parameters to 3 it was assumed that $\lambda_{SAM,C(1s)} / \lambda_{SAM,O(1s)} = \{E[C(1s)]/E[O(1s)]\}^{1/2}$ [71] and $(d/\lambda)_{ox,O(1s)} = 0.323$ from an earlier analysis of the Si(2p) spectrum for chemical oxide. From a fit to the data, $(d/\lambda)_{SAM,C(1s)} = 0.85$ and $(d/\lambda)_{SAM,O(1s)} = 0.99$ were obtained. Making use of the ellipsometric thickness measured here, $d_{SAM} = 27 \text{ \AA}$, results in $\lambda_{SAM,C(1s)} = 31.8 \text{ \AA}$, $\lambda_{SAM,O(1s)} = 27.4 \text{ \AA}$. These results are perhaps most useful to estimate $\lambda_{SAM,Ti(2p)} = 28.8 \text{ \AA}$ based on $\lambda \propto E^{1/2}$.

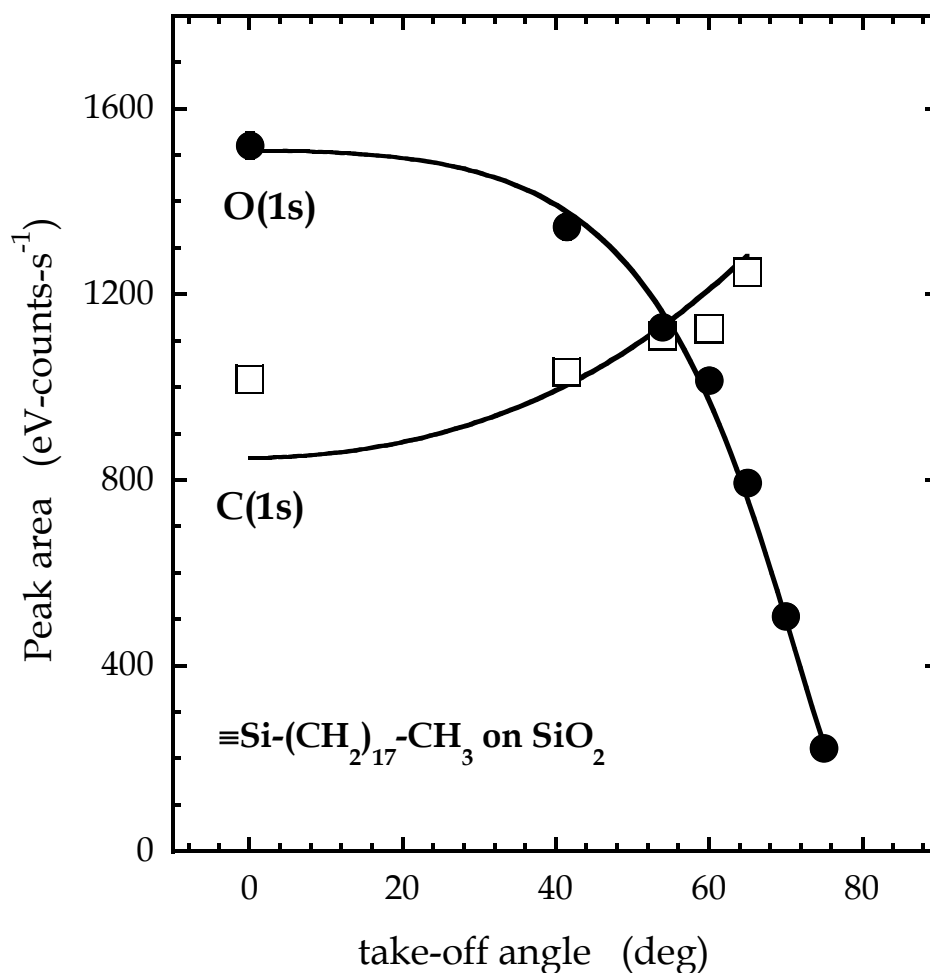


Figure 3-10 Peak areas of the O(1s) and C(1s) regions derived from XP spectra of a -CH₃ terminated SAM (≡Si-(CH₂)₁₇-CH₃) on chemical oxide as a function of take-off angle. The smooth curves are fits to the data to Eqns. (3-2) and (3-3), which account for attenuation of the photoelectrons, and the finite thickness of both the SAM and the underlying chemical oxide. Error bars are plotted and are typically smaller than the size of the data points displayed.

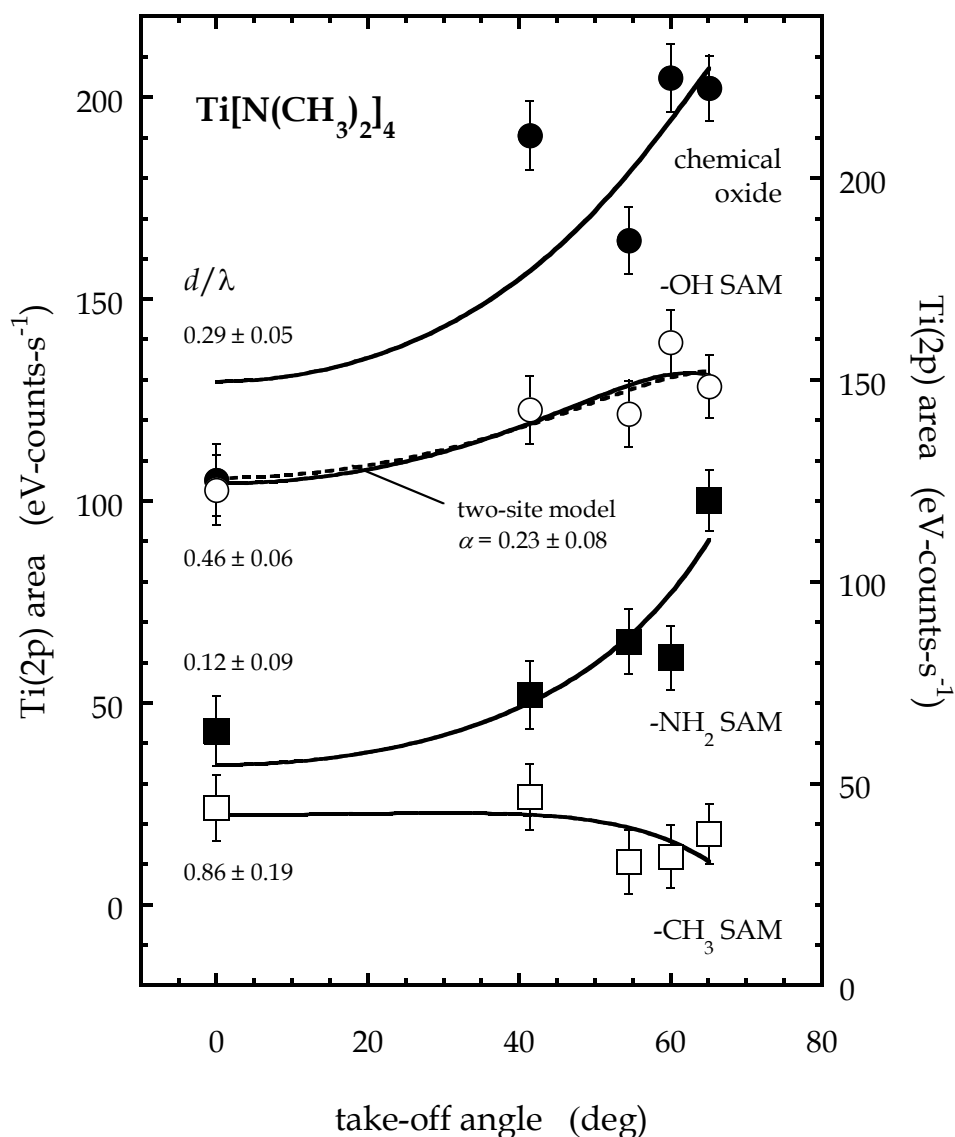


Figure 3–11 Peak area of the Ti(2p) region for $\text{Ti}[\text{N}(\text{CH}_3)_2]_4$ adsorbed on chemical oxide and the $-\text{OH}$ terminated SAM (left axis), and the $-\text{NH}_2$ and $-\text{CH}_3$ terminated SAMs (right axis) as a function of take-off angle. The smooth curves are a fit to the model described in the text. The values for the parameter d/λ (see text) are shown in each case. Also shown as a dashed curve is a fit of the data for the $-\text{OH}$ SAM to a two-site model as described in the text.

Next, to determine the spatial extent of reaction of $\text{Ti}[\text{N}(\text{CH}_3)_2]_4$ with the self-assembled monolayers, ARXPS was conducted on the four surfaces examined here, where in all cases the adsorbed layer was representative of that achieved at a saturation exposure at $T_s = 110^\circ\text{C}$. Take-off angles, from the surface normal, were varied from 0° to 65° . In Fig. 3-11 the integrated Ti(2p) area is plotted for saturated adlayers of $\text{Ti}[\text{N}(\text{CH}_3)_2]_4$ on the chemical oxide, $-\text{OH}$, $-\text{NH}_2$ and $-\text{CH}_3$ terminated SAMs as a function of take-off angle. Several qualitative observations can be made at this point. First, the Ti(2p) intensity for both the chemical oxide and the $-\text{NH}_2$ terminated SAM increases with increasing take-off angle, approximately by a factor of 2 as the angle increases from 0° to 65° . In contrast, for the $-\text{OH}$ terminated SAM the increase is much more modest, while for the $-\text{CH}_3$ terminated SAM a *decrease* is observed. Even in the absence of a detailed fit to the data, which is considered next, *these results indicate that there is something fundamentally different concerning the reaction of $\text{Ti}[\text{N}(\text{CH}_3)_2]_4$ on the $-\text{CH}_3$ terminated SAM, namely, significant penetration of the molecule to the underlying SAM/ SiO_2 interface.*

In order to analyze the results presented in Fig. 3-11, assumptions are to be made as to the distribution of $\text{Ti}[\text{N}(\text{CH}_3)_2]_4$ in the near surface region. In addition, the data set is relatively limited with five take-off angles in each case. In comparison, in reference to the data collected on the bare $-\text{CH}_3$ terminated SAM, a three parameter model was used, coupled with independent information as to the thickness of the SAM and the SiO_2 layer, to fit two sets of seven data points. The fit to the data in this case, which was excellent, revealed parameters with small standard errors (a few %). Thus, simplest model is used that can still lead to significant conclusions. The Ti in the adlayer is assumed to be arranged in a 2-D plane at a distance d from the surface. This will actually

be an excellent representation for the chemisorbed layer for the two limiting cases where: (i) reaction is solely with the terminal organic functional endgroup of the SAM, and (ii) reaction is solely at the SAM/SiO₂ interface. Photoemission from such a layer is given by:

$$I(\theta) = \left(\frac{I_0}{\cos \theta} \right) \exp \left(\frac{-d}{\lambda \cos \theta} \right) \quad (3-4)$$

where I_0 represents the unattenuated emission one would achieve at a normal take-off angle. A fit to the data involves two parameters: I_0 and d/λ where λ is the inelastic mean free path of the Ti(2p) photoelectrons. These fits are given by the smooth curves shown in Fig. 3-11 along with values obtained for the parameter d/λ . The parameter d/λ increases in the order: $-\text{NH}_2 \sim \text{chemical oxide} < -\text{OH} < -\text{CH}_3$ SAM. The value observed for the $-\text{NH}_2$ SAM, i.e. $d/\lambda = 0.12 \pm 0.09$ is consistent with the reaction of $\text{Ti}[\text{N}(\text{CH}_3)_2]_4$ solely with the terminal $-\text{NH}_2$ group. The results for the chemical oxide, $d/\lambda = 0.29 \pm 0.05$, are also consistent with $\text{Ti}[\text{N}(\text{CH}_3)_2]_4$ being located on the surface, and a finite value may reflect both the finite thickness of the adsorbed layer [the $\text{N}(\text{CH}_3)_2$ ligands may attenuate photoemission] and surface roughness. The results for the $-\text{OH}$ SAM are intermediate in character, $d/\lambda = 0.46 \pm 0.06$, and suggest that some penetration of the SAM may occur in this case. If the values for $\lambda_{\text{SAM, Ti}(2p)}$ deduced above are used, this suggests $d \sim 13.3 \pm 1.7 \text{ \AA}$, which is comparable to the thickness of the $-\text{OH}$ SAM which is 17 \AA . Finally, for the $-\text{CH}_3$ SAM, $d/\lambda = 0.86 \pm 0.19$, or $d \sim 24.8 \pm 5.5 \text{ \AA}$, indicating significant penetration of this SAM (thickness $\sim 27 \text{ \AA}$) and reaction at the SAM/SiO₂ interface. As indicated above, this was the only surface that indicated a clear decrease in the Ti(2p) intensity at more glancing take-off angles.

Additional details can be extracted concerning the reaction of $\text{Ti}[\text{N}(\text{CH}_3)_2]_4$ with the SAMs by examining further the results from XPS, specifically the peak positions and areas associated with the key elemental components in $\text{Ti}[\text{N}(\text{CH}_3)_2]_4$, and a comparison of the densities of the SAMs vs. that for Ti in the saturated adlayers. Concerning the latter, plotted in Fig. 3–12 is the saturation density of Ti vs. the SAM density, both deduced from XPS. Open symbols are the estimates for the saturation densities of Ti plotted above in Fig. 3–9. Closed symbols are the saturation density predicted by fits to the data that accounted for attenuation by the SAMs.

First the SAM expected to be totally unreactive with $\text{Ti}[\text{N}(\text{CH}_3)_2]_4$, namely the $-\text{CH}_3$ terminated SAM is considered. During these experiments, one batch of $-\text{CH}_3$ SAM (marked II here) had a density which was higher by $\sim 25\%$ than other SAMs examined here. Although unintentional, this allows the examination of the effect of SAM density on $\text{Ti}[\text{N}(\text{CH}_3)_2]_4$ adsorption in this case. As may be seen, there is a negative correlation between the density of Ti adsorbed, and that of the $-\text{CH}_3$ SAM. This is entirely as expected in this case, as the ability of $\text{Ti}[\text{N}(\text{CH}_3)_2]_4$ to penetrate the SAM to find the reactive SAM/ SiO_2 interface should increase with decreasing SAM density. These results further validate the picture of $\text{Ti}[\text{N}(\text{CH}_3)_2]_4$ adsorption on the $-\text{CH}_3$ SAM—there is no reaction with the terminal groups; it is confined completely to the SAM/ SiO_2 interface. If this negative correlation between the SAM density and the Ti density is assumed to be linear, a fit to both sets of estimates for the Ti density predicts that a density of $\sim 5.3 \times 10^{14} \text{ cm}^{-2}$ may be sufficient to prevent penetration of $\text{Ti}[\text{N}(\text{CH}_3)_2]_4$, and reaction at the SAM/ SiO_2 interface. Other assumptions, for example, including only the attenuation corrected data

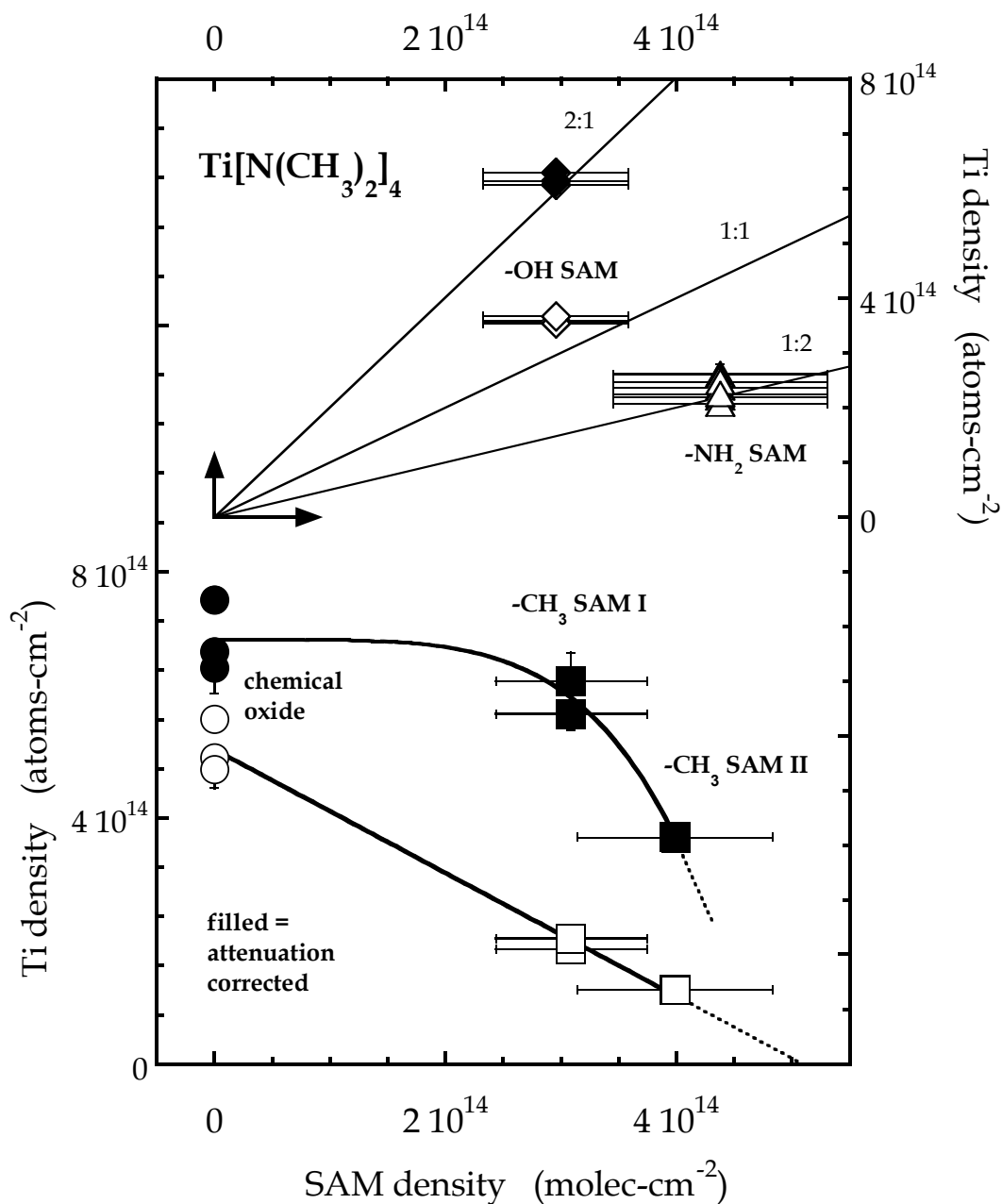


Figure 3–12 Relationship between the concentration of Ti in the saturated adlayers and the concentration of the molecules in the self-assembled monolayer: $-\text{OH}$ and $-\text{NH}_2$ terminated SAMs (upper panel) and chemical oxide and the $-\text{CH}_3$ terminated SAM (lower panel). SAM I and SAM II refer to different batches of the $-\text{CH}_3$ terminated SAM.

(but also the results on chemical oxide), lead to models where the Ti density varies in a nonlinear fashion with SAM coverage, viz., $1 - (n_{\text{SAM}}/n_{\text{SAM,sat}})^m$. A fit to this latter function gives $n_{\text{SAM,sat}} \sim 4.7 \pm 0.4 \times 10^{14} \text{ cm}^{-2}$, and $m \sim 4.8 \pm 1.9$. In either case, these results for the $-\text{CH}_3$ SAM are entirely consistent with $\text{Ti}[\text{N}(\text{CH}_3)_2]_4$ reaction at the SAM/ SiO_2 interface, which might be blocked completely by a sufficiently dense SAM.

Next, a discussion of the results for the terminal groups anticipated to be reactive is in order. First, for the $-\text{OH}$ SAM, the ratio between the density of adsorbed Ti molecules and the $-\text{OH}$ groups present on the SAM depends upon the Ti estimate used: it is $\sim 1:1$ using the model that assumes Ti is present at the surface; whereas it is $\sim 2:1$ using the model that assumes all of the Ti is below the surface ($\sim 13 \text{ \AA}$, based on the fit in Fig. 3–11). Given this intermediate result for the $-\text{OH}$ SAM a more complicated, two-site model has been used to fit the ARXPS data shown in Fig. 3–11. Briefly, this model makes use of a weighted sum of two terms, where the Ti atoms are either present in an adlayer at the surface (at depth d_{ad}), or are buried at the SAM/ SiO_2 interface (at depth d_{SAM}). The inelastic mean free paths for the photoelectrons are assumed to be identical for both layers, and the estimate for $\lambda_{\text{SAM,Ti}(2p)}$ calculated above is used. As a result, there are basically two parameters: I_0 and the quantity α , which is defined as the fraction of Ti that is bound at the surface. A fit to the data using this model is shown in Fig. 3–11. In this case $\alpha = 0.23 \pm 0.08$. In terms of absolute densities, this model predicts $1.63 \pm 0.08 \times 10^{14} \text{ Ti atoms-cm}^{-2}$ are bound at the terminal $-\text{OH}$ group of the SAM, whereas $5.47 \pm 0.73 \times 10^{14} \text{ Ti atoms-cm}^{-2}$ are at the SAM – SiO_2 interface (uncertainties do not reflect uncertainty in assumed mean free path). Concerning the former value, the Ti:SAM ratio is about 0.55, meaning each $\text{Ti}[\text{N}(\text{CH}_3)_2]_4$ molecule is

bound to ~ 2 terminal groups, or only $\sim 1/2$ of these $-\text{OH}$ terminal groups have reacted with $\text{Ti}[\text{N}(\text{CH}_3)_2]_4$.

For the $-\text{NH}_2$ SAM, the ARXPS results are very clear. Little or no penetration has occurred, and reaction is confined to the terminal group at the surface. It should be noted that based on the above results from XPS, the $-\text{NH}_2$ SAM possessed the highest density of any SAM examined in this study. This is one explanation for why penetration of this SAM and reaction at the interface was not observed. Given the certainty of the location of the reaction, the stoichiometry of the reaction can be examined in further detail in this case. As may be seen from Fig. 3-12, results are most consistent with a stoichiometry of Ti:SAM of between 1:2 and 2:3. The interpretation of these results can be made directly: either $\sim 1/2 - 2/3$ of the $-\text{NH}_2$ have reacted with $\text{Ti}[\text{N}(\text{CH}_3)_2]_4$ (e.g., $(\text{R}_2\text{N})_3\text{Ti}-\text{NH}-\text{CH}_2-\cdots$, with $1/2$ remaining unreacted), or on average $\sim 1.5-2$ $-\text{NH}_2$ groups have reacted with each $\text{Ti}[\text{N}(\text{CH}_3)_2]_4$ [e.g., $(\text{R}_2\text{N})_2\text{Ti}-(\text{NH}-\text{CH}_2-\cdots)_2$]. At this point, either of the possibilities is plausible. The highest density of Ti observed on the $-\text{NH}_2$ SAM is $2.47 \pm 0.19 \times 10^{14}$ atoms $-\text{cm}^{-2}$. If this density represents a hexagonally close-packed array of spheres, they would have a diameter of 6.8 ± 0.3 Å. This size is not unreasonable for a $\text{Ti}[\text{N}(\text{CH}_3)_2]_3(a)$ species—from the density of liquid $\text{Ti}[\text{N}(\text{CH}_3)_2]_4$ an estimate of the diameter yields 8 Å.

The extent of decomposition/loss of a ligand of $\text{Ti}[\text{N}(\text{CH}_3)_2]_4$ upon chemisorption can be assessed by an examination of the Ti(2p) and N(1s) peaks. First the ratio of the areas of these two peaks will be considered, after making suitable corrections for photoelectron cross-sections, analyzer transmission, and inelastic mean free paths. In Fig. 3-13 the N:Ti atomic ratio

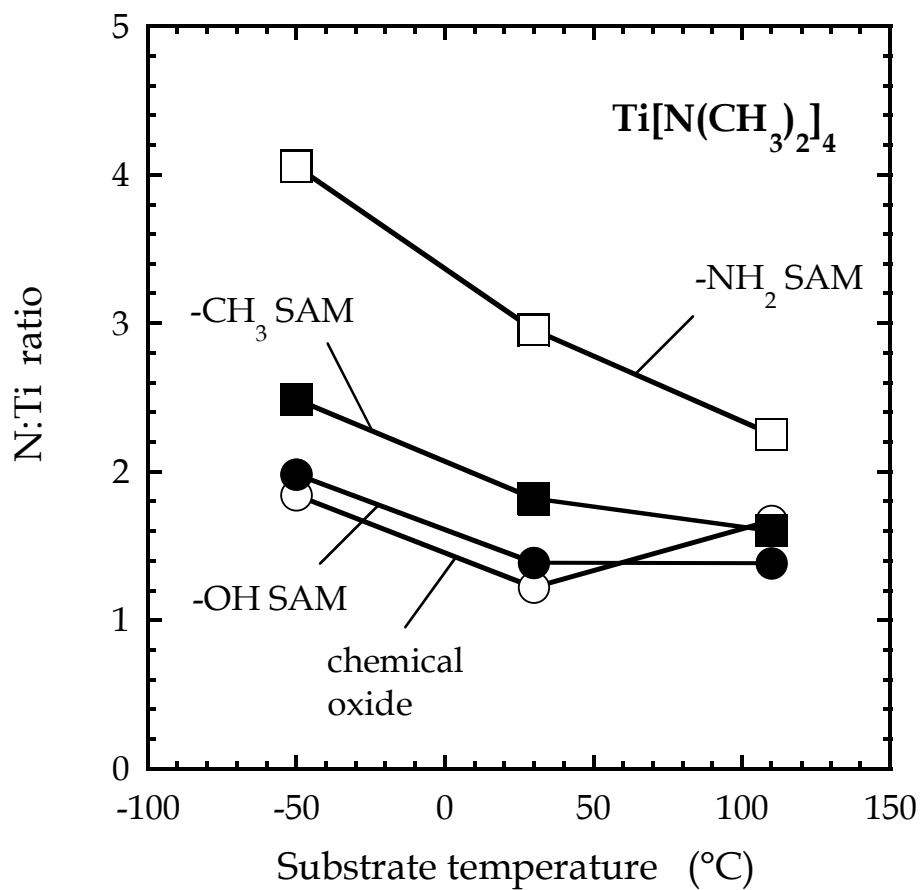


Figure 3–13 Ratio of N to Ti in the saturated adlayer, as deduced from XPS, for $\text{Ti}[\text{N}(\text{CH}_3)_2]_4$ adsorbed on chemical oxide and the $-\text{OH}$, $-\text{NH}_2$ and $-\text{CH}_3$ terminated SAMs as a function of substrate temperature.

in the adlayer is plotted as a function of the substrate temperature following exposure to $\text{Ti}[\text{N}(\text{CH}_3)_2]_4$. For unreacted $\text{Ti}[\text{N}(\text{CH}_3)_2]_4$, this ratio is of course 4:1. Two things are apparent from the figure. First, significant decomposition [i.e. loss of the $\text{N}(\text{CH}_3)_2$ ligands] is implied by the results for $\text{Ti}[\text{N}(\text{CH}_3)_2]_4$ reacting on chemical oxide, and the $-\text{OH}$ and $-\text{NH}_2$ terminated SAMs; and, second, for all surfaces examined this decomposition becomes more significant at higher temperatures (most obvious for the $-\text{NH}_2$ SAM), indicating an activated process. Chemisorption presumably involves, at minimum, loss of one $\text{N}(\text{CH}_3)_2$ ligand, thus, this ratio is expected to be either 3 or 4, depending upon the identity of the linking group ($-\text{O}-$ or $-\text{NH}-$). The results for the chemical oxide, $-\text{OH}$ and $-\text{CH}_3$ SAM seem to suggest that Ti is bound to these surfaces by 2–3 linkages, where only 1–2 $\text{N}(\text{CH}_3)_2$ ligands are retained by the parent molecule. For the $-\text{NH}_2$ SAM, based on this data alone the situation is somewhat ambiguous, as $-\text{NH}-$ is presumably the linking group. A ratio of 4 could in principle be consistent with a number of scenarios. If the data also shown in Fig. 3–12 are considered, however, some of these can safely be excluded. If the Ti:SAM ratio was taken to be 1:2, then an adlayer consisting of entirely $[(\text{CH}_3)_2\text{N}]_2\text{Ti}-(\text{NH}-\text{CH}_2-\cdots)_2$ species would give a N:Ti ratio of 4. In comparison, formation of a $[(\text{CH}_3)_2\text{N}]_3\text{Ti}-(\text{NH}-\text{CH}_2-\cdots)$ species on every other $-\text{NH}_2$ SAM would give a ratio of 5. In either event, the results for the $-\text{NH}_2$ SAM also indicate considerable loss of ligand at 110 °C, where as few as one ligand may remain attached to the parent molecule (“baseline” ratio should be 2 given assumed 1:2 Ti:SAM ratio). Clancy and co-workers [73] have recently investigated the reactions of Ti and Zr alkylamido organometallic precursors with alkyltrichlorosilane SAMs terminated with $-\text{OH}$, $-\text{NH}_2$, $-\text{CH}_3$ and $-\text{SH}$ functional groups using density functional theory. They observed a

decrease in Ti:N ratio from 1:4 to 1:3 to 1:2 for decomposition of $\text{Ti}[\text{N}(\text{CH}_3)_2]_4$ for the $-\text{NH}_2$ SAM for substrate temperatures increasing from 220 K to 300 K to 400 K respectively. Multi-site reactions of $\text{Ti}[\text{N}(\text{CH}_3)_2]_4$ on these SAMs were favorable for temperatures in excess of 220 K. Imine formation reactions were favorable at temperatures of 300 K and multiple imine formation associated with decomposition of $\text{Ti}[\text{N}(\text{CH}_3)_2]_4$ was observed at 400 K.

Examination of the chemical shift of the Ti(2p) feature can also give clues as to the nature of the species formed on the surface. The binding energy of titanium in (physisorbed) $\text{Ti}[\text{N}(\text{CH}_3)_2]_4$ has been reported to be 457.5 eV [74], whereas that for elemental Ti and Ti bound in TiN and TiO_2 are reported to be 453.89, 455.8 and 458.7 eV [59]. The Ti(2p) feature has been fitted to two peaks using Gaussian-Lorentzian product functions, identical to the procedure used above in Fig. 3-4. In all cases, peaks were referenced to the C(1s) peak, to account for effects due to the build-up of static surface charge. The following discussion will be focused on the chemical oxide and the $-\text{NH}_2$ SAM. In Fig. 3-14 is plotted the Ti(2p) binding energy vs. Ti density for adsorption on the chemical oxide (all temperatures) and the $-\text{NH}_2$ SAM (-50°C only). For chemical oxide, a linear decrease is observed in the binding energy with increasing coverage and no strong dependence on T_s is seen at a fixed coverage. This decrease in the binding energy is consistent with more Ti-O bonds at low coverage, whereas more bonding to N or perhaps other species (CH_x) is indicated at higher coverages. Reduced oxidation of the Ti center at high coverages could be due either to increasing steric limitations and reduced access to surface $-\text{OH}$ groups, or due to reactions of neighboring $\text{Ti}[\text{N}(\text{CH}_3)_2]_4$ fragments with each other forming Ti-N-Ti, or possibly Ti-N-C-Ti linkages.

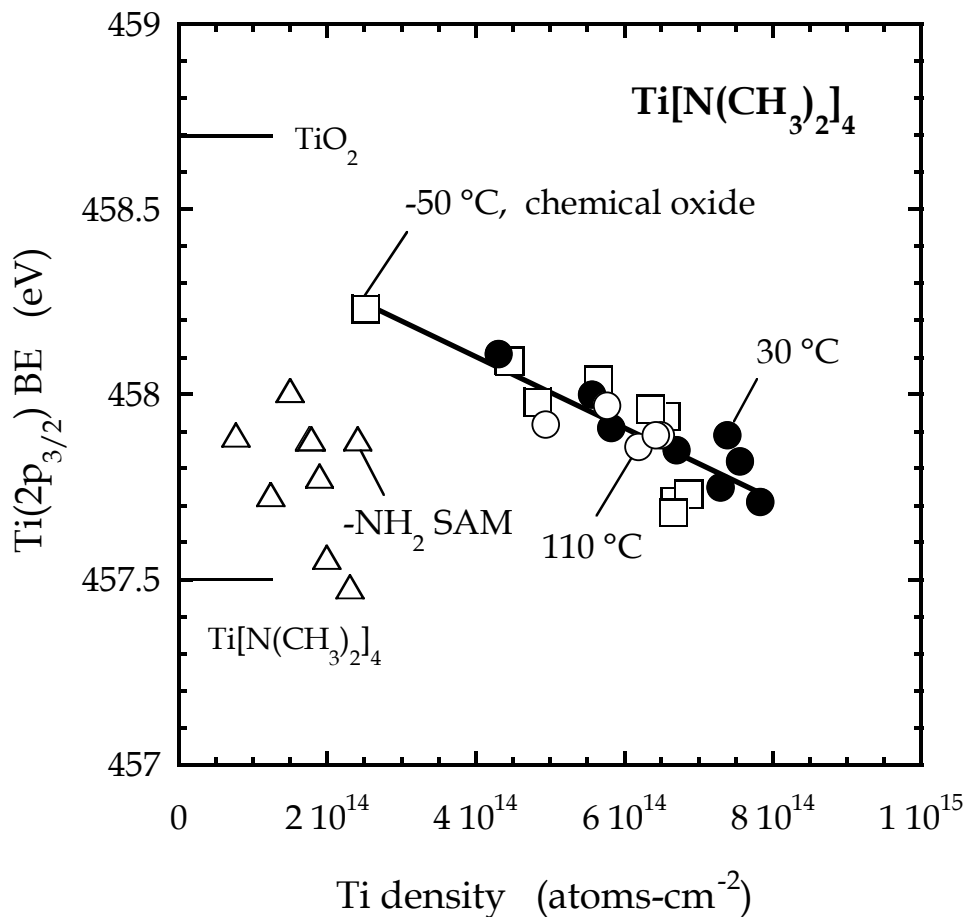


Figure 3–14 Binding energy of the Ti(2p_{3/2}) peak in the saturated adlayer [referenced to C(1s) binding energy for the same adlayer] for Ti[N(CH₃)₂]₄ adsorbed on chemical oxide and the –NH₂ terminated SAM as a function of (attenuation corrected) Ti density. Only the result for T_s = –50 °C for the –NH₂ terminated SAM is shown. Displayed also are the expected peak positions for TiO₂, and (condensed) Ti[N(CH₃)₂]₄.

Results for $\text{Ti}[\text{N}(\text{CH}_3)_2]_4$ reacting on the $-\text{NH}_2$ SAM are simpler to interpret and somewhat less revealing due to the scatter in the data. In brief, it can be seen that the binding energies are all within ~ 0.5 eV of that for $\text{Ti}[\text{N}(\text{CH}_3)_2]_4$ itself. Referring back to Figs. 3–12 and 3–13, these results are consistent with either one or two transamination reactions with the terminal $-\text{NH}_2$ groups at $T_s = -50$ °C. That is, chemical shifts associated with replacing $\text{N}(\text{CH}_3)_2$ ligands with $\text{NH}(\text{CH}_2 - \text{CH}_2 - \dots)$ should be small.

To complete a discussion of these results an attempt will be made to account for three very important observations: facile reaction of $\text{Ti}[\text{N}(\text{CH}_3)_2]_4$ with both surface $-\text{OH}$ and $-\text{NH}_2$ groups; a stoichiometry of $\text{Ti}:-\text{NH}_2$ SAM of $\sim 1:2$ indicating simple ligand exchange reactions at $T_s = -50$ °C; and increased loss of ligand at elevated substrate temperatures (110 °C). Facile reaction of $\text{Ti}[\text{N}(\text{CH}_3)_2]_4$ with surface $-\text{OH}$ is, of course, not surprising, as it is known to react violently with water. Data concerning the reaction kinetics of $\text{Ti}[\text{N}(\text{CH}_3)_2]_4$ with $-\text{OH}$ containing species are virtually non-existent; however, recent calculations [73] and experiments [75] indicate that the barrier for reaction (ligand exchange) lies below the vacuum level by $\sim 7\text{--}14$ kcal $\cdot\text{mol}^{-1}$. If an intrinsic precursor [76] exists to reaction of $\text{Ti}[\text{N}(\text{CH}_3)_2]_4$ on a surface with $-\text{OH}$ groups, a barrier below the vacuum level would indicate that the reaction probability should decrease with increasing temperature. Indeed, this is observed on the chemical oxide [75]. For reaction with $-\text{NH}_2$, it is of interest to compare to predictions based on the kinetics of transamination, $\text{Ti}[\text{N}(\text{CH}_3)_2]_4(\text{g}) + \text{NH}_3(\text{g}) \rightarrow [(\text{CH}_3)_2\text{N}]_3\text{TiNH}_2(\text{g}) + \text{HN}(\text{CH}_3)_2(\text{g})$ [47]. Cross sections for this gas phase reaction implied by this study are predicted to increase from ~ 0.44 to 4.8×10^{-19} cm 2 as T increases from 25 to 100 °C. Using n_{SAM} of 4.38×10^{14} cm $^{-2}$ and assuming a direct gas–surface reaction this implies a

reaction probability of $0.19\text{--}2.1 \times 10^{-4}$ over this same temperature range, much smaller than that observed here ($S_{R,0} \sim 0.14$, absolute). A significant dependence on temperature is also not observed, whereas the gas phase transamination reaction with NH_3 indicates a barrier of $\sim 8 \text{ kcal}\cdot\text{mol}^{-1}$ (predicts an increase in rate of ~ 2000 from $T = -50$ to $110 \text{ }^\circ\text{C}$). The biggest difference between the gas-phase reaction and reaction on a surface involves the density of -NH_2 groups—reaction on a surface is more akin to a condensed phase reaction. Recent calculations [73] have shown that the barrier for transamination can be reduced significantly ($\sim 10 \text{ kcal}\cdot\text{mol}^{-1}$) in the presence of a second attacking amido ligand. These experimental results are in agreement with this scenario where reaction on a sufficiently dense -NH_2 terminated SAM is facile and essentially unactivated.

Of equal importance is the stoichiometry of the reaction with the endgroups, and the nature of the adlayer formed at higher temperatures where increased loss of ligand is observed. The Ti:SAM ratio of $\sim 1:2$ established for reaction on the -NH_2 SAM, and less convincingly on the -OH SAM, is consistent with the loss of two ligands at $-50 \text{ }^\circ\text{C}$, with the complex making two new bonds with the terminal groups of the SAMs. Assuming hexagonal close-packing, the -NH_2 SAMs are spaced by $\sim 5.1 \text{ \AA}$, and a $\text{Ti}[\text{N}(\text{CH}_3)_2]_2$ fragment should be able to bridge these sites easily, particularly given the flexibility of the SAM alkyl backbone. Thus, at $T_s = -50 \text{ }^\circ\text{C}$, formation of a $[(\text{CH}_3)_2\text{N}]_2\text{Ti}\text{-(NH-CH}_2\text{-}\cdots)_2$ species is consistent with the data, and is perhaps the best interpretation. At elevated temperatures, loss of ligand is more extensive, but it is unclear as to the nature of these reactions. Work by previous investigators may shed some light on this situation. Unimolecular decomposition of $\text{Ti}[\text{N}(\text{CH}_3)_2]_4(\text{g})$ has been the focus of a number of

investigations [43,49–51]. The onset of decomposition has been reported to be at 177 [43], 205 [50] and 207 °C [51], all of which are significantly higher than $T_s \leq 110$ °C considered here. Evidence for the formation of decomposition products such as metallacycles and imines have been found at these elevated temperatures—formation of these species could lead to loss of ligand with no additional terminal groups involved in the reaction, if these rates are sufficiently fast at $T_s = 110$ °C on a surface, which has not been seen previously [43,50,51].

In the above experiments, metallacycle formation could lead to “carbide” (Ti–C), as opposed to “organic” carbon (alkyl and methyl carbon). For example, at much higher temperatures (350–450 °C) Fix, Gordon and Hoffman [39] observed both organic and carbide carbon in TiN thin films using *ex situ* XPS. Vepřek and co-workers [48] have also observed evidence for two, possibly three, types of carbon, in this case from *in situ* XPS following low pressure exposure of a Si(100) substrate to $\text{Ti}[\text{N}(\text{CH}_3)_2]_4$. Attempts have been made to fit C(1s) XP spectra for the –OH, –NH₂ and –CH₃ terminated SAMs, after saturation exposures to $\text{Ti}[\text{N}(\text{CH}_3)_2]_4$ at $T_s = 110$ °C, to two peaks: one at 285 eV (organic) and one at either 282 eV (carbide) or 283 eV (metallacycle, assigned by Vepřek and co-workers [48]). These attempts were unsuccessful, the low binding energy peaks were essentially zero. Goodman and co-workers have speculated that loss of H from a –CH₃ could eliminate a $\text{N}(\text{CH}_3)_2$ ligand [forming $\text{HN}(\text{CH}_3)_2$], leaving a $\text{N}(\text{CH}_3)=\text{CH}_2$ ligand [45]. In the above experiments, if a $[(\text{CH}_3)_2\text{N}]_2\text{Ti}-(\text{NH}-\text{CH}_2-\cdots)_2$ species were present, only one ligand could be removed in this fashion. Elimination of both dimethylamido ligands by H transfer from the two SAM–NH– linkages, however, could lead to an imido complex, $(\cdots\text{CH}_2\text{CH}_2\text{N})=\text{Ti}=(\text{N}-\text{CH}_2-\text{CH}_2-\cdots)$, and complete removal of the $\text{N}(\text{CH}_3)_2$ ligands. Indeed, in comparing saturation

coverages on the $-\text{NH}_2$ SAM, there is a $\sim 20\%$ reduction in the C(1s) peak for an increase in T_s from -50 to 110 $^\circ\text{C}$, and the area for the C(1s) peak at 110 $^\circ\text{C}$ is $\sim 10\%$ less than that of the bare $-\text{NH}_2$ SAM [both consistent with considerable loss of $\text{N}(\text{CH}_3)_2$ ligand]. This scenario remains an intriguing possibility, which would require additional experiments and/or theoretical calculations to verify. It is of interest to note that the bridging $-\text{O}-$ lacks such a H to eliminate the $\text{N}(\text{CH}_3)_2$ ligands, consistent with the apparent retention of 1–2 ligands on surfaces with $-\text{OH}$ present.

3.4 Conclusions

The reactions of $\text{Ti}[\text{N}(\text{CH}_3)_2]_4$ with self assembled monolayers possessing $-\text{OH}$, $-\text{NH}_2$ and $-\text{CH}_3$ terminal groups have been examined in detail. The initial probability of reaction of $\text{Ti}[\text{N}(\text{CH}_3)_2]_4$ was found to be largest on the chemical oxide surface (starting surface to form the SAMs) with $S_{R,0} \sim 0.5$ at $T_s = -50$ $^\circ\text{C}$. On the SAM-terminated surfaces, reaction probabilities followed the order: $-\text{OH} > -\text{NH}_2 > -\text{CH}_3$. In all cases the reaction probability did not vary more than a factor of two over the substrate temperature range examined, $T_s = -50$ $^\circ\text{C}$ to 110 $^\circ\text{C}$. In addition, in all cases the kinetics of adsorption, i.e. the coverage–exposure relationships, could be sufficiently well described by a first-order Langmuirian model, and the saturation coverages did not depend strongly on the substrate temperature. Angle-resolved XPS revealed that penetration of the SAMs occurred in the cases of the $-\text{OH}$ and $-\text{CH}_3$ terminated SAMs. In particular, the apparent reactivity between $\text{Ti}[\text{N}(\text{CH}_3)_2]_4$ and the $-\text{CH}_3$ SAM could be completely accounted for by assuming that reaction occurred only at the SAM/ SiO_2 interface. In contrast,

concerning the -NH_2 terminated SAM, results from ARXPS were completely consistent with $\text{Ti}[\text{N}(\text{CH}_3)_2]_4$ reaction only at the terminal -NH_2 group. Results for the -OH SAM indicated $\text{Ti}[\text{N}(\text{CH}_3)_2]_4$ reactivity at the terminal -OH group and at the SAM/ SiO_2 interface. Examination of the stoichiometry of the adlayers (i.e. the Ti:N ratio), indicated that reaction of $\text{Ti}[\text{N}(\text{CH}_3)_2]_4$ and subsequent loss of ligands was significant on all surfaces, particularly for $T_s \geq 30$ °C. On all surfaces and at -50 °C elimination of ~ 2 $\text{N}(\text{CH}_3)_2$ ligands was apparent. As substrate temperature increased from -50 to 110 °C, about one additional ligand was lost on all surfaces, except for the -NH_2 SAM where about two additional ligands were lost. On the -NH_2 SAM, saturation corresponded to one adsorbed $\text{Ti}[\text{N}(\text{CH}_3)_2]_4$ molecule per two SAM molecules, which is consistent with the steric limitation between $\text{Ti}[\text{N}(\text{CH}_3)_2]_4$ fragments expected for nearest neighbor distances of about $7\text{-}8$ Å.

3.5 References

1. *Conjugated Polymer Surfaces and Interfaces, Electronic and Chemical Structure of Interfaces for Polymer Light Emitting Devices*, edited by W. R. Salaneck, S. Stafstrom, J. -L. Bredas (Cambridge University Press: Cambridge, 1996).
2. L. Yan and Y. Gao, *Thin Solid Films* **417**, 101–106 (2002).
3. *Molecular Electronics: Science and Technology*, edited by A. Aviram and M. Ratner (Ann. NY. Acad. Sci.: New York, 1998, Vol. 852).
4. H. Ishii, K. Sugiyama, E. Ito and K. Seki, *Adv. Mater.* **11**, 605 (1999).
5. J. Chen, M. A. Reed, S. M. Dirk, D W. Price, A. M. Rawlett, J. M. Tour, D. S. Grubisha and D. W. Bennett, *NATO Science Series, II: Mathematics, Physics and Chemistry* **96**, 59 (2003).
6. B. C. Haynie, A. V. Walker, T. B. Tighe, D. L. Allara, and N. Winograd, *Appl. Surf. Sci.* **203–204**, 433 (2003).
7. Y. Hsu, T. E. F. M. Standaert, G. S. Oehrlein, T. S. Kuan, E. Sayre, K. Rose, K. Y. Lee and S. M. Rossnagel, *J. Vac. Sci. Technol. B* **16**, 3344 (1998).
8. S. M. Rossnagel, *J. Vac. Sci. Technol. B* **20**, 2328 (2002).
9. J. W. Elam, C. A. Wilson, M. Schuisky, Z. A. Sechrist and S. M. George, *J. Vac. Sci. Technol. B* **21**, 1099 (2003).
10. A. Ulman, *An Introduction to Ultrathin Organic Films, From Langmuir–Blodgett to Self-Assembly* (Academic Press: Boston, 1991).
11. L. H. Dubois and R. G. Nuzzo, *Annu. Rev. Phys. Chem.* **43**, 437 (1992).
12. A. Ulman, *Chem. Rev.* **96**, 1533 (1996).

13. H. Shin, R. J. Collins, M. R. De Guire, A. H. Heuer and C. N. Sukenik, *J. Mater. Res.* **10**, 692 (1995).
14. H. Shin, R. J. Collins, M. R. De Guire, A. H. Heuer and C. N. Sukenik, *J. Mater. Res.* **10**, 699 (1995).
15. Z. Xiao, X. Minhua, G. Jianhua, H. Dang and L. Zuhong, *Mater. Chem. Phys.* **52**, 170 (1998).
16. T. P. Niesen, J. Bill and F. Aldinger, *Chem. Mater.* **13**, 1552 (2001).
17. Y. Masuda, Y. Jinbo, T. Yonezawa and K. Koumoto, *Chem. Mater.* **14**, 1236 (2002).
18. D. R. Jung and A. W. Czanderna, *Crit. Rev. Sol. St. Mat. Sci.* **19**, 1 (1994).
19. G. C. Herdt, D. R. Jung, and A. W. Czanderna, *Prog. Surf. Sci.* **50**, 103 (1995).
20. D. R. Jung, A. W. Czanderna and G. C. Herdt, *J. Vac. Sci. Technol. A* **14**, 1779 (1996).
21. K. Konstadinidis, P. Zhang, R. L. Opila and D. L. Allara, *Surf. Sci.* **338**, 300 (1995).
22. G. L. Fisher, A. Hooper, R. L. Opila, D. R. Jung, D. L. Allara and N. Winograd, *J. Electron. Spectrosc. Relat. Phenom.* **98–99**, 139 (1999).
23. G. L. Fisher, A. E. Hooper, R. L. Opila, D. L. Allara and N. Winograd, *J. Phys. Chem. B* **104**, 3267 (2000).
24. A. Hooper, G. L. Fisher, K. Konstadinidis, D. Jung, H. Nguyen, R. Opila, R. W. Collins, N. Winograd and D. L. Allara, *J. Am. Chem. Soc.* **121**, 8052 (1999).
25. R. A. Fischer, U. Weckenmann, C. Winter, J. Kashammer, V. Scheumann and S. Mittler, *Journal de Physique IV: Proceedings* **11**, Pr3/1183 (2001).

26. J. Weiss, H. J. Himmel, R. A. Fischer and C. Woell, *Chem. Vap. Depn.* **4**, 17 (1998).
27. P. Wohlfart, J. Weiss, J. Kashammer, M. Kreiter, C. Winter, R. Fischer and S. Mittler–Neher, *Chem. Vap. Depn.* **5**, 165 (1999).
28. D. C. Bradley and I. M. Thomas, *J. Chem. Soc.* 3857 (1960).
29. D. C. Bradley and E. G. Torrible, *Can. J. Chem.* **41**, 134 (1963).
30. A. E. Kaloyeros and E. Eisenbraun, *Annu. Rev. Mater. Sci.* **30**, 363 (2000).
31. (a) M. Eizenberg, *MRS Bull.* **20**, 38 (1995). (b) D. K. Ferry, M. N. Kozicki and G. B. Raupp, *Some Fundamental Issues on Metallization in VLSI* (SPIE: San Jose, 1991).
32. S. –Q. Wang, I. Raaijmakers, B. J. Burrow, S. Suthar, S. Redkar, K. –B. Kim, *J. App. Phys.* **68**, 5176 (1990).
33. M. Moriyama, T. Kawazoe, M. Tanaka and M. Murakami, *Thin Solid Films* **416**, 136 (2002).
34. L. A. Okada and S. M. George *Appl. Surf. Sci.* **137**, 113 (1999).
35. (a) S. R. Kurtz and R. G. Gordon, *Thin Solid Films* **140**, 277 (1986). (b) M. Ritala, M. Leskela, E. Rauhala and P. Haussalo, *J. Electrochem. Soc.* **142**, 2731 (1995). (c) M. Ritala, T. Asikainen, M. Leskela, J. Jokinen, R. Lappalainen, M. Utriainen, L. Niinisto and E. Ristolainen, *Appl. Surf. Sci.* **120**, 199 (1997). (d) J. Uhm and H. Jeon, *Jpn. J. Appl. Phys.* **40**, 4657 (2001).
36. N. Yokoyama, K. Hinode and Y. Homma, *J. Electrochem. Soc.* **138**, 190 (1991).
37. K. Sugiyama, S. Pac, Y. Takahashi and S. Motojima, *J. Electrochem. Soc.* **122**, 1545 (1975).

38. K. Ishihara, K. Yamakazi, H. Hamada, K. Kamisako and Y. Tarui, *Jpn. J. Appl. Phys.* **29**, 2103 (1990).
39. (a) R. M. Fix, R. G. Gordon and D. M. Hoffman, *Mater. Res. Soc. Symp. Proc.* **168**, 357 (1990). (b) R. M. Fix, R. G. Gordon and D. M. Hoffman, *Chem. Mater.* **2**, 235 (1990).
40. (a) R. M. Fix, R. G. Gordon and D. M. Hoffman, *J. Am. Chem. Soc.* **112**, 7833 (1990). (b) R. M. Fix, R. G. Gordon and D. M. Hoffman, *Chem. Mater.* **3**, 1138 (1991).
41. I. J. Raaijmakers, R. N. Vrtis, J. Yang, S. Ramaswami, A. Lagendijk, D. A. Roberts and E. K. Broadbent, *Mater. Res. Soc. Symp. Proc.* **260**, 99 (1992).
42. A. Katz, A. Feingold, S. Nakahara, S. J. Pearton, E. Lane, M. Geva, F. A. Stevie and K. Jones, *Jpn. J. Appl. Phys.* **71**, 993 (1992).
43. L. H. Dubois, B. R. Zegarski and G. S. Girolami, *J. Electrochem Soc.* **139**, 3603 (1992).
44. (a) J. A. Prybyla, C. -M. Chiang and L. H. Dubois, *J. Electrochem. Soc.* **140**, 2695 (1993). (b) L. H. Dubois, *Polyhedron* **13**, 1329 (1994).
45. C. M. Truong, P. J. Chen, J. S. Corneille, W. S. Oh and D. W. Goodman, *J. Phys. Chem.* **99**, 8831 (1995).
46. R. G. Gordon and J. N. Musher, *J. Mater. Res.* **11**, 989 (1996).
47. B. H. Weiller, *J. Am. Chem. Soc.* **118**, 4975 (1996).
48. G. Ruhl, R. Rehmert, M. Knizova, R. Merica and S. Vepřek, *Chem. Mater.* **8**, 2712 (1996).
49. T. R. Cundari and J. M. Morse Jr., *Chem. Mater.* **8**, 189 (1996).
50. J. P. A. M. Driessen, J. Schoonman and K. F. Jensen, *J. Electrochem. Soc.* **148**, G178 (2001).

51. C. Amato–Wierda and E. T. Norton Jr., *Chem. Mater.* **13**, 4655 (2001).
52. J. –W. Lim, H. –S. Park and S– –W. Kang, *J. Electrochem. Soc.* **148**, C403 (2001).
53. H. K. Kim, J. Y. Kim, J. N. Park, Y. Kim, Y. D. Kim, H. Jeon and W. M. Kim, *J. Kor. Phys. Soc.* **41**, 739 (2002).
54. J. Y. Kim, G. H. Choi, Y. D. Kim, Y. Kim and H. Jeon, *Jap. J. Appl. Phys. Part 1* **42**, 4245 (2003).
55. J. W. Elam, M. Schuisky, J. D. Ferguson and S. M. George, *Thin Solid Films* **436**, 145 (2003).
56. A. Liebmann–Vinson, L. M. Lander, M. D. Foster, W. J. Brittain, E. A. Vogler, C. F. Majkrzak and S. Satija, *Langmuir* **12**, 2256 (1996).
57. S. R. Wasserman, Y. –T. Tao and G. M. Whitesides, *Langmuir* **5**, 1074 (1989).
58. N. Balachander and C. N. Sukenik, *Langmuir* **6**, 1621 (1990).
59. *Practical Surface Analysis: Volume I, Auger and X–ray Photoelectron Spectroscopy, 2nd ed.* Edited by M. P. Seah and D. Briggs (John Wiley and Sons: Chichester, England, 1990).
60. *Atomic, Molecular and Solid State Structure Studied by Means of Electron Spectroscopy*; K. Siegbahn, C. Nordling, A. Fahlman, A. Nordberg, K. Hamrin, J. Hedman, G. Johansson, T. Bergmark, S. Karlsson, I. Lingbren (Almquist and Wiksells: Uppsala, Sweden, 1967).
61. C. Y. Wong and S. P. Klepner, *Appl. Phys. Lett.* **48**, 1229 (1986).
62. R. R. Rye, G. C. Nelson and M. T. Dugger, *Langmuir* **13**, 2965 (1997).
63. Th. Gross, A. Lippitz, W. Unger, and B. Guttler, *Surf. Interface Anal.* **29**, 891 (2000).
64. C. L. A. Lamont and J. Wilkes, *Langmuir* **15**, 2037 (1999).

65. N. W. Ashcroft and N. D. Mermin, *Solid State Physics* (Harcourt Brace College Publishers: U.S.A., 1976).
66. C. J. Powell and A. Jablonski, *J. Vac. Sci. Technol. A* **17**, 1122 (1999).
67. S. R. Wasserman, G. M. Whitesides, I. M. Tidswell, B. M. Ocko, P. S. Pershan and J. D. Axe, *J. Am. Chem. Soc.* **111**, 5852 (1989).
68. J. H. Moon, J. W. Shin, S. Y. Kim and J. W. Park, *Langmuir* **12**, 4621 (1996).
69. K. M. R. Kallury, P. M. Macdonald and M. Thompson, *Langmuir* **10**, 492 (1994).
70. H. Lee, S. M. Lee, E. T. Ada, B. Kim, M. Weiss, S. S. Perry and J. W. Rabalais, *Nuclear Instruments and Methods in Physics Research B* **157**, 226 (1999).
71. M. P. Seah and W. A. Dench, *Surf. Interface Anal.* **1**, 2 (1979).
72. P. Kisliuk, *J. Phys. Chem. Solids* **3**, 95 (1957).
73. M. Haran, J. R. Engstrom and P. Clancy, submitted to *J. Am. Chem. Soc.* (2005).
74. J. S. Corneille, P. J. Chen, C. M. Truong, W. S. Oh and D. W. Goodman, *J. Vac. Sci. Technol. A* **13**, 1116 (1995).
75. P. F. Ma, A. Dube, A. S. Killampalli and J. R. Engstrom, in preparation.
76. W. H. Weinberg, "Dynamics of Gas-Surface Interactions," edited by C. T. Rettner and M. N. R. Ashfold (The Royal Society of Chemistry, Cambridge, 1991).

4. Nucleation of pentacene on silicon dioxide at hyperthermal energies*

4.1 Overview

The nucleation of pentacene on silicon dioxide, incident at hyperthermal energies, has been investigated with atomic force microscopy. The incident kinetic energy of the pentacene molecules strongly influences the process of adsorption – the adsorption probability decreases with increasing incident kinetic energy, indicative of trapping-mediated adsorption. In addition, the trapping probability of pentacene decreases with more glancing angles of incidence, a result inconsistent with so-called normal energy scaling. Analysis of the dependence of the island density on the growth rate in the sub-monolayer regime indicates that growth at all energies is consistent with a critical cluster containing four molecules.

4.2 Introduction

Pentacene is a promising candidate for applications in organic thin film electronics [1–3] owing to the ability to form highly ordered thin films near room temperature. Charge carrier mobilities exceeding values for amorphous silicon have been demonstrated for organic thin film transistors (OTFTs) of pentacene ($1.5 \text{ cm}^2\text{-V}^{-1}\text{-s}^{-1}$ [4]). Deposition over large areas and on flexible substrates are viable possibilities with pentacene thin films [5–6]. Despite this

* *Appl. Phys. Lett.* **87**, 033110 (2005)

strong interest in pentacene OTFTs much still remains to be learned concerning the nucleation and growth of organic thin films, as well as the correlations between their microstructure and electronic properties.

Charge transport in an OTFT is affected strongly by the first few layers that are in close contact with the gate dielectric [7], which emphasizes the importance of the initial nucleation regime. Nucleation and growth of pentacene on SiO₂ has been studied by several investigators using (thermal energy) evaporation sources in vacuum. From island size distributions and dynamic scaling arguments, Scoles and co-workers [8] proposed diffusion mediated growth was operative, with a critical island size of four molecules. In other work, these same workers found that the island density of pentacene on oxidized Si(100) was higher than that on hydrogen terminated Si (100) by two orders of magnitude [9]. Tromp and co-workers also studied the nucleation of pentacene on oxidized, H-terminated, and cyclohexene saturated Si (100) using *in situ* photoelectron emission microscopy (PEEM). These workers also found that the island density was much higher on SiO₂ compared to H- or cyclohexene terminated Si (100) [10]. Finally, Zuppiroli and co-workers [11,12] used *ex situ* AFM to examine the nucleation of pentacene on SiO₂ and found that the island density increased with the rate of deposition, and decreased with increasing temperature, consistent with homogenous nucleation, and growth via capture of diffusing admolecules.

One factor expected to affect the nucleation and growth of organic thin films is the kinetic energy of the incident molecules. Supersonic molecular beams provide an ideal tool to vary the kinetic energy of incident pentacene molecules over a useful range, i.e., on the order of, or greater than, the pentacene-pentacene and pentacene-SiO₂ binding energies. Of the few studies

that have been conducted to date on the energetic deposition of pentacene, these have focused on the growth of multilayer films [13,14] and on the performance of thin film transistors fabricated using these energetic beams [15]. In the work reported here, supersonic molecular beam techniques are used to examine explicitly the nucleation of pentacene thin films on SiO₂ under ultrahigh vacuum (UHV) conditions. In particular, the effects of both the kinetic energy and the angle of incidence of the pentacene molecules have been considered on nucleation behavior, focusing on the sub- and near monolayer regime.

4.3 Experimental methods

The experimental methods have been described in detail in section 2.2. Briefly, experiments were carried out in a custom-designed UHV chamber that has been described in detail elsewhere [16]. The base pressure of the chamber is typically $\sim 2 \times 10^{-9}$ Torr. Substrates were Si (100) wafers (Wacker-Siltronic, p-type, 4" dia., 500–550 μm thick, 38–63 $\Omega\text{-cm}$) subject to a RCA-1 clean, 15 s. HF dip and a RCA-2 clean immediately before growth of approximately 300 nm thick SiO₂ films by wet thermal oxidation at 1100 °C. Immediately prior to placement into the load-lock of the vacuum chamber, these wafers were cleaned and degreased by sonication for 15 min. in anhydrous CHCl₃ solution (99%+), sonicated in H₂O for 15 min., washed with DI water, dried with N₂ and cleaned with UV-Ozone for 10 min. This gave a clean and reproducible hydrophilic surface. Supersonic molecular beams of pentacene (99.8% Sigma-Aldrich) were generated by passing a carrier gas (He and N₂, 99.999%) over a temperature controlled container (the evaporator) located upstream of the nozzle (150 μm orifice) [17]. The flow of carrier gases, m_{cg} ,

was modulated using a mass flow controller. The doubly differentially pumped beams passed through a trumpet shaped skimmer (1.5 mm aperture, Beam Dynamics) into an antechamber and through an aperture that produced a well defined 11.4 mm \times 11.4 mm beam spot on the substrate at normal incidence. The beams could be blocked using a shutter in the antechamber, facilitating precise exposures of the substrate to the beam. Kinetic energies of the molecules, E_i , were measured using time-of-flight mass spectrometric techniques [17].

To initiate an experiment, both the nozzle and evaporator were preheated to the desired temperature (T_{noz} , T_b ; $T_{\text{noz}} - T_b \sim 150\text{--}200\text{ }^\circ\text{C}$) under a moderate flow of the carrier gas. When the temperature of the evaporator was close to the desired value, the carrier gas flow rate was set to its final value, and the intensity of the beam was measured with a quadrupole mass spectrometer (Extrel) located downstream, on the beam axis. During this time the sample was held in a chamber intermediate to the load-lock and main (growth) chambers. When the temperature of the evaporator had stabilized ($\pm 0.5\text{ }^\circ\text{C}$) to yield the desired intensity, the shutter for the beam located in the antechamber was closed and the sample was translated into the main chamber. Upon opening of the shutter, the sample was exposed to the beam and deposition was started. During exposure the sample was periodically translated perpendicular to the beam axis (beam-to-background flux $> 350:1$), thus producing areas on the substrate surface (8 areas, $1 \times 10\text{ mm}^2$ each) representing different exposure times, yet identical deposition conditions (T_{noz} , T_b , T_s , m_{cg}) [16]. Following thin film deposition and removal of the substrate from the chamber, the samples were examined *ex situ* using a Digital Instruments Dimension 3100 scanning probe microscope (Veeco Instruments) in tapping mode. Typical images

obtained were of size $20 \times 20 \mu\text{m}^2$ and subjected to a second order plane fit using Nanoscope software (v 5.0).

4.4 Results and discussion

For each experiment, an AFM image was obtained for each exposure time resulting in a series of “snapshots” at different stages in the nucleation process. Displayed in Fig. 4–1 is one such series for the nucleation of pentacene on SiO_2 at $E_i = 6.7 \text{ eV}$. As may be seen, for these conditions, clearly defined islands of pentacene nucleate within 15 s and their density remains constant as they grow. Also shown in Fig. 4–1 is a line scan for a 75 s exposure, and analysis indicates that the islands are $\sim 15.9 \pm 0.1 \text{ \AA}$ in height, which is consistent with pentacene molecules standing up in the thin film phase (15.4 \AA) [18]. It is important to note that the islands are compact at all exposure times, which for example, facilitates a straightforward analysis of the island density for each image. Coverage as a function of exposure is obtained using histogram analysis of these images (Origin 7.0, Originlabs Inc.). At 125 s, coalescence has begun, yet there appears to be minimal restructuring of the islands once two or more islands have fused. Also a second layer has begun to grow on the first, and this is clearly apparent at 300 s. The first two layers are best described as growing layer–by–layer (Frank van der Merwe or Stranski–Kranstanov), and there are no three–dimensional islands at these coverages.

The coverage of submonolayer pentacene films as a function of exposure is plotted in Fig. 4–2 for the four E_i studied: 1.5, 2.7, 4.5 and 6.7 eV. Here, the

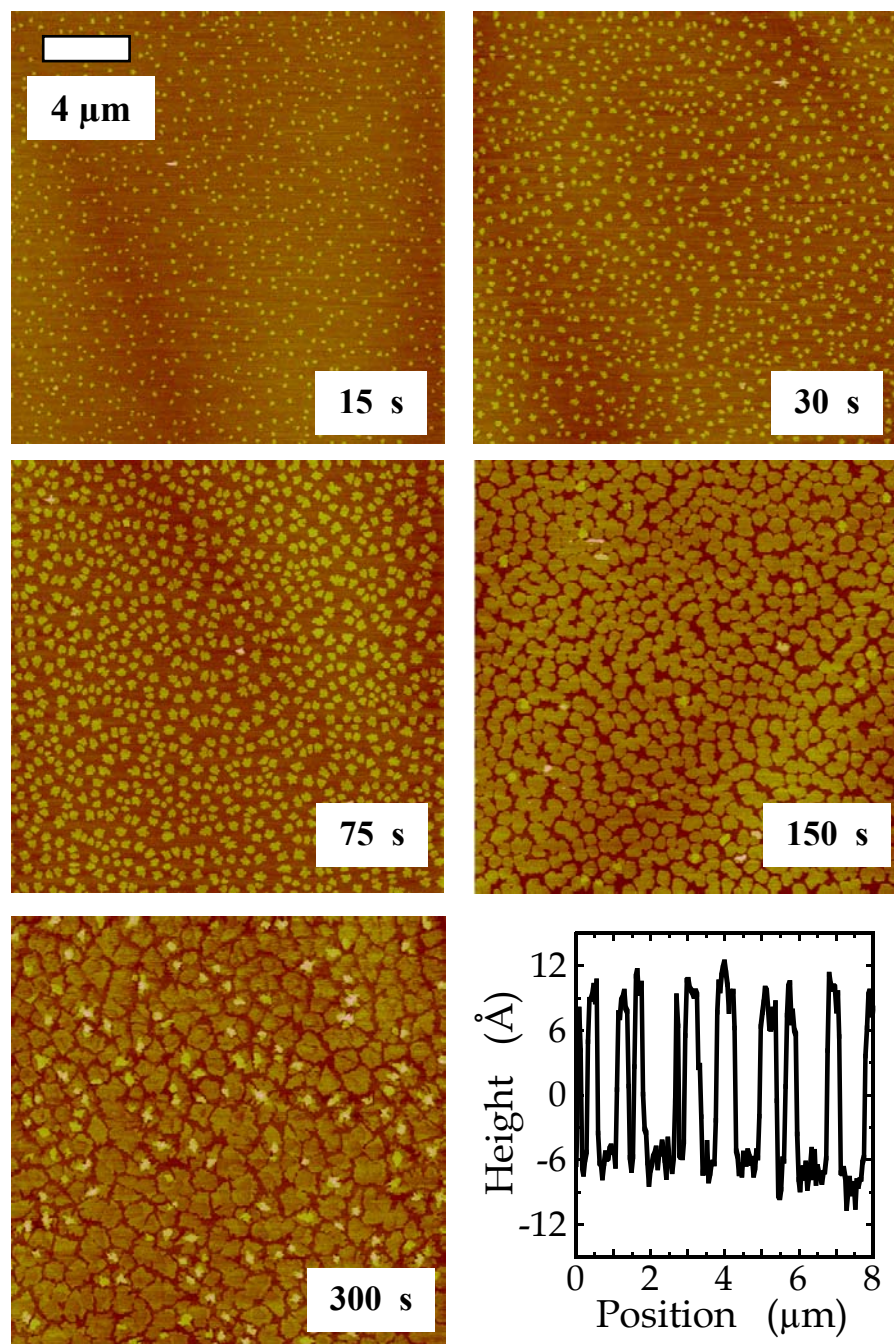


Figure 4–1 Atomic force micrographs of pentacene on SiO₂ as a function of exposure to the supersonic beam ($E_i = 6.7$ eV, $\theta_i = 0^\circ$). In each case the field of view is $20 \mu\text{m} \times 20 \mu\text{m}$. Also shown is a line scan across the image obtained at an exposure of 75 s. The height of pentacene islands deduced from this image is 1.59 nm.

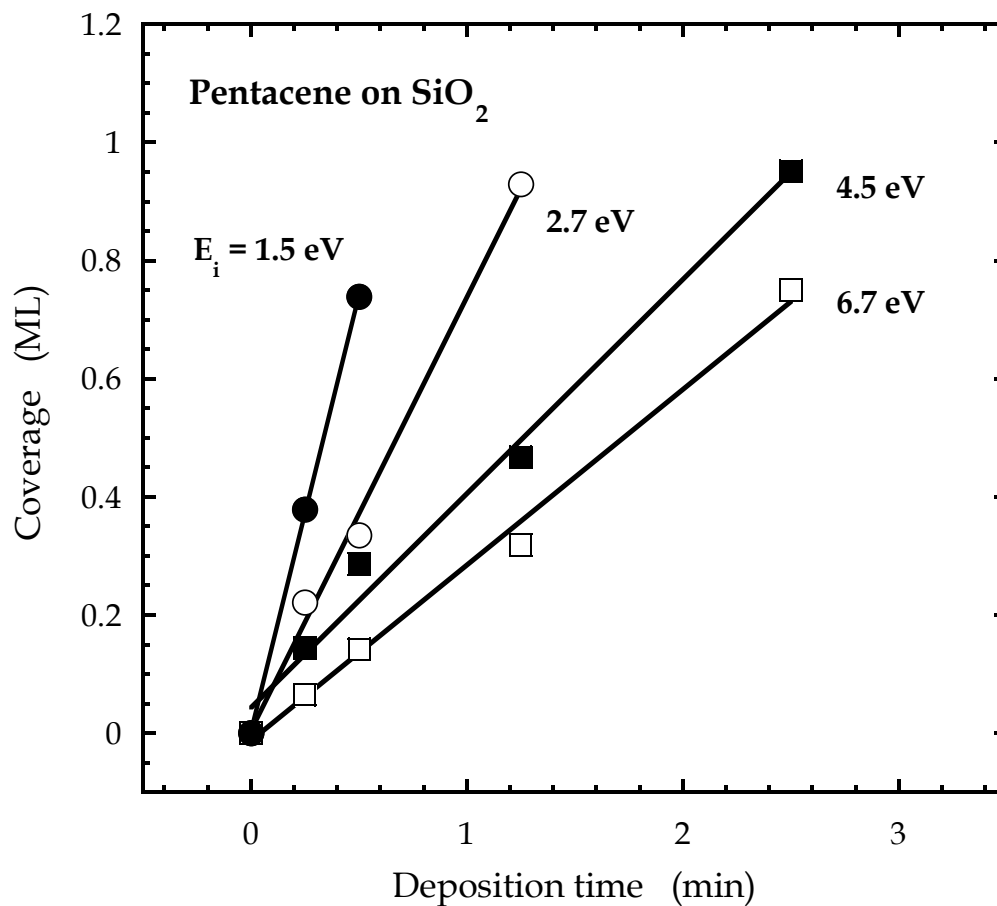


Figure 4–2 Coverage–exposure relationships, deduced from atomic force micrographs, for the adsorption of pentacene on SiO₂ at the four incident kinetic energies indicated and normal incidence. The solid lines represent linear least–squares fits to the data.

expansion conditions were varied to maintain a constant incident molecular flux, F . As may be seen, the coverage–exposure relationship is essentially linear in all cases, and the deposition rate decreases from 1.5 to 0.3 ML–min⁻¹ as E_i increases from 1.5 to 6.7 eV. This dependence on E_i is indicative of trapping–mediated adsorption of pentacene on SiO₂, where the incident kinetic energy of the molecule must be dissipated for adsorption to occur. In addition, the lack of any significant curvature in the coverage–exposure relationship, as well as any incubation period, indicates that for the submonolayer regime, trapping is approximately equivalent on bare SiO₂ and preexisting islands of pentacene. For example, more efficient trapping of pentacene on pentacene should have resulted in upward curvature—there is evidence for this. On the other hand, it would seem that molecules that are trapped on preexisting islands of pentacene incorporate into these islands, and do not start formation of a second layer, except for conditions where the coverage is on the order of 80% or greater. This is either due to efficient interlayer transport, or perhaps insertion events.

The coverage–exposure relationship has also been determined at different angles of incidence of the beam, θ_i , and from these data, (relative) probabilities of adsorption, S_A have been computed from the slope of these data in the sub–monolayer regime. In Fig. 4–3 S_A vs. θ_i is plotted for the four E_i studied here. Probabilities have been normalized with respect to the value obtained at $E_i = 1.5$ eV, and $\theta_i = 45^\circ$ (it is possible that the absolute value at this condition is less than unity). At a fixed angle of incidence, S_A decreases with increasing E_i , consistent with trapping–mediated adsorption, as discussed above. As may be seen, S_A does not change appreciably with the angle of

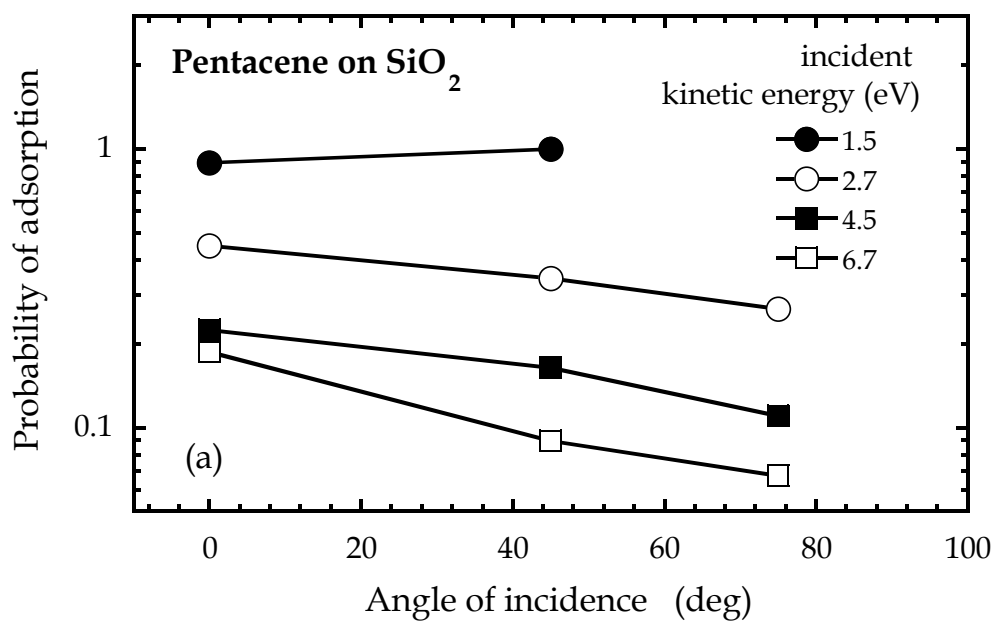


Figure 4-3 The initial probability of adsorption of pentacene on SiO₂ as a function of the angle of incidence, for four values of the incident kinetic energy. The data have been normalized to that observed for pentacene on SiO₂ at $E_i = 1.5$ eV and $\theta_i = 45^\circ$.

incidence for $E_i = 1.5$ eV, albeit for only two values of θ_i . However, at higher incident kinetic energies, S_A decreases dramatically at larger (more glancing) angles of incidence. A decrease in (trapping-mediated) S_A with increasing θ_i has only been observed in a few cases, as dissipation of the kinetic energy along the surface normal is often invoked as the requirement for trapping (normal energy scaling), particularly with atoms and simple molecules (mostly diatomics) on the surfaces of transition metals [19]. The observation of non-normal energy scaling has been attributed to the effects of substrate corrugation, (unit cell) impact parameter effects, inefficient accommodation of parallel momentum, and the role of internal energy degrees of freedom [20–24]. In terms of complexity, the results concerning the trapping of ethane on Si(100) [24] may be most comparable, where a similar (but smaller) decrease in S_A with increasing θ_i was observed.

Clearly, dissipation of the kinetic energy directed along the surface normal is not the sole factor determining the trapping of pentacene on SiO_2 . In order to quantify the contributions of perpendicular and parallel energy to the adsorption process, an empirical energy scaling function has been applied of the form $E_i f(\theta_i) = E_i(A \cos^2\theta_i + B \sin^2\theta_i)$, where $A + B = 1$, and the perpendicular (parallel) energy scales with the coefficient A (B) [22]. In the limit of $A \rightarrow 1$ normal energy scaling is recovered, and when $A = B$ total energy scaling is obtained. Displayed in Fig. 4–4 are the results of energy scaling analysis of the data shown in Fig. 4–3. Here the optimal values for A and B were determined by minimizing the mean square deviation between the scaled data and a weighted sum of two *sech* functions. As may be seen, a value of $A = 0.37 \pm 0.002$ ($B = 0.63$) describes the data best. In terms of this model,

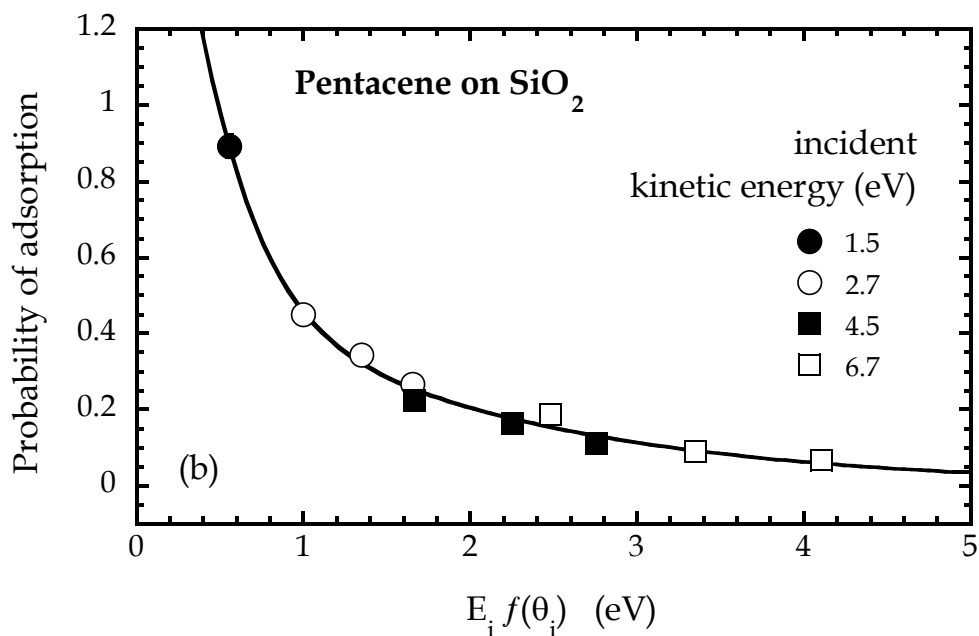


Figure 4-4 Initial (normalized) probability of adsorption of pentacene on SiO₂ as a function of scaled incident kinetic energy, $E_i f(\theta_i) = E_i(A \cos^2\theta_i + B \sin^2\theta_i)$. To find the optimum value of A the scaled data were fit to a weighted sum of two *sech* functions, which is shown as the smooth curve.

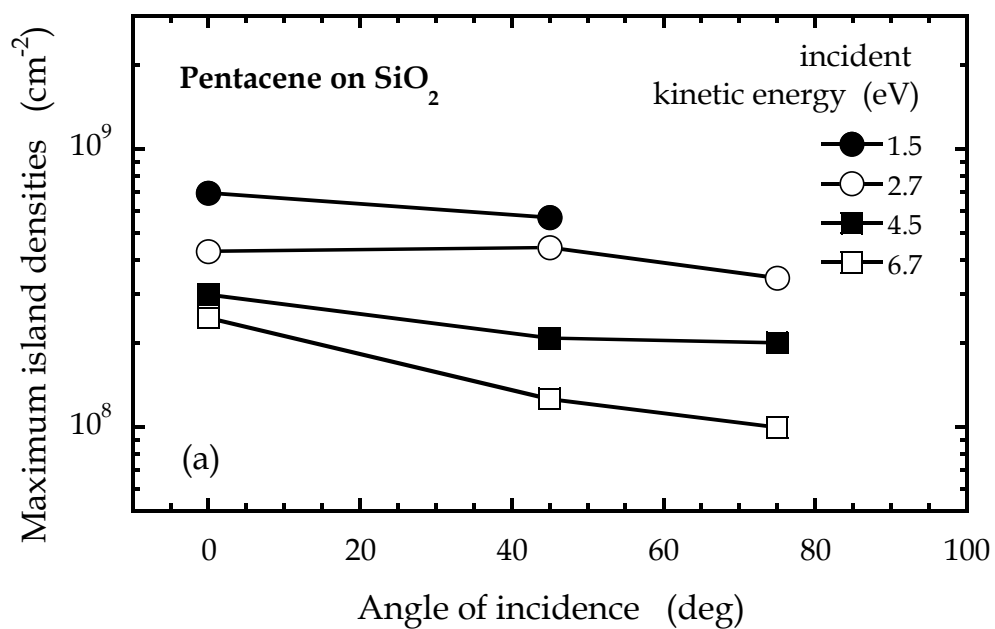


Figure 4-5 Maximum island densities for pentacene on SiO₂ as a function of the angle of incidence, for four values of the incident kinetic energy.

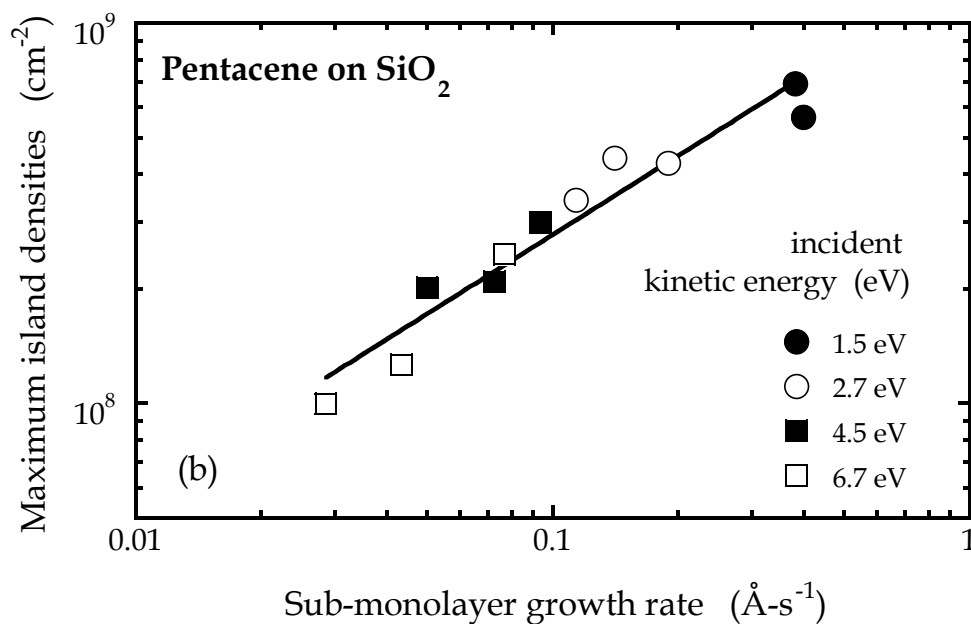


Figure 4–6 Maximum island densities for pentacene on SiO₂ vs. the sub-monolayer growth rate, using the same data set presented in Fig. 4–5. Data are presented for all incident kinetic energies and angles of incidence. The solid line represents a power law least-squares fit to the data.

which is admittedly too simplistic, and the data, a limited set of 11 conditions, accommodation of parallel and perpendicular momentum are roughly equally important.

Next, the morphological aspects of the pentacene islands that are formed in the sub-monolayer regime are examined. As indicated above, the island density once nucleated does not change appreciably during island growth — thus it has reached a maximum. In Fig. 4–5 the maximum island density, N_{\max} , is plotted as a function of the angle of incidence for the four values of E_i considered above. As may be seen, there are strong similarities between how N_{\max} depends on E_i and θ_i , and the dependence for S_A both decrease with increasing E_i and increasing θ_i . This suggests that there may be a connection between N_{\max} and S_A , or more appropriately the growth rate, $GR = S_A F$.

In terms of atomistic nucleation theory [25], for these reaction conditions and in the sub-monolayer regime, the model for complete condensation in two dimensions is used. In this regime, the maximum island density should scale with the growth rate via a power law where $N_{\max} \propto GR^{i/(i+2)}$, and i represents the size of the critical nucleus. In Fig. 4–6 N_{\max} vs. GR is plotted. As may be seen, the data is well represented by a power law expression, and a fit to the data gives a slope of 0.69 ± 0.06 , and $i = 4.5 \pm 1.3$. It is of interest to note that this value for the size of the critical nucleus is similar to those estimated recently, $i = 4$ [8] and 6 [10]. These results would suggest that for the range of kinetic energies that have been examined here, $E_i = 1.5\text{--}6.7$ eV, E_i does not significantly affect the nucleation process except how it affects S_A and hence the growth rate.

4.5 Conclusions

The nucleation of pentacene on SiO₂ has been studied using energetic molecular beams. The first monolayer essentially completes before the second layer begins to nucleate. The adsorption of pentacene is trapping mediated and accommodation of parallel momentum is as important as that of perpendicular momentum. The variation of the maximum island density with deposition conditions can be understood in terms of nucleation theory with a critical nucleus size of four molecules.

4.6 References

1. R. J. Hamers, *Nature* **412**, 489 (2001).
2. C. D. Dimitrakopoulos and P. R. L. Malenfant, *Adv. Mater.* **14**, 99 (2002).
3. S. R. Forrest, *Chem. Rev.* **97**, 1793 (1997).
4. Y. Lin, D. Gundlach, S. Nelson and T. Jackson: *IEEE Electron Device Lett.* **18**, 606 (1997).
5. D. Knipp, R. A. Street, B. Krusor, R. Apte and J. Ho, *J. Non-Cryst. Solids* **1042**, 299 (2002).
6. C. Sheraw, L. Zhou, J.-R. Huang, D. Gundlach, T. Jackson, M. G. Kane, I. G. Hill, M. S. Hammond, J. Campi and B. K. Greening, *Appl. Phys. Lett.* **80**, 1088 (2002).
7. A. Dodabalapur, L. Torsi and H. E. Katz, *Science* **268**, 270 (1995).
8. R. Ruiz, B. Nickel, N. Koch, L. C. Feldman, R. F. Haglund, Jr., A. Kahn, F. Family and G. Scoles, *Phys. Rev. Lett.* **91**, 136102-1 (2003).
9. R. Ruiz, B. Nickel, N. Koch, L. C. Feldman, R. F. Haglund, A. Kahn, F. Family and G. Scoles, *Phys. Rev. B* **67**, 125406 (2003).
10. F. -J. Meyer zu Heringdorf, M. C. Reuter and R. M. Tromp, *Appl. Phys. A* **78**, 787 (2004).
11. S. Pratontep, M. Brinkmann, F. Nüesch and L. Zuppiroli, *Synth. Met.* **146**, 387 (2004).
12. S. Pratontep, M. Brinkmann, F. Nüesch and L. Zuppiroli, *Phys. Rev. B* **69**, 165201 (2004).
13. L. Casalis, M. F. Danisman, B. Nickel, G. Bracco, T. Toccoli, S. Iannotta and G. Scoles, *Phys. Rev. Lett.* **90**, 206101-1 (2003).
14. S. Iannotta and T. Toccoli, *J. Polymer Sc. B* **41**, 2501 (2003).

15. F. De Angelis, T. Toccoli, A. Pallaoro, N. Coppedè, L. Mariucci, G. Fortunato and S. Iannotta, *Synth. Met.* **146**, 291 (2004).
16. S. E. Roadman, N. Maity, J. N. Carter and J. R. Engstrom, *J. Vac. Sci. Technol. A* **16**, 3423 (1998).
17. T. W. Schroeder, Ph. D thesis, Cornell University, 2004.
18. C. C. Mattheus, A. B. Dros, J. Baas, G. T. Oostergetel, A. Meetsma, J. L. de Boer and T. T. M. Palstra, *Synth. Met.* **138**, 475 (2003).
19. C. T. Rettner, D. J. Auerbach, J. C. Tully and A. W. Kleyn, *J. Phys. Chem.* **100**, 13021 (1996).
20. L. A. DeLouise, *Chem. Phys. Lett.* **180**, 140 (1990).
21. M. Head-Gordon and J. C. Tully, *Surf. Sci.* **268**, 113 (1992).
22. M. C. McMaster, S. Schroeder and R. J. Madix, *Surf. Sci.* **297**, 253 (1993).
23. L.-Q. Xia and J. R. Engstrom, *J. Chem. Phys.* **101**, 5329 (1994).
24. C. T. Reeves, B. A. Ferguson, C. B. Mullins, G. O. Sitz, B. A. Helmer and D. B. Graves, *J. Chem. Phys.* **111**, 7567 (1999).
25. J. A. Venables, G. D. T Spiller and M. HanbÄucken, *Rep. Prog. Phys.* **47**, 399 (1984).

5. Nucleation of pentacene thin films on silicon dioxide modified with hexamethyldisilazane

5.1 Overview

The nucleation and growth of pentacene on silicon dioxide surfaces modified with hexamethyldisilazane, $\text{HN}[\text{Si}(\text{CH}_3)_3]_2$, has been examined using supersonic molecular beam techniques and atomic force microscopy. Similar to growth on clean SiO_2 surfaces, the rate of deposition at a fixed incident flux decreases with increasing kinetic energy of the incident pentacene, indicative of trapping mediated adsorption. Unlike clean, unmodified SiO_2 surfaces, however, growth on the modified surface exhibits the characteristics of heterogeneous nucleation, where the maximum island density is independent of the deposition rate. Deposition in the sub-monolayer regime involves island growth, except that on the modified surface the islands are two molecules high, unlike the one molecule high islands observed on clean SiO_2 .

5.2 Introduction

Organic thin film electronics is attracting considerable interest due in part to the use of pentacene in organic thin film transistors (OTFTs) [1–4]. Pentacene thin films can be highly ordered when deposited near room temperature. Deposition over large areas and/or on flexible substrates [5–6] are also viable possibilities and the resulting films have exhibited excellent electrical properties. Despite a strong interest in pentacene OTFTs much still

remains to be learned concerning the fundamental mechanisms involved in the nucleation and growth of organic thin films on dielectric surfaces, especially those that have been modified to produce devices with superior electrical properties.

It is well known that the interface between pentacene and the dielectric is critical to charge transport in an OTFT [7], which highlights the importance of the initial nucleation regime and the nature of the dielectric in the case of bottom gate devices. Recent studies have examined the effects of surface modification of dielectrics such as SiO₂, using self-assembled and/or organic monolayers, on OTFT performance. Hexamethyldisilazane, HN[Si(CH₃)₃]₂ (HMDS) [8–9], and octadecyltrichlorosilane, CH₃–(CH₂)₁₇–SiCl₃ (ODTS) [10–12], have been popular choices for surface modification. HMDS has long been employed to improve the adhesion of photoresists to SiO₂ surfaces, while ODTS molecules have been extensively studied for the formation of self-assembled monolayers. Aoyagi and co-workers have shown that modification of SiO₂ substrates with HMDS results in OTFTs with improved off currents, which was attributed to a reduction in density of interfacial charge trapping states [8]. Bao and co-workers [9] have also studied the deposition of pentacene on SiO₂ modified with HMDS, using (thermal energy) evaporation sources in vacuum. These workers observed 2ML thick pentacene films deposited on O₂ plasma treated SiO₂, SiO₂ modified with HMDS and SiO₂ modified with OTS had similar unit cell dimensions. They also reported high mobilities ($3.5 \pm 0.5 \text{ cm}^2\text{-V}^{-1}\text{-s}^{-1}$) for OTFTs fabricated using SiO₂ modified with HMDS as the gate dielectric. Although the nucleation of pentacene on SiO₂ has been studied extensively [13–17], insight into the fundamental

processes involved in nucleation on SiO₂ surfaces modified by organic monolayers such as HMDS has yet to be achieved.

Among the parameters that can be exploited to modify thin film deposition processes is the incident kinetic energy of the depositing species. Making use of supersonic molecular beam techniques [18,19] the kinetic energy of molecules can be varied over a useful range, e.g., on the order of, or greater than, the pentacene–pentacene and pentacene–substrate binding energies. Of the few studies that have been conducted to date on the energetic deposition of pentacene, these have focused on the growth of multilayer films [20,21] and on the performance of thin film transistors fabricated using these energetic beams [22]. Recently, supersonic molecular beam techniques have been used to study the nucleation of pentacene on SiO₂ (thermal oxide) [23]. Here the growth rate at fixed incident flux was observed to decrease with increasing kinetic energy, while nucleation was best described as being homogenous with a critical nucleus of approximately 4–5 molecules. In the work reported here, supersonic molecular beam techniques are used to examine explicitly the nucleation of pentacene thin films on SiO₂ modified with HMDS under ultrahigh vacuum (UHV) conditions. In particular, the effects of kinetic energy of the pentacene molecules on nucleation are considered, focusing on the sub- and near monolayer regime, and these results are compared and contrasted to what has been observed on SiO₂ (described in Chapter 4).

5.3 Experimental methods

A detailed description of the experimental apparatus and methods is included in section 2.2. A brief description is provided in this section. The

experiments were carried out in a custom-designed UHV chamber [19], and many of the experimental procedures are similar to those reported previously [23]. The base pressure of the chamber was typically no greater than 2×10^{-9} torr. Substrates were Si (100) wafers (Wacker-Siltronic, p-type, 100 mm dia., 500–550 μm thick, 38–63 $\Omega\text{-cm}$) subject to a RCA-1 clean, 15 s HF dip and a RCA-2 clean followed by growth of ~ 300 nm thick SiO_2 films by wet thermal oxidation at 1100 $^\circ\text{C}$. Next these wafers were cleaned and degreased by sonication for 15 min. in anhydrous CHCl_3 solution (>99%), sonicated in H_2O for 15 min., washed with DI water, dried with N_2 and cleaned with UV-Ozone for 10 min. Finally, HMDS was deposited from the vapor phase using a YES LP-III Vapor Prime Oven after successive evacuation and purge cycles to dehydrate the substrate held at 150 $^\circ\text{C}$. Deposition time was 5 min. at a pressure of 6 Torr. These substrates were then inserted into the vacuum chamber via a fast entry load-lock.

Supersonic molecular beams of pentacene (99.8% Sigma-Aldrich Corp.) seeded in a carrier gas (He or N_2 , 99.999%) produced a well defined $11.4 \times 11.4 \text{ mm}^2$ spot on the substrate at normal incidence (beam-to-background flux > 350:1). Temperatures for the *in situ* evaporator and the supersonic nozzle source were typically, $T_{\text{evap}} \sim 250$ $^\circ\text{C}$, and $T_{\text{noz}} \sim 300$ $^\circ\text{C}$. Kinetic energies of the molecules, E_i , were measured using time-of-flight mass spectrometric techniques [24]. Beam intensity was monitored with a quadrupole mass spectrometer (Extrel) located downstream and on the beam axis. Once the desired intensity was obtained, the sample, which was at room temperature ($T_s = 23 \pm 3$ $^\circ\text{C}$), was translated into the beam. During exposure the sample was periodically translated perpendicular to the beam axis, producing areas on the substrate surface (8 areas, $1 \times 10 \text{ mm}^2$ each)

representing different exposure times, yet identical deposition conditions (E_i , T_s) [19]. Following thin film deposition and removal of the substrate from the chamber, the samples were examined *ex situ* using atomic force microscopy (AFM) in the tapping mode (Digital Instruments Dimension 3100). Images obtained were typically 5×5 or $20 \times 20 \mu\text{m}^2$ in size and were subjected to a second order plane fit using Nanoscope software (v 5.0).

5.4 Results and discussion

The SiO_2 substrates modified with HMDS were characterized by contact angle, x-ray photoelectron spectroscopy (XPS) and AFM. Advancing and receding angles were $51.5 \pm 1.4^\circ$ and $28.8 \pm 2.1^\circ$ (*cf.* a static measurement of 53.76° [25]). From XPS, the C(1s) peak is well described by a single chemically shifted component, i.e. $-\text{CH}_3(\text{a})$. Using a polycrystalline Au sample as a reference standard, and employing techniques described previously [26] the coverage of $-\text{CH}_3(\text{a})$ (a product of HMDS chemisorption) is estimated to be $6.87 \pm 1.44 \times 10^{14} \text{ molec}\text{-cm}^{-2}$. The thickness of the HMDS layer can be estimated from angle resolved XPS of a feature from the underlying substrate, namely the O(1s). Employing an inelastic mean free path of 27.4 \AA for these photoelectrons results in a thickness of $9.3 \pm 1.7 \text{ \AA}$. Finally, from AFM, the root mean square roughness of the films is found to be $\sim 2 \text{ \AA}$. It is to be noted in passing that the roughness is on the order of the value for the underlying SiO_2 , suggesting a relatively uniform and conformal organic thin film.

For each experiment, an AFM image was obtained for each exposure time resulting in a series of “snapshots” at different stages in the nucleation and

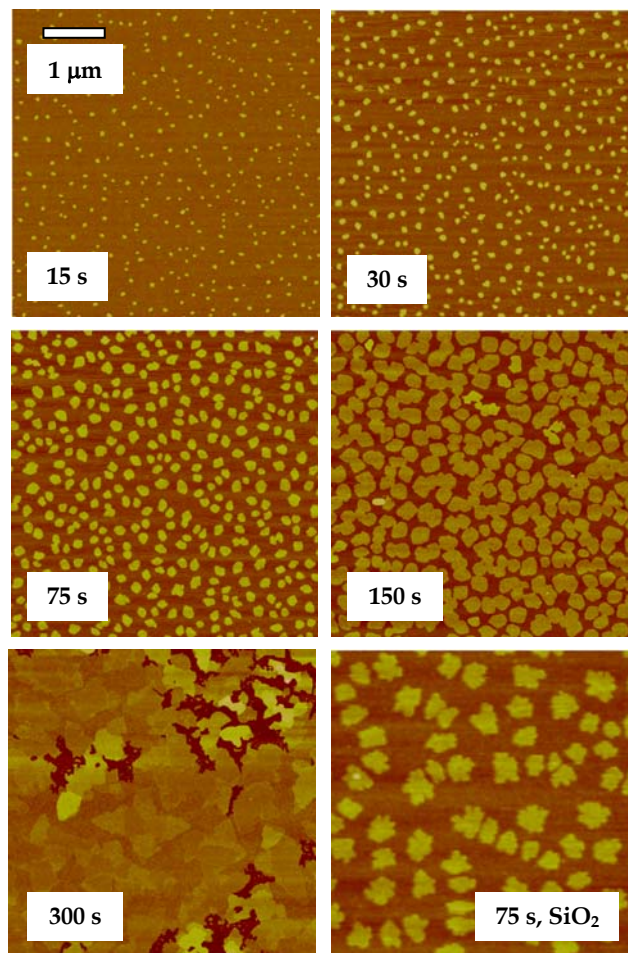


Figure 5–1 Atomic force micrographs of pentacene on SiO₂ surfaces modified with HMDS as a function of exposure to the supersonic beam ($E_i = 6.7$ eV, normal incidence). In each case the field of view is $5 \mu\text{m} \times 5 \mu\text{m}$. Also shown in the bottom right corner is a micrograph of pentacene on clean SiO₂ for otherwise identical deposition conditions and an exposure of 75 s.

growth process. Displayed in Fig. 5–1 is one such series for the nucleation of pentacene on SiO₂ modified with HMDS at $E_i = 6.7$ eV and $T_s = 23 \pm 3$ °C. A micrograph for the nucleation of pentacene on clean SiO₂ for the same conditions is also shown [23]. For these conditions, clearly defined islands of pentacene nucleate within 15 s and are compact. In addition, examination of a similar series of images for $E_i = 1.5, 2.7$ and 4.5 eV reveals similar behavior—quick formation of relatively compact islands that grow and eventually coalesce. Analysis of the images for $E_i = 6.7$ eV indicates that the island densities for exposures of 15, 30 and 75 s are $4.4, 2.3$ and 1.5×10^9 cm⁻², i.e., the maximum island density has been reached at an exposure of no more than 15 s. Most striking, however, is the fact that at an identical exposure of 75 s and for identical deposition conditions, a much larger island density is observed on the SiO₂ substrate that has been modified with HMDS.

In addition to a different island density, closer inspection of the data indicates key differences between how pentacene grows on the two surfaces. Specifically, growth of the second layer *vis a vis* the first layer commences much quicker on SiO₂ surfaces modified with HMDS. In order to better quantify this behavior, histograms (Origin 7.0, Originlabs Inc.) of the height distribution of the AFM images of these pentacene films have been obtained as a function of exposure for growth on both surfaces. These data reveal that for equivalent coverages of less than approximately a monolayer (ML) the growth involves more than a single layer on the SiO₂ surface modified with HMDS. In Fig. 5–2, the occupancy of the first and second layers, obtained from an analysis of the histograms (two examples are shown) is plotted, as a function of the total amount of material deposited for $E_i = 6.7$ eV. The results are similar

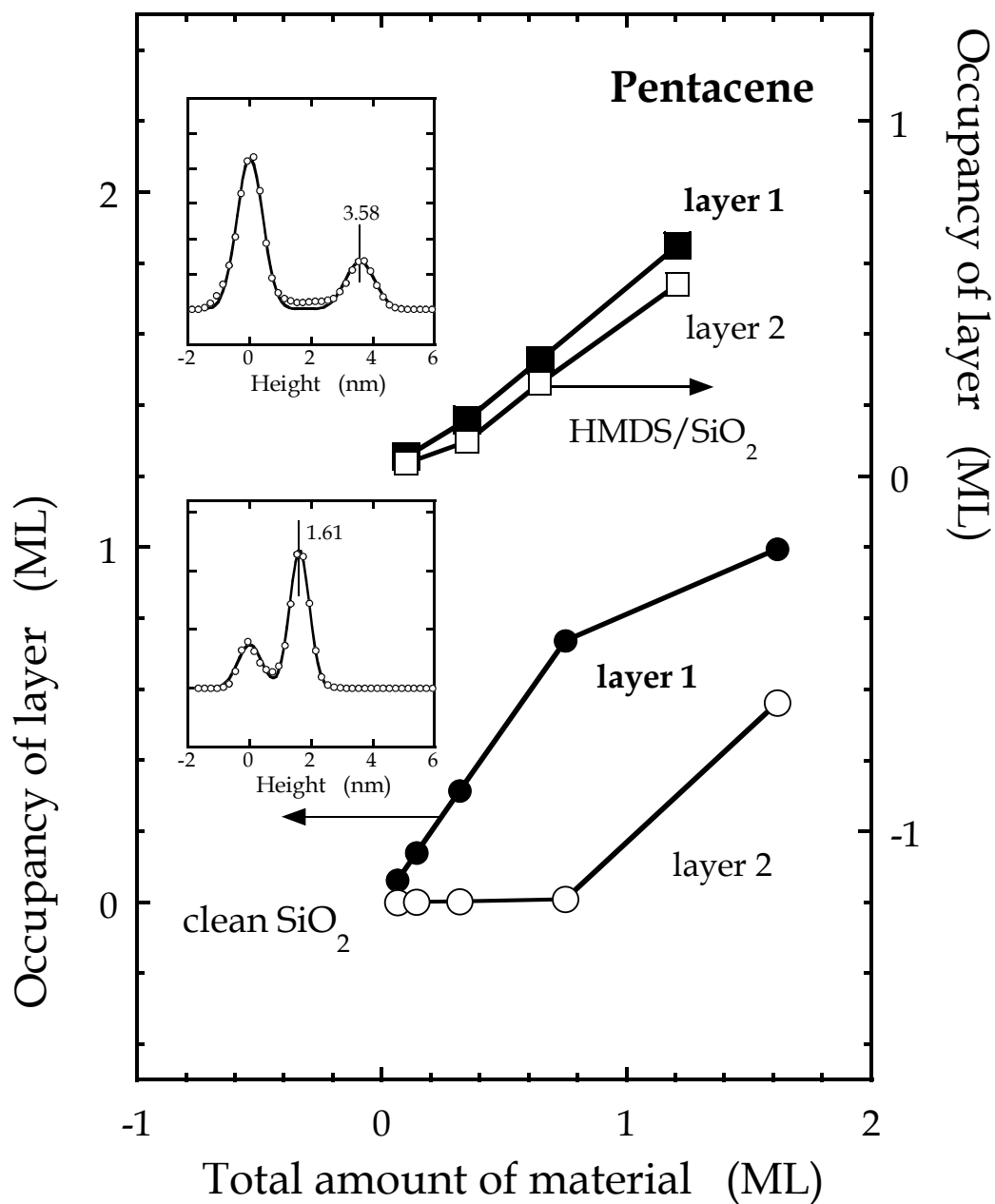


Figure 5–2 Occupancy of the first and second monolayers of pentacene as a function of total amount of material deposited on clean SiO₂ and SiO₂ modified with HMDS. Also shown are example of two histograms that were used to generate the data that is displayed in the figure.

for $E_i = 1.5, 2.7$ and 4.5 eV. As may be seen, on clean SiO_2 for a total deposit of ~ 0.75 ML essentially all of the pentacene is in the first layer (spacing between main peaks in the histogram is 16.1 ± 0.01 Å, *cf.* 16.1 Å monolayer thickness obtained by grazing incidence x-ray diffraction [27]). Only as the coverage approaches a monolayer is growth evident in the second layer. In contrast, on SiO_2 modified with HMDS, growth of the first and second layers occurs almost simultaneously (spacing between main peaks in the displayed histogram is 35.8 ± 0.02 Å, average value for 18 micrographs is 30.9 ± 7.0 Å). In fact the occupancy of the second layer is nearly that of the first layer for total coverages up to 2 ML. Thus, it appears on these surfaces, that there is a strong tendency towards forming islands that are 2 ML high, as contrasted with the 1 ML high islands observed on clean SiO_2 .

The kinetics of pentacene thin film deposition on the SiO_2 surfaces modified with HMDS has also been examined as a function of incident kinetic energy of the pentacene molecules. Here, the expansion conditions were varied to maintain a constant incident molecular flux, F . The relationship between exposure and total material deposited is essentially linear in all cases, and the deposition rate decreases from 3.46 to 0.47 ML -min^{-1} as E_i increases from 1.5 to 6.7 eV. This dependence of the growth rate at fixed incident flux on E_i is indicative of trapping-mediated adsorption of pentacene on SiO_2 modified with HMDS. Similar behavior has been observed on clean SiO_2 where for an identical set of conditions the deposition rate has been found to decrease from 1.49 to 0.29 ML -min^{-1} [23].

From the total material deposited–exposure relationships relative probabilities of adsorption can be computed as a function of incident kinetic energy for both surfaces and these results are plotted in Fig. 5–3. Here results

are normalized to the set of conditions that gave the highest growth rate: $E_i = 1.5$ eV, $T_s = 23$ °C, and the SiO₂ surface modified with HMDS. As may be seen, in both cases the adsorption probability decreases monotonically with increasing E_i , and the differences are modest in the implied dependence on E_i on the two surfaces. However, the absolute values for the adsorption probability on the modified surface exceed that on clean SiO₂ by about a factor of two. More efficient trapping on the surface modified with HMDS could be due to an increase in the binding energy of pentacene on the modified surface, or the $-\text{CH}_3(\text{a})$ groups might be more effective in accommodating the kinetic energy of the incident pentacene in the form of rotational and vibrational motion.

Next, follows a discussion of the nature of nucleation in the sub-monolayer regime for pentacene on SiO₂ modified with HMDS. For the deposition conditions described above, the island density quickly reaches a maximum and decays slowly as the islands coalesce as the first monolayer, or more accurately bilayer, is completed. In previous work on clean SiO₂ it was found that the maximum island density vs. growth rate was well described by a power law, apparently independent of the incident kinetic energy and angle of incidence of the pentacene (except for how they influence the growth rate). Thus, on clean SiO₂ the data were best described by a model that assumed that nucleation was homogeneous involving a critical nucleus of 4–5 molecules. In order to compare these results to the results reported here, in Fig. 5–4 the maximum island density vs. (sub-monolayer) growth rate is plotted for pentacene on both surfaces. As may be seen, on SiO₂ modified with HMDS, the maximum island density lies between $1.7\text{--}4.4 \times 10^9$ cm⁻², and shows no

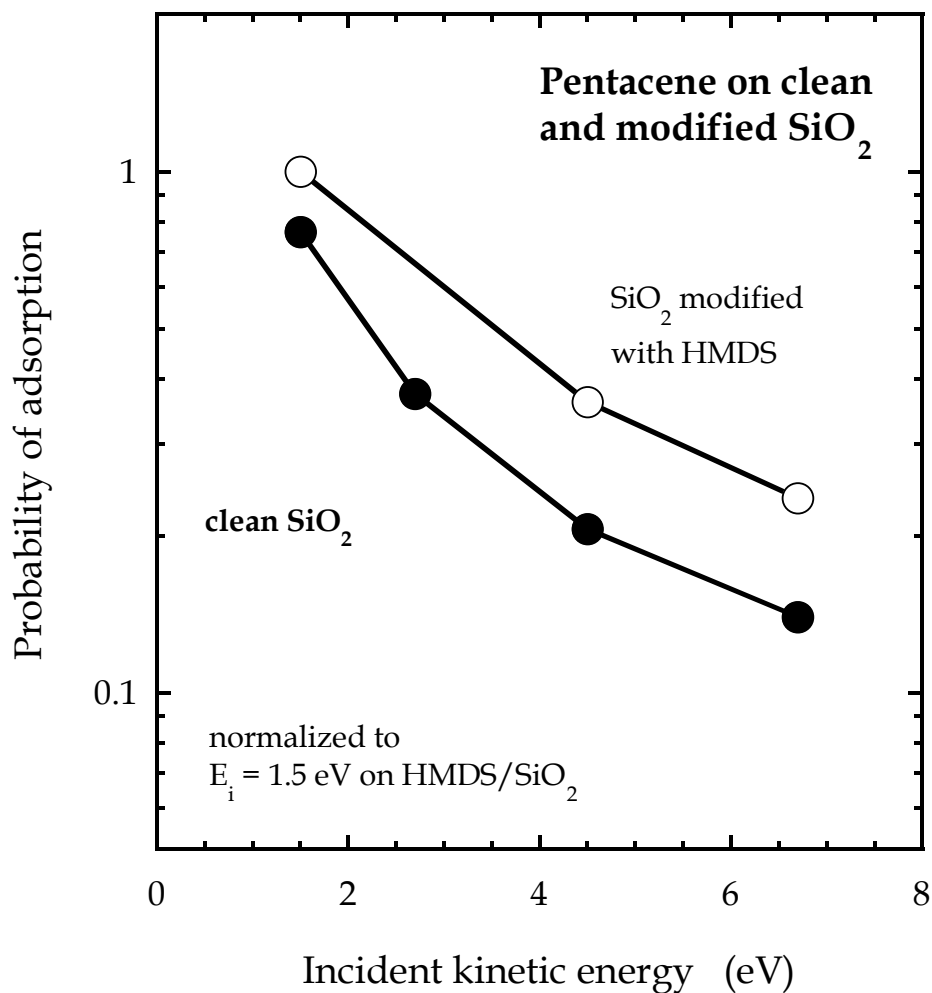


Figure 5–3 The probability of adsorption of pentacene on clean SiO₂ and SiO₂ modified with HMDS as a function of incident kinetic energy. The data have been normalized to that observed for pentacene on SiO₂ modified with HMDS at $E_i = 1.5$ eV.

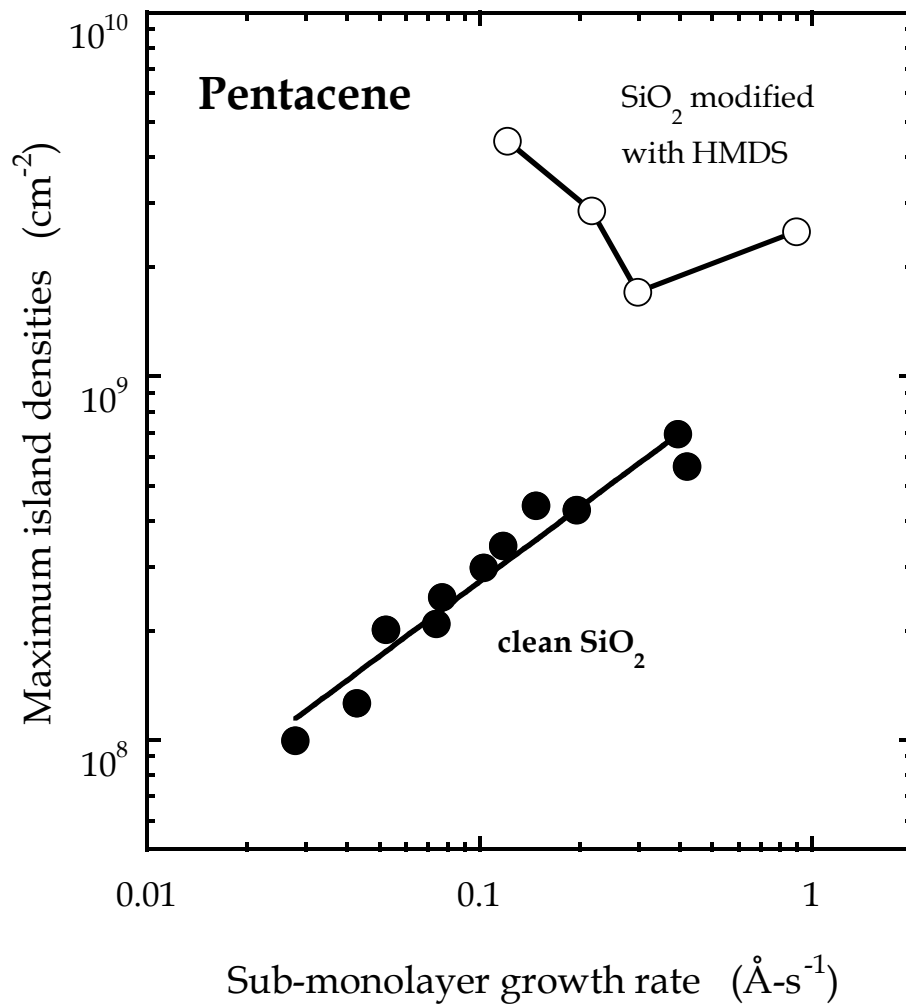


Figure 5–4 Maximum island densities for pentacene on clean SiO₂ [21] and SiO₂ modified with HMDS as a function of the growth rate in the sub-monolayer regime. For clean SiO₂, the solid line represents a power law least-squares fit of the data.

identifiable trend with growth rate (or incident kinetic energy), albeit there are only four data points (a fit gives an anomalous negative slope). At a growth rate of $\sim 0.12 \text{ \AA-s}^{-1}$, the island density on the SiO_2 surface modified with HMDS exceeds that on clean SiO_2 by a factor of ~ 13 , at a higher growth rate of 0.4 \AA-s^{-1} , it is a factor of ~ 3 . Although the diffusivity and the size of the critical nucleus may indeed be different on the SiO_2 surface modified with HMDS, giving a different slope in the case of homogeneous nucleation, an alternative explanation is more plausible. In particular, heterogeneous nucleation is a likely possibility, where pentacene nucleates preferentially at specific sites on the SiO_2 surface modified with HMDS, such as defects in the organic monolayer.

5.5 Conclusions

The nucleation of pentacene on SiO_2 surfaces modified with HMDS has been examined and several differences and some similarities to growth on clean SiO_2 have been observed. First, the kinetics of growth in terms of the probability of adsorption on the two surfaces is similar and exhibits the characteristics of trapping, which becomes less efficient at higher incident kinetic energies. Trapping is more efficient on the surface modified with HMDS. Two key differences are observed concerning the density and nature of the islands that are formed before a continuous thin film is deposited. First, on the SiO_2 surface modified with HMDS the islands that are formed are predominantly two molecules high. As there is no direct structural information on these islands, e.g., from x-ray diffraction, the possibility that a different structural phase is formed cannot be excluded, and this could be the cause for

the observed island morphology. Clearly, HMDS has produced a change in the pentacene–substrate interaction and consequently the energetics of single vs. double molecular high islands. The second difference that has been observed involves the maximum island density, which is much larger on the SiO₂ surface modified with HMDS. The fact that this density exhibits no identifiable trend with the growth rate, unlike what is observed on clean SiO₂, suggests a change in the mechanism for nucleation to one that is heterogeneous and defect-mediated. Likely defects include unmodified SiO₂–like areas on the surface, or perhaps regions that possess particularly high densities of CH₃(*a*) groups. More detailed characterization of the organic monolayer might help resolve this issue.

5.6 References

1. R. J. Hamers, *Nature* **412**, 489 (2001).
2. C. D. Dimitrakopoulos and P. R. L. Malenfant, *Adv. Mater.* **14**, 99 (2002).
3. S. R. Forrest, *Chem. Rev.* **97**, 1793 (1997).
4. Y. -Y. Lin, D. J. Gundlach, S. F. Nelson and T. N. Jackson: *IEEE Electron Device Lett.* **18**, 606 (1997).
5. D. Knipp, R. A. Street, B. Krusor, R. Apte and J. Ho, *J. Non-Cryst. Solids* **299**, 1042 (2002).
6. C. D. Sheraw, L. Zhou, J.-R. Huang, D. J. Gundlach, T. N. Jackson, M. G. Kane, I. G. Hill, M. S. Hammond, J. Campi and B. K. Greening, *Appl. Phys. Lett.* **80**, 1088 (2002).
7. A. Dodabalapur, L. Torsi and H. E. Katz, *Science* **268**, 270 (1995).
8. I. Yagi, K. Tsukagoshi and Y. Aoyagi, *Appl. Phys. Lett.* **86**, 103502 (2005).
9. H. Yang, T. J. Shin, M. M. Ling, K. Cho, C. Y. Ryu and Z. Bao, *J. Am. Chem. Soc.* **127**, 11542 (2005).
10. M. Shtein, J. Mapel, J. B. Benziger and S. R. Forrest, *Appl. Phys. Lett.* **81**, 268 (2002).
11. D. Knipp, R. A. Street, A. Völkel and J. Ho, *J. Appl. Phys.* **93**, 347 (2003).
12. H. Klauk, M. Halik, U. Zschieschang, G. Schmid, W. Radlik and W. Weber, *J. Appl. Phys.* **92**, 5259 (2002).
13. R. Ruiz, B. Nickel, N. Koch, L. C. Feldman, R. F. Haglund, Jr., A. Kahn, F. Family and G. Scoles, *Phys. Rev. Lett.* **91**, 136102-1 (2003).
14. R. Ruiz, B. Nickel, N. Koch, L. C. Feldman, R. F. Haglund, A. Kahn and G. Scoles, *Phys. Rev. B* **67**, 125406 (2003).

15. F. –J. Meyer zu Heringdorf, M. C. Reuter and R. M. Tromp, *Appl. Phys. A* **78**, 787 (2004).
16. S. Pratontep, M. Brinkmann, F. Nüesch and L. Zuppiroli, *Synth. Met.* **146**, 387 (2004).
17. S. Pratontep, M. Brinkmann, F. Nüesch and L. Zuppiroli, *Phys. Rev. B* **69**, 165201 (2004).
18. L.–Q. Xia, M. E. Jones, N. Maity and J. R. Engstrom, *J. Vac. Sci. Technol. A* **13**, 2651 (1995).
19. S. E. Roadman, N. Maity, J. N. Carter and J. R. Engstrom, *J. Vac. Sci. Technol. A* **16**, 3423 (1998).
20. L. Casalis, M. F. Danisman, B. Nickel, G. Bracco, T. Toccoli, S. Iannotta and G. Scoles, *Phys. Rev. Lett.* **90**, 206101–1 (2003).
21. S. Iannotta and T. Toccoli, *J. Polymer Sc. B* **41**, 2501 (2003).
22. F. De Angelis, T. Toccoli, A. Pallaoro, N. Coppedè, L. Mariucci, G. Fortunato and S. Iannotta, *Synth. Met.* **146**, 291 (2004).
23. A. S. Killampalli, T. W. Schroeder and J. R. Engstrom, *Appl. Phys. Lett.* **87**, 033110 (2005).
24. T. W. Schroeder, Ph. D thesis, Cornell University, 2004.
25. S. C. Lim, S. H. Kim, J. H. Lee, M. K. Kim, D. J. Kim and T. Zyung, *Syn. Met.* **148**, 75 (2005).
26. A. S. Killampalli, P. F. Ma and J. R. Engstrom, *J. Am. Chem. Soc.* **127**, 6300 (2005).
27. S. E. Fritz, S. M. Martin, C. D. Frisbie, M. D. Ward and M. F. Toney, *J. Am. Chem. Soc.* **126**, 4084 (2004).

6. Supersonic gas source deposition of pentacene thin films

6.1 Overview

The deposition of pentacene, incident at hyperthermal energies, on thermal silicon dioxide and silicon dioxide modified with hexamethyldisilazane (HMDS), has been investigated with atomic force microscopy. Multilayer pentacene films exhibit lamellar structure with three-dimensional grains on thermal SiO₂. Incident kinetic energy of pentacene molecules strongly influences the probability of adsorption of pentacene on a depositing film – probability decreases with increase in incident kinetic energy indicative of trapping-mediated physisorption. Further, multilayer deposition rates are enhanced at higher incident kinetic energies indicative of the possibility of insertion of pentacene molecules into the growing film. The ratio of multilayer to submonolayer deposition rates scales with incident kinetic energy, E_i and incident angle θ_i as $E_i \cos^n \theta_i$ where $n = 0.5$, indicative of non-normal energy scaling. Roughness scaling of pentacene thin films yields values for the growth exponent $\beta > 0.5$ for all deposition conditions indicative of rapid roughening. Film thickness is found to decrease with increasing substrate temperature owing to desorption. Films deposited at -73 °C are smoother than films deposited at higher deposition temperatures possibly due to the formation of an amorphous phase. Finally, modification of silicon dioxide with HMDS does not influence film morphology in the multilayer regime, i.e. beyond the first few monolayers in close contact with the substrate.

6.2 Introduction

Organic materials are being extensively studied for electronic and optoelectronic applications as they are relatively inexpensive and facilitate processing at lower temperatures on a wide variety of substrates compared to their inorganic counterparts. In addition, material properties can be tuned through modifications of molecular structure. Recent studies have emphasized the strong correlations between physical and electronic properties of thin films of these materials with the choice of substrate and conditions of deposition [1]. Consequently, detailed knowledge of fundamental processes occurring during deposition of organic thin films is crucial to improving their performance in electronic applications.

In the last two decades, a theoretical framework has been established relating thin film growth mechanisms to a set of scaling exponents describing the dependence of surface roughness on film thickness and lateral length scale. More recently, a few researchers have attempted to utilize dynamic scaling analysis to characterize organic thin films deposited from small molecules, at conditions far from equilibrium [2–6]. Bredas and co-workers evaporated sexithienyl films on freshly cleaved mica substrates in high vacuum and studied the effect of substrate temperature as well as post-deposition annealing on film morphology using atomic force microscopy (AFM) in contact mode. Films deposited at substrate temperatures < 200 °C [2] were granular, self-affine over 1–2 orders of magnitude and growth proceeded by diffusion (roughness exponent α belonged to the Kardar–Parisi–Zhang (KPZ) universality class). For substrate temperatures higher than 200 °C, Zamboni and co-workers [3] observed, using AFM in contact mode, that film morphology transformed from

grain aggregates to a lamellar structure and the roughness exponent ($\alpha = 0.7$) revealed that deposition evolved into a strong adsorption regime. These films were self-affine over 3 orders of magnitude. Further, Biscarini and co-workers [4] also employed AFM in contact and tapping modes and observed that when these films were deposited at room temperature and annealed above 165 °C, they became smooth and featureless and the roughness exponent α was employed as an effective metric for this transition. Struth and co-workers [5] determined scaling exponents for thin films of an organic semiconductor, diindenoperylene (DIP), deposited on atomically smooth SiO₂ substrates in ultrahigh vacuum (UHV) employing AFM, x-ray reflectivity and diffuse x-ray scattering. They observed unusually rapid growth of roughness and lateral correlations characterized by a roughness exponent α of 0.684 and a growth exponent β of 0.748. The latter being above a value of 0.5 is indicative of the phenomenon of “rapid roughening” of the organic film. Recently, Biscarini and co-workers [6] also employed scaling arguments with parameters extracted from the analysis of AFM images, to correlate film morphology with charge transport for sexithienyl films.

Pentacene, a promising organic semiconductor [7, 8], is known to form highly ordered thin films near room temperature. Charge carrier mobilities ($1.5 \text{ cm}^2\text{-V}^{-1}\text{-s}^{-1}$ [9]) exceeding values for amorphous silicon ($1 \text{ cm}^2\text{-V}^{-1}\text{-s}^{-1}$) have been demonstrated for organic thin film transistors (OTFTs) of pentacene. Supersonic molecular beams provide an excellent tool to tune the incident kinetic energy of pentacene molecules which can strongly influence thin film deposition on a variety of substrates. There have been relatively few studies of energetic deposition of pentacene molecules. Scoles and co-workers [10] observed layer by layer growth of highly ordered pentacene thin films at

~200 K deposited on Ag (111), with an incident kinetic energy of 5 eV, using *in situ* low energy atomic diffraction. Iannotta and co-workers [11] also deposited pentacene films with beams of incident kinetic energy 0.3 eV and 5.5 eV and found, using atomic force microscopy, that crystal size increased with energy from 100 – 200 nm to 1 – 2 μm , with the latter films yielding organic thin film transistors with mobilities of $0.5 \text{ cm}^2\text{-V}^{-1}\text{-s}^{-1}$ [12]. Recently, the nucleation of pentacene thin films on bare SiO_2 [13] was investigated and the incident kinetic energy of the pentacene molecules was found to strongly influences the process of adsorption – the adsorption probability decreases with increasing incident kinetic energy, indicative of trapping-mediated adsorption. In addition, the trapping probability of pentacene decreased with more glancing angles of incidence, a result inconsistent with so-called normal energy scaling. Analysis of the dependence of the island density on the growth rate in the sub-monolayer regime indicated that growth at all energies is consistent with a critical cluster containing four molecules. The nucleation of pentacene thin films on SiO_2 substrates modified with hexamethyldisilazane (HMDS) was also studied. Adsorption was found to proceed by trapping but occurred at defect sites [14]. In addition, islands in the submonolayer regime were two molecules tall and island density was larger on the modified surface by a factor of $\sim 3 - 13$.

In this chapter, fundamental phenomena involved in the ultrahigh vacuum deposition of thin films of pentacene using supersonic molecular beams are investigated. The effect of incident kinetic energy and angle of pentacene molecules on thin film deposition has been examined. Deposition has been carried out on bare SiO_2 surfaces and SiO_2 surfaces modified using an organic monolayer of hexamethyldisilazane (HMDS). The effect of substrate temperature on kinetics of film deposition and film morphology has also been

examined. Finally, the first experimental measurements of scaling exponents for thin pentacene films deposited on flat and inert thermal SiO₂ substrates as well as SiO₂ substrates modified with HMDS are reported and these exponents are used to understand mechanisms involved in the deposition process.

6.3 Experimental procedures

Apparatus and experimental procedures have been described in detail in section 2.2. A brief description is included in this section. Thin film deposition experiments were carried out in a custom-designed UHV chamber [15]. The base pressure of the chamber prior to deposition experiments was always $\sim 2 \times 10^{-9}$ torr. Substrates were 4" Si (100) wafers and subjected to an RCA-1 clean, 15 sec HF dip and RCA-2 clean immediately before growth of ~ 300 nm SiO₂ by wet thermal oxidation at 1100 °C. Immediately prior to placement into the load-lock of the vacuum chamber, these wafers were cleaned and degreased by sonication for 15 min. in anhydrous CHCl₃ solution (99%+) and 15 min. in deionized (DI) H₂O, washed with DI water, dried with N₂ and cleaned with UV-Ozone for 10 min. HMDS was deposited from the vapor phase after successive evacuation and purge cycles to dehydrate the substrate held at 150 °C. Deposition time was 5 min. at a pressure of 6 torr. These processes gave a clean and reproducible hydrophilic or hydrophobic surface. Supersonic molecular beams of pentacene (99.8% Sigma-Aldrich) were generated by passing a carrier gas (He and N₂, 99.999% Air Gas) over a temperature controlled container (the evaporator) located upstream of the nozzle. The flow of carrier gases, m_{cg} , was modulated using a mass flow controller (MKS). The nozzle (heatable) consisted of 0.25" dia. stainless steel tubing, with a 125 μ m

thick plate of stainless steel welded at its end. This plate had a 150 μm orifice machined into it. The doubly differentially pumped beams passed through a trumpet shaped skimmer (1.5 mm aperture, Beam Dynamics) into an antechamber and through an aperture that produced a well defined 0.45" \times 0.45" beam spot on the substrate at normal incidence. Beam energies (E_i) obtained were 1.5 eV (determined from time of flight measurements [16]) by seeding pentacene in 10 sccm N_2 , and 2.7 eV, 4.5 eV and 6.7 eV by seeding in 10, 25 and 70 sccm of He respectively. The beams could be blocked using a shutter in the antechamber, facilitating precise exposures of the substrate to the beam. Beam intensity was monitored with a quadrupole mass spectrometer (Extrel) located downstream and on the beam axis. Once the desired intensity was obtained, the sample at temperature T_s , was translated into the beam and rotated to the desired angle of incidence (θ_i). During exposure the sample was periodically translated perpendicular to the beam axis, producing areas on the substrate surface (8 areas, $1 \times 10 \text{ mm}^2$ each) representing different exposure times, yet identical deposition conditions (E_i , θ_i , T_s). The flux of pentacene molecules in these beams was maintained a constant for all incident kinetic energies and angles of incidence.

Following removal from the chamber, the samples were examined *ex situ* using a Digital Instruments Dimension 3100 microscope (Veeco Instruments) in tapping mode. Typical images obtained were of size $20 \times 20 \mu\text{m}^2$ and subjected to a second order plane fit using Nanoscope software (v 5.0). One dimensional PSD spectra (1DPSD) can be used to characterize the roughness and surface structure and also to obtain scaling exponents [17–19] (details are provided in section 2.2.5.2). 1DPSDs were calculated using the same software along the fast scan direction and single line PSDs were averaged. For each scan length L ,

spatial frequencies range between $1/L$ and the Nyquist frequency $256/L$. The growth exponent β was determined by plotting film root mean square (RMS) roughness R obtained from AFM images using Nanoscope software (v 5.0), as a function of thickness t . Data were fit to a power law yielding this exponent.

Pentacene film thicknesses were determined by ellipsometry using values of 1.46 for the refractive index of bare silicon dioxide and SiO_2 modified with HMDS and 1.43 for the pentacene film [20] (details in section 2.2.5.1). The estimated error in these measurements is $\pm 1 \text{ \AA}$.

6.4 Results and discussion

6.4.1 Multilayers on SiO_2

Pentacene films nucleate on SiO_2 forming a layer of unimolecular height which completes $> 80\%$ before the second layer nucleates [13]. After layer by layer growth for the first two layers, growth becomes three-dimensional. AFM images of multilayer films deposited with an incident kinetic energy of 6.7 eV and normal incidence are displayed in Fig. 6-1. A line scan across the image obtained for an exposure of 2400 s reveals the surface to be quite rough. Film thickness is $\sim 357 \text{ \AA}$ while the surface roughness is 50 \AA . A zoomed image of the thick film indicates the presence of distinct grains with individual terraces separated by approximately the height of a single molecule of pentacene, as seen in a line scan across this AFM image.

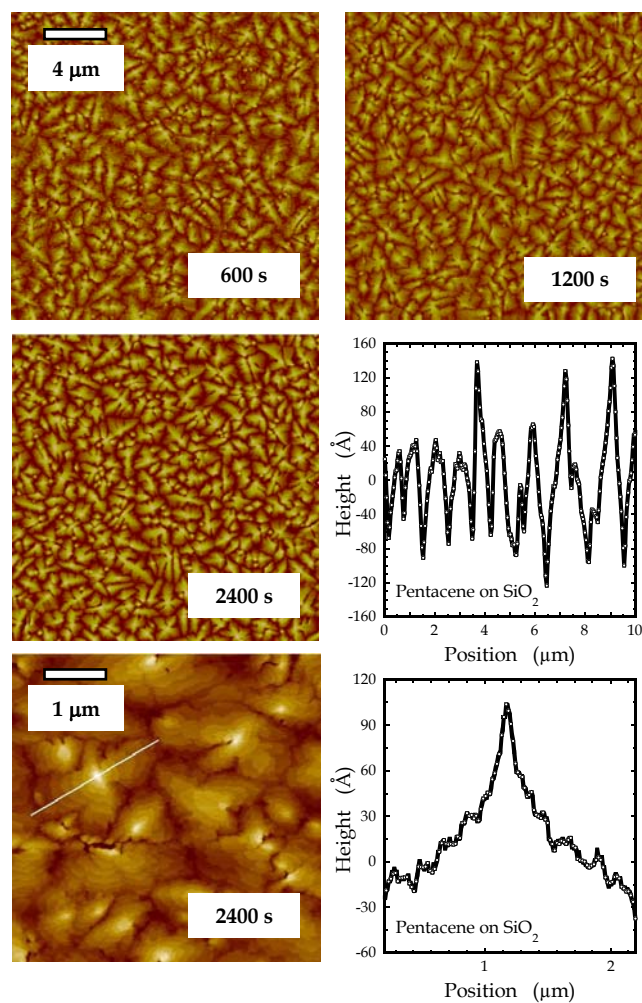


Figure 6–1 Atomic force micrographs of multilayer films of pentacene deposited on SiO_2 for a sequence of exposures to the supersonic beam ($E_i = 6.7 \text{ eV}$, $\theta_i = 0^\circ$). In each case the field of view is $20 \mu\text{m} \times 20 \mu\text{m}$. Similar images were obtained for other incident kinetic energies, deposition times and angles of incidence. A line scan across the image obtained for an exposure of 2400 s reveals a rough surface. However, a zoomed $5 \mu\text{m} \times 5 \mu\text{m}$ image of this film indicates individual grains exhibiting a lamellar structure.

Film thickness obtained from ellipsometry are plotted as a function of deposition time in Fig. 6–2 for four incident kinetic energies ($E_i = 1.5$ eV, 2.7 eV, 4.5 eV and 6.7 eV) and three angles of incidence (0° , 45° and 75°). Data were fitted well by a quadratic model. The roughness of the film may be responsible for the apparent flattening in deposition rate with increasing deposition time (resulting from ellipsometry) and to avoid inclusion of any artifacts, the coefficient of the linear term was used to estimate deposition rates. These deposition rates were normalized to the rate obtained for a film deposited using an incident kinetic energy of 1.5 eV and $\theta_i = 45^\circ$, to yield relative probabilities of adsorption of pentacene on a multilayer. These probabilities of adsorption $S_{A,m}$ exhibit a strong dependence on incident kinetic energy and incident angle as shown in Fig. 6–3. $S_{A,m}$ decreases with incident kinetic energy consistent with trapping mediated physisorption. $S_{A,m}$ does not change appreciably with angle of incidence for the 1.5 and 2.7 eV beams. However, for higher energy beams, it decreases dramatically with more glancing angles of incidence. This is indicative of non-normal energy scaling – dissipation of the kinetic energy directed along the surface normal is not the sole factor determining the trapping of pentacene on SiO_2 . In order to quantify the contributions of perpendicular and parallel energy to the adsorption process, an empirical energy scaling function has been applied with the form $E_i f(\theta_i) = E_i (A \cos^2 \theta_i + B \sin^2 \theta_i)$, where $A + B = 1$, and the perpendicular (parallel) energy scales with the coefficient A (B) [21]. In the limit of $A \rightarrow 1$ normal energy scaling is recovered, and when $A = B$ total energy scaling is obtained. Displayed in Fig. 6–4 are the results of energy scaling analysis of the data shown in Fig. 6–3. Here the optimal values for A and B were determined

Figure 6–2 Thickness–exposure relationships, deduced from ellipsometry measurements, for the adsorption of pentacene on a pentacene multilayer at the four incident kinetic energies indicated and three angles of incidence (a) 0° , (b) 45° and (c) 75° . The smooth curves represent second order polynomial least–squares fits to the data.

(a)

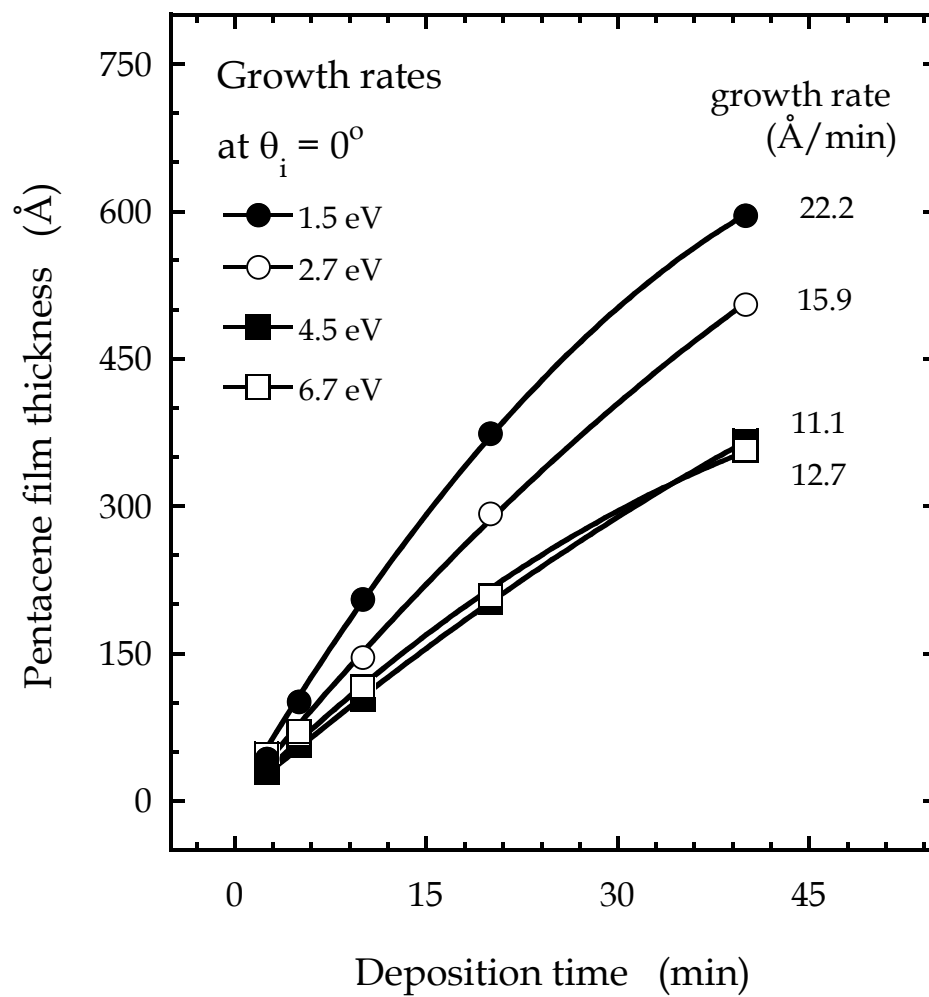


Figure 6-2 (Continued)

(b)

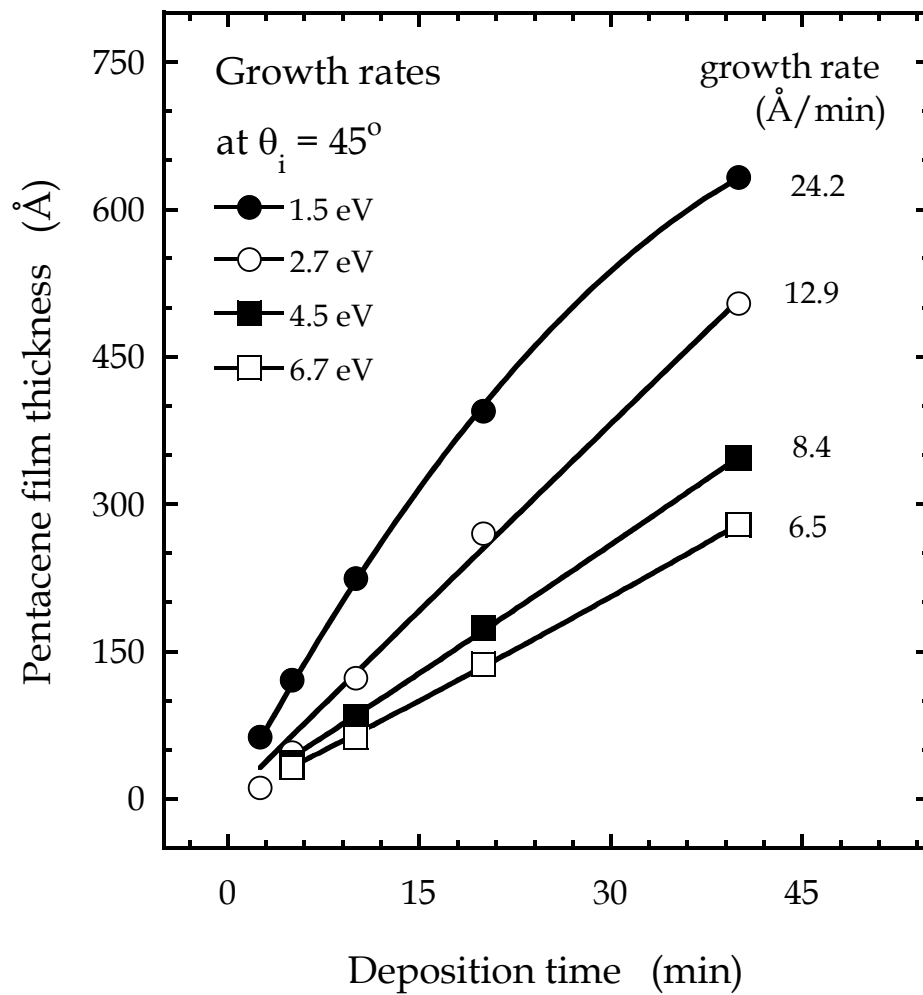
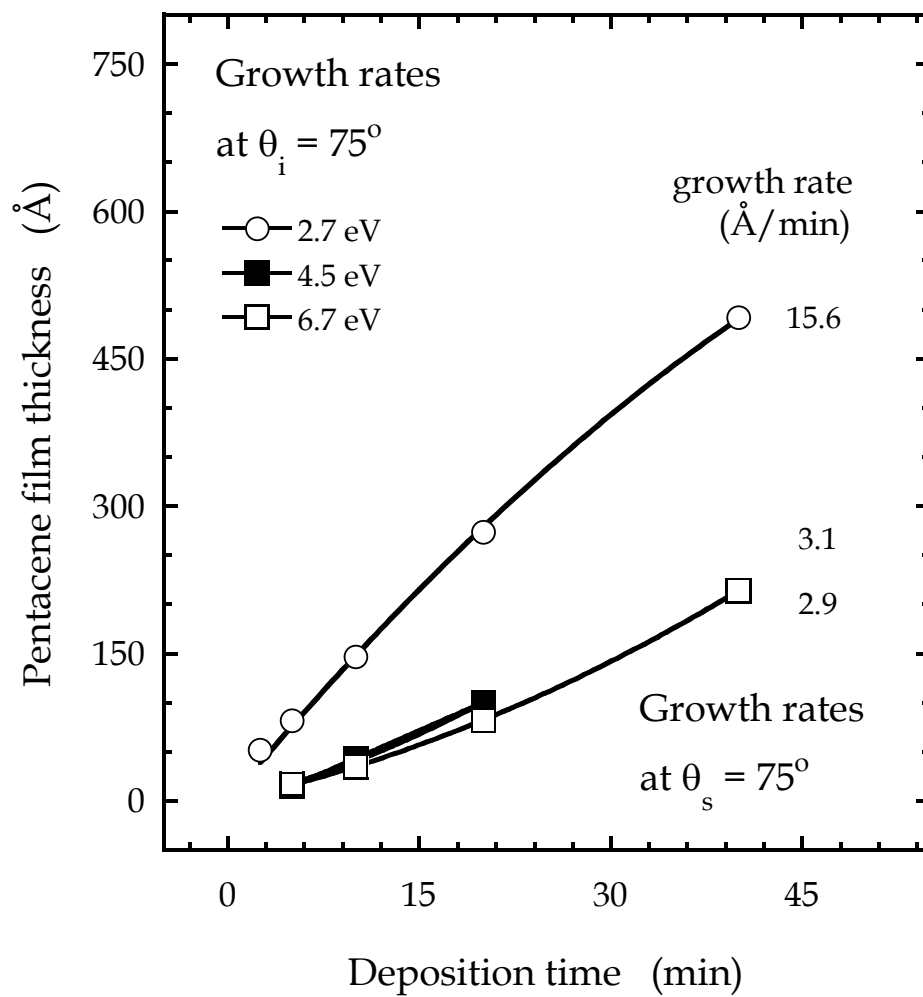


Figure 6-2 (Continued)

(c)



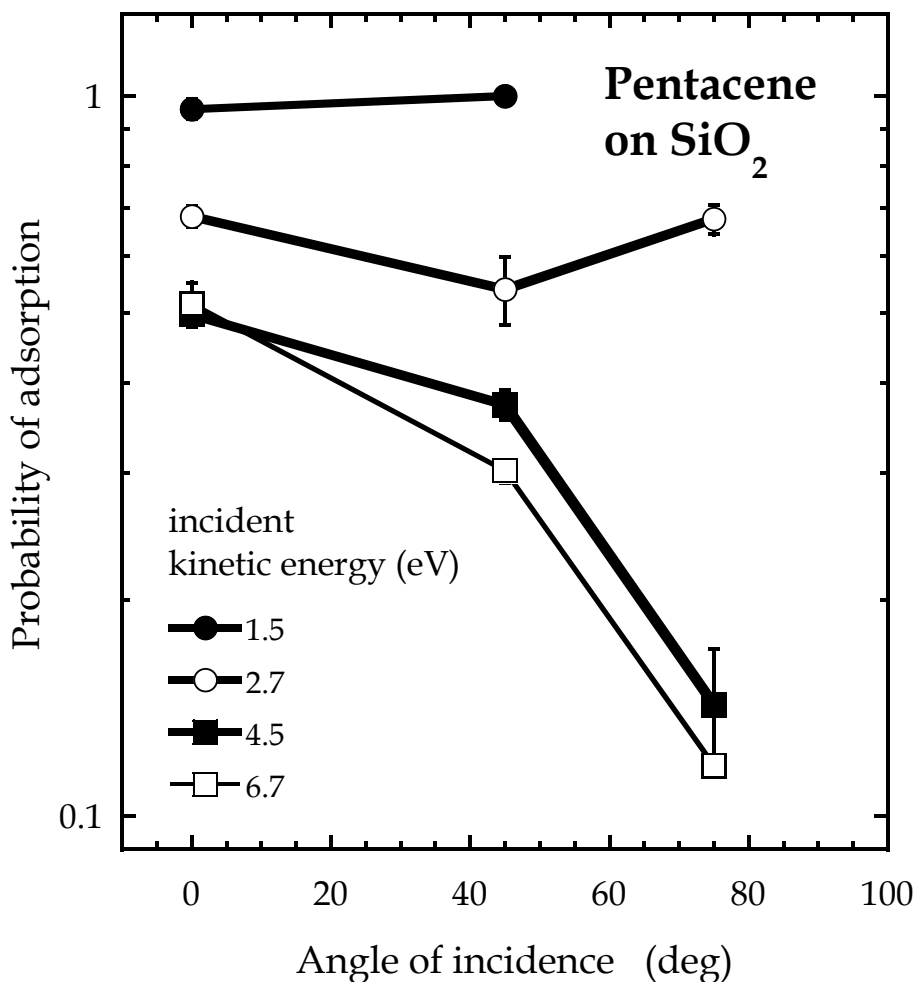


Figure 6–3 Probability of adsorption of pentacene on a thin film as a function of incident kinetic energy and angle of incidence (degrees from surface normal). The solid lines are indicative of the trend of decreasing adsorption probability with increasing angle. The data have been normalized to values observed for $E_i = 1.5\text{eV}$ and $\theta_i = 45^\circ$.

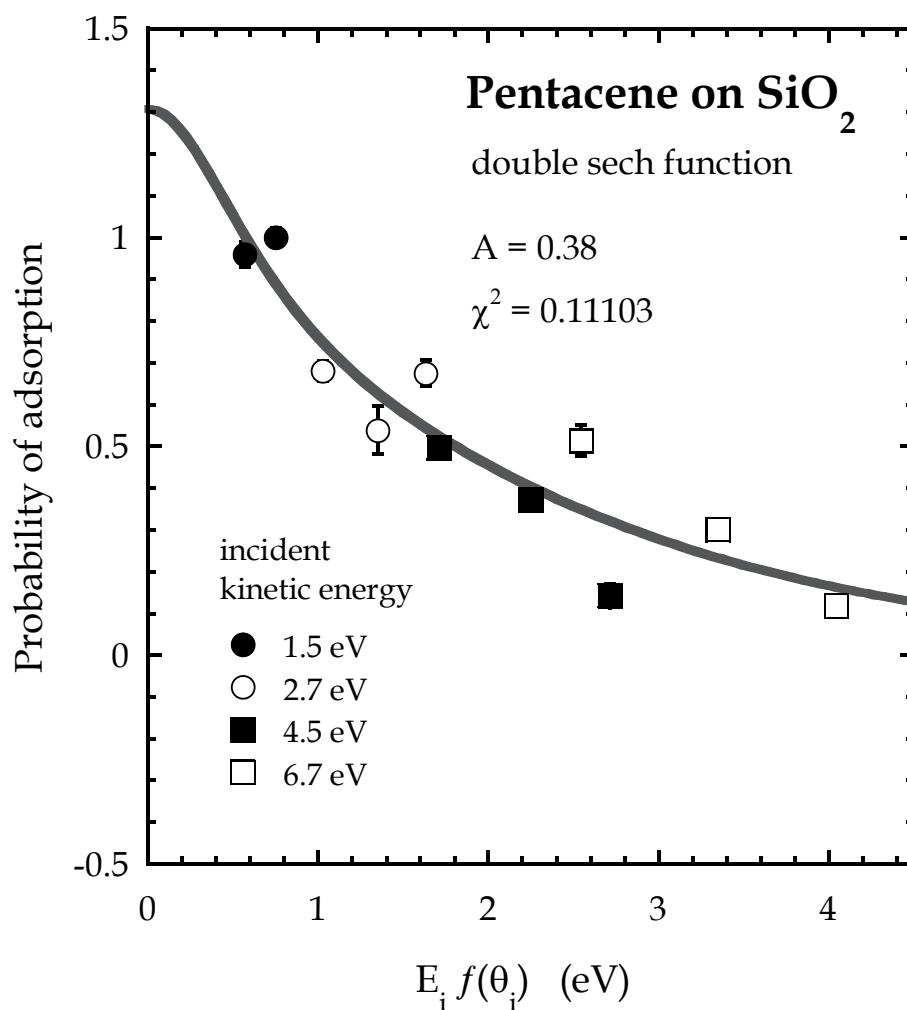


Figure 6-4 Initial (normalized) probability of adsorption of pentacene onto a multilayer on SiO₂ as a function of scaled incident kinetic energy, $E_i f(\theta_i) = E_i(A \cos^2\theta_i + B \sin^2\theta_i)$. To find the optimum value of A the scaled data were fit to a weighted sum of two *sech* functions, which is shown as the smooth curve.

by minimizing the mean square deviation between the scaled data and a weighted sum of two *sech* functions. As may be seen, a value of $A = 0.38$ ($B = 0.62$) describes the data best. In terms of this model, which is admittedly too simplistic, and the data, a limited set of 11 conditions, accommodation of parallel and perpendicular momentum are roughly equally important.

The decrease in trapping with more glancing angles of incidence has been observed for collisions between inert gas atoms like Ar and protruding CF_x segments of perfluorinated polyethers (PFPE) [22]. In this work, Minton and co-workers argued energy transfer was more efficient at angles close to normal incidence during the initial collision and there were more collisions per encounter. At glancing incidence, owing to the rough nature of the interface, atoms striking the top regions of three-dimensional protrusions need deflect only slightly as they scatter in forward directions with small energy losses. For perpendicular approach, atoms which initially scatter away from the surface must be deflected by 90° or more and lose a substantial fraction of their energy to leave the interface while those deflected toward the surface would at least undergo another collision. Those deflected toward or along the interface would undergo multiple collisions, enhancing the chances that an atom would lose enough energy to be momentarily bound to the surface.

Interesting insight into the deposition process can be gained by comparing the deposition rate in the multilayer regime to the corresponding rate in the submonolayer regime for the same film. The ratio of these deposition rates is plotted in Fig. 6-5 for all incident kinetic energies and angles of incidence examined. The multilayer deposition rate accelerates with increase in energy compared to the submonolayer rate and the ratio is highest for the

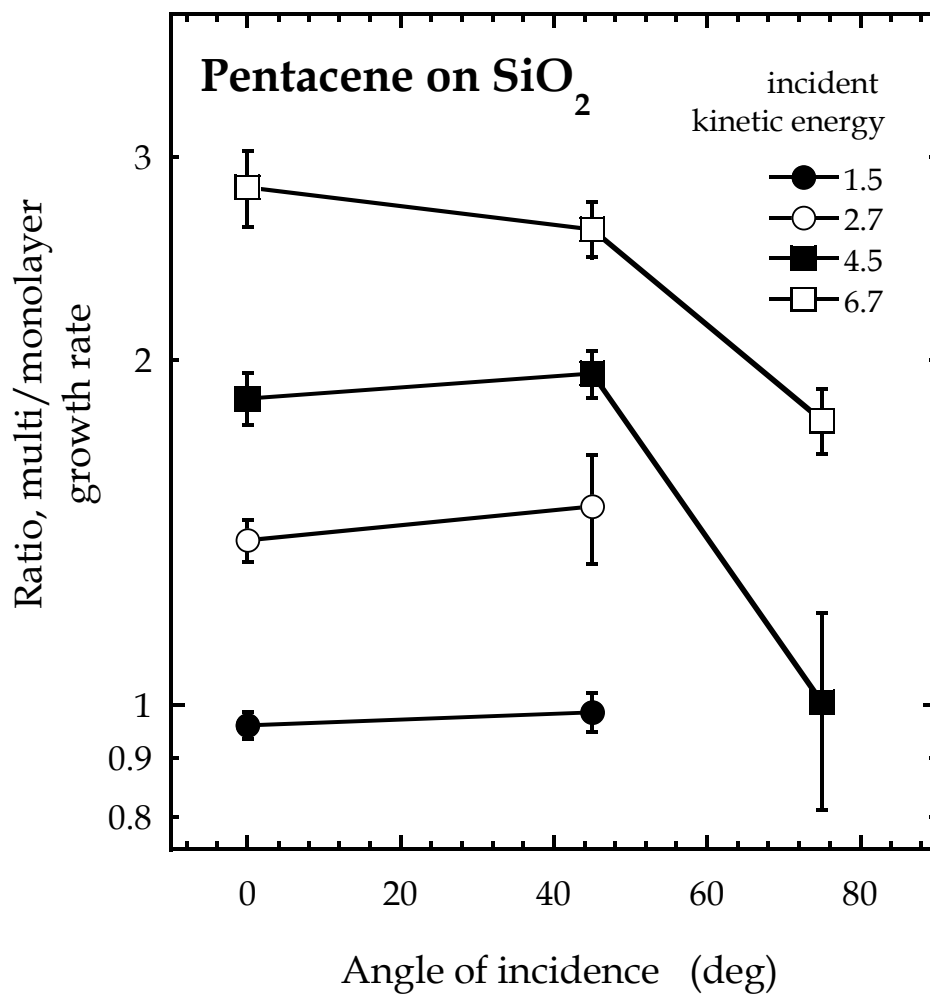


Figure 6–5 Ratio of multilayer and submonolayer deposition rates as a function of incident kinetic energy and angle of incidence (degrees from surface normal). The solid lines are indicative of the trend of decreasing ratios with increasing angle.

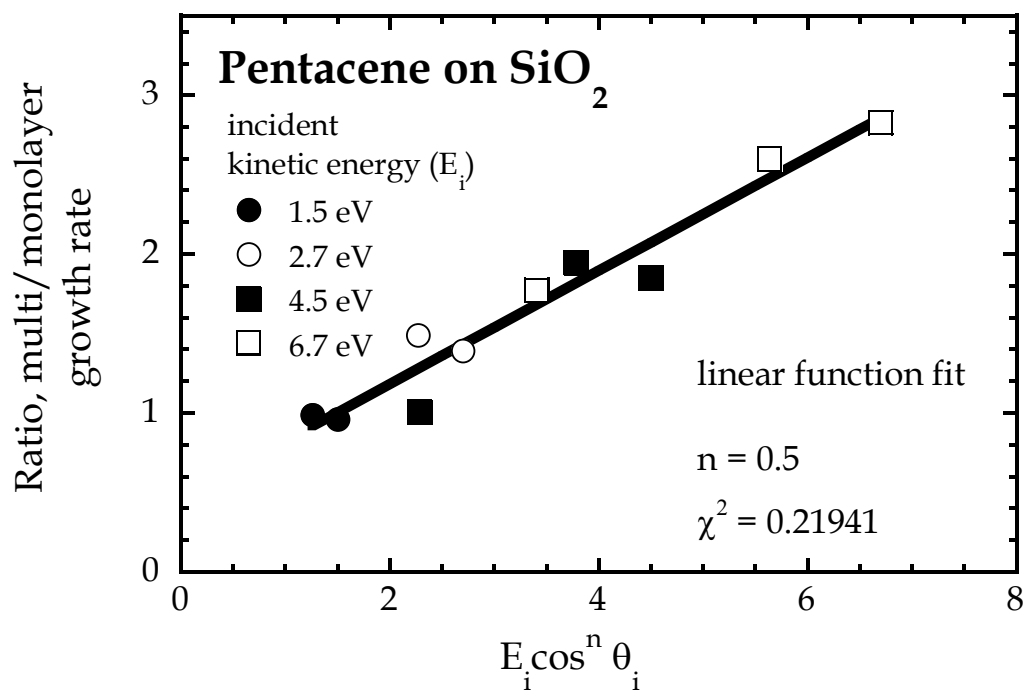


Figure 6–6 The ratio of multilayer to submonolayer deposition rates as a function of scaled incident kinetic energy, $E_i f(\theta_i) = E_i \cos^n \theta_i$. To find the optimum value of n , the scaled data were fitted to a linear function, which is shown as the solid line.

6.7 eV beam at normal incidence where this could be indicative of more efficient trapping (possibly by insertion of molecules into a depositing film). For more glancing angles of incidence, multilayer deposition rates drop faster with respect to the submonolayer deposition rate. In order to get further insight into multilayer deposition, the ratio of deposition rates was scaled with incident kinetic energy using the function $E_{jf}(\theta_i) = E_i \cos^n \theta_i$. The standard deviation of the scaled data with respect to a fit of the scaled data to a linear function has been minimized in order to obtain the scaling exponent n . If $n = 0$, total energy scaling would result with no dependence on angle of incidence. If $n = 2$, energy scaling would be normal and the normal component would be the sole contributor to the process of adsorption. The ratio of deposition rates as a function of scaled incident kinetic energy is plotted in Fig. 6–6. A scaling exponent of $n = 0.5$ describes the data best. This indicates that adsorption in the multilayer relative to adsorption in the submonolayer regime is intermediate in character with respect to total and normal energy scaling. The observation of non-normal energy scaling has been attributed to the effects of substrate corrugation, (unit cell) impact parameter effects, inefficient accommodation of parallel momentum, and the role of internal energy degrees of freedom [23–26].

The morphology of thick pentacene films has been investigated by AFM. Shown in Fig. 6–7 are AFM images of pentacene films deposited at four incident kinetic energies: 1.5 eV, 2.7 eV, 4.5 eV and 6.7 eV at normal incidence. Total deposition time was 40 min. in all cases. For all cases, film deposition proceeds by Stranski–Krastanov growth [13]. As mentioned earlier, the films exhibit individual grains with lamellar structure. In addition, grain size increases with increasing energy from 1.5 eV to 4.5 eV. It is important to

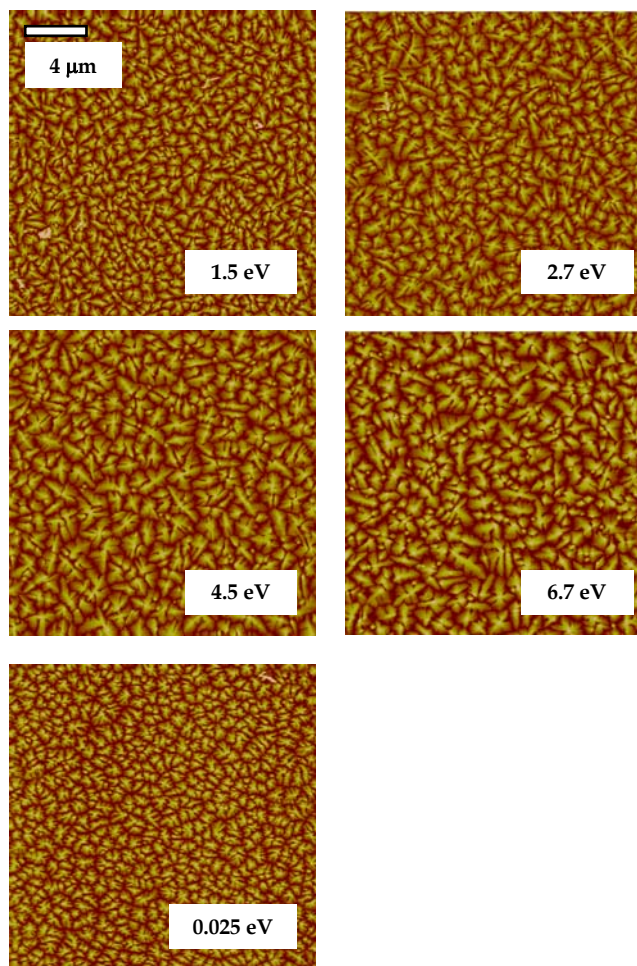


Figure 6–7 Atomic force micrographs of pentacene thin films deposited on SiO₂ for four different incident kinetic energies, a fixed deposition time of 40 min. and normal incidence. Also shown for comparison, is the micrograph for a film deposited by thermal evaporation. All films were deposited at room temperature.

recall that all these films were deposited at room temperature and the flux was maintained constant. Also shown for comparison is an AFM image of a film evaporated onto bare SiO₂ at a similar deposition rate (0.3 Å/s). The grain size is smallest for the evaporated film and increases with increasing incident kinetic energy. The decrease in probabilities of adsorption $S_{A,m}$ in the multilayer regime could be partially responsible for this phenomenon.

Fundamental insight into the process of film deposition can be gained by studying the temporal evolution of the interface width w and the lateral correlation length ξ of these films. The interface width is a measure of the roughness of the surface while the lateral correlation length is a measure of spatial periodicity in the film. A computed value of the average roughness is the root-mean-square variation (i.e. standard deviation) of the surface height profile from the mean height and is given by:

$$w = \left| \frac{1}{N} \sum_{i=1}^N (h_i - h_{mean})^2 \right|^{1/2} \quad (6-1)$$

where N is the number of data points of the profile, h_i are the points that describe the relative vertical height of the surface and h_{mean} is the mean height of the surface. Dynamic scaling theory predicts that both w and ξ increase with time according to power laws $w(t) \sim t^\beta$ and $\xi(t) \sim t^{\beta/\alpha}$. The roughness exponent α and growth exponent β are indicative of different growth mechanisms. For example, some of these growth mechanisms are random deposition, random deposition with surface diffusion, ballistic deposition and solid-on-solid deposition [27]. Values of α and β have been predicted for the individual growth mechanisms both by numerical simulations and theoretical models. In

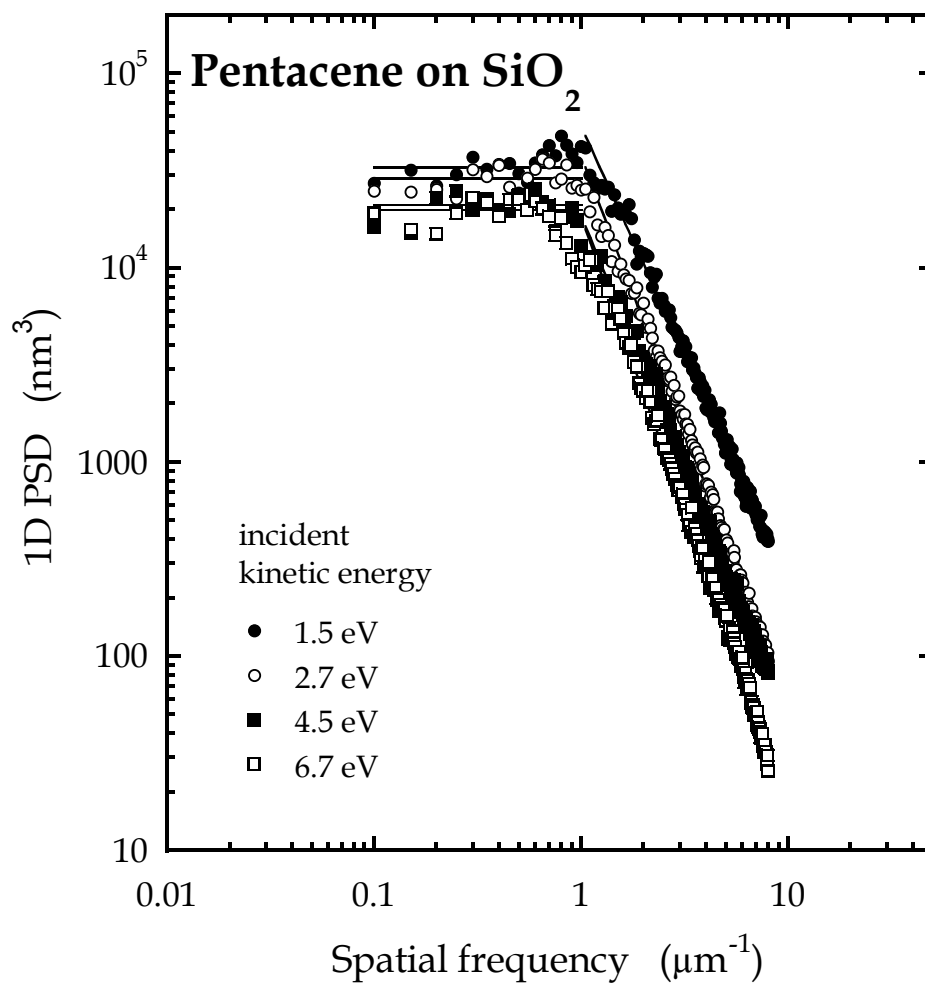


Figure 6–8 Evolution of the one dimensional power spectral density (1DPSD) as a function of spatial frequency for the four incident kinetic energies (1.5 eV, 2.7 eV, 4.5 eV, 6.7 eV) at normal incidence. Best fit lines yielding parameters K_0 and γ are shown within the self-affine data range.

this work, α was obtained from 1DPSD analysis and β from plots of film thickness as a function of roughness.

Shown in Fig. 6–8 are 1DPSD curves for pentacene films. The PSDs exhibit two distinct regions: (i) a plateau region ($1/L$) at low spatial frequencies denoting the absence of nonlocal correlations along the line scans, and (ii) a frequency–dependent and decaying branch indicative of the self–affine nature of the film. The highest frequency range is discarded since it is affected readily by noise and aliasing. The range of the intersection between the self–affine branch and the plateau defines the inverse of the correlation length ξ :

$$\xi = \exp\left\{\frac{\ln[PSD(1/L)] - \ln K_0}{\gamma}\right\} \quad (6-2)$$

As may be seen from Fig. 6–8, the self–affine part of the spectrum spans one order of magnitude for these films deposited at room temperature. The roughness scaling exponent α is obtained from this self–affine segment of each 1DPSD curve. This process is repeated to extract α from each AFM image. As a result, data for α for each individual exposure are obtained for the four incident kinetic energies and three angles of incidence. The value of α , averaged for all exposures in the multilayer regime for each deposition experiment, is plotted for all incident kinetic energies and two angles of incidence, 0° and 75° (Fig. 6–9). As may be seen, the value of α does not change appreciably with incident kinetic energy. The average value of α for all energies is 0.73 at an angle of incidence of 0° and 0.87 at an angle of incidence of 75° . This α maps the range within the predictions of diffusion–limited aggregation ($\alpha = 1$ [28]) and molecular beam epitaxy (MBE) growth controlled

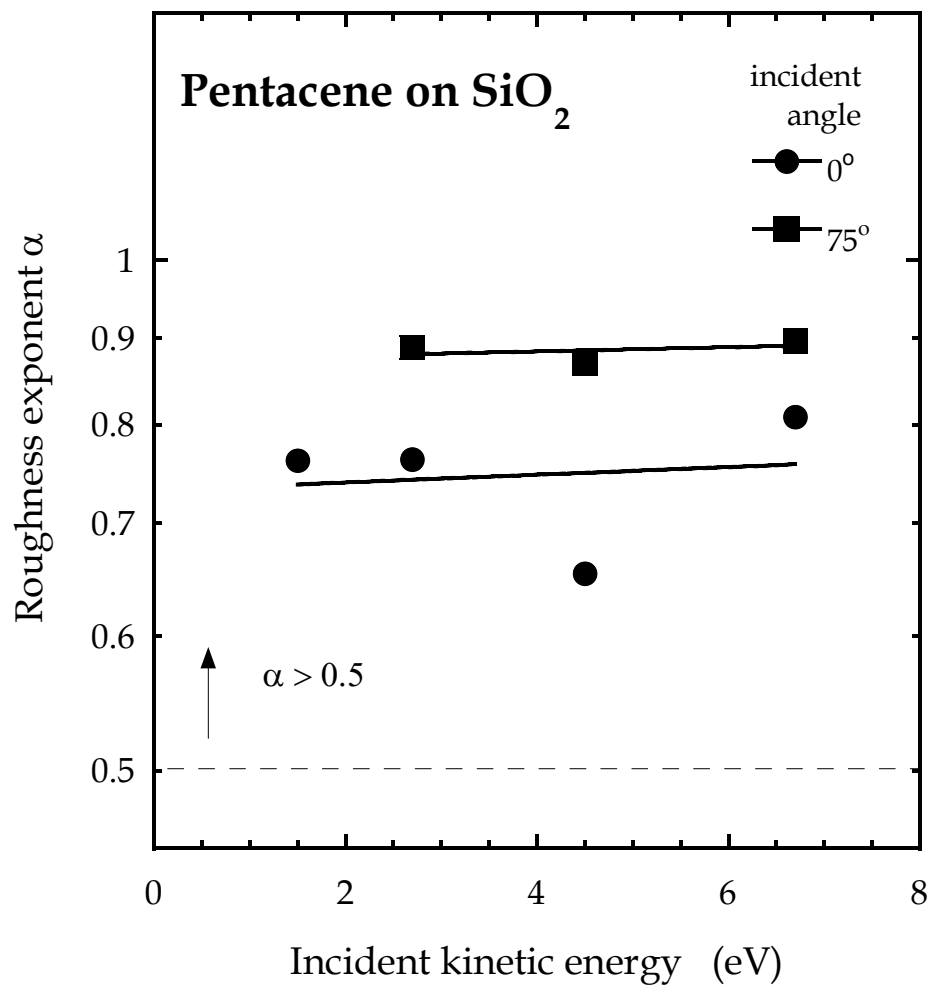


Figure 6–9 Roughness exponent α as a function of incident kinetic energy for two angles of incidence, 0° and 75°. The solid lines are linear fits to the data.

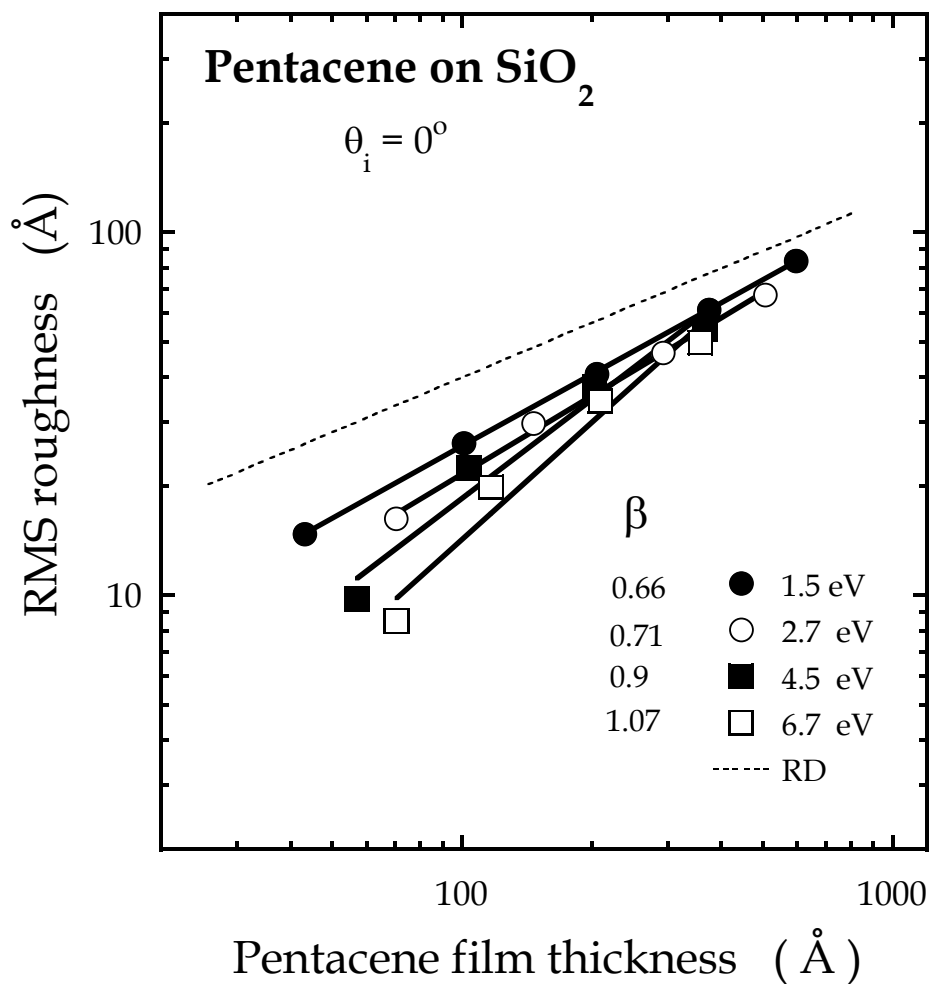


Figure 6–10 Root mean square (RMS) roughness as a function of film thickness for pentacene films deposited with four incident kinetic energies at normal incidence. The solid lines are power law fits used to obtain the growth exponent β . The dotted line indicates the limit of roughness for random deposition (RD).

by adsorption at kink sites with the rate limiting step being the motion of molecules across steps ($\alpha = 0.66$ [29]). A similar range of values for α has been observed for thin films of the organic molecule sexithienyl when deposition was carried out on ruby mica substrates. $\alpha = 1.0$ and decayed to 0.7 when substrate temperature was increased from 25 – 200 °C [3]. This was consistent with the evolution of domain size and shape in these films.

For a self-affine surface, film roughness scales with film thickness through a power law with a characteristic exponent β , called the growth exponent. All pentacene films deposited at four incident kinetic energies and three angles of incidence exhibit self-affine character. As a result, film roughness (from AFM images) can be plotted as a function for film thickness (as probabilities of adsorption vary with incident kinetic energy and angle of incidence, film thickness is a better measure of the deposition process than deposition time) as shown in Fig. 6–10. As may be seen, for incident kinetic energies of 1.5 – 6.7 eV at normal incidence, the slope and hence growth exponent β is found to increase from 0.66 ± 0.01 to 1.07 ± 0.15 . It is important to note that the inspected range of film thickness covers two orders of magnitude and no systematic deviation from the power law trend is observed. From the figure it is apparent that pentacene films are smoother when deposited at higher incident kinetic energies. However, with increasing thickness, films deposited at a higher energy roughen quicker than films deposited at lower energies.

Values of $\beta > 0.5$ are indicative of the phenomenon of “rapid roughening” that has garnered widespread interest in the last few years. Two primary mechanisms of growth-induced surface roughening have been described previously, namely (i) kinetic roughening and (ii) mound growth. In

the former case, roughness occurs owing to competition between random spatial inhomogeneities in the local deposition rate and surface smoothing through surface diffusion related processes. In mound growth, reduced interlayer transport results in a pattern of three-dimensional growth. Values of $\beta = 0.8$ have been observed for mound growth in computer simulations [30]. Both in kinetic roughening and in mound growth, if there are no spatial correlations between impinging molecules and their neighboring sites and surface diffusion and desorption are non-existent, the result is a limiting case called random deposition (RD). For random deposition, the roughness of the film σ_{RD} is related to film thickness t as $\sigma_{RD} = d_{pen} (t/d_{pen})^{1/2}$ where d_{pen} is the thickness of a monolayer of pentacene. This model is plotted for comparison in Fig. 6–10. Roughness beyond σ_{RD} is not possible without a positive flux of molecules from lower to higher layers. As may be seen, for the film thicknesses examined in this study, roughness is always lower than the RD limit. However, the evolution of surface roughness suggests that there will be a critical thickness t_{RD} where surface roughness will cross the RD limit. This is due to a growth exponent $\beta > 1/2$. Rapid roughening has been observed for several inorganic material systems and a few organic systems [5, 18, 30–38]. Table 6–1 lists material systems, substrate temperature and values of the roughness and growth exponents obtained in these cases. Among organic material systems, Bernat and co-workers [18] used AFM to study the self-affine scaling of polymer films deposited using inductively coupled rf driven plasma discharge. The reactants were trans-2-butene and hydrogen. Amorphous polymer films which were deposited had a chemical structure resembling highly cross-linked polyethylene. Values of α and β increased

Table 6–1 Rapid roughening of thin films [5, 18, 30–38].

Ref.	Film	Substrate	T _s	α	β
[31]	Cu	Cu(100)	200 K	~ 1	0.56
[18]	CH _{1.3}	Si	318 K	0.9–1.0	0.7–1.0
[32]	Pb	Pb(100)	363 K	1.33 ± 0.05	0.77 ± 0.05
[33]	Si	Si(111)	633 K	0.36 ± 0.05	0.7 ± 0.1
[34]	W	Si(100)	623 K and 823 K	0.84 ± 0.05	0.37 ± 0.09 0.54 ± 0.09
[35]	Al	SiO ₂ /Si(100)	298 K		0.55
[36]	NiMnSb	MgO(100)	423 K 523 K 573 K		0.6 ± 0.1 0.75 ± 0.1
		Si(100)	423 K 523 K		0.4 ± 0.1 0.55 ± 0.1
[30]	Ag	Ag(100)	230 – 300 K		0.65–0.8
[5]	DIP*	4000 Å SiO ₂ /Si(100)	418 ± 5 K	0.684 ± 0.06	0.748 ± 0.05
[37]	CrN	B doped Si(100)	< 303 K	1.57 ± 0.03	0.87 ± 0.1
[38]	BPAPC	Si	RT	–	1.05 ± 0.05

* $1/z = \beta/\alpha = 0.92 \pm 0.2$

from 0.9 to 1.0 and from 0.7 to 1 respectively with a decrease in deposition rate from 2 to 1 $\mu\text{m}/\text{hour}$. High pressures of 75 mtorr used for the polymerization process were suggested to induce shadow instabilities resulting in larger values of β . As mentioned earlier, Struth and co-workers. obtained a value of $\alpha = 0.68$ and $\beta = 0.748$ for films of the organic semiconductor diindenoperylene [5]. They postulated that lateral inhomogeneities, associated with orientational degrees of freedom of the DIP molecules, were responsible for this unusually rapid increase in roughness. Most recently, Samwer and co-workers [38] deposited films of bisphenol A polycarbonate (BPAPC) using pulsed laser deposition. At an angle of incidence of 55° , a value of $\beta = 1.05$ was obtained for thicknesses upto 200 Å which was attributed to shadowing effects.

For the case of pentacene thin films, deposition rates decrease with increasing incident kinetic energy at normal incidence. This decrease in deposition rate is characterized by a value of $\alpha = 0.73$ and an increase in the growth exponent β from 0.66 ± 0.01 to 1.07 ± 0.15 . A similar trend has been observed for plasma deposited polymer films [18] as described above. From Fig. 6–9 it may be seen that α is larger at glancing angles of incidence for all the four incident kinetic energies. This could be attributed to shadowing effects. At these glancing angles of incidence, a large area of the substrate is shadowed by three-dimensional faceted grains (c.f. Fig. 6–1). As a result, a molecule that reaches the substrate might not be able to incorporate as efficiently at the bottom of these grains in comparison to their top. This would result in growth becoming more three-dimensional with an accompanying increase in surface roughness. A plot of the growth exponent β for the incident kinetic energies of 2.7 – 6.7 eV and three angles of incidence is presented in

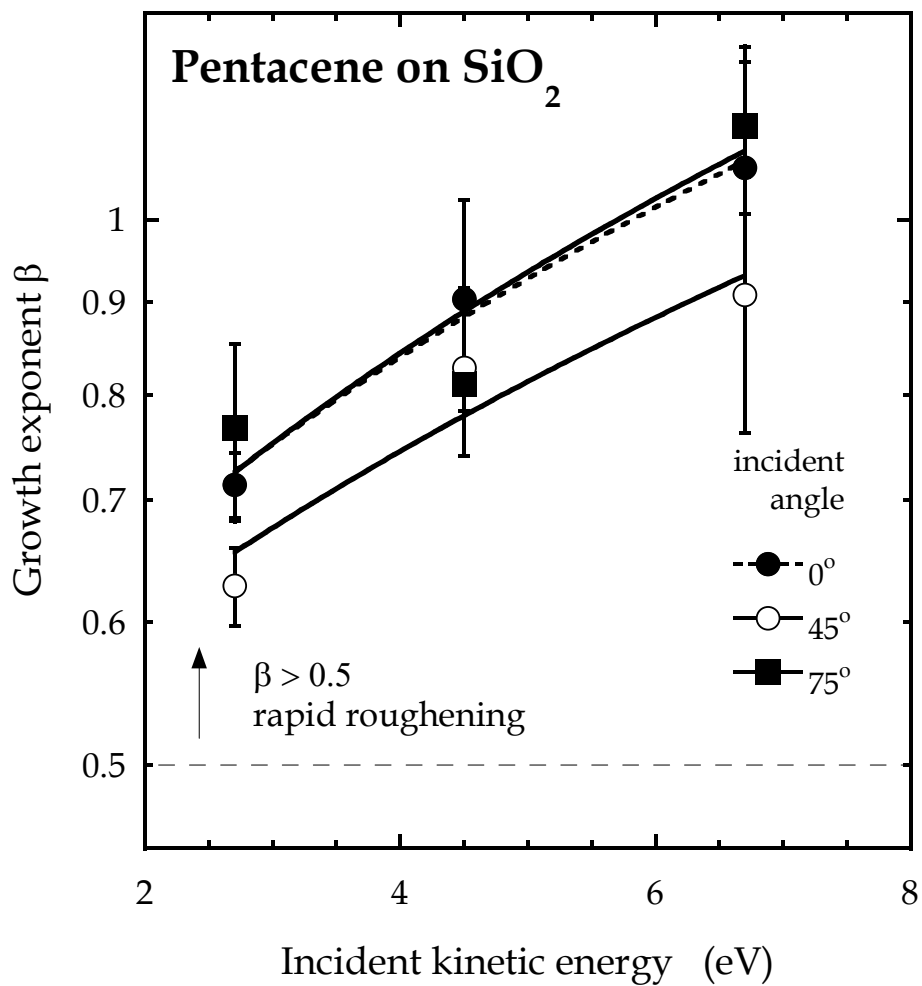


Figure 6–11 Growth exponent β as a function of incident kinetic energy for three angles of incidence: 0°, 45° and 75°. The solid lines are linear fits to the data.

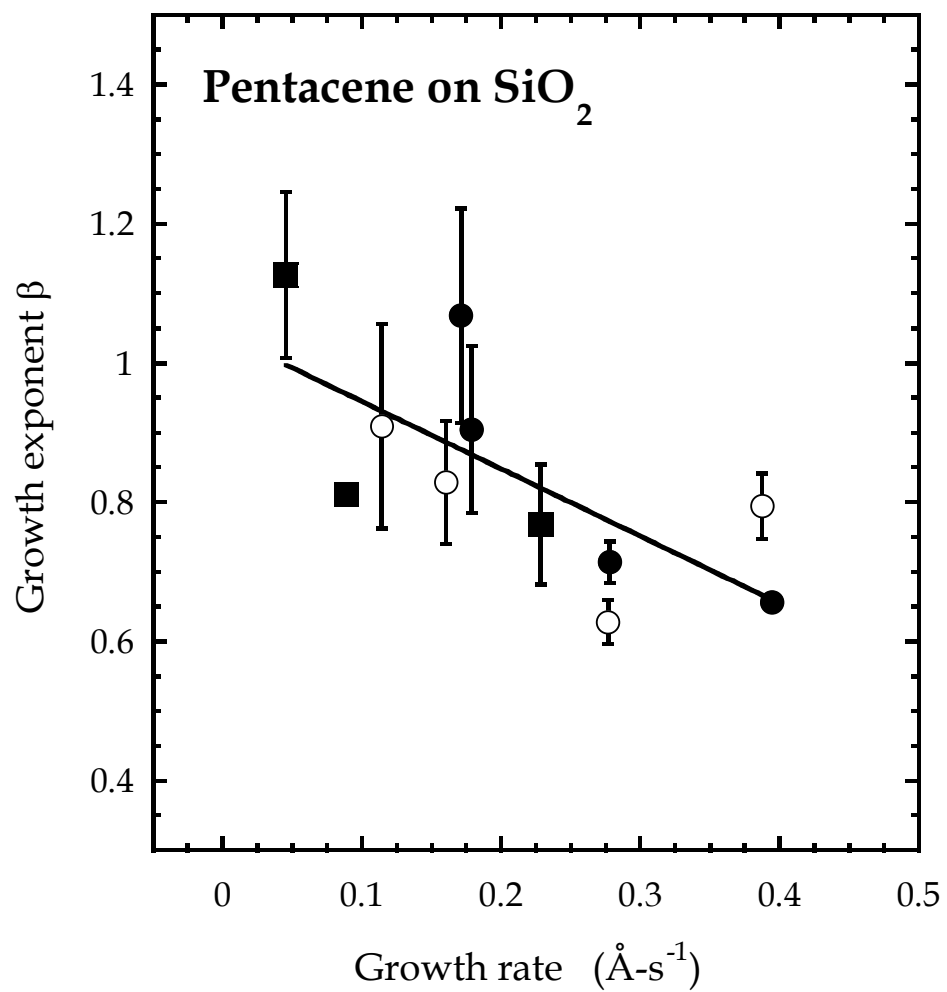


Figure 6–12 Growth exponent β as a function of film deposition rates ($\text{\AA}\text{-s}^{-1}$). The solid line is a linear fit to the data.

Fig. 6–11. As may be seen, β increases with incident energy for all angles of incidence. β is lower at an angle of incidence of 45° in comparison to angles of 0° and 75° . Competition between energetic and geometric effects could be responsible for this trend. In other words, the normal component of incident kinetic energy decreases with more glancing angles of incidence. This could contribute to lowering the value of β (going 0° to 45°). However, shadowing is far more pronounced at a glancing angle of incidence of 75° and this could enhance the process of roughening. Finally, a plot of β as a function of deposition rate is presented in Fig. 6–12. As may be seen, β increases with decreasing deposition rate. This is counterintuitive as larger deposition rates normally contribute to roughening of deposited films. Therefore, the situation is more complex with different contributions from energetic and geometric effects.

6.4.2 Effect of substrate temperature

Pentacene films were deposited at three substrate temperatures (-73°C , 30°C and 75°C), four incident kinetic energies (1.5, 2.7, 4.5 6.7 eV) and two sets of deposition rates. For the first set, deposition rates ranged from $0.02 - 0.3 \text{ \AA/s}$ and for the second set, deposition rates ranged from $0.15 - 0.86 \text{ \AA/s}$. For each individual incident kinetic energy, deposition rates were 2–4 times larger for the second set. Further, fluxes were constant for a given energy as a function of temperature, but were not constant for different energies in both sets. In general, the fluxes for the 1.5 and 6.7 eV beams were nearly equal but fluxes for the 2.7 and 4.5 eV beams were lower by a factor of

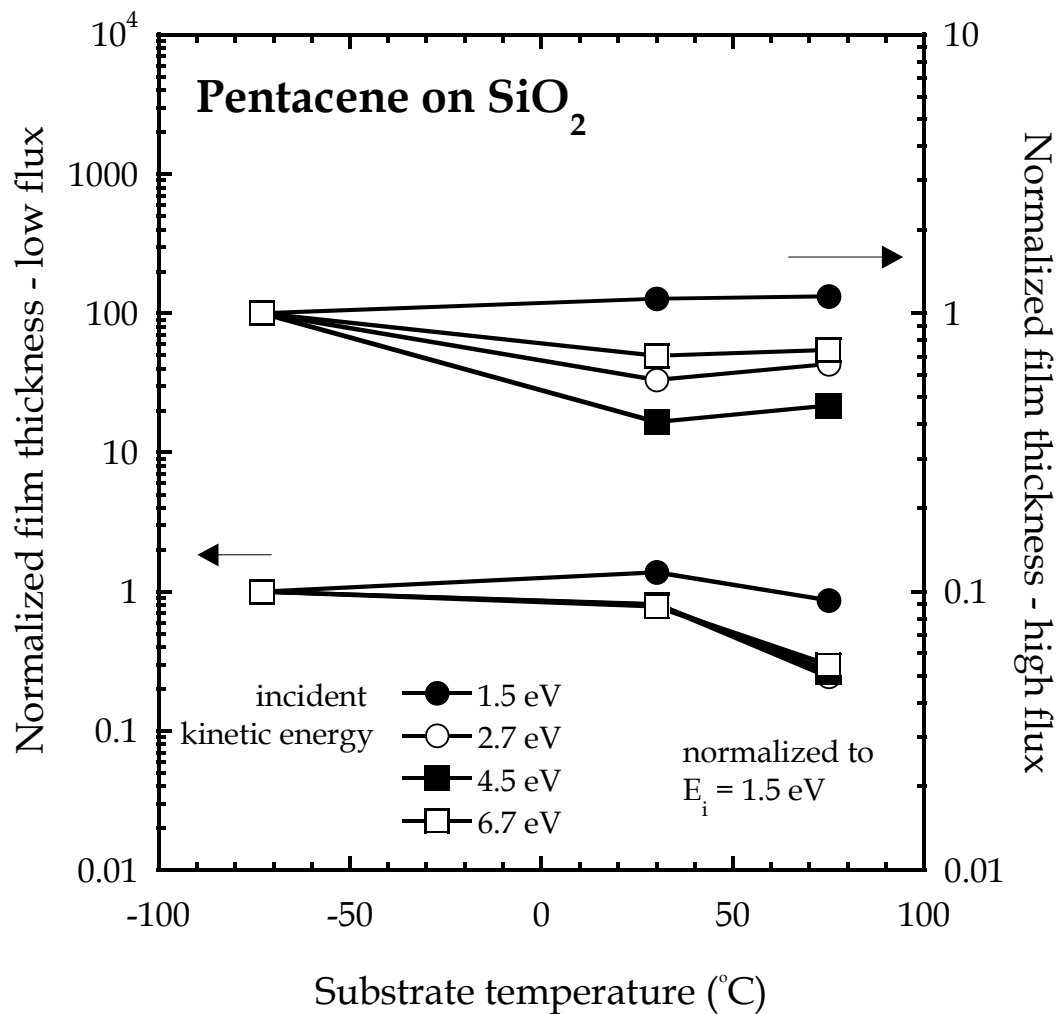


Figure 6–13 Pentacene film thickness as a function of substrate temperature for four incident kinetic energies and two sets of fluxes (see text). Data have been normalized for each energy with the value obtained at $-73 \text{ }^\circ\text{C}$. The solid lines are indicative of the trend of decreasing film thickness with increasing substrate temperature.

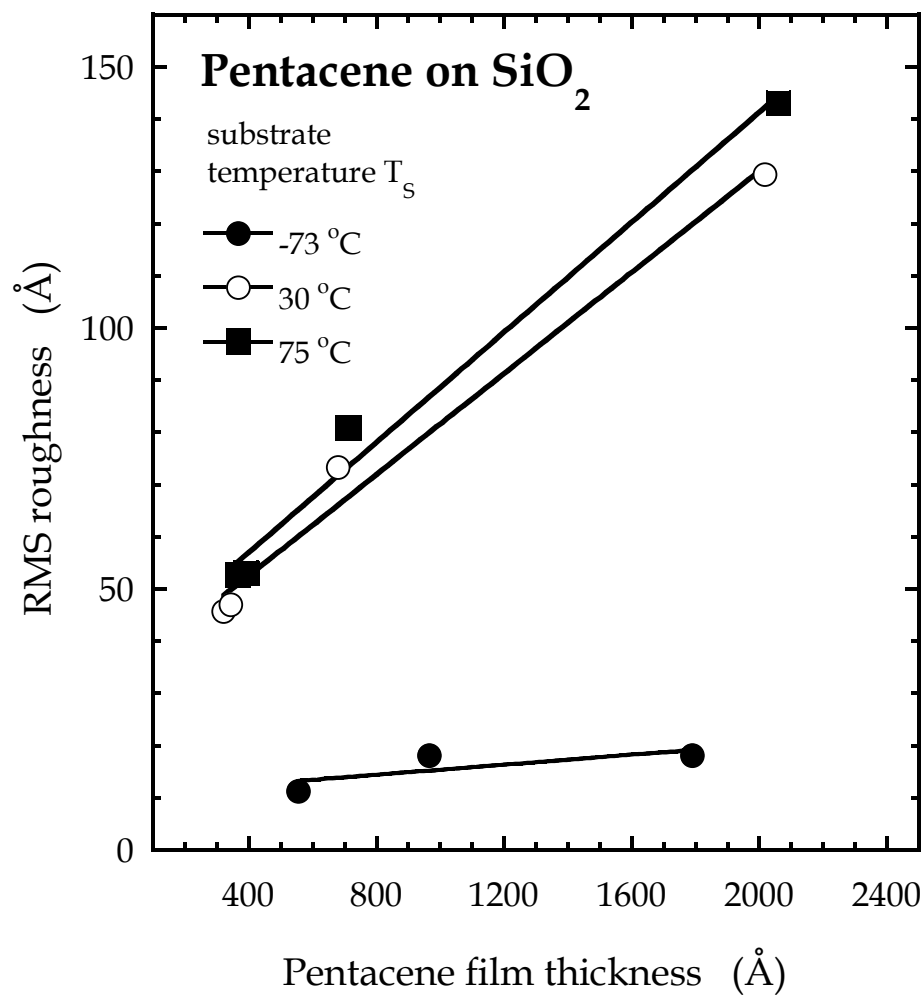


Figure 6–14 Root mean square (RMS) roughness as a function of film thickness for pentacene films deposited at the three substrate temperatures (T_s): $-73\text{ }^\circ\text{C}$, $30\text{ }^\circ\text{C}$ and $75\text{ }^\circ\text{C}$. The solid lines are linear fits to the data indicative of an increase in roughness with film thickness for $T_s = 30\text{ }^\circ\text{C}$ and $75\text{ }^\circ\text{C}$.

3–4 and 2–3 respectively. Film thicknesses are plotted as a function of substrate temperature in Fig. 6–13. Data have been normalized to the thickness at $-73\text{ }^{\circ}\text{C}$. For the set of data at a lower deposition rate, thickness remains nearly constant when temperature is increased from $-73\text{ }^{\circ}\text{C}$ to $30\text{ }^{\circ}\text{C}$ for all incident kinetic energies and drops by a factor of 2–3 at higher substrate temperatures. For the data at a higher deposition rate, thickness decreases with increasing temperature at higher incident kinetic energies (2.7 – 6.7 eV). For both sets of deposition rates, desorption becomes significant at the higher substrate temperature of $75\text{ }^{\circ}\text{C}$ contributing to a decrease in thickness of the film. If the two extremes in incident kinetic energy, 1.5 eV and 6.7 eV were considered, where the incident fluxes are nearly similar (within 10%), the higher incident kinetic energy results in a more dramatic decrease in film thickness. This could be attributed to lower trapping probability at higher incident kinetic energies (trapping probability at 6.7 eV is $\sim 40\%$ of trapping probability at 1.5 eV at room temperature) coupled with more desorption at higher substrate temperatures.

Film RMS roughness as a function of film thickness is plotted in Fig. 6–14 for the higher set of deposition rates. Films deposited at $-73\text{ }^{\circ}\text{C}$ (at three different incident kinetic energies of 1.5 eV, 2.7 eV and 6.7 eV) are much smoother than films deposited at higher temperatures (at the above three energies and 4.5 eV). These films are quite thick, i.e. 500 – 2000 Å and relatively smooth (roughness of 10 – 20 Å). In addition, unlike these films, films deposited at the higher substrate temperatures of $30\text{ }^{\circ}\text{C}$ and $75\text{ }^{\circ}\text{C}$ exhibit a far more dramatic increase in roughness with film thickness, which is to be expected from earlier results (c.f. Fig. 6–10). AFM images (Fig. 6–15) reaffirm

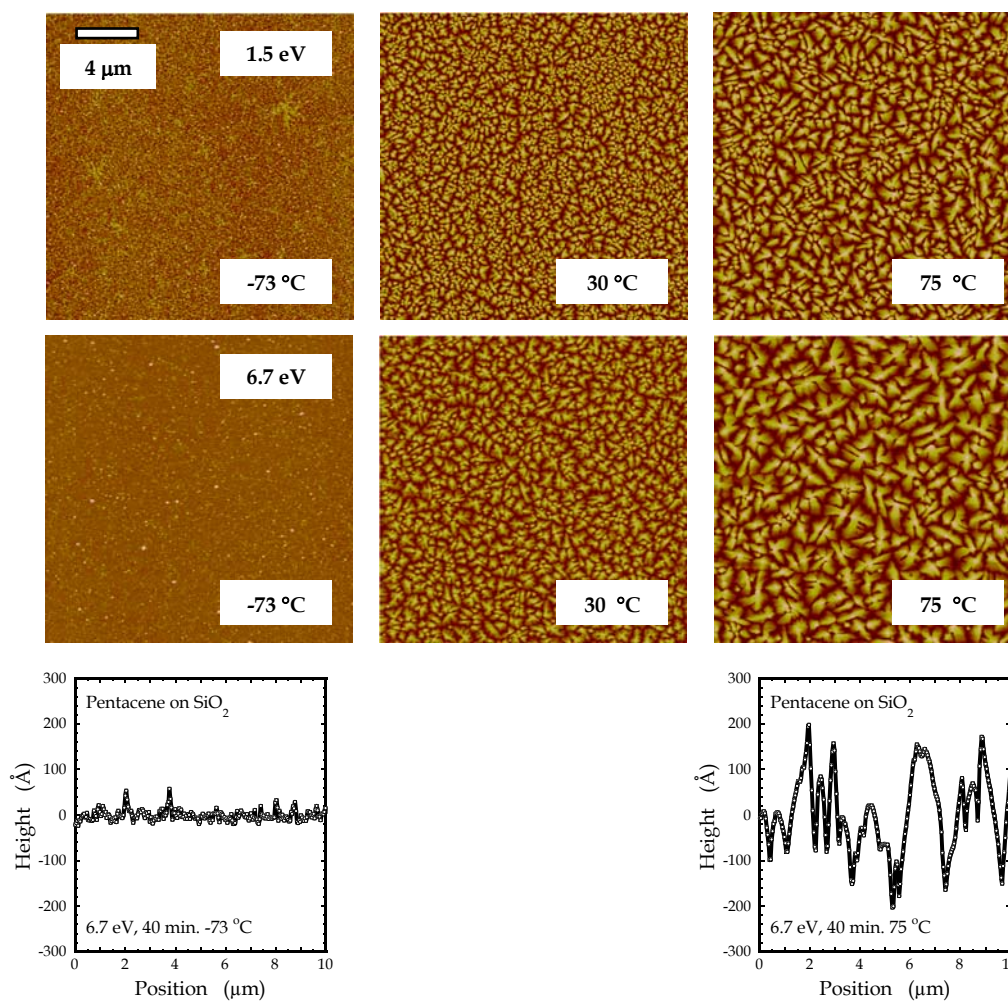


Figure 6–15 Atomic force micrographs of pentacene thin films deposited on SiO₂ for two incident kinetic energies ($E_i = 1.5$ eV and 6.7 eV, $\theta_i = 0^\circ$) and three substrate temperatures ($T_s = -73$, 30 and 75 °C). In each case the field of view is $20 \mu\text{m} \times 20 \mu\text{m}$. These are representative micrographs of film morphology. Similar images were obtained for films deposited with other incident kinetic energies ($E_i = 2.7$ and 4.5 eV) at normal incidence for all three substrate temperatures. Also shown are line scans across the AFM images of the films deposited at $E_i = 6.7$ eV and $T_s = -73$ °C and 75 °C.

that films deposited at the lowest temperature appear smooth (as indicated by the line scan in Fig. 6–15) without large features unlike the films deposited at room temperature or higher, where individual grains can be clearly observed. Further, the size of these grains increases with incident kinetic energy (1.5 eV to 6.7 eV) as seen previously and also with substrate temperature. From AFM images, the roughness exponent α can be determined for films deposited at -73°C and 75°C . For the 1.5 eV beam, α increases from 0.34 to 1.13 and for the 6.7 eV beam from 0.74 to 1.4. Values of α close to 1 indicate a structure that has grown under diffusional control. The increase in α with an increase in temperature is indicative of a cross-over to a different growth mechanism, belonging either to the Kardar–Parisi–Zhang (KPZ) class (characterized by $\alpha = 0.34$) [39], the molecular beam epitaxy (MBE) class (characterized by $\alpha = 0.66$) [29] or the diffusion-limited aggregation class (characterized by $\alpha = 1.0$) [28]. α has been used as an effective tool in the determination of phase transitions in organic thin films. Biscarini and co-workers [4] found thin sexithienyl films vacuum deposited on mica substrates underwent a phase transition at 160°C . This was marked by a change in the value of α from 1 to 0.48 suggesting a transition from diffusion controlled growth to a mechanism which is a combination of the above two mechanisms.

Gan and co-workers [40] deposited pentacene films on quartz substrates as a function of substrate temperature. From optical absorption spectra, they concluded that films deposited below -90°C were amorphous. Using x-ray diffraction, Ozaki and co-workers [41] determined that pentacene films deposited on quartz substrates at a higher substrate temperature and deposition rate of -50°C and 10 \AA/s respectively were amorphous. Also using x-ray diffraction, Dimitrakopoulos and co-workers [42] observed that films deposited

on SiO₂ at -196 °C and a deposition rate of 0.5 Å/s were amorphous. This was attributed to the low mobility of admolecules at the surface. When these films were brought to room temperature, randomly oriented crystallites were observed and their size and orientation did not change over time. More recently, Im and co-workers [43] deposited pentacene films by thermal evaporation on SiN_x/p-Si substrates. Films deposited with the substrate held at 60 °C and a high deposition rate of 7Å/s did not have any x-ray diffraction peaks and were consequently amorphous. Therefore, amorphous pentacene films can be deposited over a wide range of substrate temperatures and incident fluxes. These results seem to indicate the possibility that films deposited at -73 °C could correspond to a different phase of pentacene. Further studies are underway to understand film structure at these substrate temperatures using x-ray diffraction techniques.

6.4.3 Multilayers on SiO₂ modified with hexamethyldisilazane

The nucleation of pentacene films on SiO₂ substrates modified with HMDS results in islands that are two molecules tall, i.e. the second layer nucleates along with the first layer [14]. The third layer is also more dendritic than the second layer on bare SiO₂. Beyond the first few layers, film morphology consists of three-dimensional grains and is similar to deposition on bare SiO₂ as may be seen from AFM images showing film evolution for an incident kinetic energy of 6.7 eV and normal incidence (c.f. Fig. 6-16). Films are rough with a root mean square roughness for the film of thickness 355 Å (deposited for 2400 s) being 37.6 Å. For films deposited on bare SiO₂ a film

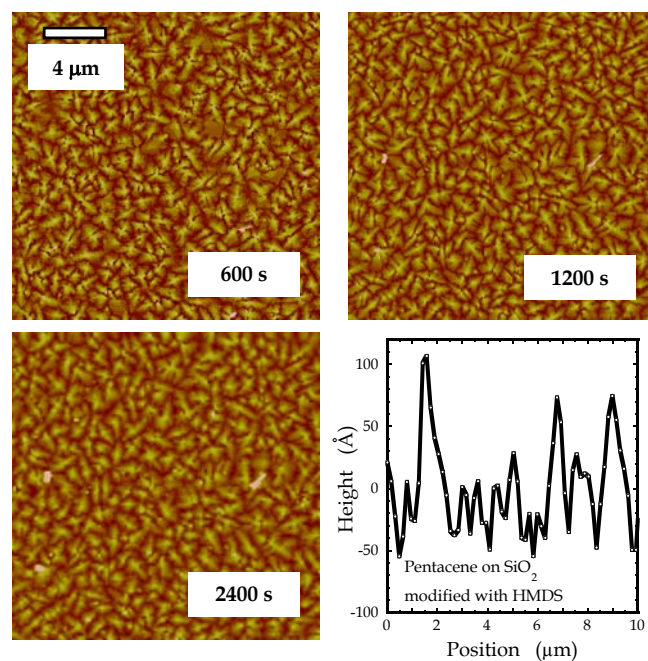


Figure 6–16 Atomic force micrographs of pentacene thin films deposited on SiO₂ modified with HMDS for a sequence of exposures to the supersonic beam ($E_i = 6.7$ eV, $\theta_i = 0^\circ$). In each case the field of view is $20 \mu\text{m} \times 20 \mu\text{m}$. These are representative micrographs of film evolution. Similar images were obtained for other incident kinetic energies and normal incidence. A line scan across the image obtained for an exposure of 2400 s is also shown.

Figure 6–17 (a) Thickness–exposure relationships, deduced from ellipsometry measurements, for the adsorption of pentacene on a pentacene multilayer at the four incident kinetic energies and normal incidence. The substrate was SiO₂ modified with HMDS. (b) The probability of adsorption of pentacene on a multilayer deposited on SiO₂ modified with HMDS and bare SiO₂ as a function of incident kinetic energy at normal incidence. The data have been normalized to that observed for pentacene on SiO₂ at $E_i = 1.5$ eV. Solid lines are indicative of the trend of decreasing probabilities of adsorption with increasing incident kinetic energy.

(a)

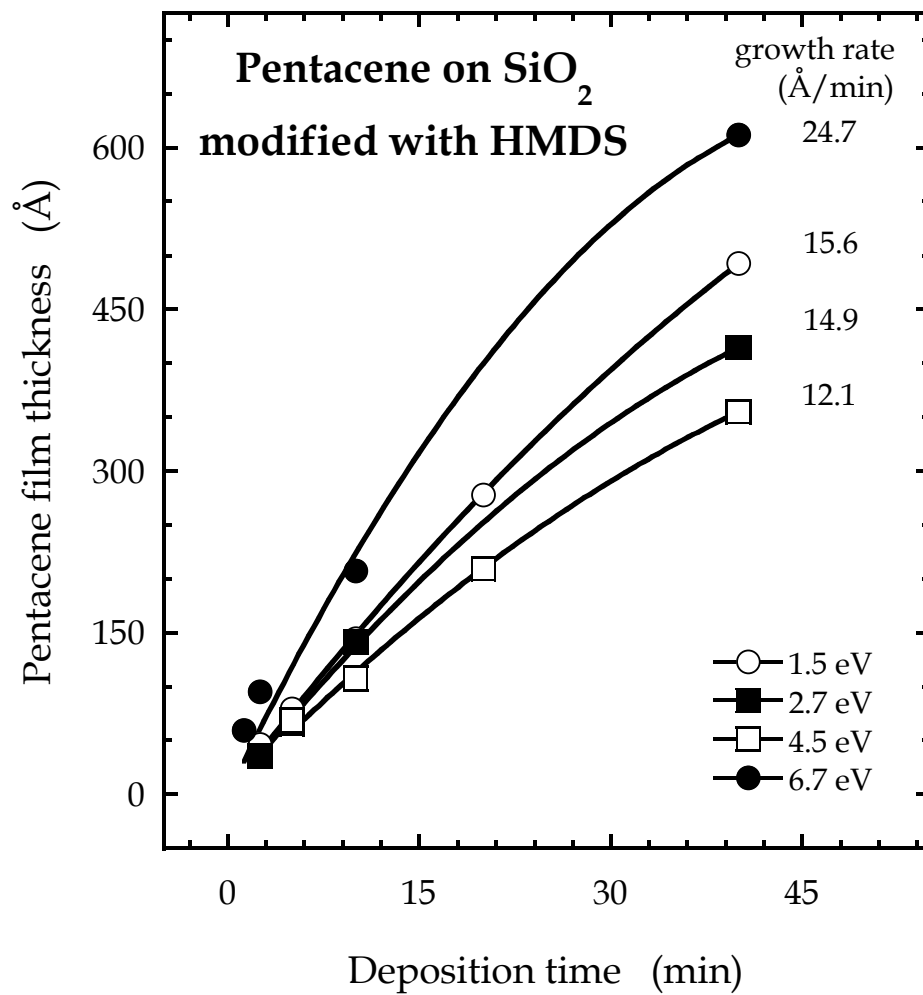
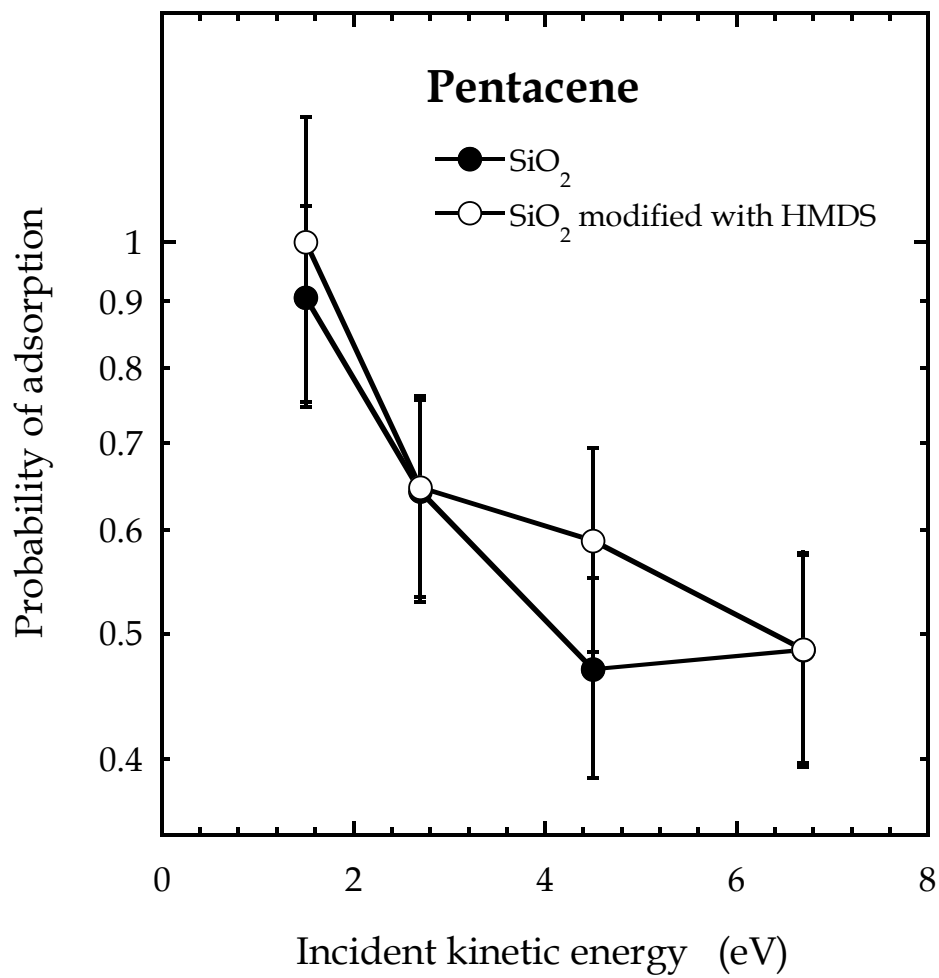


Figure 6-17 (Continued)

(b)



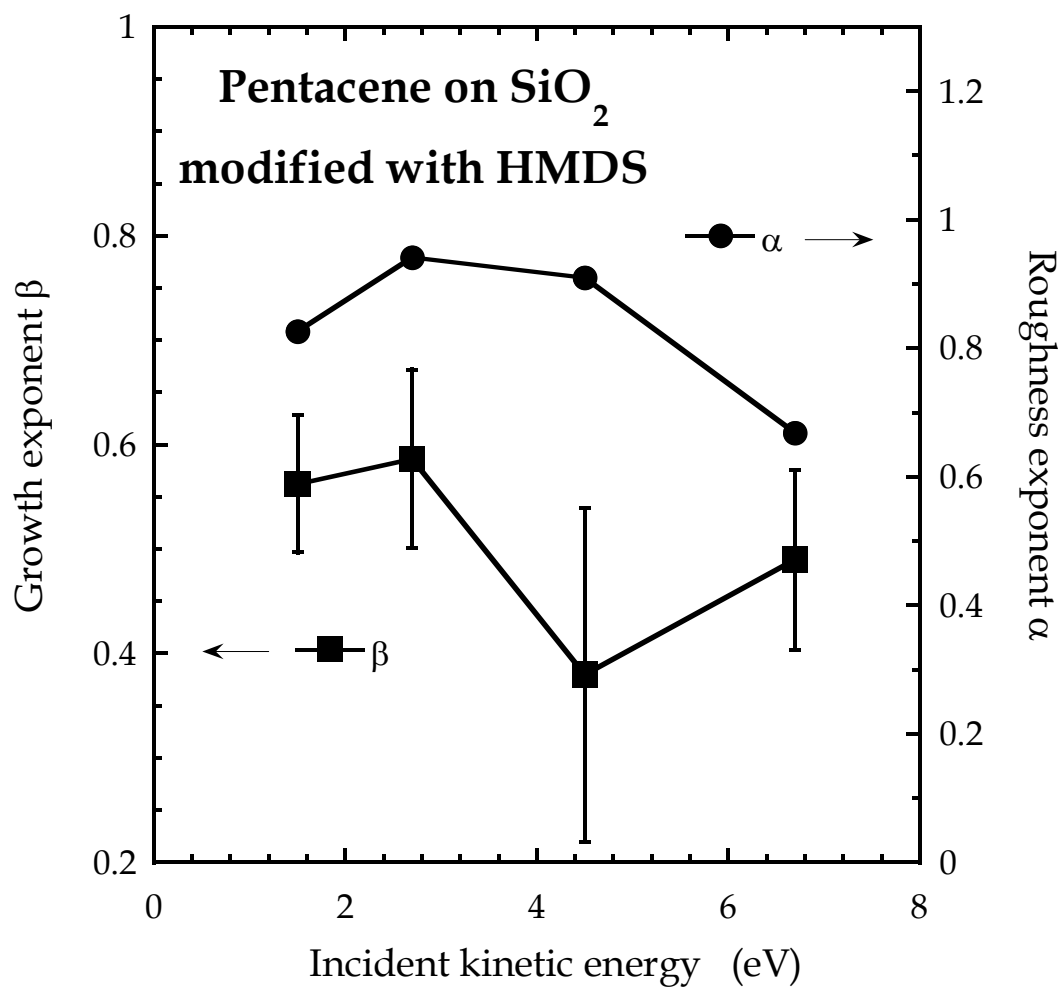


Figure 6–18 Roughness exponent α and growth exponent β as a function of incident kinetic energy for pentacene thin films deposited on SiO₂ modified with HMDS at normal incidence. Deposition time was 40 min. for all energies. Solid lines are indicative of the lack of a trend in exponents with incident kinetic energy.

thickness of 357 Å corresponds to a RMS roughness of 49.7 Å. As a result, deposition on SiO₂ modified by HMDS results in smoother films for an incident kinetic energy of 6.7 eV.

Film thickness as a function of exposure has been plotted in Fig. 6–17(a) for pentacene on SiO₂ modified with HMDS. Data are fit well by a quadratic model with the coefficient of the linear term used to determine deposition rates. Deposition rate on SiO₂ modified with HMDS is higher at 1.5 eV in comparison to bare SiO₂ by a factor of 2. With increasing energy, deposition rate decreases from 24.7 to 12.1 Å/min. This is indicative of trapping of pentacene on pentacene molecules similar to deposition on SiO₂. Probabilities of adsorption, $S_{A,m}$, can be determined from deposition rates in the multilayer regime and these values are plotted in Fig. 6–17(b) and compared to probabilities on multilayers on SiO₂. All values have been normalized to the value for deposition on SiO₂ modified with HMDS at 1.5 eV. For all energies, these probabilities are similar for deposition on SiO₂ modified with HMDS. Thus, modification of the surface of SiO₂ with HMDS resulted in dramatic differences in film morphology in the submonolayer regime [14] but beyond the first few monolayers, film deposition rates and morphology are similar and the probability of adsorption of pentacene on a depositing film does not change significantly in the multilayer regime.

Roughness and growth exponents α and β have been determined for pentacene films deposited on SiO₂ modified with HMDS (plotted in Fig. 6–18 as a function of incident kinetic energy). Values for α for the multilayer films do not show any significant trend with incident kinetic energy and range from 0.7 – 0.9. Values for β also do not show any trends with incident kinetic energy and range from 0.38 ± 0.16 to 0.59 ± 0.09 indicative of rapid roughening. However, these values for β are lower than those observed for deposition on

bare SiO₂. This indicates that films roughen slower on a modified surface in comparison to the bare SiO₂ surface. This could be one of the reasons for organic thin film transistors (OTFTs) fabricated from pentacene films deposited on SiO₂ modified with HMDS showing better performance characteristics than films deposited on bare SiO₂ [44].

6.5 Conclusions

Pentacene thin films have been deposited on bare SiO₂ and SiO₂ modified with hexamethyldisilazane (HMDS) using a supersonic molecular beam. Beyond the first few monolayers, film morphology become three-dimensional as seen by atomic force microscopy (AFM). Pentacene film thickness decreases with increasing incident kinetic energy while the incident flux is maintained a constant. This is indicative of trapping-mediated adsorption of pentacene molecules on a multilayer film. The ratio of multilayer to submonolayer deposition rate scales with incident kinetic energy (E_i) and incident angle (θ_i) as $E_i \cos^n \theta_i$ where the exponent $n = 0.5$. This is indicative of the importance of non-normal energy to film deposition. All deposited films exhibit a growth exponent $\beta > 0.5$ indicative of rapid roughening. β also increases with more glancing angles of incidence owing to shadowing effects. Film thickness decreases with increasing substrate temperature owing to significant desorption at higher temperatures. Films deposited at a substrate temperature of -73 °C are significantly smoother than films deposited at higher temperatures of 30 °C and 75 °C respectively possibly due to the formation of an amorphous phase. Deposition of pentacene films on SiO₂ modified with

HMDS results in similar three-dimensional structures. However, β is lower on these substrates indicative of a slower process of roughening.

6.6 References

1. F. -J. Meyer zu Heringdorf, M. C. Reuter and R. M. Tromp, *Nature* **412**, 517 (2001).
2. F. Biscarini, P. Samorí, A. Lauria, P. Ostoja, R. Zamboni, C. Taliani, P. Viville, R. Lazzaroni and J. L. Brédas, *Thin Solid Films* **284**, 439 (1996).
3. F. Biscarini, P. Samorí, O. Greco and R. Zamboni, *Phys. Rev. Lett.* **78**, 2389 (1997).
4. P. Viville, R. Lazzaroni, J. L. Brédas, P. Moretti, P. Samorí and F. Biscarini, *Adv. Mater.* **10**, 57 (1998).
5. A. C. Dürr, F. Schreiber, K. A. Ritley, V. Kruppa, J. Krug, H. Dosch and B. Struth, *Phys. Rev. Lett.* **90**, 016104–1 (2003).
6. F. Dinelli, M. Murgia, P. Levy, M. Cavallini and F. Biscarini, *Phys. Rev. Lett.* **92**, 116802–1 (2004).
7. C. D. Dimitrakopoulos and P. R. L. Malenfant, *Adv. Mater.* **14**, 99 (2002).
8. S. R. Forrest, *Chem. Rev.* **97**, 1793 (1997).
9. Y. -Y. Lin, D. J. Gundlach, S. F. Nelson and T. N. Jackson: *IEEE Electron Device Lett.* **18**, 606 (1997).
10. L. Casalis, M. F. Danisman, B. Nickel, G. Bracco, T. Toccoli, S. Iannotta and G. Scoles, *Phys. Rev. Lett.* **90**, 206101–1 (2003).
11. S. Iannotta and T. Toccoli, *J. Polymer Sc. B* **41**, 2501 (2003).
12. F. De Angelis, T. Toccoli, A. Pallaoro, N. Coppedè, L. Mariucci, G. Fortunato and S. Iannotta, *Synth. Met.* **146**, 291 (2004).
13. A. S. Killampalli, T. W. Schroder and J. R. Engstrom, *Appl. Phys. Lett.* **87**, 033110 (2005).

14. A. S. Killampalli and J. R. Engstrom, manuscript submitted to *Appl. Phys. Lett.*, October 2005.
15. S. E. Roadman, N. Maity, J. N. Carter and J. R. Engstrom, *J. Vac. Sci. Technol. A* **16**, 3423 (1998).
16. T. W. Schroeder, Ph. D thesis, Cornell University, 2004.
17. P. Dumas, B. Bouffakhreddine, C. Amra, O. Vatel, E. Andre, R. Galindo and F. Salvan, *Europhys. Lett.* **22**, 717 (1993).
18. G. W. Collins, S. A. Letts, E. M. Fearon, R. L. McEachern and T. P. Bernat, *Phys. Rev. Lett.* **73**, 708 (1994).
19. C. Douketis, Z. Wang, T. L. Haslett and M. Moskovits, *Phys. Rev. B* **51**, 11022 (1995).
20. S. P. Park, S. S. Kim, J. H. Kim, C. N. Whang and S. Im, *Appl. Phys. Lett.* **80**, 2872 (2002).
21. M. C. McMaster, S. Schroeder, and R. J. Madix, *Surf. Sci.* **297**, 253 (1993).
22. M. E. King, K. M. Fiehrer, G. M. Nathanson and T. K. Minton, *J. Phys. Chem. A* **101**, 6556 (1997).
23. L. A. DeLouise, *Chem. Phys. Lett.* **180**, 140 (1990).
24. M. Head-Gordon and J. C. Tully, *Surf. Sci.* **268**, 113 (1992).
25. L.-Q. Xia and J. R. Engstrom, *J. Chem. Phys.* **101**, 5329 (1994).
26. C. T. Reeves, B. A. Ferguson, C. B. Mullins, G. O. Sitz, B. A. Helmer, and D. B. Graves, *J. Chem. Phys.* **111**, 7567 (1999).
27. A. -L. Barabási and H. E. Stanley, *Fractal Concepts in Surface Growth*, (Cambridge University Press, Cambridge, United Kingdom 1995).
28. D. E. Wolf and J. Villain, *Europhys. Lett.* **13**, 389 (1990).
29. Z. -W. Lai and S. Das Sarma, *Phys. Rev. Lett.* **66**, 2348 (1991).

30. K. J. Caspersen, A. R. Layson, C. R. Stoldt, V. Fournée, P. A. Thiel and J. W. Evans, *Phys. Rev. B* **65**, 193407–1 (2002).
31. H. –J. Ernst, F. Fabre, R. Folkerts and J. Lapujoulade, *Phys. Rev. Lett.* **72**, 112 (1994).
32. K. Fang, T. –M. Lu and G. –C. Wang, *Phys. Rev. B* **49**, 8331 (1994).
33. C. J. Lanczycki, R. Kotlyar, E. Fu, Y. –N. Yang, E. D. Williams and S. Das Sarma, *Phys. Rev. B* **57**, 13132 (1998).
34. L. Vázquez, R. C. Salvarezza, E. Albano, A. J. Arvia, A. H. Creus, R. A. Levy and J. M. Albella, *Chem. Vap. Depn.* **4**, 89 (1998).
35. A. E. Lita and J. E. Sanchez, Jr., *J. Appl. Phys.* **85**, 876 (1999).
36. J. –P. Schlomka, M. Tolan and W. Press, *Appl. Phys. Lett.* **76**, 2005 (2000).
37. J. Xu, L. Yu and I. Kojima, *J. Appl. Phys.* **94**, 6827 (2003).
38. J. Hachenberg, C. Streng, E. Súske, S. Vauth, S. G. Mayr, H. –U. Krebs and K. Samwer, *Phys. Rev. Lett.* **92**, 246102–1 (2004).
39. M. Kardar, G. Parisi and Y. –C. Zhang, *Phys. Rev. Lett.* **56**, 889 (1986).
40. K. O. Lee and T. T. Gan, *Chem. Phys. Lett.* **51**, 120 (1977).
41. T. Minakata, H. Imai and M. Ozaki, *J. Appl. Phys.* **72**, 4178 (1992).
42. C. D. Dimitrakopoulos, A. R. Brown and A. Pomp, *J. Appl. Phys.* **80**, 2501 (1996).
43. M. H. Choo, J. H. Kim and S. Im, *Appl. Phys. Lett.* **81**, 4640 (2002).
44. A. S. Killampalli, A. Papadimitratos, G. G. Malliaras and J. R. Engstrom, manuscript to be submitted to *Adv. Mater.* (2005).

7. Organic thin film transistors of pentacene films deposited using supersonic molecular beams

7.1 Overview

Organic thin film transistors (OTFTs) with pentacene thin films and gold top contacts have been fabricated. Films were deposited using an energetic molecular beam. Incident kinetic energy can be used to modify the size of individual grains at room temperature. This is directly correlated to increase in mobility of OTFTs and data are best described by a model for charge transport based on thermionic emission. Modification of the SiO₂ surface with HMDS does not alter morphology in the multilayer regime in a significant manner. However, OTFTs fabricated on SiO₂ substrates modified with HMDS exhibit higher mobilities, stronger gate modulation and lower off currents in comparison to ones fabricated on bare SiO₂. Higher inverse subthreshold slopes for devices on SiO₂ modified with HMDS reveal that there could be reduced charge trapping at this interface.

7.2 Introduction

Electronics based on organic materials has garnered extensive interest in the past two decades [1,2] with potential advantages being low cost, flexibility associated with choice of substrate and processing conditions. Important applications include thin film transistors and photovoltaic devices based on either small organic molecules [3,4] or conjugated polymers [5–7]. Pentacene

is an excellent molecule for applications in organic electronics owing to the ability to form highly ordered thin films near room temperature [8–9] with charge carrier mobilities of $1.5 - 3 \text{ cm}^2\text{-V}^{-1}\text{-s}^{-1}$ [10–11]. Performance characteristics of pentacene thin film transistors can be strongly influenced by the first few layers in close contact with the dielectric in devices with top contact configuration [12]. Consequently, modification of dielectric substrates with organic or self-assembled monolayers has been studied to improve performance of OTFTs. Hexamethyldisilazane (HMDS) [13–15] and octadecyltrichlorosilane (OTS) [15–18] have been organic layers of choice for surface modification.

Zyung and co-workers [13] deposited 100 nm thick pentacene thin films on O_2 plasma cleaned SiO_2 , SiO_2 spin coated with hexamethyldisilazane (HMDS) and SiO_2 coated with octadecyltrichlorosilane (OTS) by solution processing. Bottom contact OTFTs with modified SiO_2 substrates exhibited higher mobilities of 0.16 and $0.29 \text{ cm}^2\text{-V}^{-1}\text{-s}^{-1}$ in comparison to $0.1 \text{ cm}^2\text{-V}^{-1}\text{-s}^{-1}$ on bare SiO_2 . On-off current ratios were 10^5 in all cases. Bao and co-workers [14] fabricated top contact OTFTs with 60 nm thick pentacene films deposited on SiO_2 substrates modified with HMDS (using a vapor priming oven) and OTS (deposited from vapor phase in a dessicator). They obtained larger saturation currents for transistors fabricated on SiO_2 surfaces modified with HMDS and also a higher mobility of $3.4 \pm 0.5 \text{ cm}^2\text{-V}^{-1}\text{-s}^{-1}$ compared to $0.5 \pm 0.15 \text{ cm}^2\text{-V}^{-1}\text{-s}^{-1}$ on SiO_2 treated with OTS. The better performance was attributed to morphological differences in island geometry in the sub-monolayer regime while multilayer films yielded similar crystallographic structure for all surface treatments. Aoyagi and co-workers [15] deposited 30 nm thick pentacene films on SiO_2 substrates spin coated with

HMDS and top contact OTFTs were fabricated. While multilayer morphology was not altered by surface treatment, OTFTs exhibited dramatic off current suppression and mobility enhancement. Reduction in the number of trap states at the pentacene/SiO₂ interface was postulated to be responsible for improved performance.

The growth of organic thin films and thereby the performance of OTFTs can be strongly influenced by the kinetic energy of the incident molecules. Supersonic molecular beams provide an ideal tool to vary the kinetic energy of incident pentacene molecules over a useful range, i.e., on the order of, or greater than, the pentacene–pentacene and pentacene–SiO₂ binding energies. Iannotta and co-workers [19] examined the energetic deposition of pentacene films. Initial results were obtained for OTFTs fabricated using these films on SiO₂/Si with Au bottom and top contacts. Films deposited with an incident kinetic energy of pentacene of 5.5 eV were constituted by grains with dimensions on the order of 2–3 μm while films deposited with a lower incident kinetic energy of 0.4 eV had grains with dimensions of a few hundred nm. They suggested that morphological variations were responsible for the former films resulting in top contact OTFTs with better mobilities of 0.5 cm²–V^{–1}–s^{–1}. Bottom contact devices resulted in mobilities of 0.085 cm²–V^{–1}–s^{–1} with no dependence of performance on incident kinetic energy. In the work reported here, supersonic molecular beams have been used to examine explicitly the effect of incident kinetic energy on performance of TFTs of pentacene films deposited under ultrahigh vacuum (UHV) conditions. The effects of substrate modification on device performance have been studied, utilizing both bare SiO₂/Si and SiO₂/Si substrates modified with HMDS. HMDS was chosen as the substrate modifier owing to its advantages of air stability, short molecular

length and ease of vapor processing. Typical performance characteristics considered include mobility, ratio of currents in the on and off states ($I_{\text{on}}/I_{\text{off}}$), threshold voltage (V_{th}) and inverse subthreshold slope (S).

7.3 Experimental methods

The apparatus and experimental methods employed [20,21] have been described in detail in section 2.2. In brief, the experiments were carried out in a custom-designed UHV chamber with typical base pressures of $\sim 2 \times 10^{-9}$ torr. Samples were heavily doped p-type and n-type silicon wafers of size $16.75 \text{ mm} \times 16.75 \text{ mm}$. $\sim 3100 \text{ \AA}$ of silicon dioxide was grown by wet thermal oxidation at $1100 \text{ }^\circ\text{C}$. Immediately prior to deposition of pentacene films, SiO_2 substrates were subject to sonication in chloroform, DI water and a UV-Ozone treatment. HMDS films were deposited on UV-Ozone cleaned SiO_2 substrates using a Yield Engineering Systems (YES) oven. These films were smooth and defect free with a density of methyl groups of $6.87 \pm 1.44 \times 10^{14} \text{ molec-cm}^{-2}$ [22]. All pentacene films were deposited using a supersonic beam source at room temperature. Deposition time was 40 min. in all cases. Beam intensity was monitored for every experiment using a quadrupole mass spectrometer (Extrel) located downstream, on the beam axis. Intensity was maintained a constant for different incident kinetic energies. Following deposition of $\sim 400 \text{ \AA}$ thick pentacene films at four different incident kinetic energies, 1.5, 2.7, 4.5 and 6.7 eV and normal incidence, substrates were removed from the chamber and stored in a dry box before organic thin film transistors were fabricated. Shown in Fig. 7-1 are typical configurations for OTFTs. For these experiments, top

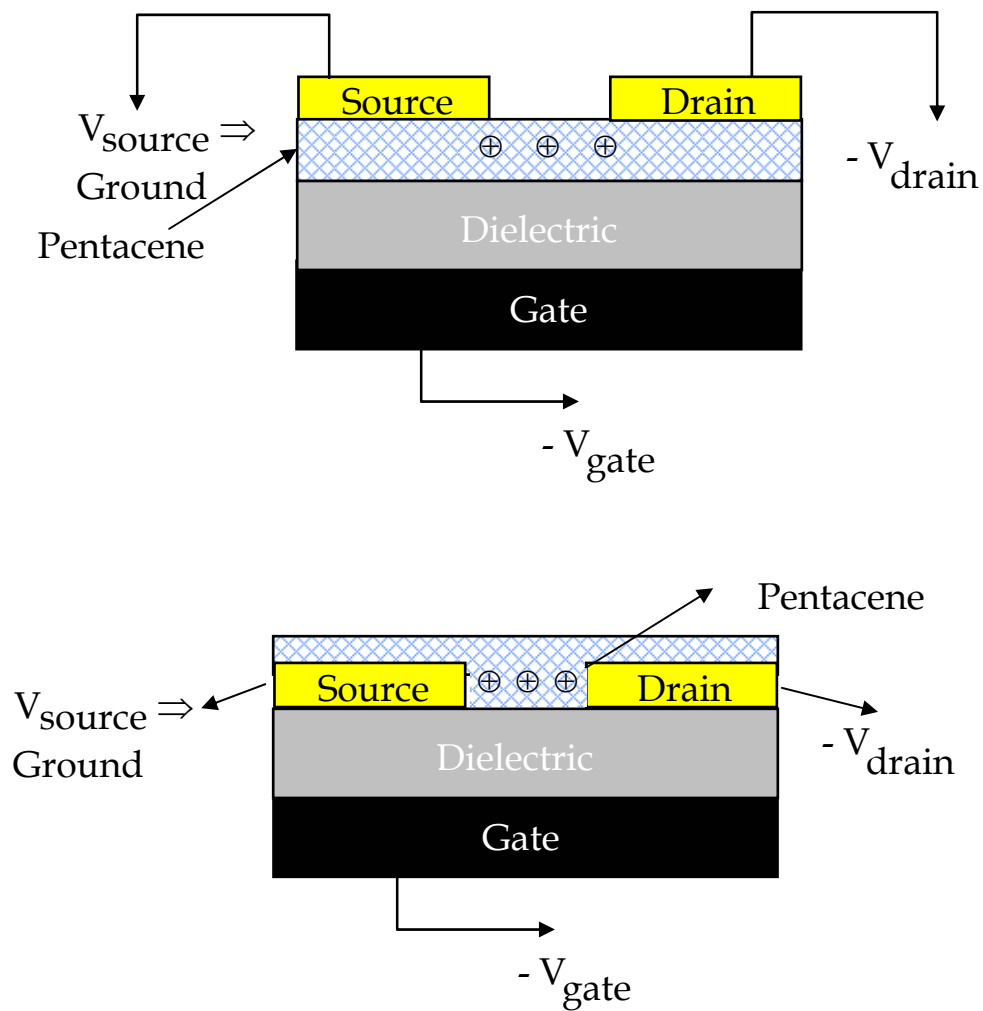


Figure 7-1 Top and bottom contact configurations for organic thin film transistors (OTFTs) fabricated using semiconducting films.

drain and source gold contacts were employed. These contacts were 250 Å thick and were thermally sublimed at a rate of 4 Å-s^{-1} using a shadow mask to define between 9 to 12 transistors per sample, 3 per row having a channel length of 31.25, 75 and 125 μm respectively. Electrical characterization was carried out using a four-point probe station under vacuum (10^{-6} torr) at room temperature (details in section 2.2.6). The field-effect mobility, μ_{FE} was extracted from the saturation regime.

Samples from identical deposition runs were also examined separately *ex situ* using a Digital Instruments Dimension 3100 scanning probe microscope (Veeco Instruments) in tapping mode. Typical images obtained were of size $20 \mu\text{m} \times 20 \mu\text{m}$ and subjected to a second order plane fit using Nanoscope software (v 5.0). One dimensional PSD spectra (1DPSD) have been used to characterize the surface structure [23–25] (details in section 2.2.5.2). 1DPSDs were determined using Nanoscope software along the fast scan direction and single line PSDs were averaged. For each scan length L , spatial frequencies range between $1/L$ and the Nyquist frequency $256/L$.

7.4 Results and discussion

AFM images were obtained for each multilayer film at different exposure times resulting in a series of “snapshots” at different stages of the deposition process. Displayed in Fig. 6–7 were images of pentacene films deposited for 40 min. at normal incidence with $E_i = 1.5, 2.7, 4.5$ and 6.7 eV on bare SiO_2 at room temperature. Also shown for comparison was a micrograph of a film deposited by thermal evaporation with a deposition rate of 0.3 Å/s . As

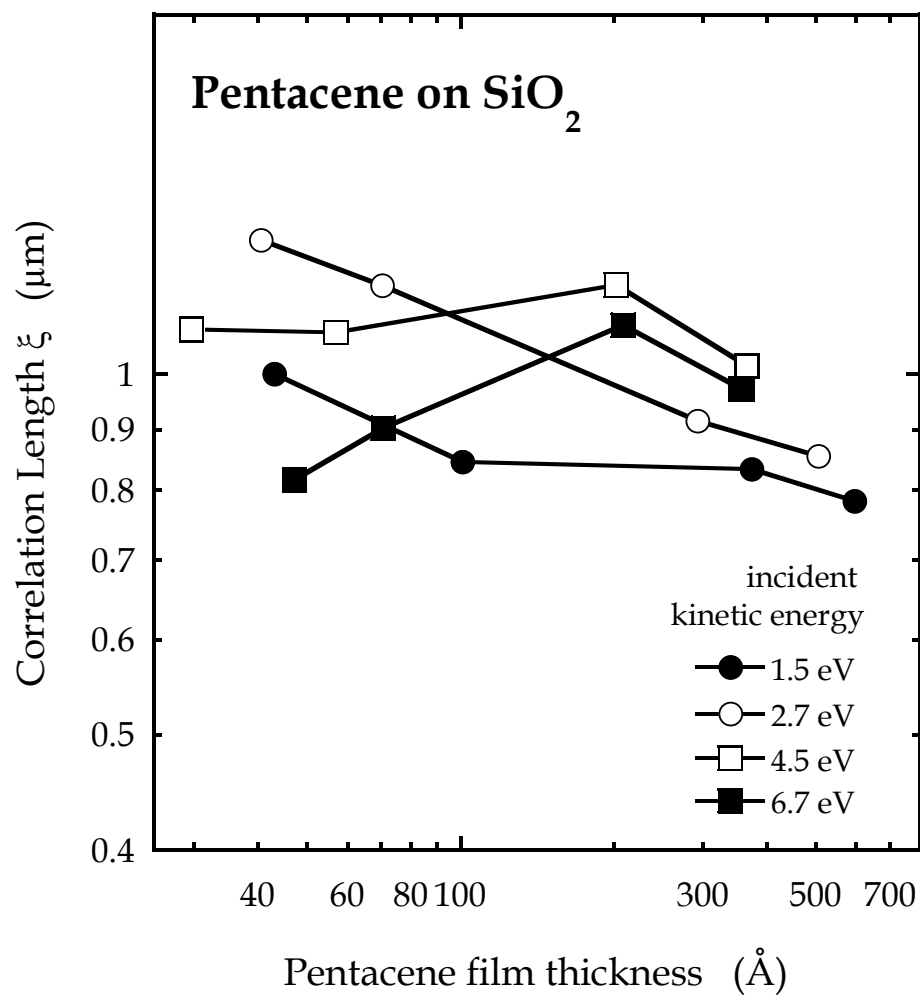


Figure 7–2 Correlation length obtained from one–dimensional power spectral density (1DPSD) analysis of AFM images plotted as a function of thickness for pentacene thin films deposited on SiO_2 for four incident kinetic energies: 1.5, 2.7, 4.5 and 6.7 eV at normal incidence.

may be seen, grains are smallest in the evaporated film and the size of individual grains increases with incident kinetic energy from 1.5 eV to 4.5 eV. From one-dimensional power spectral density (1DPSD) curves for each AFM image, a correlation length characteristic of topography can be extracted [26]. Plotted in Fig. 6–8 were 1DPSD curves for pentacene films deposited for 40 min. at the four different incident kinetic energies. The PSDs exhibited two distinct regions: (i) a plateau PSD ($1/L$) at low spatial frequencies denoting the absence of nonlocal correlations along the line scans, and (ii) a frequency-dependent decaying branch indicative of the self-affine nature of the film. This branch is taken as the self-affine range. The high frequency range is discarded since it is affected readily by noise and aliasing. The range of the intersection between the self-affine branch and the plateau yields the inverse of the correlation length ξ :

$$\xi = \exp\left\{\frac{\ln[PSD(1/L)] - \ln K_0}{\gamma}\right\} \quad (7-1)$$

As may be seen from Fig. 6–8, films are the self-affine enabling the extraction of a correlation length. Plotted in Fig. 7–2 is evolution of correlation length as a function of thickness of pentacene films. Beyond a thickness of 100 Å, there is not a significant change in correlation length. As a result a thickness-averaged correlation length (Fig. 7–3) can be determined for each incident kinetic energy for pentacene films deposited on bare SiO₂ and SiO₂ modified with HMDS. Films deposited with an incident kinetic energy of 1.5 eV exhibit smaller thickness-averaged correlation lengths in comparison to films deposited at high incident kinetic energy. Therefore, this correlation

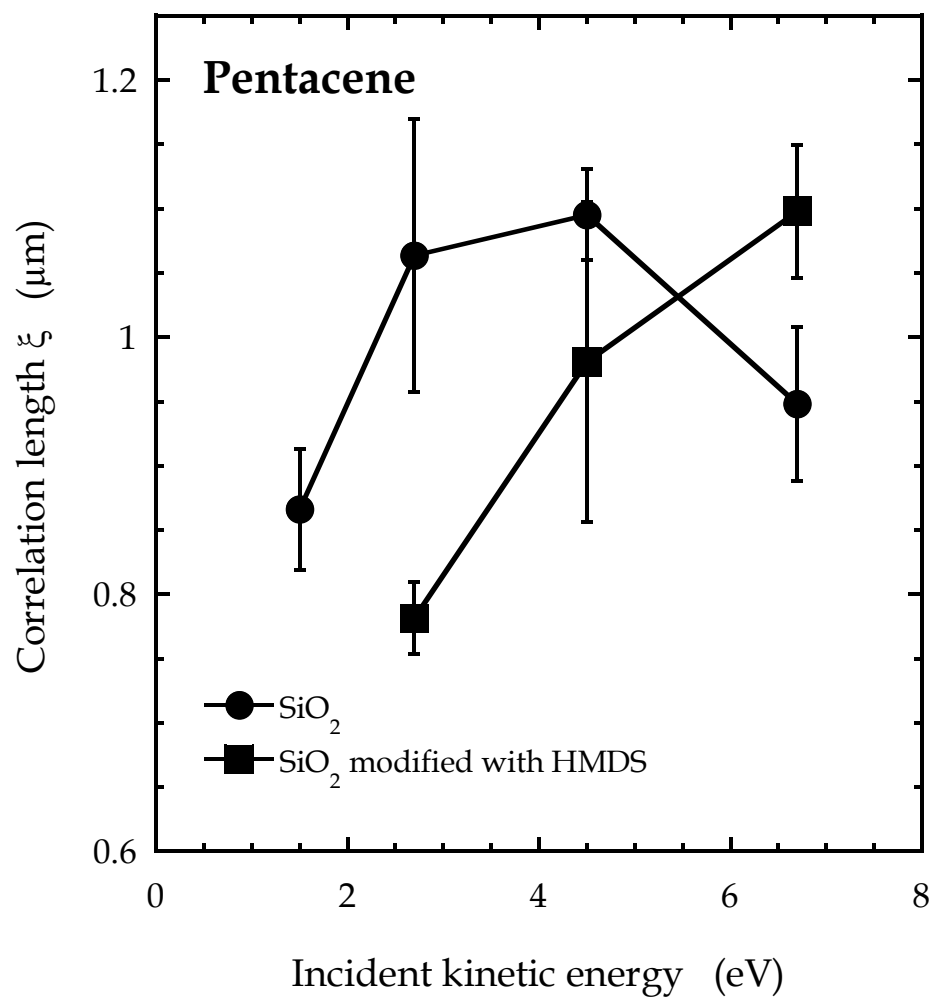


Figure 7–3 Thickness–averaged correlation length from 1DPSD analysis of AFM images plotted as a function of incident kinetic energy for pentacene thin films deposited on SiO_2 and SiO_2 modified with HMDS. Solid lines are a linear least squares fit to the data.

Figure 7–4 Mobility of organic thin film transistors plotted as a function of thickness–averaged correlation length obtained from one–dimensional power spectral density (1DPSD) analysis of AFM images of pentacene films deposited on (a) SiO₂ and (b) SiO₂ modified with HMDS. Deposition time was 40 min. in all cases. The solid lines represent linear least square fits to the data.

(a)

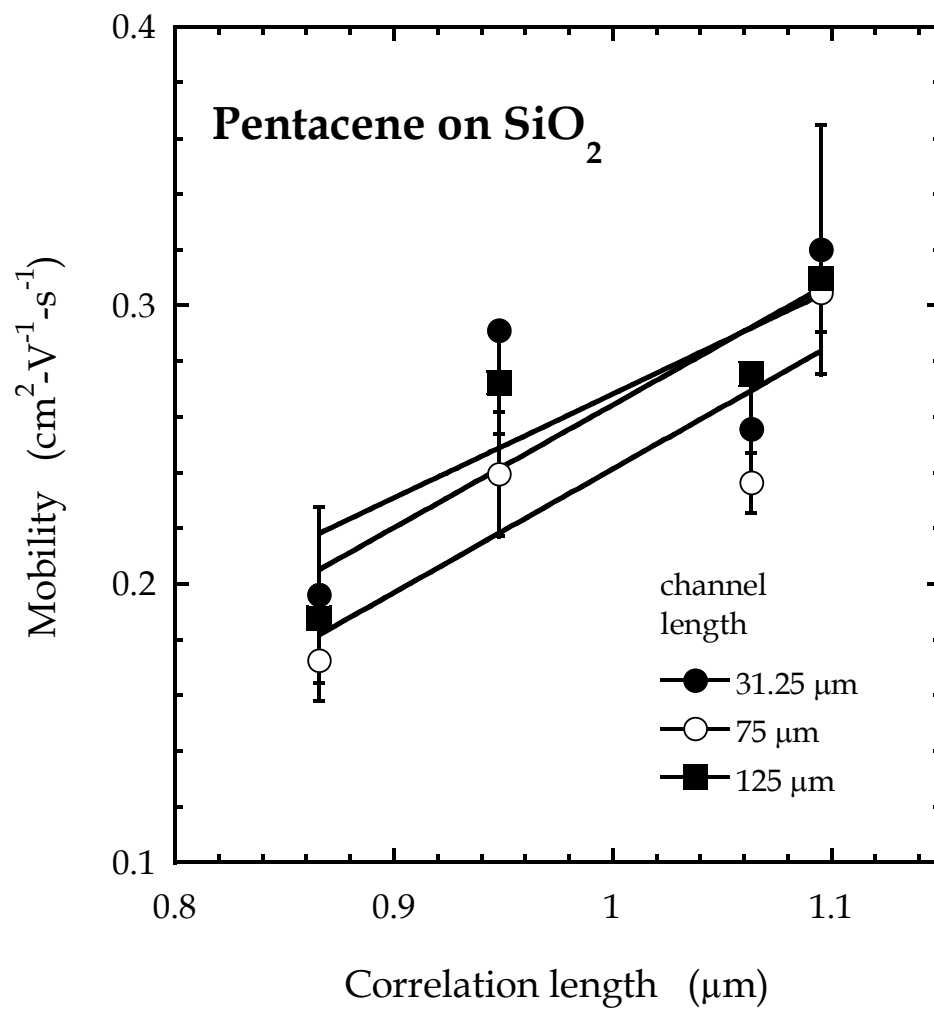
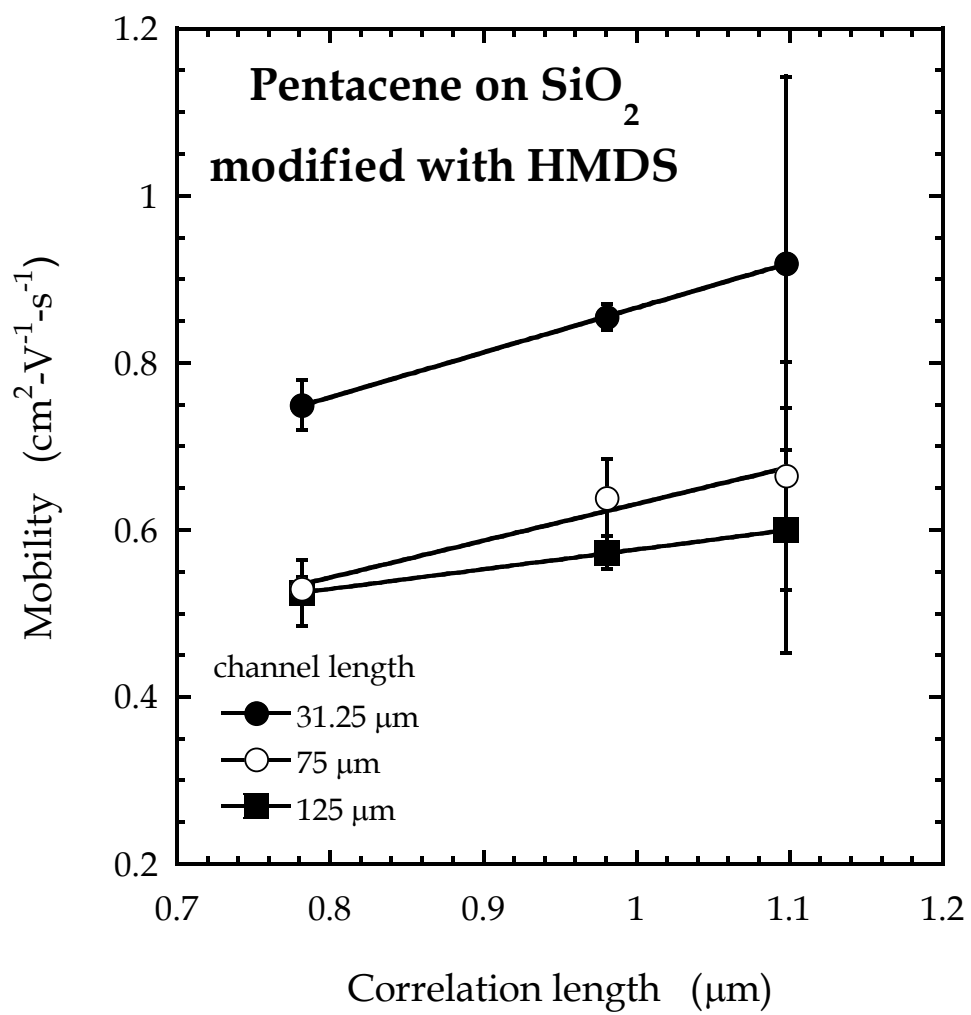


Figure 7-4 (Continued)

(b)



length is a direct measure of grain size in deposited films and can be used as a metric to quantify performance of OTFTs fabricated using these films.

Similar AFM images were obtained for films deposited on SiO₂ modified with HMDS. Film morphology was similar and thickness-averaged correlation lengths were extracted from 1DPSD curves (for incident kinetic energies of 2.7 – 6.7 eV). These correlation lengths are also plotted in Fig. 7-3 and are similar to films deposited on bare SiO₂. Modification of the SiO₂ substrate with HMDS results in larger island densities with islands being two molecules tall [22] but beyond the first few monolayers, differences in morphology between films deposited on both these substrates were not found to be substantial (c.f. section 6.4.3).

Knowing that film morphology could be improved with larger incident kinetic energy, OTFTs were fabricated from pentacene films deposited on bare SiO₂ and SiO₂ substrates modified with HMDS. Plotted in Fig. 7-4 are mobilities for OTFTs as a function of correlation length extracted from above 1DPSD analysis for (a) SiO₂ and (b) SiO₂ modified with HMDS. Three different channel lengths of 31.25 μm, 75 μm and 125 μm were employed. From the figure, it is clear that mobilities increase with thickness-averaged correlation length which in turn increases for films deposited with higher incident kinetic energies. Substantial improvement in mobility is also obtained by modifying the SiO₂ substrate with HMDS. Mobility is determined by the contributions from charge transport through bulk grains (μ_g) and through grain boundaries (μ_b) [27] as:

$$\frac{1}{\mu} = \frac{1}{\mu_g} + \frac{1}{\mu_b} \quad (7-2)$$

If $\mu_g \gg \mu_b$, overall mobility is determined by charge transport at grain boundaries. A Schottky barrier can be assumed to form at the inter-grain region [28], if the Debye length $L_D = (\epsilon_s kT/q^2 N)^{1/2}$ which is characteristic of charge screening in individual grains is much smaller than the size l of a grain. In this expression, ϵ_s is the permittivity of pentacene, T is absolute temperature at which the measurement is made, q is electronic charge and N is the charge carrier concentration. A doping level of 10^{17} cm^{-3} [28] and $T = 300 \text{ K}$ yields an estimate for L_D to be $\sim 10 \text{ nm}$. From Fig. 7-3 correlation lengths ξ for pentacene films are $800 - 1200 \text{ nm}$ which reflects grain size. As a result $\xi \gg L_D$ and mobility is then determined by thermionic emission at grain boundaries, i.e.

$$\mu = \mu_b = \frac{q v_m \xi}{8kT} \exp\left(-\frac{E_b}{kT}\right) \quad (7-3)$$

where E_b is the barrier for thermionic emission and v_m is the electron mean velocity. From Fig. 7-4 it is clear that the data are fit well by a linear model [24] which seems to indicate that:

- (i) the correlation length is a direct measure of grain size,
- (ii) mobility is strongly influenced by charge transport at grain boundaries,
- (iii) thermionic emission is the dominant mechanism for charge transport at grain boundaries.

Also from Fig. 7-4 it is apparent that mobilities decrease with increasing channel length. This seems to corroborate the fact that charge transport is strongly influenced at grain boundaries. Contact resistance is not playing a vital role in determining electronic properties.

Table 7–1 Performance characteristics of organic thin film transistors fabricated from pentacene films with a channel length of 75 μm . Two substrates, SiO_2 and SiO_2 modified with hexamethyldisilazane (HMDS) are compared.

Substrate	Mobility (μ) ($\text{cm}^2\text{-V}^{-1}\text{-s}^{-1}$)	$I_{\text{on}} / I_{\text{off}}$	V_{th} (V)	Inverse Subthreshold slope (S) (dec-V^{-1})
SiO_2	0.27	5.8×10^3	-18.43	0.73
SiO_2 modified with HMDS	0.79	8.4×10^4	-26.7	2.55

Figure 7–5 Drain–to–source current plotted as a function of drain–to–source voltage for pentacene thin film transistors fabricated on (a) SiO₂ and (b) SiO₂ modified with HMDS. Deposition energy was 6.7 eV at normal incidence and channel length was 75 μm for these transistors.

(a)

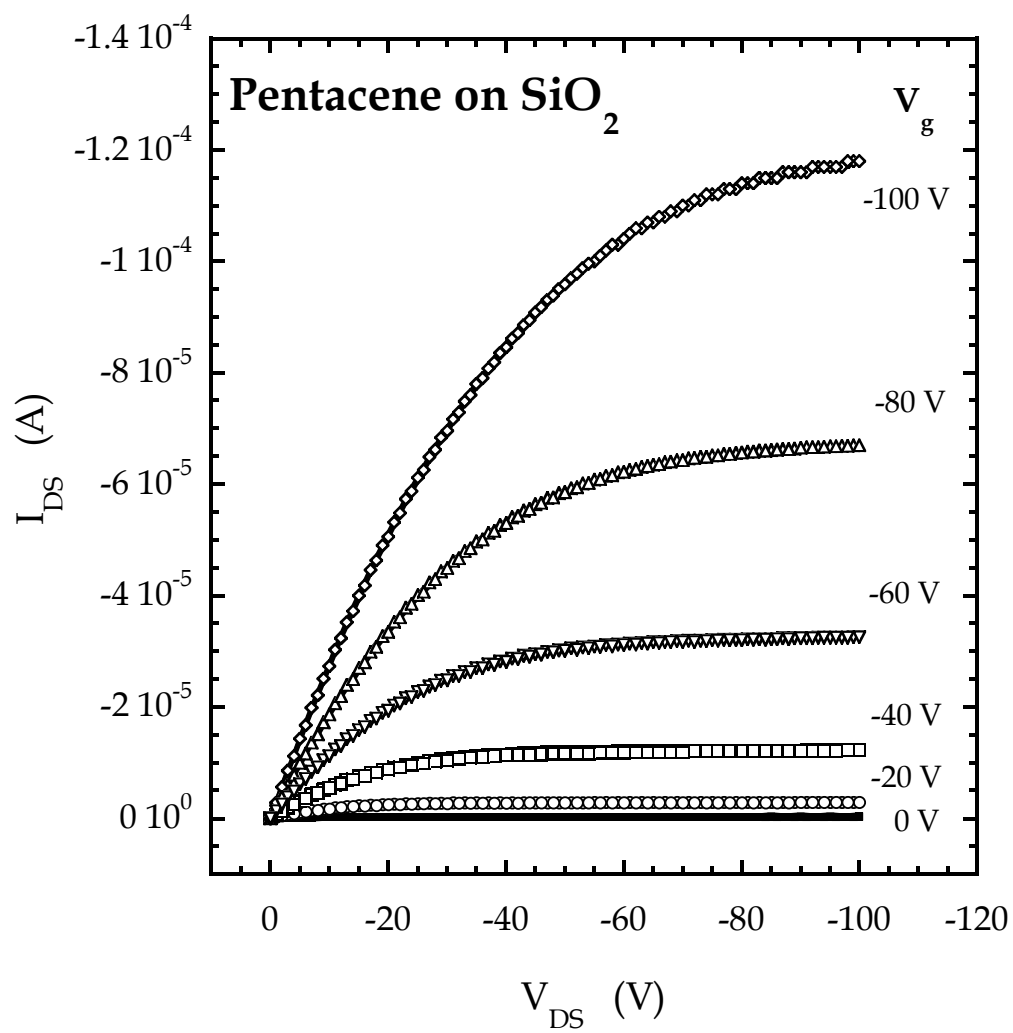
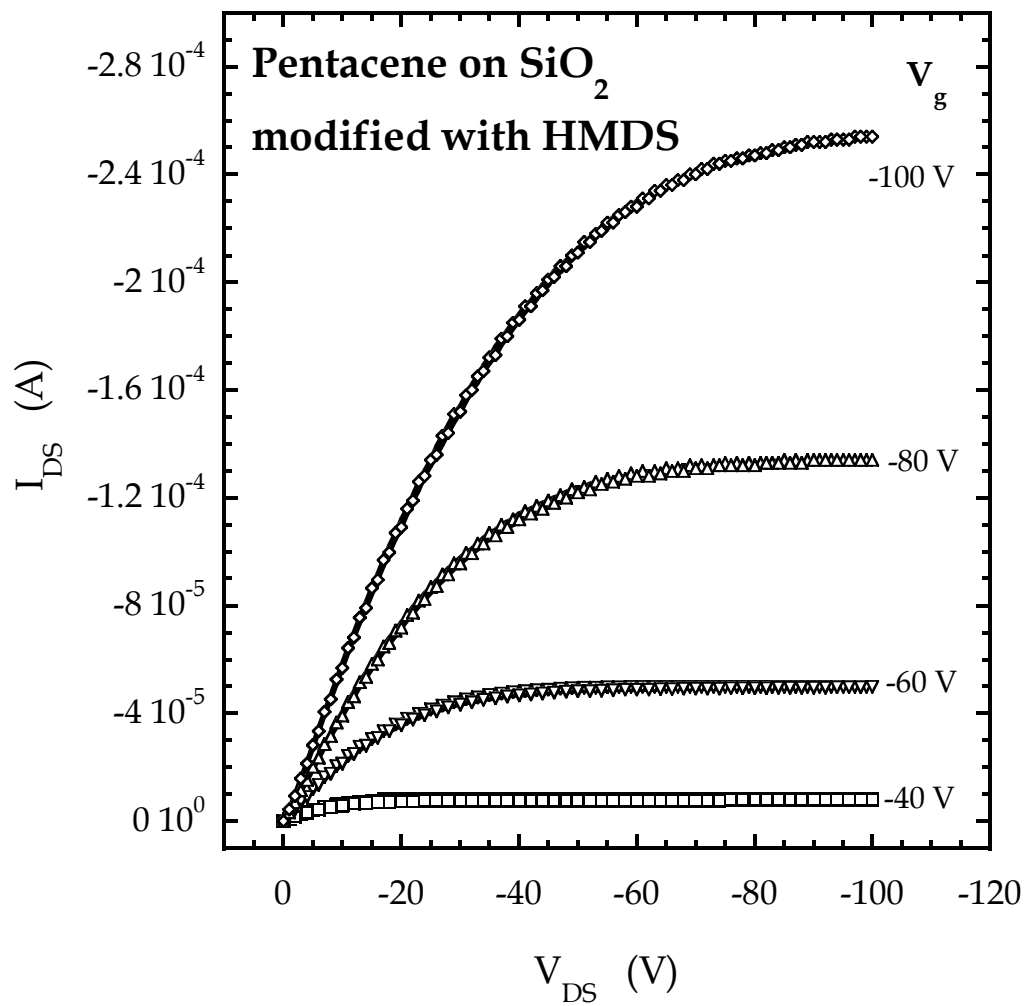


Figure 7-5 (Continued)

(b)



Other studies have also revealed strong connections between mobility and grain size [27, 29]. Hajlaoui and co-workers [27] deposited films of octithiophene at substrate temperatures ranging from room temperature to 170 °C on glass. Grain dimensions increased from 60 nm to 330 nm and this was correlated linearly with increase in OTFT mobility from 0.11 to 0.28 cm²-V⁻¹-s⁻¹. Street and co-workers [29] also found mobilities increased with grain size from 0.12 – 0.55 cm²-V⁻¹-s⁻¹ for pentacene films deposited on thermally grown SiO₂. Again, substrate temperature was increased to obtain larger grains. In these experiments, the substrates were held at room temperature. Incident flux was also constant for different energies. As a result, larger grains at higher energies could be the result of the decrease in probability of adsorption with increasing energy coupled with longer diffusion lengths at the surface owing to larger intrinsic kinetic energy.

The highest mobility of 1.374 cm²-V⁻¹-s⁻¹ was recorded for an OTFT on SiO₂ modified with HMDS, for a channel length of 31.25 μm and an incident kinetic energy of 6.7 eV. The on-off ratio and inverse subthreshold slope were 2.2 × 10¹ and 0.238 dec-V⁻¹ respectively and were reasonable for a device with this channel length.

I_{DS} vs. V_{DS} data for OTFTs on (a) bare SiO₂ and (b) SiO₂ modified with HMDS for a channel length of 75 μm and incident kinetic energy of 6.7 eV are plotted in Fig. 7-5. Performance characteristics are included in Table 7-1. Higher mobilities were obtained in general for a channel length of 31.25 μm but I_{on}/I_{off} values were poor. As may be seen, the OTFT on SiO₂ shows a weaker gate modulation than OTFTs on SiO₂ modified with HMDS. This is revealed in the value of S which is in general higher for the latter set of devices (S_{avg} = 2.6 ± 1.6 dec-V⁻¹) in comparison to the former

($S_{\text{avg}} = 0.6 \pm 0.13 \text{ dec-V}^{-1}$) where the error bars are statistical estimates. While saturation currents are within a factor of 2 ($10^{-4} - 10^{-5} \text{ A}$) for both substrates, OTFTs fabricated on SiO_2 modified with HMDS exhibit larger on currents and smaller off currents ($10^{-8} - 10^{-12} \text{ A}$) in comparison to bare SiO_2 ($10^{-5} - 10^{-8} \text{ A}$) for channel lengths of 75 μm and 125 μm . Further, $I_{\text{on}}/I_{\text{off}}$ increases with increasing channel length for both substrates. This increase is far more dramatic for SiO_2 substrates modified with HMDS resulting in much better switching properties and higher field effect mobilities in general. Aoyagi and co-workers [15] observed similar trends with OTFTs on bare SiO_2 and SiO_2 modified with HMDS.

Finally, OTFTs deposited on SiO_2 modified with HMDS exhibit larger threshold voltages (-21 to -43 V) in comparison to devices fabricated on bare SiO_2 (-9 to -19 V). Iwasa and co-workers [30] fabricated bottom contact thin film transistors with pentacene and C_{60} as the semiconducting organic films. They used a heavily doped p-type Si wafer with 400 nm SiO_2 as the bottom gate electrode. Bottom contacts were deposited on the SiO_2 layer and self-assembled monolayers (SAMs) were deposited in unexposed areas after the SiO_2 was irradiated with UV light. These workers observed a shift in threshold voltage from -11 V to 17 V for OTFTs fabricated with untreated and $(\text{CF}_3)(\text{CF}_2)_7(\text{CH}_2)_2\text{Si}(\text{OC}_2\text{H}_5)_3$ treated SiO_2 substrates respectively. For thiol SAMs deposited on metal substrates, the dipole alignment of thiol molecules could play an important role in modulation of the work function of the metal [31,32]. As a result, on SiO_2 surfaces, the ordering of SAMs molecules with molecular dipoles could produce a built-in electric field on the TFT, which is superimposed on to the externally applied gate field. These results indicate that OTFTs on SiO_2 modified with HMDS perform much better than those on are

SiO₂ with larger inverse subthreshold slopes, lower off currents and higher mobilities.

7.5 Conclusions

In conclusion, organic thin film transistors with top contacts have been fabricated from pentacene thin films deposited using supersonic molecular beams. Films deposited with higher incident kinetic energy exhibit bigger grains. Grain size (described by a correlation length) increases from 800 – 1200 nm and mobility is found to increase with grain size. Mobility is best described by charge transport dominated by thermionic emission at grain boundaries. Contact resistance is not found to play a crucial role in these OTFTs. Modification of the SiO₂ surface with HMDS does not alter morphology of multilayer pentacene films in a significant manner. However, OTFTs fabricated on SiO₂ substrates modified with HMDS exhibit higher mobilities, stronger gate modulation (inverse subthreshold slopes are higher by two orders of magnitude) and lower off currents in comparison to ones fabricated on bare SiO₂. Lower subthreshold slopes for devices on SiO₂ modified with HMDS reveal that there could be reduced charge trapping at this interface.

7.6 References

1. C. D. Dimitrakopoulos and P. R. L. Malenfant, *Adv. Mater.* **14**, 99 (2002).
2. G. Horowitz, *Adv. Mater.* **10**, 365 (1998).
3. C. W. Tang and S. A. VanSlyke, *Appl. Phys. Lett.* **51**, 913 (1987).
4. K. Kudo, M. Yamashina and T. Moriizumi, *Jpn. J. Appl. Phys* **23**, 130 (1984).
5. J. H. Burroughes, D. D. C. Bradley, A. R. Brown, R. N. Marks, K. Mackay, R. H. Friend, P. L. Burns and A. B. Holmes, *Nature* **347**, 539 (1990).
6. F. Ebisawa, T. Kurokawa and S. Nara, *J. Appl. Phys.* **54**, 3255 (1983).
7. A. Tsumura, H. Koezuka and T. Ando, *Appl. Phys. Lett.* **49**, 1210 (1986).
8. R. Ruiz, D. Choudhary, B. Nickel, T. Toccoli, K. -C. Chang, A. C. Mayer, P. Clancy, J. M. Blakely, R. L. Headrick, S. Iannotta and G. G. Malliaras, *Chem. Mater.* **16**, 4497 (2004).
9. S. R. Forrest, *Chem. Rev.* **97**, 1793 (1997).
10. Y. -Y. Lin, D. J. Gundlach, S. F. Nelson and T. N. Jackson: *IEEE Electron Device Lett.* **18**, 606 (1997).
11. T. W. Kelley, L. D. Boardman, T. D. Dunbar, D. V. Muyres, M. J. Pellerite and T. P. Smith, *J. Phys. Chem. B* **107**, 5877 (2003).
12. A. Dodabalapur, L. Torsi, and H. E. Katz, *Science* **268**, 270 (1995).
13. S. C. Lim, S. H. Kim, J. H. Lee, M. K. Kim, D. J. Kim and T. Zyung, *Syn. Met.* **148**, 75 (2005).
14. H. Yang, T. J. Shin, M. -M. Ling, K. Cho, C. Y. Ryu and Z. Bao, *J. Am. Chem. Soc.* **127**, 11542 (2005).

15. I. Yagi, K. Tsukagoshi and Y. Aoyagi, *Appl. Phys. Lett.* **86**, 103502–1 (2005).
16. M. Shtein, J. Mapel, J. B. Benziger and S. R. Forrest, *Appl. Phys. Lett.* **81**, 268 (2002).
17. D. Knipp, R. A. Street, A. Völkel and J. Ho, *J. Appl. Phys.* **93**, 347 (2003).
18. H. Klauk, M. Halik, U. Zschieschang, G. Schmid, W. Radlik and W. Weber, *J. Appl. Phys.* **92**, 5259 (2002).
19. F. De Angelis, T. Toccoli, A. Pallaoro, N. Coppedè, L. Mariucci, G. Fortunato and S. Iannotta, *Synth. Met.* **146**, 291 (2004).
20. S. E. Roadman, N. Maity, J. N. Carter and J. R. Engstrom, *J. Vac. Sci. Technol. A* **16**, 3423 (1998).
21. A. S. Killampalli, T. W. Schroeder and J. R. Engstrom, *Appl. Phys. Lett.* **87**, 033110 (2005).
22. A. S. Killampalli and J. R. Engstrom, submitted to *Appl. Phys. Lett.* October 2005.
23. P. Dumas, B. Bouffakhreddine, C. Amra, O. Vatel, E. Andre, R. Galindo and F. Salvan, *Europhys. Lett.* **22**, 717 (1993).
24. G. W. Collins, S. A. Letts, E. M. Fearon, R. L. McEachern and T. P. Bernat, *Phys. Rev. Lett.* **73**, 708 (1994).
25. C. Douketis, Z. Wang, T. L. Haslett and M. Moskovits, *Phys. Rev. B* **51**, 11022 (1995).
26. F. Biscarini, P. Samorí, O. Greco and R. Zamboni, *Phys. Rev. Lett.* **78**, 2389 (1997).
27. G. Horowitz and M. E. Hajlaoui, *Adv. Mater.* **12**, 1046 (2000).
28. G. Horowitz, M. E. Hajlaoui, and R. Hajlaoui, *J. Appl. Phys.* **87**, 4456 (2000).

29. D. Knipp, D. K. Murti, B. Krusor, R. Apte, L. Jiang, J. P. Lu, B. S. Ong and R. A. Street, *Mater. Res. Soc. Symp. Proc.* **665**, 207 (2002).
30. S. Kobayashi, T. Nishikawa, T. Takenobu, S. Mori, T. Shimoda, T. Mitani, H. Shimotani, N. Yoshimoto, S. Ogawa and Y. Iwasa, *Nat. Mat.* **3**, 317 (2004).
31. I. H. Campbell, S. Rubin, T. A. Zawodzinski, J. D. Kress, R. L. Martin, D. L. Smith, N. N. Barashkov and J. P. Ferraris, *Phys. Rev. B* **54**, 14321 (1996).
32. I. H. Campbell, J. D. Kress, R. L. Martin, D. L. Smith, N. N. Barashkov and J. P. Ferraris, *Appl. Phys. Lett.* **71**, 3528 (1997).

8. Summary

Interfaces between inorganic materials and organic molecules are becoming increasingly important with several key applications emerging in the areas of molecular and organic electronics, barrier layers and other components of integrated circuits as well as process steps involved in the semiconductor industry. A well collimated effusive beam is a useful tool to study the formation of interfaces between metalorganic species and self-assembled monolayers (SAMs) which are model organic surfaces. In combination with x-ray photoelectron spectroscopy (XPS), vital information concerning reaction kinetics, spatial extent and stoichiometry of reaction can be obtained.

Our efforts directed at the formation of inorganic-organic interfaces involving reaction of a transition metal coordination complex with self-assembled monolayers represent one of the earliest studies in the field. Employing a microcapillary array doser as an effusive source for the metal complex, this is the first such study from our research group as well. Specifically, the reactions of tetrakis(dimethylamido)titanium, $\text{Ti}[\text{N}(\text{CH}_3)_2]_4$, with self assembled monolayers possessing $-\text{OH}$, $-\text{NH}_2$ and $-\text{CH}_3$ terminal groups have been examined (Chapter 3). The initial probability of reaction of $\text{Ti}[\text{N}(\text{CH}_3)_2]_4$ was found to be largest on the chemical oxide surface (starting surface to form the SAMs). On the SAM-terminated surfaces it was found that reaction probabilities followed the order: $-\text{OH} > -\text{NH}_2 > -\text{CH}_3$. In all cases the reaction probability did not vary more than a factor of 2 over the substrate temperature range examined, $T_s = -50\text{ }^\circ\text{C}$ to $110\text{ }^\circ\text{C}$. In addition, in all cases the kinetics of adsorption, i.e. the coverage-exposure relationships, could be

sufficiently well described by a first-order Langmuirian model, and the saturation coverages did not depend strongly on the substrate temperature. Angle-resolved XPS revealed that penetration of the SAMs occurred in the cases of the $-\text{OH}$ and $-\text{CH}_3$ terminated SAMs. In particular, the apparent reactivity between $\text{Ti}[\text{N}(\text{CH}_3)_2]_4$ and the $-\text{CH}_3$ terminated SAM could be completely accounted for by assuming that reaction occurred only at the SAM/ SiO_2 interface. In contrast, concerning the $-\text{NH}_2$ terminated SAM, results from ARXPS were completely consistent with $\text{Ti}[\text{N}(\text{CH}_3)_2]_4$ reaction only at the terminal $-\text{NH}_2$ group. Results for the $-\text{OH}$ SAM indicated $\text{Ti}[\text{N}(\text{CH}_3)_2]_4$ reactivity at the terminal $-\text{OH}$ group and at the SAM/ SiO_2 interface. Examination of the stoichiometry of the adlayers (i.e. the Ti:N ratio), indicated that reaction of $\text{Ti}[\text{N}(\text{CH}_3)_2]_4$ and subsequent loss of ligands was significant on all surfaces, particularly for $T_s \geq 30$ °C. On all surfaces and at -50 °C elimination of ~ 2 $\text{N}(\text{CH}_3)_2$ ligands was apparent. As substrate temperature increased from -50 to 110 °C, about one additional ligand was lost on all surfaces, except for the $-\text{NH}_2$ terminated SAM where about 2 additional ligands were lost. On the $-\text{NH}_2$ terminated SAM, saturation corresponded to one adsorbed $\text{Ti}[\text{N}(\text{CH}_3)_2]_4$ molecule per two SAM molecules, which is consistent with the steric limitation between $\text{Ti}[\text{N}(\text{CH}_3)_2]_4$ fragments expected for nearest neighbor distances of about $7\text{--}8$ Å. Studies examining the formation of similar interfaces are essential to establishing a comprehensive database useful for a wide array of applications as mentioned above.

Organic semiconductors are also being widely studied for future applications in electronics and optoelectronics. Advantages include lower processing costs and processing temperatures, compatibility with a wide variety of substrates including flexible ones and the ability to control properties of the

film by modification of either the structure of the precursor molecule or the interface between the organic film and a suitable substrate. Supersonic molecular beams have been employed as sources for deposition of thin films of pentacene, an organic semiconductor, on bare SiO₂ surfaces and SiO₂ surfaces modified with hexamethyldisilazane (HMDS). A key difference in deposition of organic materials, compared to more conventional inorganic materials like metals, semiconductors and oxides, involves the presence of strong covalent and ionic bonding in the latter class of materials, whereas organic materials are often bound by rather weak dispersion (van der Waals) forces and are often known to crystallize in different phases, separated in total energy by amounts on the order of a few $k_B T$. As a consequence, considerable promise exists in the use of energy tunable molecular beams for the deposition of organic thin films. The first studies of energetic deposition of the organic semiconductor, pentacene, have been carried out in our research group with a new ultrahigh vacuum system designed for experiments at the Cornell High Energy Synchrotron Source (CHESS).

Chapter 4 dealt with the nucleation of pentacene on SiO₂ using these energetic molecular beams. The first monolayer essentially completes before the second layer begins to nucleate. The adsorption of pentacene is trapping mediated and accommodation of both perpendicular and parallel momentum are equally important to the process of adsorption. The variation of the maximum island density with deposition conditions can be understood in terms of atomistic nucleation theory with a critical nucleus size of four molecules.

The nucleation of pentacene on SiO₂ surfaces modified with HMDS has been detailed in Chapter 5 and several differences and some similarities to growth on clean SiO₂ have been observed. First, the kinetics of growth in terms

of the probability of adsorption on the two surfaces is similar and exhibits the characteristics of trapping, which becomes less efficient at higher incident kinetic energies. Trapping is more efficient on the surface modified with HMDS. Two key differences are observed concerning the density and nature of the islands that are formed before a continuous thin film is deposited. First, on the SiO₂ surface modified with HMDS, the islands that are formed are predominantly two molecules high. As there is no direct structural information on these islands, e.g., from x-ray diffraction, the possibility that a different structural phase is formed cannot be excluded, and this could be the cause for the observed island morphology. Clearly, HMDS has produced a change in the pentacene–substrate interaction and consequently the energetics of single vs. double molecular high islands. The second difference that has been observed involves the maximum island density, which is much larger on the SiO₂ surface modified with HMDS. The fact that this density exhibits no identifiable trend with the deposition rate, unlike what is observed on clean SiO₂, suggests a change in the mechanism for nucleation to one that is heterogeneous and defect-mediated. Likely defects include unmodified SiO₂-like areas on the surface, or perhaps regions that possess particularly high densities of CH₃(a) groups. More detailed characterization of the organic monolayer might help resolve this issue.

Pentacene thin film deposition has been described in Chapter 6. Films have been deposited on bare SiO₂ and SiO₂ modified with hexamethyldisilazane (HMDS) and morphology becomes three-dimensional beyond the first few monolayers as seen by atomic force microscopy (AFM). Pentacene film thickness decreases with increasing incident kinetic energy while the incident flux is maintained a constant. This is indicative of trapping-mediated

adsorption of pentacene molecules on a multilayer film. The ratio of multilayer to submonolayer deposition rate scales with incident kinetic energy (E_i) and incident angle (θ_i) as $E_i \cos^n \theta_i$ where the exponent $n = 0.5$. This is indicative of the importance of non-normal energy to film deposition. All deposited films exhibit a growth exponent $\beta > 0.5$ indicative of rapid roughening. β also increases with more glancing angles of incidence owing to shadowing effects. Initial experiments have been carried out to study the effect of substrate temperature on the kinetics of film deposition and film morphology. Film thickness decreases with increasing substrate temperature owing to significant desorption at higher temperatures. Films deposited at a substrate temperature of $-73\text{ }^\circ\text{C}$ are significantly smoother than films deposited at higher temperatures of $30\text{ }^\circ\text{C}$ and $75\text{ }^\circ\text{C}$ respectively. This could be associated with a change in microstructure and additional experiments involving x-rays as a probe of film structure at CHESS will prove useful. Deposition of pentacene films on SiO_2 modified with HMDS results in similar three-dimensional structures. However, β is lower on these substrates indicative of a slower process of roughening.

Finally, electronic properties of pentacene films deposited using supersonic beams have been studied by fabricating organic thin film transistors with top contacts (Chapter 7). These devices exhibit reasonable performance characteristics with reasonable saturation and off currents, threshold voltages and subthreshold slopes. While the requirements for industrial applications have been met in some cases, further optimization of deposition and fabrication processes could result in an improvement in these characteristics. Incident kinetic energy can be used to tune grain size at room temperature. Films deposited with higher incident kinetic energy exhibit bigger grains. Grain size

(described by a thickness-averaged correlation length) increases from 800 – 1200 nm and mobility is found to increase with grain size. Mobility is best described by charge transport dominated by thermionic emission at grain boundaries. Contact resistance is not found to play a crucial role in these OTFTs. One approach to improve performance characteristics has been the modification of the SiO₂ surface with HMDS. This modification does not alter film morphology in the multilayer regime. However, OTFTs fabricated on SiO₂ substrates modified with HMDS exhibit higher mobilities, stronger gate modulation (inverse subthreshold slopes are higher by two orders of magnitude), higher saturation currents and lower off currents in comparison to transistors fabricated on bare SiO₂. Higher inverse subthreshold slopes reveal that there could be reduced charge trapping at the interface between the pentacene film and SiO₂ modified with HMDS. These OTFTs also exhibit higher threshold voltages which could be attributed to generation of an additional electric field owing to dipole interactions at the semiconductor–dielectric interface. In conclusion, supersonic gas source deposition has been demonstrated to be a promising technique for controlled deposition of organic semiconductor films with good electrical properties.

9. Appendices

9.1 Temperature calibration

Shown in Fig. 9–1 are temperature calibration curves relating the temperature at the surface of the sample with respect to the temperature registered by a thermocouple mounted at the back of the sample heater for the manipulator mounted on the molecular beam scattering chamber (section 2.1). Temperature at the surface of the sample was measured by placing a second thermocouple between the sample of size 16.75 mm × 16.75 mm and the retaining ring. The sample holder was of the picture frame assembly type with an open back. The smooth curves in Fig. 9–1 represent fits to a polynomial function:

$$T = A + B * V + C * V^2 + D * V^3 \quad (9-1)$$

where T is the temperature of either the surface of the sample or the back of the heater and V is the voltage supplied to the heater. The sample was actively cooled with liquid nitrogen at the same time. The best fit to the data for sample temperature yielded the following parameters: $A = -15.028$, $B = -141.99$, $C = 141.49$ and $D = -24.496$. These calibration curves were employed in controlling sample temperature during experiments involving the formation of inorganic–organic interfaces between $\text{Ti}[\text{N}(\text{CH}_3)_2]_4$ and self-assembled monolayers with $-\text{OH}$, $-\text{NH}_2$ and $-\text{CH}_3$ terminal groups.

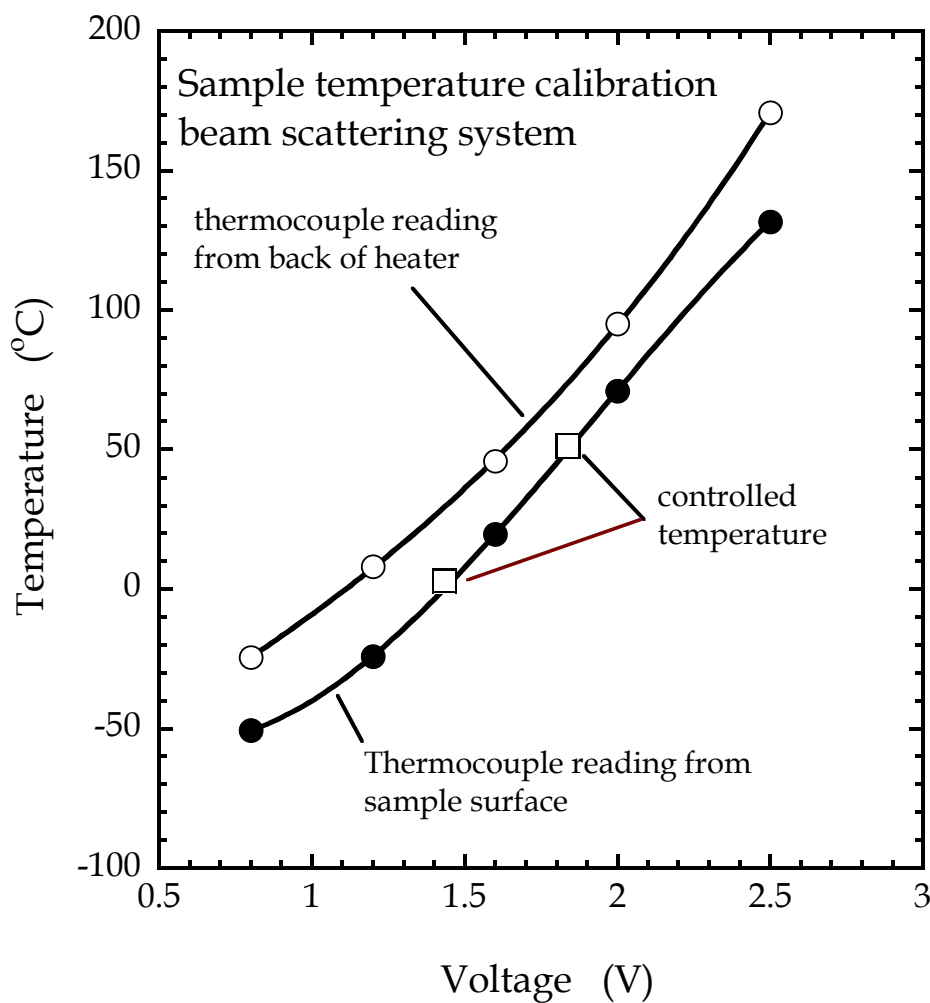


Figure 9-1 Temperature calibration curve for Si wafers of size 16.75 mm × 16.75 mm mounted on the picture frame platen for the manipulator on the beam scattering chamber. The thermocouple reading on the back of the heater is calibrated to the temperature at the surface using a second thermocouple clamped in-between the sample surface and the retaining ring. The smooth curves are polynomial fits to the data.

Shown in Fig. 9–2 are temperature calibration curves relating the temperature at the surface of the sample with respect to the temperature registered by a thermocouple mounted at the back of the sample heater for the manipulator mounted on the thin film deposition system (G–Line system) (section 2.2.7.1). Samples were Si wafers of size 16.75 mm × 16.75 mm mounted on the Mo solid back platen provided with a transferable thermocouple used to measure the temperature at the surface of the sample. This transferable thermocouple was sandwiched between the sample and a mounting clip. The smooth curves in Fig. 9–2 represent fits to the polynomial function in Eqn. (9–1) where T is the temperature of either the surface of the sample or the back of the heater and V is the voltage supplied to the heater. The sample was actively cooled with liquid nitrogen at the same time. The best fit to the data for sample temperature yielded the following parameters: $A = -101.57$, $B = 50.94$, $C = 1.1218$ and $D = 0.05625$. These calibration curves were employed in controlling sample temperature during experiments involving the deposition of pentacene thin films employing a supersonic molecular beam.

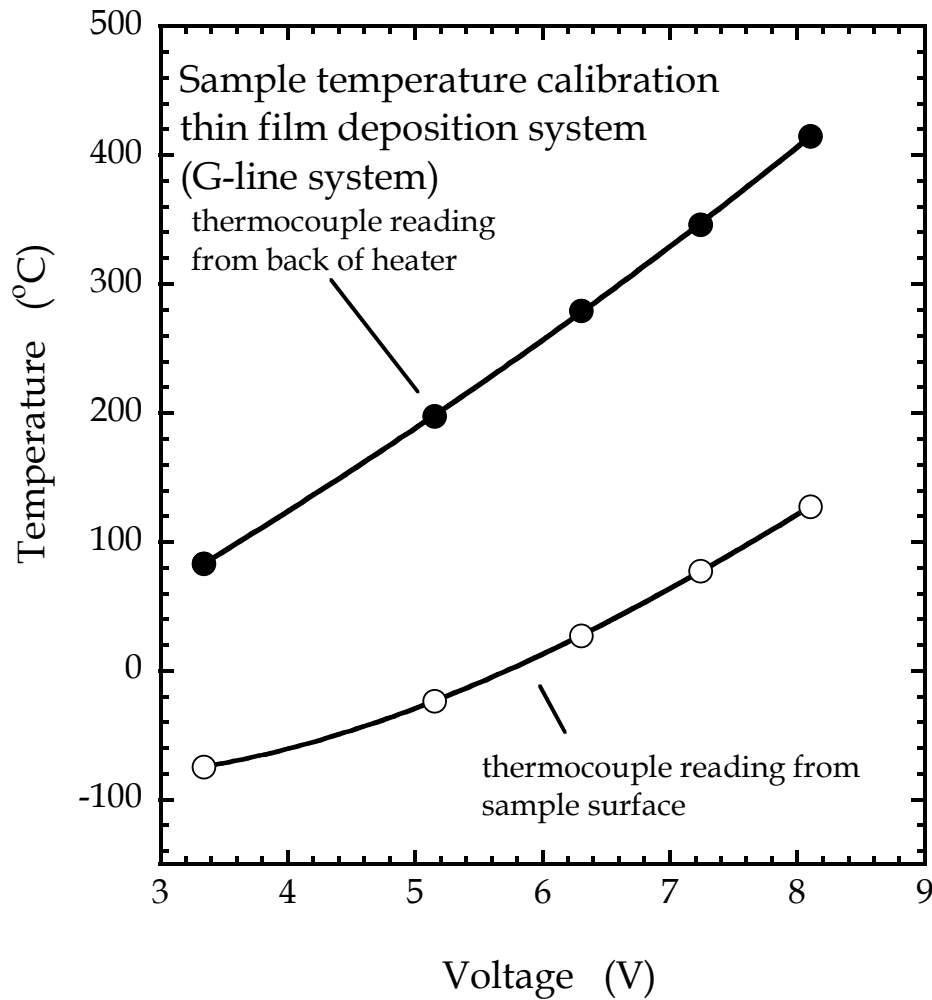


Figure 9-2 Temperature calibration curve for Si wafers of size 16.75 mm × 16.75 mm mounted on a Mo platen with clips. The manipulator for this platen was mounted on the thin film deposition system (G-Line system). The thermocouple reading on the back of the heater is calibrated to the temperature at the surface using a transferable thermocouple clamped between the surface of the sample and a clip. The smooth curves are polynomial fits to the data.

9.2 Heatable skimmer mounting plate

A mounting plate was designed for the skimmer of the thin film deposition system (G-Line system) (described in section 2.2.7.1). The AUTOCAD drawing is shown in Fig. 9-3. The skimmer was built out of macor so that it would be electrically isolated from the vacuum system. In addition, the mounting plate could be positioned in the forward or rear position. Silver plated threaded rods were employed to move the plate to the rear position.

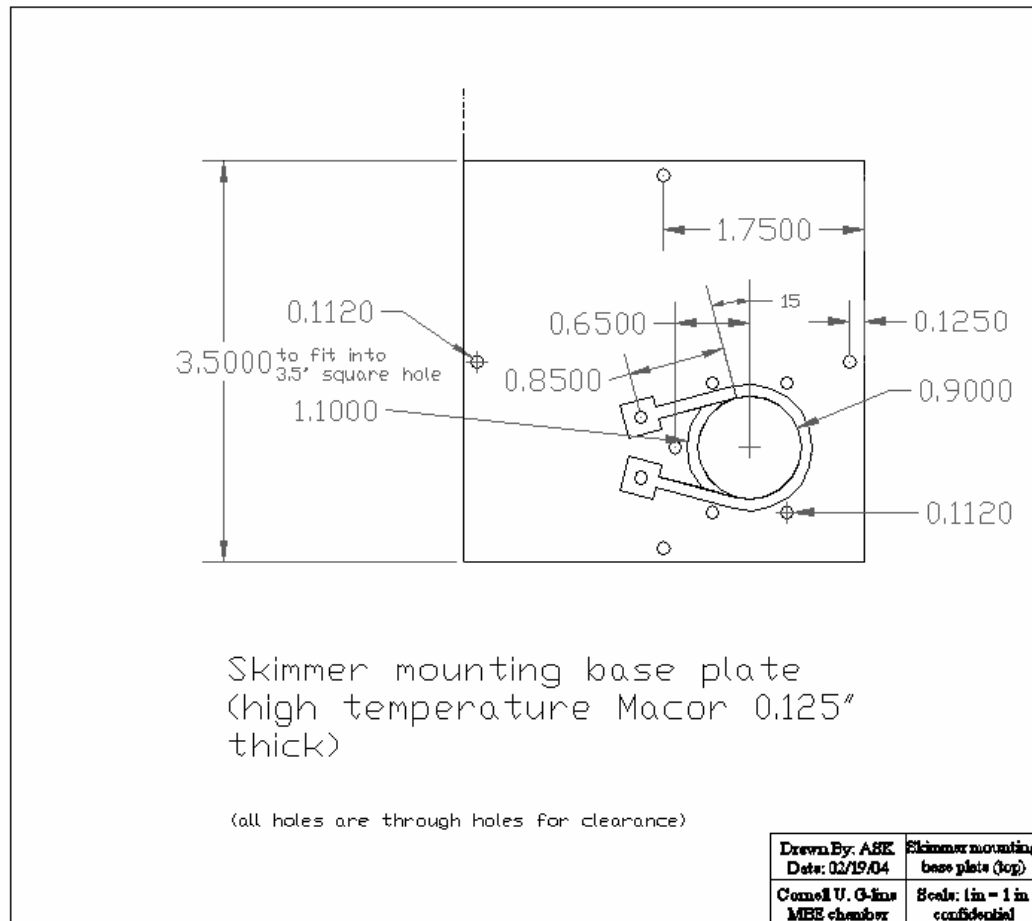


Figure 9–3 AUTOCAD drawing (front view) of macor mounting plate for skimmer on the thin film deposition system (G-Line system). Both forward and rear positions are accessible.